Very-high-energy γ-ray observations of pulsar wind nebulae and cataclysmic variable stars with MAGIC and development of trigger systems for IACTs

Rubén López Coto

Departament de Física

Universitat Autònoma de Barcelona

A thesis submitted for the degree of

PhilosophiæDoctor (PhD)

2 July 2015

2

The imaging atmospheric Cherenkov technique and the IACTs MAGIC and CTA

In this chapter we will describe the concept behind the detection of gamma rays through the imaging atmospheric Cherenkov technique. We will also describe the IACT arrays on which this thesis focuses: the Major Atmospheric Gamma-ray Imaging Cherenkov (MAGIC) telescopes and the Cherenkov Telescope Array (CTA). The hardware and techniques used to analyze the data of MAGIC will be described in detail. We will give an overview of the CTA project, together with a brief description of the telescope types involved in the project.

2.1 The imaging atmospheric Cherenkov technique

The EM spectrum spans more than 20 orders of magnitude in energy from radio to TeV gamma rays. The atmosphere is transparent to most of the radiation up to the UV, but higher energy photons do not penetrate into the atmosphere due to their interaction with the air molecules. A picture showing the bounds of the EM spectrum and the transparency of the atmosphere to all of them is shown in Figure 2.1. To detect those photons, one has to use satellites where they have not been blocked yet. Unfortunately, due to the low fluxes, the collection area offered by satellites is not large enough at energies exceeding 100 GeV.

Due to the interaction with the atmospheric nuclei, VHE particles produce cascades, also known as EASs. As the relativistic charged particles produced in the cascade move faster than the speed of light in the atmosphere, they produce Cherenkov light at wavelengths ranging from IR to UV. In the following, we will give a more detailed description of the shower development in the atmosphere and the way we can detect the Cherenkov light using optical telescopes. For a

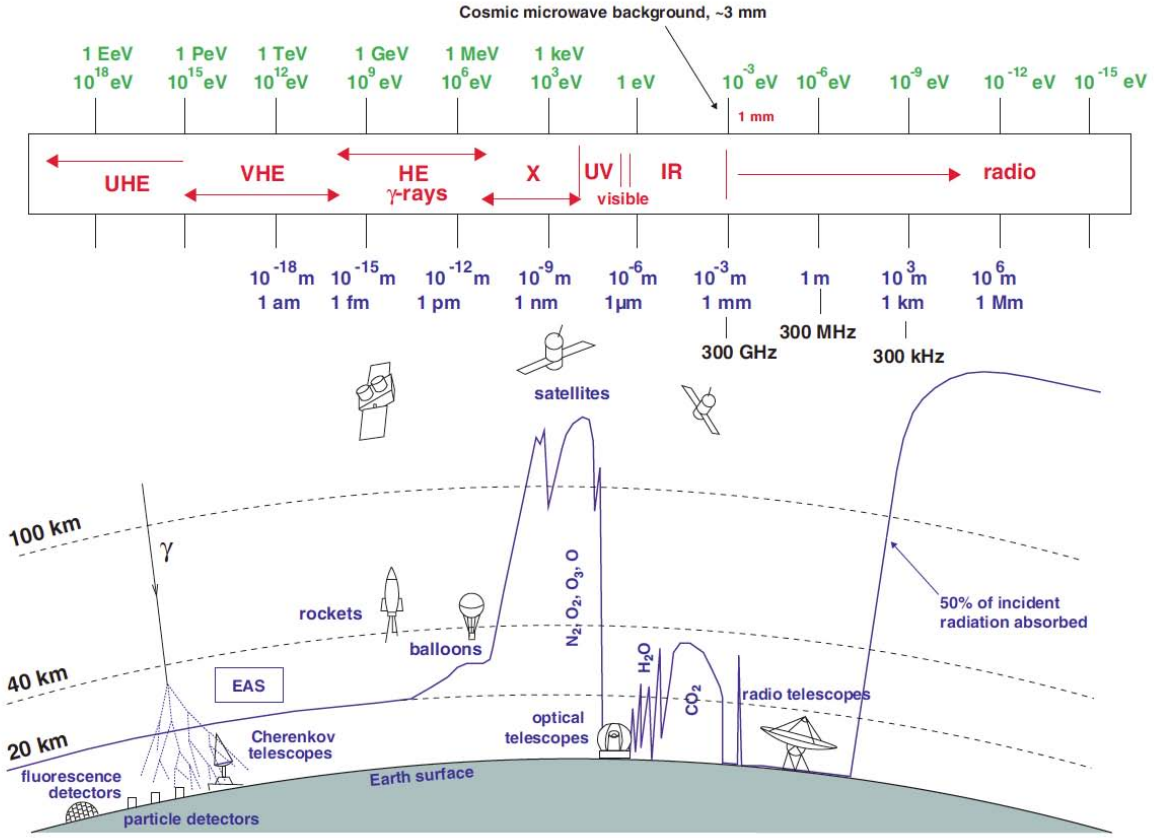

Figure 2.1: The bounds of the EM spectrum (above) as seen from the altitude where photons are fully absorbed in the atmosphere (below). From Longair (1992); Moralejo (2000); Wagner (2006).

more detailed review, see Engel et al. (2011).

2.1.1 Types of showers

To describe the particle interaction with the air nuclei it is better to describe the atmosphere in terms of the so-called *atmospheric depth* X, which is the product of particle density and distance or the amount of mass per unit of area that an incident particle encounters on its path. For vertical incidence, the atmospheric depth at sea level is $X_{\text{air}} \sim 1013$ g cm^{-2}. We will describe the characteristics of the particle cascades produced depending on the primary particle initiating the shower.

2.1.1.1 EM showers

When a gamma ray enters into the atmosphere, if its energy is $E \gtrsim 20$ MeV, it undergoes $e^{\pm}$ pair creation in the presence of an air nucleus. These e^- and e^+ suffer bremsstrahlung if their energy exceeds the critical energy $E_C = 86$ MeV, which is the energy for which energy losses by

bremsstrahlung and ionization are equal. The bremsstrahlung process produces photons that are still very energetic, undergoing further pair production. Eventually, a so-called EM shower of e^-, e^+ and gamma rays develops (see left panel of Figure 2.2). The energy loss dE of an e^- with path dx due to bremsstrahlung can be written as:

$$\frac{dE}{dx} = -\frac{E}{X_0^e} \tag{2.1}$$

where X_0^e=37.2 g cm^{-2} is the radiation length for an e^- (or e^+) in air. The radiation length of a γ-ray photon X_0^γ can be written as a function of that of the electron: X_0^γ=7/9X_0^e. An EM shower is roughly symmetric with respect to the shower axis. The first interaction point is not very dependent on the γ-ray energy and is situated at a height of about 20–30 km above sea level (a.s.l.) for a vertically incident particle. Roughly speaking, the number of particles is doubled each step of the cascade, and the energy of the particles halved. When the energy of $e^\pm$ reaches E_C, the cascading stops and the number of particles is maximum. The height a.s.l. at which this condition is fulfilled is known as *height* of the shower maximum ($H_{\max}$). This height is inversely proportional to the logarithm of the energy $H_{\max} \propto 1/\ln(E)$ of the primary gamma ray.

2.1.1.2 Hadronic showers

When the primary particle generating the EAS is a hadron, the first interaction with an atmospheric nucleus is governed by the strong force. In this process, mostly pions are created (90%, in roughly equal proportions $\pi^0 : \pi^+ : \pi^- \rightarrow$ 1:1:1) as well as kaons (10%) and light baryons (p, $\bar{\text{p}}$, n, $\bar{\text{n}}$) in a much smaller proportion. Hadrons and pions undergo further collisions. The shower grows until the energy per nucleon reaches the minimum energy required for pion production decay (∼1 GeV). In addition pions decay into photons, e^-, e^+ and muons, generating secondary EM and muon-initiated showers. The pionic and muonic decays involved in a hadronic shower are the following:

$$\begin{array}{lll} \pi^0 \longrightarrow \gamma\gamma & ; \quad \pi^+ \longrightarrow \mu^+\nu_\mu & ; \quad \pi^- \longrightarrow \mu^-\bar{\nu}_\mu \\ \mu^+ \longrightarrow e^+\nu_e\bar{\nu}_\mu & ; \quad \mu^- \longrightarrow e^-\bar{\nu}_e\nu_\mu & \end{array}$$

As illustrated in the right panel of Figure 2.2, several EM subcascades are generated. Apart from that, due to the strong interaction, the transverse momentum of secondary hadrons is larger than that of leptons in EM showers, therefore hadronic showers are wider.

The timing of the showers is also important to differentiate them. γ-ray initiated showers develop in less than 3 ns for impact parameters smaller than the hump (the region where the Cherenkov photon density is highest), while hadron-initiated ones take more than 10 ns to develop. Figure 2.3 shows MC simulations of two EASs produced by a gamma ray and a proton of the same energy. One can clearly see the γ-ray showers are more "beamed" than proton showers.

2.1.2 Cherenkov light

The existence of Cherenkov light was first proposed by Pavel Cherenkov (Cherenkov 1934). It is an effect produced by ultrarrelativistic charged particles moving at a speed faster than the speed

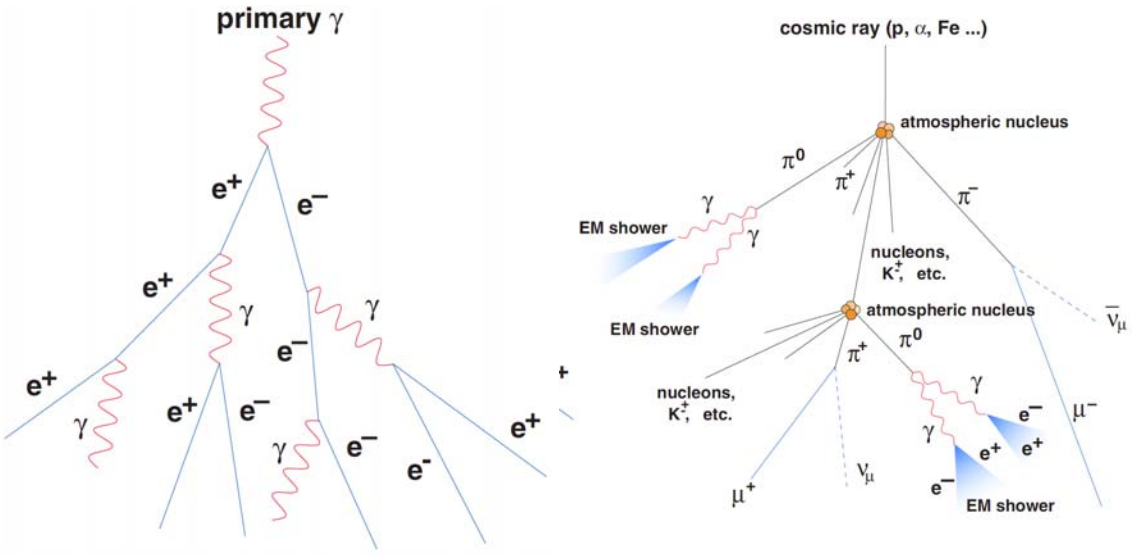

Figure 2.2: Scheme of an EM (left panel) and hadronic (right panel) initiated showers. Taken from Wagner (2006).

of light in the medium. A charged particle moving at a speed v in a medium with refraction index n, the medium polarizes along its track. If the speed of the particle is $v < c/n$, where c is the speed of light in vacuum, the polarization is symmetrical and no electric field is produced at long distances (see Figure 2.4a). On the other hand, if the speed of the particle is $v > c/n$ it moves faster than the EM radiation that induces the polarization, which is not symmetric anymore as shown in Figure 2.4b. To compensate the effect of a non-symmetric dipole medium, an EM shock wave called Cherenkov radiation is produced. This radiation is emitted in the form of a cone at an angle θ (see Figure 2.4c) such as:

$$\cos\theta = \frac{c}{v\, n(\lambda)} \tag{2.2}$$

where $n(\lambda)$ is the spectral index of the medium, which depends on the wavelength of the Cherenkov light. The number of Cherenkov photons produced by an ultrarrelativistic particle as a function of the length and wavelength is given by (Yao et al. 2006):

$$\frac{d^2N}{dx\, d\lambda} = \frac{2\pi\alpha}{\lambda^2}\left(1 - \frac{c^2}{v^2\, n^2(\lambda)}\right) \approx 370 \sin^2\theta(\lambda)\ [\mathrm{eV}^{-1}\mathrm{cm}^{-1}] \tag{2.3}$$

where $\alpha \approx 1/137$ is the fine structure constant and λ the wavelength.

Cherenkov light produced in the atmosphere The cascades originated in the atmosphere contain several relativistic particles that travel faster than the speed of light in the atmosphere. The fact that showers should produce Cherenkov light was pointed out by Blackett (1948) and later measured by Jelley & Porter (1963). According to the Cherenkov light propagation shown

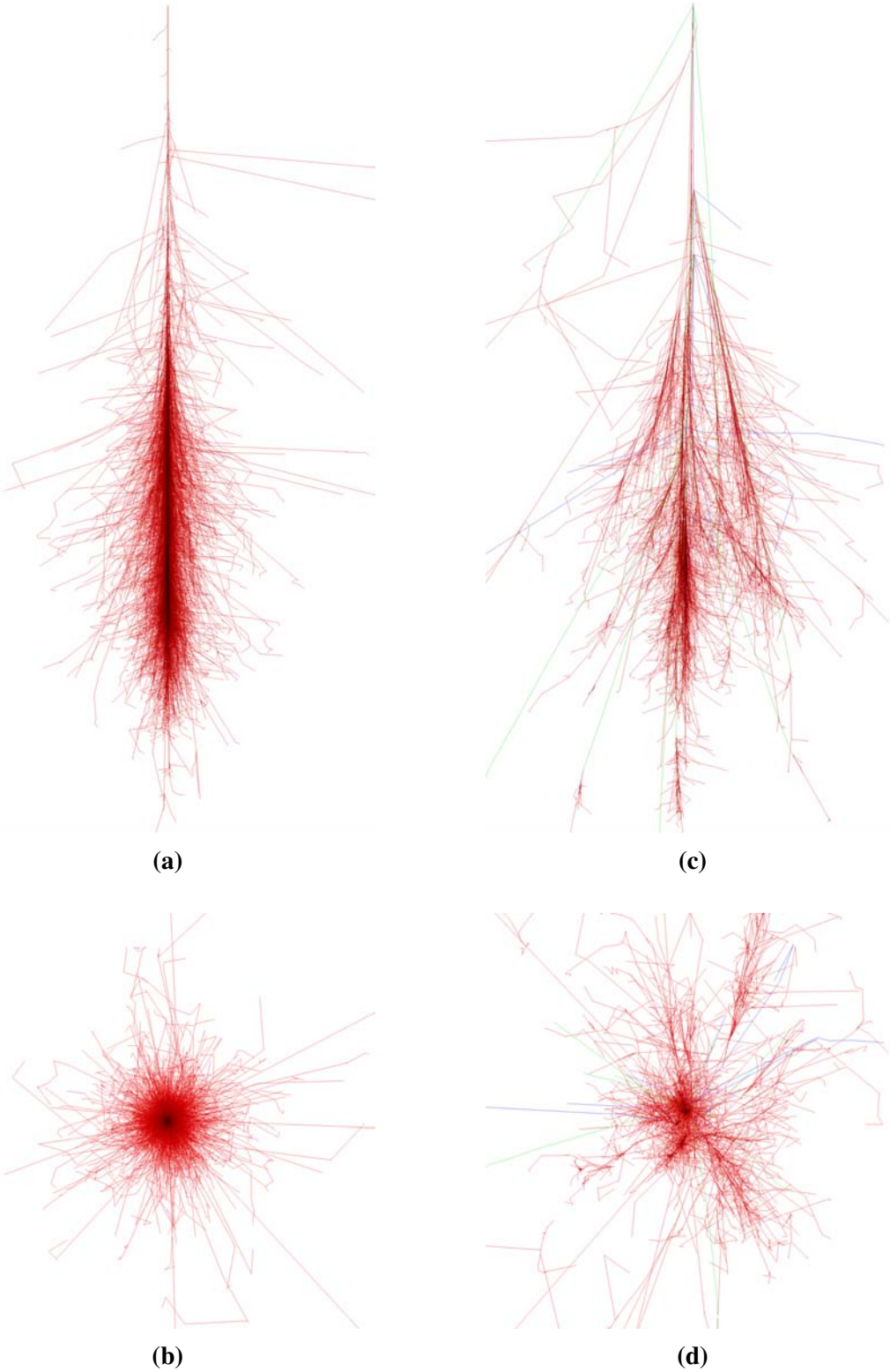

Figure 2.3: Upper left panel: 100 GeV γ-ray shower particle track. **Lower left panel:** The same γ-ray shower seen on the transversal plane. **Upper right panel:** 100 GeV proton shower particle track. **Lower right panel:** The same proton shower seen on the transversal plane. Red lines correspond to e^- , e^+ and γ-ray tracks, green for muons and blue for hadrons.

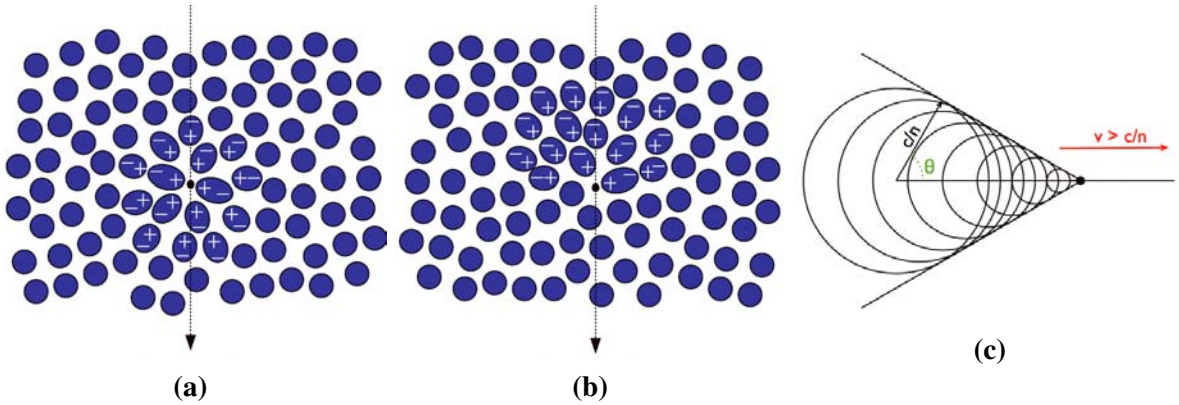

Figure 2.4: Left panel: Polarization of a medium when a charge particle crosses it moving at a speed $v < c/n$. **Middle panel:** Polarization of a medium when a charge particle crosses it moving at a speed $v > c/n$. **Right panel:** Schematic view of the Cherenkov radiation emitted by the particle shown in the middle figure.

in Figure 2.4c, a vertical incident ultrarrelativistic particle illuminates a doughnut ring on the ground. The superposition of the rings generated by all the particles emitting Cherenkov light form a circle on the ground. Since $(n-1) \sim \mathcal{O}(10^{-4})$ in the air, the maximum angle from equation 2.2 is $\theta \lesssim 1^{\circ}$.

From equation 2.3 we see that the number of Cherenkov photons is inversely proportional to the square of their wavelength. From here it derives that most of the photons are emitted in the UV, as can be seen in Figure 2.5. The observed spectrum is different from the emitted one due to several attenuation processes that occur in the particles track: Rayleigh scattering off air molecules ($\propto \lambda^{-4}$), that mainly affects the UV photons; Mie scattering off aerosols, water droplets and dust; UV absorption by ozone molecules; and infrared absorption due to H_2O and CO_2. Due to all these processes, the maximum of Cherenkov light observed at 2200 m a.s.l. in a shower peaks at around 330 nm, independent on the energy of the incident particle (see Figure 2.5).

For vertical incident gamma rays, the Cherenkov photon density is almost constant in a ring with radius $\lesssim 120$ m centered in the core of the shower as it is shown in Figure 2.6. It is higher in the region known as the *hump* and then it fades away. The *hump* is produced by the increase in the angle θ due to a change in the refracting index of the atmosphere at different heights. The energy of an incident γ-ray photon is proportional to the Cherenkov photon density detected on the ground, fact used to reconstruct their energy. In the case of hadrons, this relation is not fulfilled, as can be seen in Figure 2.7.

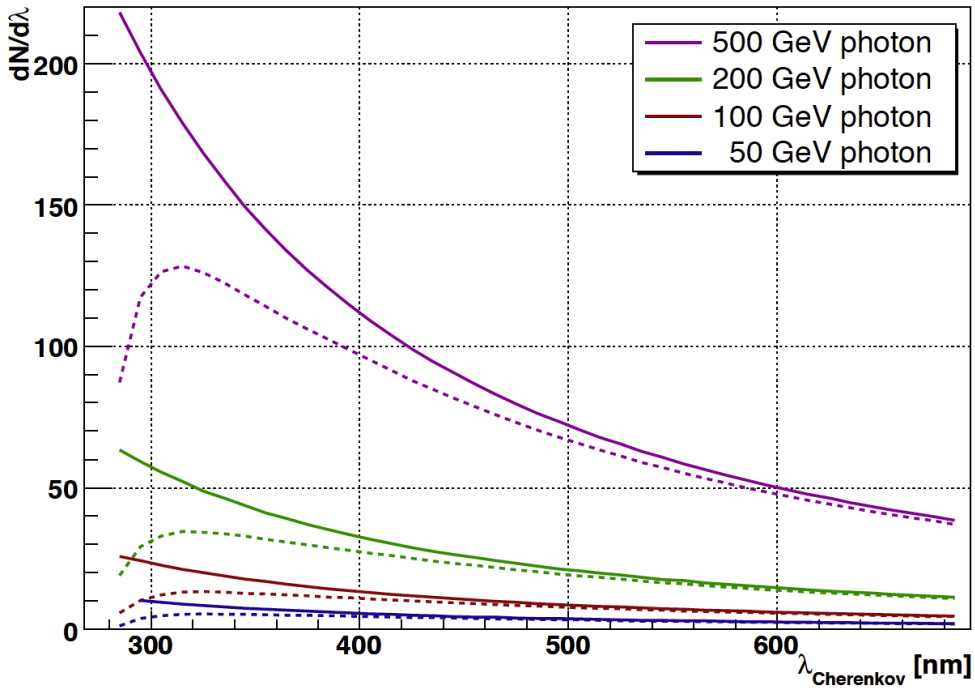

Figure 2.5: Cherenkov light spectrum emitted for γ-ray showers of different energies. The solid lines correspond to the emitted spectrum at 10 km height and the dashed ones to that detected at 2200 m a.s.l.

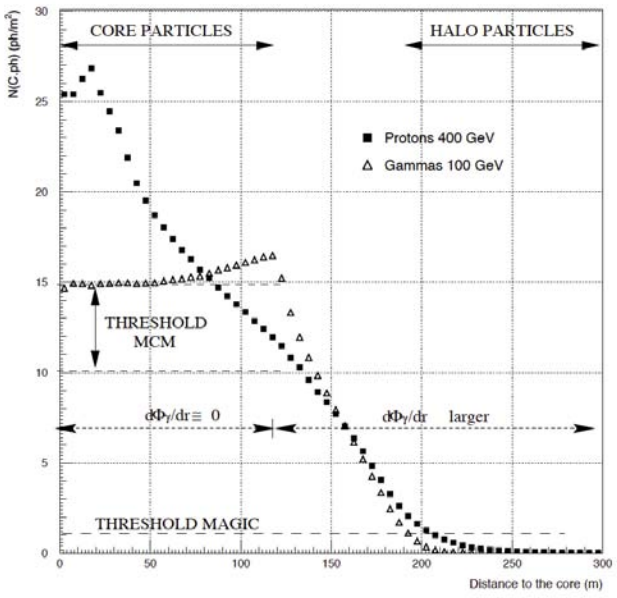

Figure 2.6: Lateral Cherenkov distribution density for a shower produced by a gamma ray of 100 GeV and a proton of 400 GeV. Taken from (Barrio et al. 1998).

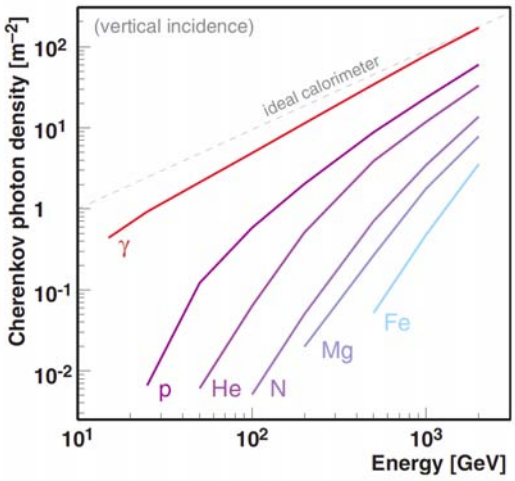

Figure 2.7: Cherenkov photon density as a function of the energy for different incident particles (Wagner 2006; Oser et al. 2001)

2.1.3 The imaging technique

The main purpose of the imaging atmospheric Cherenkov technique is to combine the spatial and temporal information of the measured light to produce images of the showers and differentiate between hadron and γ-initiated showers. To achieve this, IACTs have large reflectors that collect the maximum amount of Cherenkov light from a single shower possible and pixelized cameras equipped with very fast response pixels. The events are triggered by systems that record them only when several pixels are above a certain threshold for a short time (the shorter the time, the less Night Sky Background (NSB) that is integrated). They are also equipped with fast readout systems to record and reconstruct the narrow signals the photodetectors issue when they are excited by photons.

The reflectors used are usually Davies-Cotton, that have a good off-axis performance, but are not isochronous. When the reflector size increases, the arrival timing difference to the camera plane of light reflected by different segments of the mirror becomes important and parabolic reflectors are used because they are isochronous, although they have large coma aberration for off-axis angles. The pixels are usually fast, high-Quantum Efficiency (QE) Photomultiplier Tubess (PMTs), although there have been recent developments on cameras using Silicon PhotoMultiplier (SiPM) showing a good performance (Bretz et al. 2014).

An scheme of how the technique works is shown in Figure 2.8. The reason of using more than one telescope is to proper reconstruct the direction of the incident γ-ray and have a better background suppression. IACT systems usually work in stereoscopic mode, recording only the events triggered by more than two telescopes in a given time window.

Sources of background: Hadrons are arriving almost isotropically to the atmosphere, therefore the background contribution will come from everywhere. In fact, most of the events recorded by IACTs have hadronic origin (the proportion with respect gamma rays is $\sim 1000:1$ at 1 TeV for a strong source as Crab). The energy distribution of the hadronic background follows a power-law distribution $dN/dE \propto E^{-2.7}$. As it was described in the previous sections, the showers produced by primary particles of different origin have different shapes when projected in the camera (see Figure 2.9). γ-ray showers produce elliptical images on the ground, while hadron-like cascades produce more irregular images. This fact is used at the analysis level to distinguish between EM showers and hadronic ones (see Section §2.2.3.3).

There are other sources of background, such as muons, that usually form ring-like images on the camera plane and can also be rejected because of their shape. On the other hand, there are also irreducible sources of isotropic background, such as cosmic $e^{\pm}$, that produce EM cascades identical to those produce by gamma rays, or diffuse gamma rays coming from the galactic plane as they were measured by Abramowski et al. (2014a).

Apart from Cherenkov photons, one has the contribution of the Night Sky Background (NSB), that are background photons propagating isotropically in the night sky. The NSB contribution in la Palma was measured to be $(1.75 \pm 0.4)10^{12}$ ph m^{-2} sr^{-1} s^{-1} between 300 nm and 600 nm (Mirzoyan & Lorenz 1994).

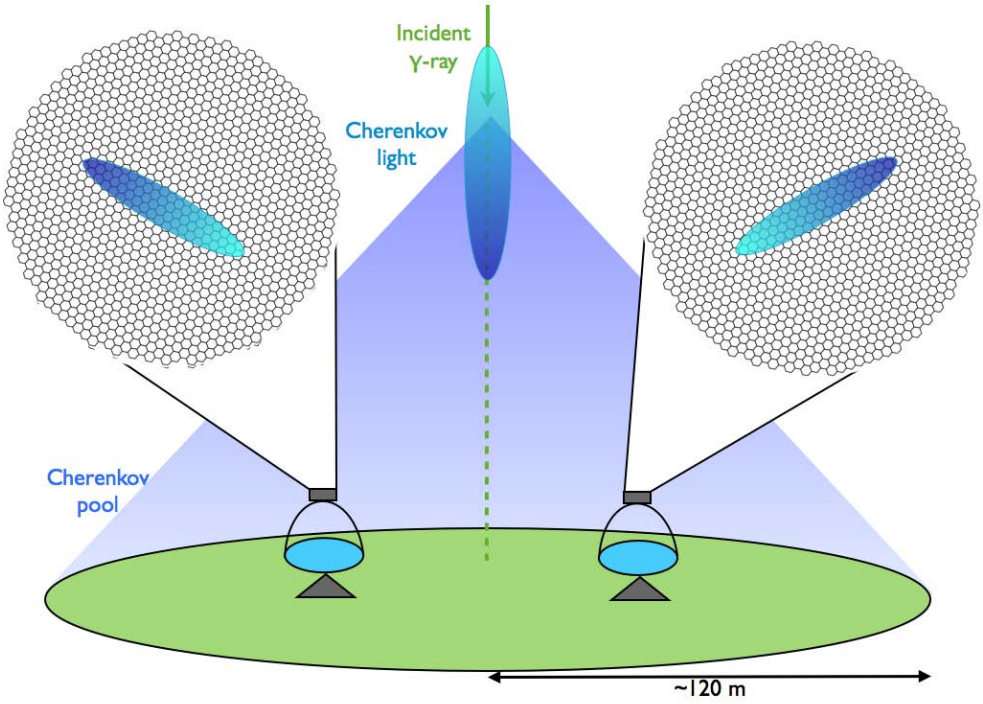

Figure 2.8: Scheme of the imaging atmospheric Cherenkov technique.

Differences between observations at large Zenith distance (Zd): As some of the observations of this thesis were performed at high Zd (up to Zd=70°), we will give a brief description of the differences between the shower development and their imaging at different Zd. When observing at high Zd, the shower development takes place in the uppest layers of the atmosphere. This implies a larger path for the shower to go through the atmosphere, being approximately $L' \simeq L/\cos(Zd)$. The diameter of the plane perpendicular to the reflector follows the same relation $l' \simeq l/\cos(Zd)$. Since the amount of light reflected by the mirrors is proportional to the amount of light arriving to the plane perpendicular to the reflector, the photon density ρ arriving to the camera is proportional to the diameter square of the plane perpendicular to the reflector $\rho \propto l^2$ and the relation between the light density at high Zd ρ' and the one at Zd=0 ρ is:

$$\rho' \propto l'^2 \propto \frac{\rho}{\cos^2(Zd)} \tag{2.4}$$

therefore larger attenuation and lower Cherenkov photon density at the observation level (see Figure 2.10).

The reduction of Cherenkov light on the ground causes an increase in the energy threshold. It should theoretically increase with the Zd as $E_{\text{threshold}} \propto \cos^{-2}(Zd)$ due to the decrease in Cherenkov photon density, but is measured to increase faster with increasing Zd due to the worst imaging of the showers and the loss of discrimination power between the hadronic and EM ones. The worsening of the energy threshold is on the other hand compensated by an increase in the collection area of the telescope. As the Cherenkov light pool is larger when observing showers

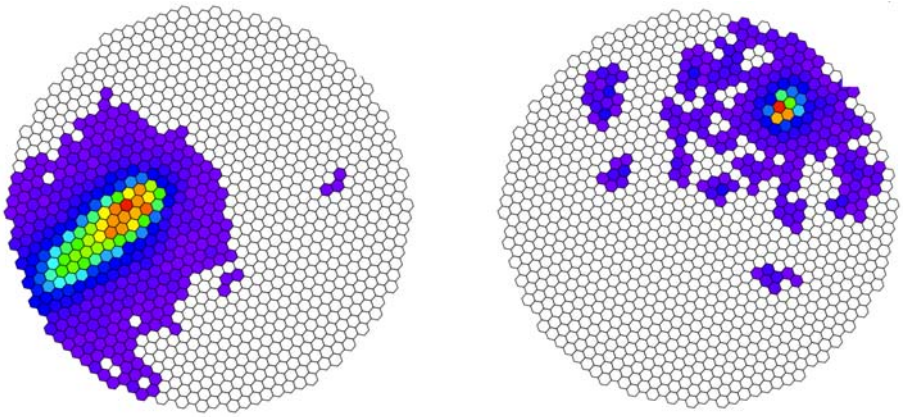

Figure 2.9: Example of an image of a γ-ray (left panel) and hadron (right panel) showers.

at high Zd, the collection area increases.

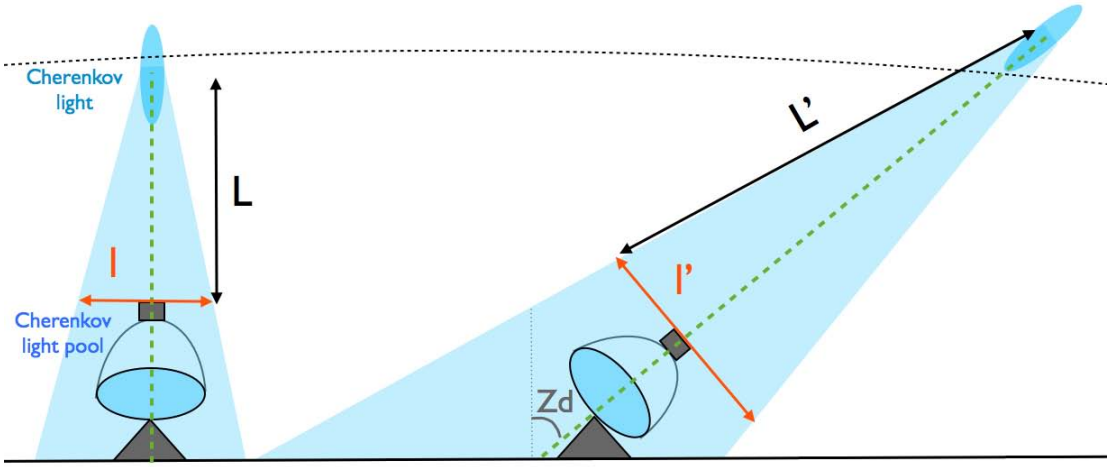

Figure 2.10: Difference in the shower development between low Zd (left telescope) and high Zd (right telescope) observations. We can see that the distance from the camera to the point in the atmosphere where the showers start to develop is smaller for low Zd observation (L) than for high Zd observations (L'). The diameter of the Cherenkov light pool in the plane perpendicular to the reflector is also larger for high Zd observations ($l' \simeq l/\cos(Zd)$).

2.2 MAGIC

The Florian Goebel Major Atmospheric Gamma-ray Imaging Cherenkov (MAGIC) telescopes are a stereoscopic system of two 17 m diameter IACTs located on the Canary island of La Palma, Spain (28.8°N, 17.9° W at 2225 m a.s.l). The system is specially designed to achieved the lowest possible energy threshold and a fast response to transient phenomena. MAGIC I started to take scientific data in 2004 and MAGIC II in 2009 (see Figure 2.11). During the summers of 2011 and 2012 the system underwent a major upgrade of the digital trigger, readout systems, and one of the cameras (Aleksić et al. 2014f) to make it homogenous and improve its performance. The MAGIC data analyzed in this thesis were taken both in stand-alone (only with MAGIC II) and stereo modes, hence both observation modes will be described.

Figure 2.11: Picture of the two MAGIC telescopes on the island of la Palma.

2.2.1 Hardware description

We will describe in the following the main components of the MAGIC telescopes. We will give a detailed description of the data acquisition and the electronic chain components relevant for data taking.

2.2.1.1 Structure and drive

The telescope mount is alt-azimuthal. The dish, moving in zenith and supporting the mirrors is identical in both telescopes and consists of a frame of octagonal shape made of carbon fibre-epoxy tubes joined by aluminum knots (see Figure 2.12). The structure is rigid and light-weight

(less than 20 tons including mirrors and camera support). The lower structure moving in Azimuth (Az) is made of steel tubes and weighs a total of 65 tons including the undercarriage (Figure 2.12). To hold the camera, there is a aluminum circular tube anchored to the main structure by ten pairs of steel cables. The deformation of the structure is less than 3.5 mm for any of the telescope orientations (Bretz et al. 2009), which is corrected using the Active Mirror Control (AMC) described in Section §2.2.1.2.

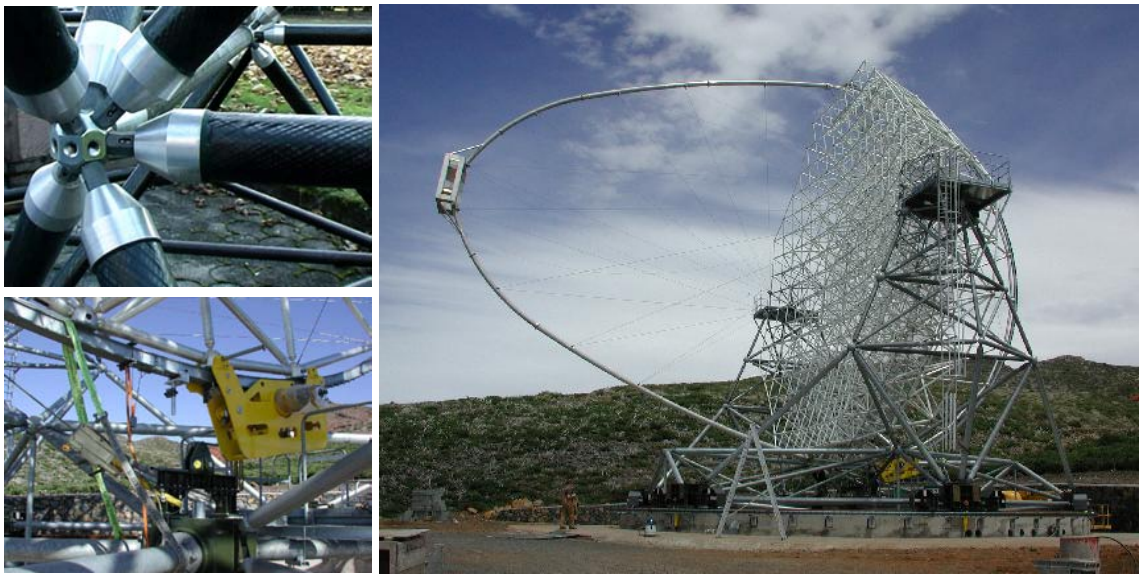

Figure 2.12: Top left: Aluminum knot where several carbon fibre-epoxy tubes join. **Bottom left:** Zenith motor. **Right:** Telescope mount without mirrors.

The range of movement spans from -90° to 318° in Az and from -70° to 105° in Zd. There are two 11 kW motors in two of the six bogies composing the Az undercarriage and one motor of the same power for the zenith axis (see Figure 2.12). The telescope's GRB mode allows to move 180° in 20 s. The telescope position is measured by three 14-bit shaft encoders, one of them in the Az axis and two in the zenith one. The telescope can track sources with an accuracy of 0.02°. To account of the deformation of the telescope structure, the pointing of the telescope is calibrated taking pictures of stars at different Zd and Az using a CCD camera installed in the middle of the reflector dish (*T-point* camera). In addition to the information given by the shaft encoders, the telescope pointing is constantly monitored by another CCD camera (*Starguider* camera), mounted in the center of the mirror dish as well. It measures the position of the telescope camera (with a ring of LEDs placed at the camera edge) respect to background stars and compares it to the latest available bending model (Figure 2.13).

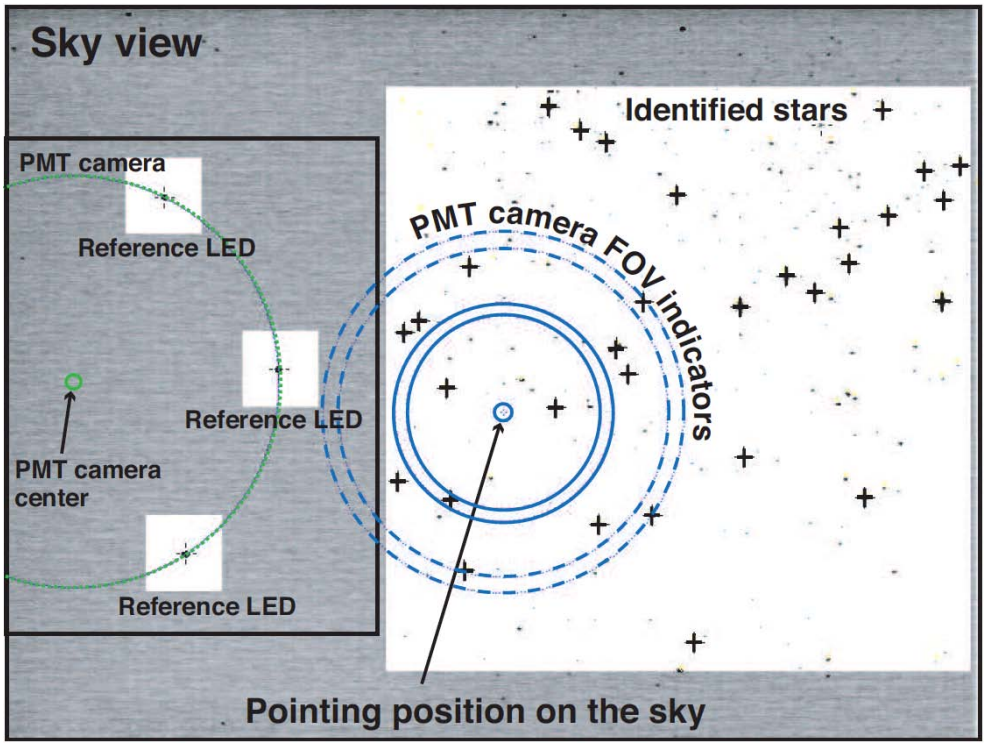

Figure 2.13: Picture of the starguider camera installed in the central part of the MAGIC telescope. Taken from Wagner (2006).

2.2.1.2 Reflector and mirrors

The reflector has $f = D = 17$ m, being f and D the focal length and diameter of the parabolic reflector dish. Parabolic mirrors are isochronous. As the time spread of Cherenkov signals is 1–2 ns, Cherenkov pulses are not significantly broadened, the signal extraction time is reduced and less noise is integrated. The Point Spread Function (PSF) for each of the mirrors r_{39}, defined as the diameter of the camera that contains 39% of the light of a point-like source, is $r_{39} \sim 10$ mm wide at the camera on-axis plane. Each of the mirrors has a spherical shape with radii ranging from 34 m to 36.7 m to match the parabolic shape of the reflector. The total mirror surface of both telescopes is ~ 236 m^2. The reflective surface is tessellated with 1 m $\times$ 1 m facets (see Figure 2.14a). In MAGIC I, each of the 247 facets contains four 0.5 m $\times$ 0.5 m aluminum honeycomb mirrors. In MAGIC II, there are 143 facets with single 1 m $\times$ 1 m all-aluminum mirrors on a honeycomb structure and 104 facets with single 1 m $\times$ 1 m glass-honeycomb-glass mirrors (see Figure 2.14b). Each of the facets is controlled by the AMC software described in the following.

Active Mirror Control The AMC is the part of the hardware in charge of correcting mirror focusing depending on the Zd for correcting for the deformations of the telescope. The system consists of two actuators per mirror panel. Each actuator can move the mirror with a precision of less than 20 μm corresponding to a shift in the camera plane of the light spot of less than 1 mm (Biland et al. 2008). The system adjusts the focusing of the mirror using Look-Up Tables

(a) Mirrors of MAGIC I **(b)** Mirrors of MAGIC II

Figure 2.14

(LUTs) binned in Zd and Az. An optical PSF of r_{39} ~11 mm can be reached, very close to the theoretical minimum, which is the PSF of a single mirror. The AMC system also contains a high-sensitivity CCD camera called SBIG camera, used for measurements of the PSF of single and multiple-mirrors.

2.2.1.3 Camera

Each camera is one of the most important parts of the telescope. The cameras are made of high-QE PMTs (also known as pixels) to collect as much Cherenkov light as possible, fast response to integrate the minimum NSB possible and low gain to allow observing during moonlight conditions. Each of the PMTs is coupled to a light collector called *Winston cone* that increases the light collection efficiency and prevents the collection of photons coming with large angles with respect to the reflector, avoiding the collection of some light reflected by the ground and part of the isotropically distributed NSB. The first camera of MAGIC I had a different design as the current one, which is a clone of that installed in MAGIC II when it started operation. Since there were not data analyzed in this thesis with the old MAGIC I camera, we will only describe the current one.

The camera has a circular shape with ~1.2 m diameter and a weight of ~850 kg (see Figure 2.15a). It has a Field of View (FoV) of 3.5° diameter and is composed of 1039 uniformly distributed PMTs. The camera also contains the power and cooling system, optical fibers and the electronics necessary to transmit signals to the *Counting House (CH)* where they are digitized. In front of the Winston cones there is a plexiglass window to protect the camera from the environment. To protect the camera from sun light and other external agents, it is equipped with movable lids.

PMTs PMTs are grouped in 169 clusters of 7 pixels, 127 of the clusters fully equipped and 42 (the outer ones) only partially. Each of the clusters is easily accessible from the back side of the camera for pixel exchanging (see Figure 2.15b). Each PMT has a 0.1° FoV. The PMTs are Hamamatsu R10408 6-dynode photo-tubes with spherical photocathode and ~32-34 % QE at

350 nm wavelength (Nakajima et al. 2013). Each of the clusters is equipped with a slow control processor which controls several parameters of the PMT, as setting High Voltage (HV) or reading Direct Current (DC) currents. The HV is produced by a Cockroft-Walton type DC-DC converter. The PMT gain is $\sim 3\times10^4$ and the typical HV set is ~1250 V. After the PMT, the signal is further amplified by a low-noise pre-amplifier to account for the low gain of the PMT. The clusters are also equipped with a pulse generator that allows injecting signals to the pre-amplifier for testing purposes.

The analogue electronic signals are converted into optical signals by Vertical Cavity Surface Emitting Lasers (VCSELs) after the pre-amplifier stage. They are transmitted to the CH by 162 m long optical fibers.

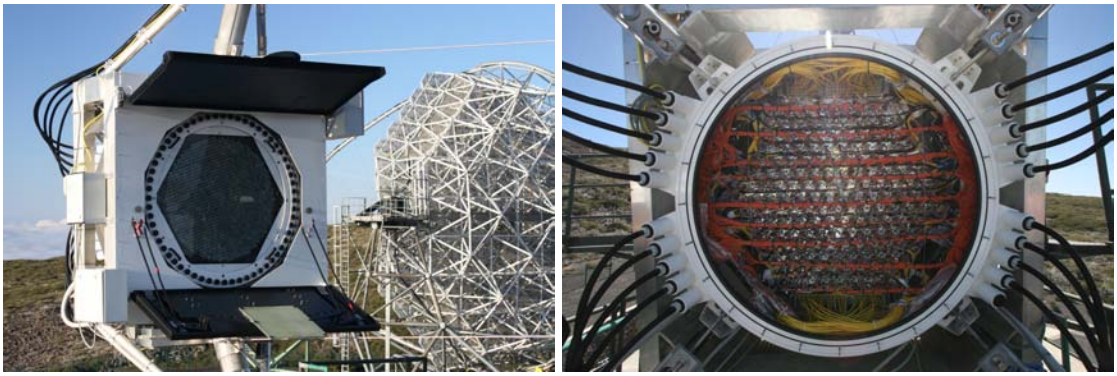

(a) Front view of the MAGIC II camera. **(b)** Back view of the MAGIC II camera.

Figure 2.15

2.2.1.4 Calibration system

To flat field the PMT gain, obtain the conversion factor between the counts of the digitizers to number of photoelectrons (phe) and the conversion between Flash Analog-to-Digital Converter (FADC) timing into an absolute timing, the MAGIC telescope needs a calibration system. It consists of a Nd-YAG laser, operating at 355 nm with 0.7 ns pulse width. To obtain a dynamic range, two rotating filter wheels can attenuate the laser beam, so that the signal produced in a PMT ranges between 1 and 1000 phe. To achieve an homogenous distribution of the calibration light at the camera plane, the laser beam is diffused using an integrating (Ulbricht) sphere. The system is placed in the center of the reflector dish.

2.2.1.5 Receivers

Trigger, readout electronics and Data AcQuisition (DAQ) are placed in a CH. We will describe the electronic chain that is followed by the signals coming from the telescope. The optical signals coming from the telescope through the optical fibers enter the so-called receiver boards where they are converted back to electric ones by photodiodes. The electric signals are then split into a trigger and a readout branch.

2.2.1.6 Trigger system

Digital trigger The current trigger system installed in the MAGIC telescopes for normal operation is a digital trigger composed of three stages (Paoletti et al. 2007):

- ⊙ *Level 0 (L0)* trigger: Signals in the individual pixels go through discriminators with a given threshold. It is installed in the receiver boards and it issues a square signal of adjustable width every time the analog input of the telescope is over the Discriminator Threshold (DT).
- ⊙ *Level 1 (L1)* trigger: It is a digital filter that searches for spatial and time coincidence of pixels that pass the L0 trigger. Pixels are grouped in 19 hexagonal overlapping cells called *macrocells*. Each hexagon is composed by 37 pixels, one of which is blind (see Figure 2.16, left panel). When a pixel is above the threshold, an LVDS signal of 5.5 ns phe is sent to the L1 board. If n Next Neighbour (NN) pixel signals overlap, the L1 issues a valid trigger. There are different NN multiplicites implemented in the L1 trigger (n=2,3,4 or 5). The one currently used for stereo observations is n = 3, having an effective overlapping trigger gate of 8 – 9 ns. The NN configuration implies that the pixels above the threshold must be in a close compact configuration, being every pixel in the group in contact with at least other two (except for the 2NN configuration). The output signal of each of the 19 macrocells is processed by a Trigger Processing Unit (TPU) that merges them into an OR gate. The macrocells cover a region of ∼2.5° diameter (Figure 2.16, right panel).
- ⊙ *Level 3 (L3)* trigger: It receives the output of the TPU from both telescopes and stretches it to achieve 100 ns width. It searches for an overlapping between the stretched signals of both telescopes in an effective time window of ∼ 180 ns.

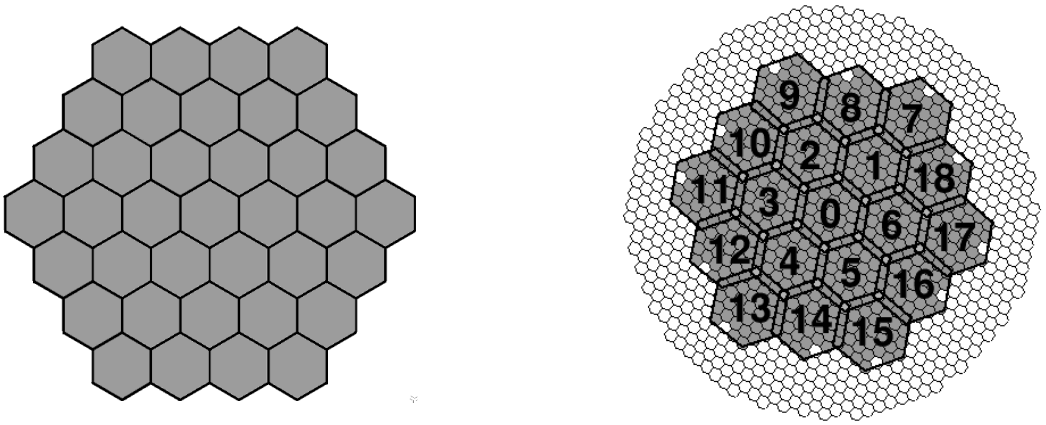

Figure 2.16: The left figure is a picture of a single L1 macrocell, each of the hexagons corresponding to one pixel. The right one is the distribution of the L1 trigger macrocells in the MAGIC camera. The numbers are the ones used in the hardware identification of the macrocells. The lines are imaginary hexagons limiting each of the macrocells.

Other trigger options MAGIC was designed to achieve the lowest possible energies. At the lowest energies, cosmic events are similar to "accidental" ones produced by noise. Several trigger options have been installed to discriminate accidentals from showers.

Sum trigger-II The Sum trigger-II is a trigger system based on the same concept as the Sum trigger designed for MAGIC I (Rissi et al. 2009), which allowed the discovery of VHE pulsed emission from the Crab pulsar above 25 GeV (Aliu et al. 2008). It adds up the analog signals from several pixels in 19-pixel macrocells. To minimize the effect of signals produced by After Pulses (APs) in the PMTs, the signal of every pixel is "clipped" before the analogue sum: if it exceeds a certain value, the analogue clipped signal that is sent to the adder is ideally constant. With the clipping of the signals, we avoid issuing valid triggers due to the signal coming from one or two pixels in the whole macrocell. The output of the adder enters a DT. The DT that is currently set in the MAGIC telescopes is of the order of several tens of phe to achieve the lowest possible energy threshold without exceeding the recording limit of the DAQ. For further information about Sum trigger-II, see (García et al. 2014).

Topo-trigger Special trigger option developed during this thesis that makes use of the digital macrocell information of both telescopes to record more low energy events. It has been simulated, tested and is currently under commissioning. A detailed description can be found in Chapter §4.

2.2.1.7 Readout

The readout is the part of the electronic chain that digitizes and temporarily stores the analogue signals from the telescope. We will briefly describe the history of the readouts used in MAGIC and then give a deeper explanation of the readout currently used, the Domino Ring Sampler (DRS) version 4.

Glimpse to the previous readouts used in MAGIC

Siegen: Between the beginning of MAGIC (~2003) and February 2007, MAGIC operated with a readout known as *Siegen*. The readout consisted of a dual gain 300 MSample/s system. Using this option, the readout system was too slow to handle the ~2 ns signals coming from the PMTs and they had to be stretched to 6-7 ns. Due to the stretching of the signals, the differences between signals produced by gamma rays, cosmic events or NSB were smoothed and the performance worse than with a faster readout. The dead time of the system was 25 μs.

MUX: in February 2007, the MAGIC I readout was upgraded to a 2 GSample/s system which made use of a fiber-optic multiplexing technique (MUX). Multiplexing was possible thanks to the low duration of the signals (~ few ns) and the trigger rate (it was typically ~ 1 kHz), resulting in a low duty-cycle for the digitizer. The system was custom-made in order to reduce the cost and consumption and instead of using a FADC for each readout channel, a single

FADC could handle 16 channels (Mirzoyan et al. 2002; Bartko et al. 2005). The dead time of the system was 25 μs.

DRS2 When MAGIC II was constructed, it was equipped with a readout based on the DRS2 analog memory chip. The working principle of the DRS is the following (see Figure 2.17): the signal coming from the receiver board is sequentially connected to an array of 1024 capacitors by fast switches synchronized to an external clock. Each of the capacitors is charged by the analogue signal of the corresponding pixel for a time that is proportional to the period of the clock controlling the switching (the so-called Domino wave). The capacitors are overwritten after 1024 clock cycles. When a trigger is received, the Domino wave stops and the charge stored in the 1024 capacitors is digitized by an Analog-to-Digital Converter (ADC). Later on, only 80 capacitors are stored by the DAQ, but as the whole buffer needs to be read, the dead time of the system is 500 μs. This means that for a stereo trigger rate of ~300 Hz, the dead time is 15%. DRS2 chips are highly non-linear and temperature dependent devices that need to be constantly calibrated. A complete description of the DRS2 chips can be found in (Bitossi 2009).

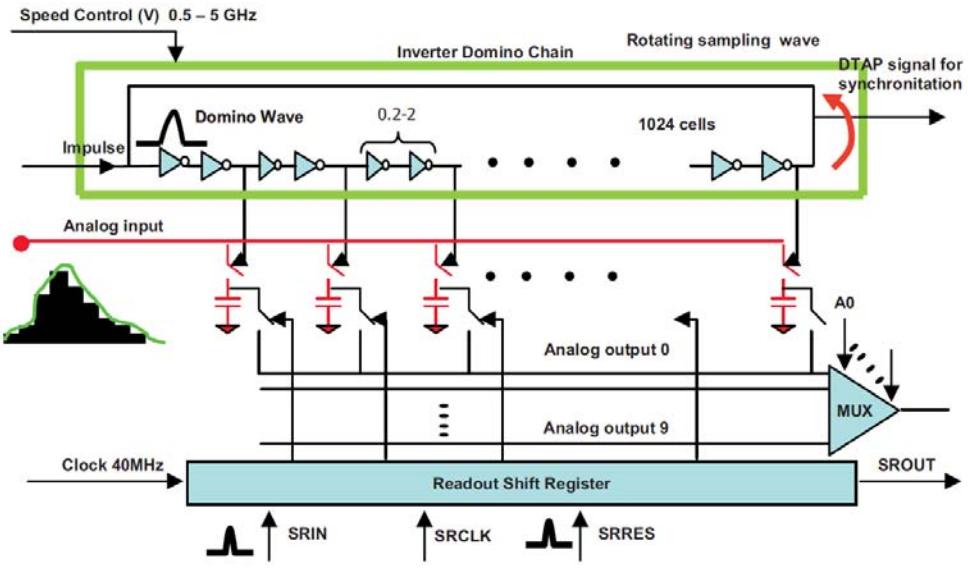

Figure 2.17: Schematic view of the DRS chip. Taken from Bitossi (2009).

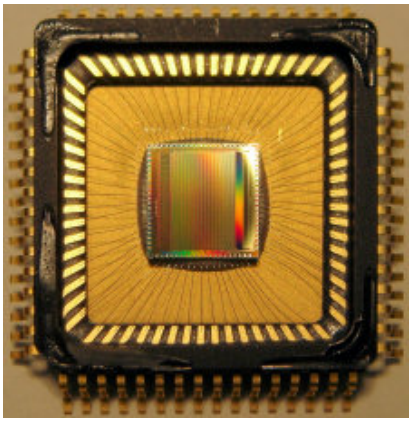

Figure 2.18: Picture of the DRS4 chip currently used in the MAGIC telescopes.

DRS4 To reduce the non-negligible dead time of the telescope using the DRS2 chip and to converge to one single readout in both telescopes, in December 2011 the MUX readout in MAGIC I and the DRS2 readout in MAGIC II were replaced by a readout based on the DRS4 chip. The DRS4 chip works basically like a DRS2 chip. They are still temperature dependent, so they still have to be calibrated on a regular basis, but they are linear and when a trigger is issued, only a Region of Interest (RoI) of 60 capacitors is read at 33 MHz, reducing the dead time to 27 μs. Additional advantages with respect to the DRS2 chip are a larger bandwidth (700 MHz instead of 200 MHz) and a lower pedestal noise (0.7 phe per cell, a factor 2 lower). For a detailed characterization, see Sitarek et al. (2013) and for a picture of a DRS4 chip, see Figure 2.18.

DRS chips are installed in especially designed boards called PULSer And Recorder (PULSAR). PULSAR boards are general purpose VME interface boards used in high energy physics. Each PULSAR board hosts 4 mezzanines, each mezzanine contains 3 chips and a single DRS4 chip has 8 channels, so every PULSAR board can digitize 96 pixels.

The data from the RoI of the DRS4 chip are read by the DAQ program. It interfaces with the PULSAR boards through FILAR cards and HOLA boards, which are respectively PCI cards installed in the DAQ computer and mezzanines installed in the PULSAR boards. The signal is transmitted from the HOLA to the FILAR boards via optical S-Link. The DAQ program then runs three threads in parallel: reading, analyzing and storing. There are 14 PULSAR boards to digitize all the pixels in a telescope, and there are two additional PULSAR boards with special funcionalities: the "digital PULSAR" that adds digital information to the data such as trigger number and absolute time, and the "busy PULSAR", which stops the triggers when the system is processing an event or an error occurs (Tescaro et al. 2009, 2013).

Rate limiter: The current DAQ can handle a short-term event rate up to 3 kHz. When the telescope was illuminated by car flashes, or what is more important, when bright stars suddenly entered in the FoV while repositioning to a GRB, the DAQ crashed due to the very high stereo rate. It takes several minutes to recover from such a crash. A "rate limiter" was installed to momentarily block triggers when the rate exceeds 1 kHz.

2.2.1.8 Other subsystems

Timing system The absolute time is generated by a Rubidium clock with a precision of 3×10^{-11} in 1 second. The Rubidium clock is a high-precision system, however it drifts over long time scales. To correct it, the device is synchronized every second to a GPS signal with a precision of the order of nanoseconds. The absolute time enters the data stream through the PULSAR.

Central pixel The central pixel of both MAGIC cameras is a modified PMT designed to detect variations of the optical flux of rapid-variability sources such as pulsars (Lucarelli et al. 2008). The pixel has a modified DC branch and a dedicated readout. The whole central cluster of the MAGIC camera was modified to host the necessary additional electronics, so it can be used for regular and optical observations.

Weather station A Reinhardt MWS 5MW weather station is installed on the roof of the CH of the MAGIC telescope. It measures the temperature, pressure, humidity and wind speed and direction every second to determine if atmospheric conditions allow observations. For the atmospheric safety limits see §2.2.2.2.

LIght Detection And Ranging (LIDAR) An elastic single-wavelength LIDAR is installed in the dome of the CH (Fruck et al. 2014). The LIDAR is equipped with a 5 mW Q-switched, pulsed Nd:YAG laser with a 532 nm wavelength, a 60 cm diameter, 1.5 m focal length Al mirror, a robotic equatorial mount, an Hybrid Photo Detector (HPD) capable of single photon counting and a computer equipped with an FADC card which digitizes the output of the HPD. The LIDAR operates as follows: it sends light pulses up to the atmosphere and they are backscattered by clouds or aerosols. The arrival time distribution of the backscattered photons registered at the HPD can be used to measure the transparency of the atmosphere.

Pyrometer The pyrometer is a device that computes the transparency of the atmosphere by measuring the temperature of the sky. It is installed in the MAGIC I reflector and points parallel to the telescope. It measures IR radiation in the 8–14 μm range and fits it to a blackbody spectrum. If the sky is cloudy, it reflects thermal radiation from the Earth and the sky temperature is higher. This temperature is used to determine a parameter known as *cloudiness*, that gives an estimate of the transparency of the atmosphere. It is defined as:

$$\frac{T_{\text{low}} - T_{\text{meas.}}}{T_{\text{low}} - T_{\text{up}}} \tag{2.5}$$

where $T_{\text{meas.}}$ is the measured temperature of the sky, T_{up}=200 K corresponds to the best condition of the sky and T_{low}=250 K to the worst.

AllSky camera The AllSky camera is a monochrome AllSky-340 camera manufactured by SBIG. It points to the zenith and has a FoV of 360° in Az and almost 90° in Zd. It takes an image of the sky every 2 minutes, with an automatically adjusted exposure time. The images taken by the camera are automatically uploaded to a server and can be monitored online.

MAGIC OnLine Analysis (MOLA) MOLA is a multithreaded C++ program used to obtain on-the-flight estimations on the γ-ray emission from sources in the FoV observed by MAGIC (Tescaro et al. 2013). It runs three parallel threads: two reading threads used to gather the single-telescope charge and arrival time of the events and an analysis thread that matches and reconstruct the events from the two telescopes. It computes the θ^2 plot with respect to the candidate source

position and it also produces light curves of the measured γ-ray flux and skymaps. The program is specially used for nightly estimations on the flux of variable γ-ray sources such as blazars. Its most remarkable achievement was the discovery of a very rapid flare on the IC 310 galaxy while observing NGC 1275 and the extension of those observations (Aleksić et al. 2014a)

GRB monitoring alert system A GRB monitoring program runs in the background of one of the CH computers. It receives information of the GRB from the GRB Coordinate Network (GCN) and evaluates the observability of the received alerts following several criteria (distance to the Sun and to the Moon, Zd, uncertainty on the position). If the alert fulfills all the criteria, the Central Control (CC) takes control of the observation and automatically points the telescope to the GRB location.

2.2.2 Data taking

Figure 2.19: Filter for moonlight observations.

MAGIC standard operation and under which it achieves its best performance is under so-called "*dark* conditions" (i.e. when the moon absent from the sky). The total amount of available *dark* time amounts to ~1600 h/yr. About ~65% of the available dark time is observed and the rest is loss due to bad weather or technical problems. Thanks to the low gain of the PMTs, MAGIC can also observe during moonlight conditions up to 75% of the moon phase and only has to stop observations on the 3 to 4 full-moon nights. Filters for moonlight observations (see Figure 2.19) similar to those currently being used by VERITAS (Staszak 2014), are currently being commissioned and will allow the extension of the observations to any moon phase.

The default data taking mode of MAGIC is the stereo mode. The mean L0 DT is set to ~4.5 phe in both telescopes (slightly higher in MAGIC II due to the higher mirror reflectivity), although the individual pixel DT is controlled by means of an Individual Pixel Rate Control (IPRC). It sets the DT of individual pixels and controls that the L0 rate is contained within the limits established. Currently, for *dark* observations, the usual L0 rate is ~800 kHz. The IPRC decreases the L0 DT when the rate is lower than 250 kHz and increases it when the rate is larger than 1.2 MHz. For *moon* observations, the usual L0 rate is ~500 kHz, the DTs are decreased when the L0 rate is lower than 150 kHz and they are increased when the L0 rate is larger than 700 kHz. The L1 rates for standard operation are ~15 kHz in both telescopes, leading to an accidental stereo rate of 40 Hz (the calculation of the stereo accidental rate is explained in Section §4.1). During the operation and to ensure a correct calibration of the readout, there are also 25 Hz of interleaved calibration events and 25 Hz of interleaved pedestal events recorded.

The L3 stereo rate recorded by the DAQ is 250-350 Hz, so the current cosmic rate recorded is between 200-300 Hz.

The CC of the telescope, called SuperArehucas, takes care of all the subsystems of the telescope. It sends and receives reports with the state of all the hardware subsystems every second and allows the observers to control their most important functionalities. A detailed description of the CC program can be found in Zanin (2011).

2.2.2.1 Pointing modes

The MAGIC telescope takes data in two different pointing modes: the *ON/OFF* and the *wobble* modes:

- *ON/OFF:* In the ON/OFF mode, the position of the target is tracked at the center of the camera. Two different types of observations have to be performed: *ON* observations with the source in the center of the camera, and *OFF* observations, preferably under similar Zd/Az conditions on a region where no γ-ray emission is expected.

- *Wobble:* This pointing mode was first proposed by Fomin et al. (1994) and it consists on tracking alternative positions in the sky that are at a slight offset from the center of the camera. For MAGIC the usual offset is 0.4° and each position is observed during 20 minutes. It has the advantage that no dedicated OFF observations have to be performed because the OFF is taken simultaneously. If only one OFF position is selected, it is taken in the opposite position of the camera with respect to the camera center as it is shown in Figure 2.20a. More than one simultaneous OFF positions are possible, as can be seen in Figure 2.20b. The collection of more background events allows increasing the significance due to the more precise background determination. In addition, the background is evaluated from the same data sample as the signal, hence it matches its Zd/Az distribution and background light conditions. The main drawbacks from this observation mode are: a loss on γ-ray efficiency of the order of 15-20% because the source is 0.4° from the center of the camera and a systematic uncertainty in the background determination due to the camera inhomogeneities. These inhomogeneities are caused by dead pixels in the camera, non-flat trigger efficiency in the whole camera and insufficient flat fielding of the camera due to the gain differences between PMTs.

Independent of the pointing mode, working in stereoscopic mode makes the telescope acceptance dependent on the relative pointing of the telescopes. Only the events triggering both telescopes are recorded, therefore there will be more recorded events from the showers developed between the two telescopes and this is what is called the *stereo blob*. This problem was partially solved after the upgrade, when the system was homogenized and the trigger regions made equivalent. Currently, most of the observations carried out with MAGIC are in *wobble* mode.

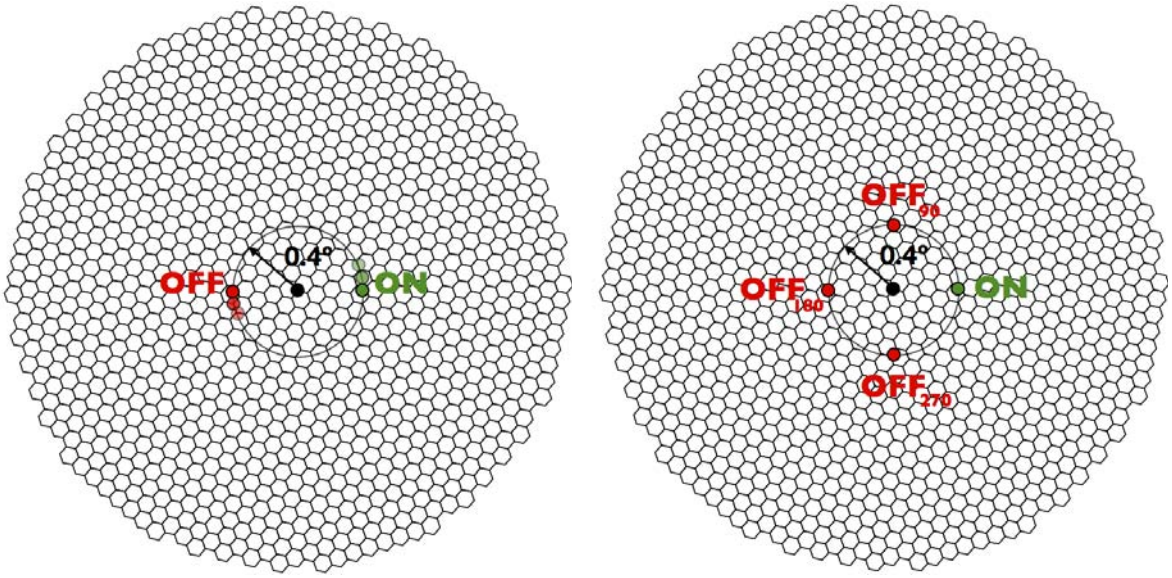

(a) Wobble mode with 1 OFF.

(b) Wobble mode with 3 OFFs.

Figure 2.20: Schematic view of the *wobble* pointing mode. The black circle marks the center of the camera. A region placed 0.4° from the source is tracked, being the source all the time situated at this distance from the center of the camera (green circle). The simultaneous background is taken all the moment from a region situated in the opposite side of the circle with center in the center of the camera and radius 0.4° (red circle in the left figure) in the case of 1 OFF region. In the case of 3 or more OFF regions, the background is taken from regions separated the same distance from one another in the aforementioned circle as it is shown in the right figure. The subindex of the OFF regions determine the angle turned in the circle counted counterclockwise from the ON region.

2.2.2.2 Safety limits

There are several atmospheric or technical conditions under which the telescope cannot be operated without taking the risk of seriously damage it. Here are the safety limits that should be fulfilled:

- ⊙ Wind gusts < 40 km/h
- ⊙ Wind mean speed < 50 km/h
- ⊙ Humidity < 90%
- ⊙ Average PMT current < 30 μA
- ⊙ Individual PMT current < 47 μA
- ⊙ Zd > 1.5°

2.2.2.3 Data types

There are different data types that can be taken with MAGIC. In the following, we find a summary of the most common ones that have to be taken every night:

- ⊙ **Pedestal subtraction run (B):** Taken at the beginning of the night to calibrate the baseline of the DRS capacitors and set the zero level to 10000 counts to avoid problems with negative values due to the noise fluctuations. It has to be taken at least one hour after the electronic was switched on because of the temperature dependency of the DRS chips.
- ⊙ **Pedestal run (P):** It records randomly triggered events (usually 2000 per run) which contain only noise. It has to be taken with the camera open to evaluate the effect of the NSB and readout noise to calculate the pedestal offset to be subtracted in the calibration of the data.
- ⊙ **Calibration run (C):** It contains events triggered by the calibration system. They are later used in the analysis to calibrate the data.
- ⊙ **Data run (D):** It contains all the events that issued valid triggers from the telescopes. They are mainly cosmic events, although it also contains interleaved calibration and pedestal events, together with accidental events triggered by noise. They correspond to approximately 20 minutes of data taking, the time that one wobble lasts. Data runs are divided into subruns which contain ∼1 Gb of data, corresponding to ∼2 minutes of data.

2.2.3 Data analysis

The standard software for MAGIC data analysis is called MAGIC Analysis and Reconstruction Software (MARS) (Zanin et al. 2013). It converts the raw ADC counts recorded by the DAQ into high-level products using a collection of programs written in C++ language that makes use of ROOT[1] libraries. The final purpose of the software is to reconstruct the primary particle generating the cascade and determine the direction and energy of the γ-ray candidates. In the following there is a summary of the processes performed by MARS:

- ⊙ *Calibrate* the digital signals contained in the raw data and convert the information to phe (§2.2.3.2).
- ⊙ *Image cleaning* and calculation of the *image parameters* for single-telescope (§2.2.3.3).
- ⊙ *Merge* the data from both telescopes and calculate the *stereo image parameters* (§2.2.3.5).
- ⊙ *Train* Random Forest (RF) for γ/hadron separation, fill LUTs for energy reconstruction and reconstruct the shower direction (§2.2.3.6).
- ⊙ *Apply* RFs and LUTs to the data to calculate the *hadronness*, reconstructed energy and arrival direction of each event (§2.2.3.6).

[1] http://root.cern.ch/drupal/

⊙ Calculate *signal significance* (§2.2.3.7), *skymaps* (§2.2.3.8), *spectra* and *light curves* (§2.2.3.9).

A scheme of the aforementioned process followed by the data is shown in Figure 2.21. We will give a detailed description of the programs in the following sections.

2.2.3.1 Monte Carlo simulation

As IACTs cannot be calibrated with a source of gamma rays, one has to trust on simulations to reconstruct the energy and incoming direction of the events. The Monte Carlo (MC) simulation is performed outside the MARS framework and is composed of three stages (for further information, see Majumdar et al. (2005)):

⊙ The *atmospheric simulation* is performed using the `Corsika` 6.019 program (Heck et al. 1998), which simulates air showers. As an atmospheric model, we have used the so-called "MagicWinter" containing a mixture of N_2 (78.1 %), O_2 (21.0%) and Ar (0.9%). The model to describe hadronic interactions is FLUKA, together with the QGSJet-II model for high-energy interactions. Electromagnetic interactions are simulated using the EGS4 model. MAGIC simulations work with a modified version of CORSIKA that stores the information of the direction and position in the ground of the Cherenkov photons produced in the shower.

⊙ The simulation of the telescope's *mirror response* to the incoming Cherenkov light and its absorption in the atmosphere, is done by the `reflector` program. It uses the Elterman model for the aerosol distribution in the atmosphere (Elterman 1964). It simulates the absorption of Cherenkov photons in the atmosphere and their reflection in the telescope's dish and calculates their position and arrival time at the camera plane.

⊙ The response of the PMTs and the readout electronics are simulated using the `camera` program. The measured QE of the PMTs is taken into account to simulate the pixel response, the trigger is simulated and the measured readout noise is also included in the simulation. The program also simulates the effect of the measured PSF of the individual mirror facets and their error in the alignment.

Recently, a new simulation program integrated in the MARS framework that simulates the reflector and camera response called `matelsim` has been developed (López 2013). However this program is still under testing and the official MAGIC simulation programs are still `reflector` and `camera`.

The output of the `camera` program has the same format as the raw data after converting it to ROOT data format, so it can be analyzed using the same software. For data analysis, only simulations of gamma rays are necessary, however one can also simulate with CORSIKA several types of particles and in MAGIC also $e^{\pm}$, p and He^{++} are used for performance studies. For most of the sources, gamma rays are simulated in a ring of 0.4° radius centered in the camera center (known as *ringwobble* MC, see Figure 2.22a). However, for the analysis of extended sources or sources situated at different off-axis angles, *diffuse* gamma rays are simulated in a circle with

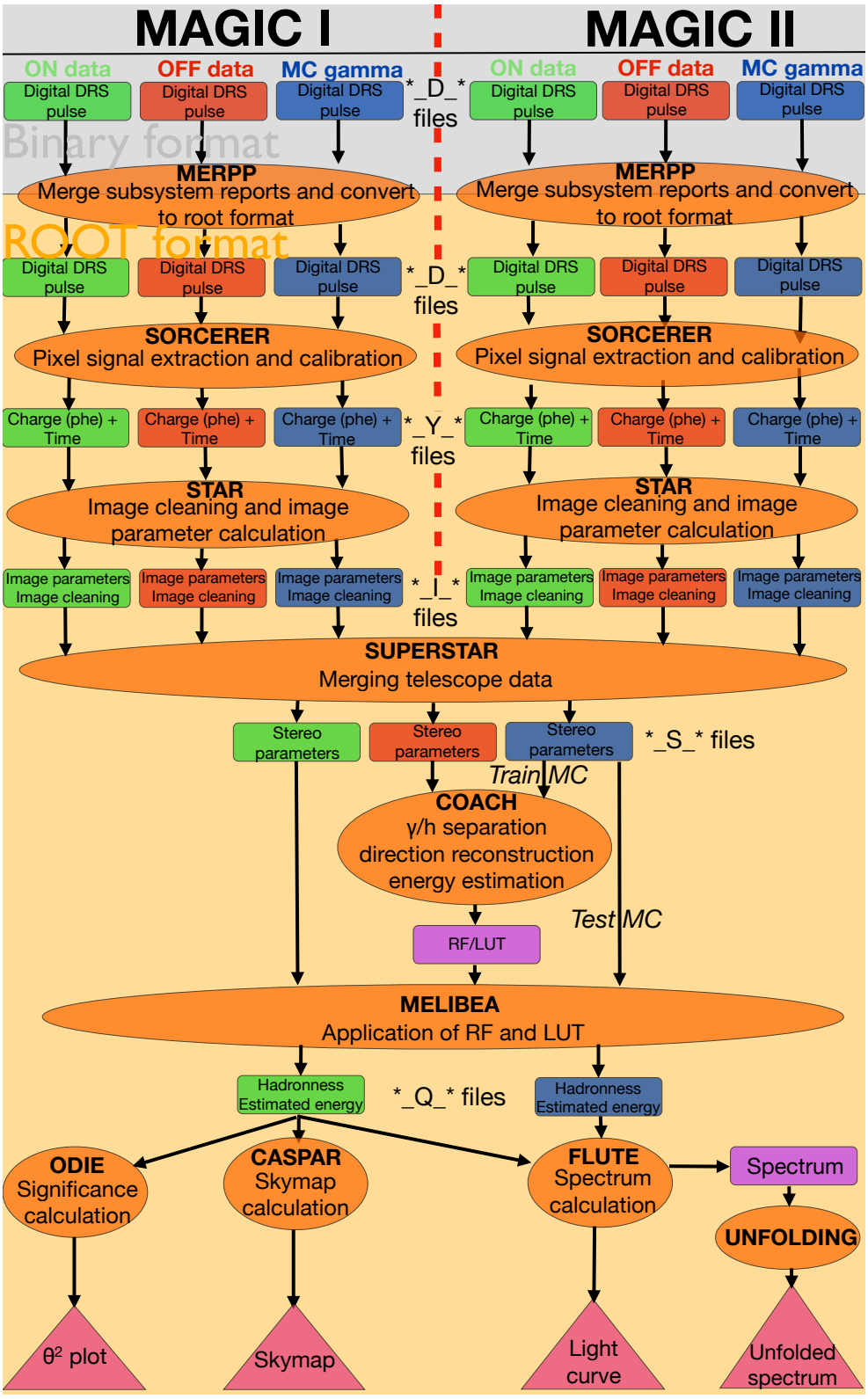

Figure 2.21: Scheme of the MAGIC analysis chain.

radius 1.5° centered in the center of the camera (see Figure 2.22b). MC gamma rays are produced in ranges of Zd: low (5°–35°), medium (35°–50°), high (50°–62°) and very-high (62°–70°) Zd. The distribution of generated MC gamma rays is flat in cos(Zd) in each of the ranges. The ranges are selected to have similar coverage in cos(Zd) in all bins.

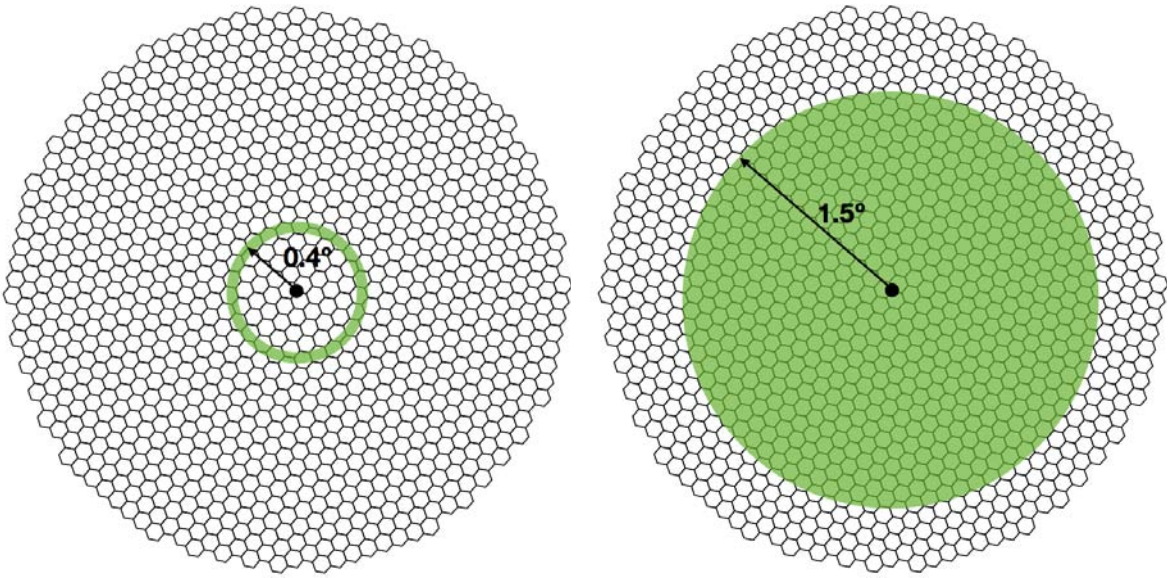

Figure 2.22: Ringwobble (left panel) and diffuse (right panel) MC schemes. The green shaded area is the one where the MC gamma rays are simulated.

2.2.3.2 Signal extraction and calibration

The raw data, with the output of the digitizers in counts vs time is converted to ROOT format by a program called `merpp` (MERging and Preprocessing Program) which also merges the data file and the subsystem reports.

Once the data is in ROOT format, it can be calibrated to convert ADC counts into number of phe. The old calibration program was called `callisto` (CALibrate LIght Signals and Time Offsets), but after the installation of the DRS4 readout in both telescopes, a new program called `sorcerer` (Simple, Outright Raw Calibration; Easy, Reliable Extraction Routines) was developed to handle DRS-related problems. 60 "time slices" are stored for each pixel, corresponding to 60 capacitors, each of them containing the number of ADC counts in 0.5 ns). The pedestal subtracted from each time slice depends not only on the capacitor that is read, but also on the last time it was read. After the pedestal is subtracted, the *sliding window* algorithm is used to extract the signal. It takes the maximum resulting from integrating 6 consecutive slices. The signal arrival time is the average position of the selected 6 slices weighed with the ADC counts contained in each of them.

The conversion from ADC counts to number of phe is performed using the *F-factor* method (Mirzoyan 1997). For calibration pulses it is assumed that the number of phe follows a Poisso-

nian distribution with mean N and standard deviation $\sqrt{N}$. The distribution of measured charge in ADC counts Q has a mean $\langle Q \rangle$ and a deviation σ_Q which is wider than pure Poissonian expectations due to noise in the PMT e^- multiplication process. The relative amplitude of both distributions can be written as follows:

$$F\frac{\sqrt{N}}{N} = \frac{\sigma_Q}{\langle Q \rangle} \tag{2.6}$$

where F is the so-called *F-factor*, which is different for each PMT and must be measured in the laboratory. The electronic chain also contributes to the broadening of the peaks, but this contribution is negligible with respect to the effect of the PMT. Since the spread of *F-factor* for the PMTs of each telescope is small, one can take one single *F-factor* for each of the telescopes. The conversion factor m between ADC counts and phe is then given by:

$$m = \frac{N}{\langle Q \rangle} = F^2 \frac{\langle Q \rangle}{\sigma_Q^2} \tag{2.7}$$

As the gain of the VCSELs is not constant in time, m must be updated using calibration events interleaved with cosmic events at a rate of 25 Hz.

2.2.3.3 Image parameter calculation and image cleaning

From this step on, the shower images are parametrized and the pixel information is lost. The program performing all these computations is called `star`. The charge and arrival time information are used for the analysis and only pixels that contain useful information about the shower are kept for the shower parametrization (see Figure 2.23). The algorithm to remove the noisy pixels is called *image cleaning* (Aliu et al. 2009; Lombardi 2011).

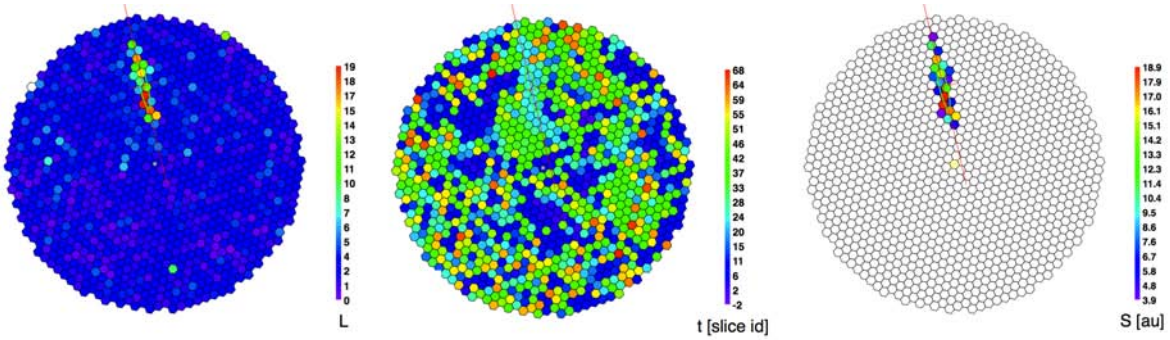

Figure 2.23: Signal charge (left panel), arrival times (middle panel) and cleaned image (right panel).

In the *absolute* image cleaning method, a pixel is considered a "core pixel" if its charge is above a certain threshold Q_c , if it is adjacent to another core pixel and if its arrival time does not differ from the mean arrival time of the core of the image by more than Δt_c. Boundary pixels are defined as the ones above a threshold Q_b, that are adjacent to at least one *core* pixel and if their arrival time does not differ from the arrival time of that *core* pixel a time larger than Δt_b.

For the single-telescope data used in the analysis of Chapter §9, the values used to define *core* and *boundary* pixels are the following:

$$Q_c = 8phe; \quad Q_b = 4phe$$
$$\Delta t_c = 4.5ns; \quad \Delta t_b = 1.5ns$$

In the *sum* image cleaning method, the algorithm searches for 2, 3 or 4 neighboring pixels (2NN, 3NN, 4NN) with a summed charge above a certain threshold Q_c in a time window t_c. To prevent from large signals due to APs, each pixel's signal is clipped before the sum. The threshold values and the time windows applied to search for *core* pixels with the *sum* algorithm can be found in Table 2.1. Once the *core* pixels are selected, the *boundary* ones are the ones at least neighbour to one *core* pixel, their charge is larger than 3.5 phe and their arrival time difference with respect to their *core* neighbour pixel is smaller than 1.5 ns.

Topology	Q_c [phe]	t_c[ns]
2NN	2×10.8	0.5
3NN	3×7.8	0.7
4NN	4×6	1.1

Table 2.1: *Sum* cleaning charge and time parameters.

Once the *core* and boundary pixels are selected, the resulting images are parametrized and this is the information that is stored in the data. The image parameters used in the MAGIC analysis are the following:

Hillas parameters An ellipse is fit to the pixels after cleaning. The momenta of this fit up to second order are used to parametrize the image (Hillas 1985):

- ⊙ **Size:** Total charge (in phe) contained in the image. It is related to the energy of the primary γ-ray if the shower falls close to the telescope (usually $\lesssim$ 120 m).
- ⊙ **Width:** RMS spread along the minor axis of the ellipse fitting the image. It is a measurement of the lateral development of the shower.
- ⊙ **Length:** RMS spread along the major axis of the ellipse fitting the image. It is a measurement of the longitudinal development of the shower.
- ⊙ **Center of Gravity (CoG):** Center of gravity of the image. It is computed as the mean of the X and Y weighted mean signal along the camera coordinates.
- ⊙ **Conc(N):** Fraction of the image concentrated in the N brightest pixels. It measures how compact the shower is and tends to be larger in gamma rays.

A shower image with some of the *Hillas parameters* can be seen in Figure 2.24.

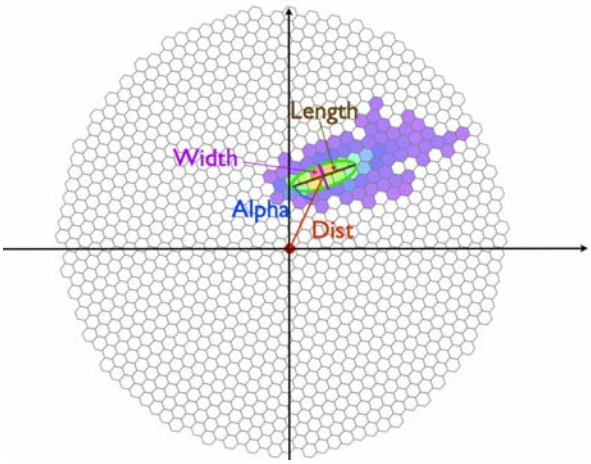

Figure 2.24: Picture showing some of the *Hillas parameters*.

Source-dependent parameters: They are still related to the physical properties of the shower, but they depend on the expected position of the source.

- ⊙ **Dist:** Angular distance from the source expected position in the camera to the CoG of the shower image. This parameter is larger for the showers with larger impact parameter.
- ⊙ **Alpha:** Angle between the ellipse major axis and the line connecting the expected source position to the CoG of the shower image. As the showers produced by gamma rays coming from the shower should point to the source position in the camera, this angle is small for γ-like showers.

Time parameters: Since γ-like events are shorter in time than hadron-like events, time information is also useful to discriminate between hadron and γ-induced showers.

- ⊙ **Time RMS:** RMS of the arrival times of the pixel that survived the *image cleaning*. It is smaller for γ-like showers.
- ⊙ **Time gradient:** Slope of the linear fit to the arrival time projection along the major axis of the ellipse. It measures the direction of the shower development, positive if coming to the expected source position and negative otherwise.

Image quality parameters: They are used to evaluate if the image is very noisy or if it is well contained in the camera.

- ⊙ **LeakageN:** Fraction of the size of the source contained in the N outermost rings of the camera.
- ⊙ **Number of islands:** Number of non-connected pixels that survived the image cleaning.

Directional parameters: They discriminate between the head (top part of the shower) and tail (bottom part of the shower). Typical showers have higher charge concentration in the head than in the tail.

- ⊙ **Asymmetry:** Signed distance between the shower's CoG and the pixel with the highest charge. It is positive when the pixel with the highest charge is closer to the camera center than the CoG.
- ⊙ **M3Long:** Third moment of the shower image along its major axis. It follows the same sign criterium as the Asymmetry parameter.

2.2.3.4 Data quality selection

Data affected by technical problems, bad weather or different light conditions (e.g. data taken under moonlight conditions) should be separated from the "good" dataset. Some of this data could be recovered, follow a parallel analysis and their final products merged with those of the "good" dataset, although most of the times they are rejected.

To distinguish between good and bad quality data, we use several indicators. We plot the number of visible stars the starguider detect and the average *cloudiness* for every subrun. If the *cloudiness* is above 40, the data is considered of bad quality. We also plot the *rate* above a low *size* cut (usually 50 phe). This allows to reject accidental events and plot the real cosmic rate. This rate is different depending on the Zd. We can empirically correct the rate multiplying it by $\cos^{-1}(Zd)$. For a dark night with good weather conditions, the cosmic rate corrected by the Zd is constant. This empirical correction is valid up to Zd~50°. For the same observation period and for each telescope, where we expect a similar rate for good quality nights, we calculate the average cosmic rate and we accept data with a rate within 15% of the average rate. The subruns outside this range might be affected by atmospheric extinction or technical problems and are rejected. The average rate is different for each of the telescopes: MAGIC II rate is usually higher than MAGIC I due to the higher reflectivity of the mirrors installed in MAGIC II. A plot where a typical data quality rate plot is shown in Figure 2.25.

2.2.3.5 Stereo image parameter calculation

Once good-quality data have been selected, the `superstar` program merges the two telescopes data. One can now reconstruct the three-dimensional shower development and determine several parameters useful for the energy and direction reconstruction. Some of them are shown in Figure 2.26a.

- ⊙ **Impact point:** The impact point on the ground is calculated using the crossing point of the major axis of the two shower images and the position of each telescope (see Figure 2.26b).
- ⊙ **Shower axis:** The shower axis is given by the crossing point of the major axis of the two superimposed shower images in the camera plane, as can be seen in Figure 2.26c. This

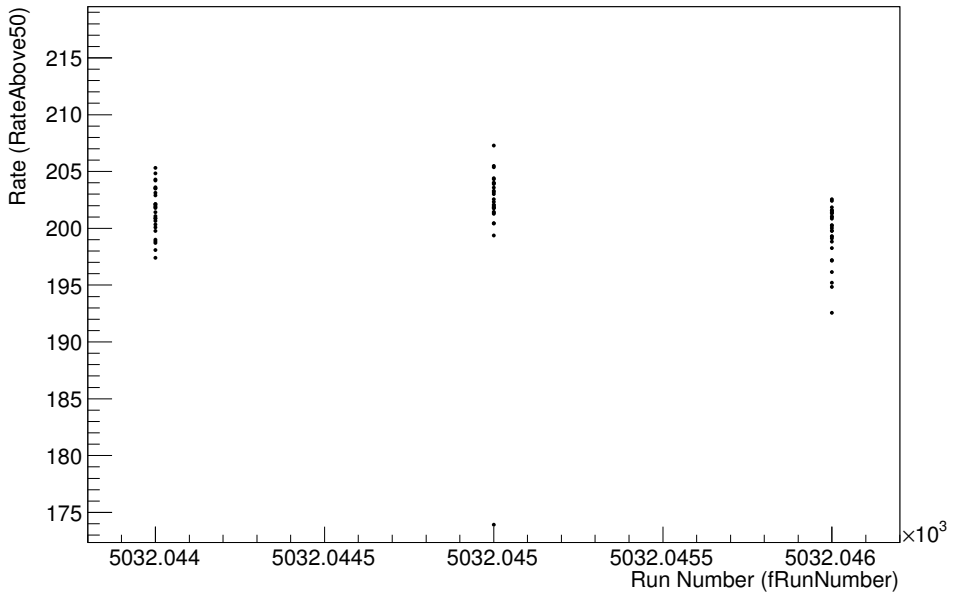

Figure 2.25: Rate plot for the data quality selection for MAGIC I rate (for *size*>50 phe) is plotted as a function of run number. Each of the points corresponds to the rate of a 2-minute subrun.

is the so-called *crossing point* method to calculate the shower direction (Aharonian et al. 1997b; Hofmann et al. 1999). The more powerful *disp* method will be described in Section §2.2.3.6.

⊙ **Height of shower maximum:** Using the shower axis, together with the angle at which the CoG of the image is measured with respect to each telescope, one can estimate the height of the shower maximum ($H_{\max}$). The $H_{\max}$ is in inverse proportion to the energy, as it was shown in Section §2.1.1.1. This parameter is strongly correlated with the shower energy and is a powerful γ/hadron discriminator.

⊙ **Impact parameter:** Calculated as the perpendicular distance between the shower axis and the pointing direction of each telescope.

⊙ **Cherenkov radius:** It is computed as the radius of the ring of Cherenkov light pool produced by an e^- with the critical energy of 86 MeV at the height of shower maximum.

⊙ **Cherenkov photon density:** Cherenkov photon density on the ground of a shower produced by an e^- with an energy of 86 MeV at the height of the shower maximum.

2.2.3.6 Event separation and characterization

Even for a strong γ-ray source as the Crab Nebula, the number of hadron events that survive image cleaning is ∼3 orders of magnitude larger than the one of gamma rays. The purpose of the

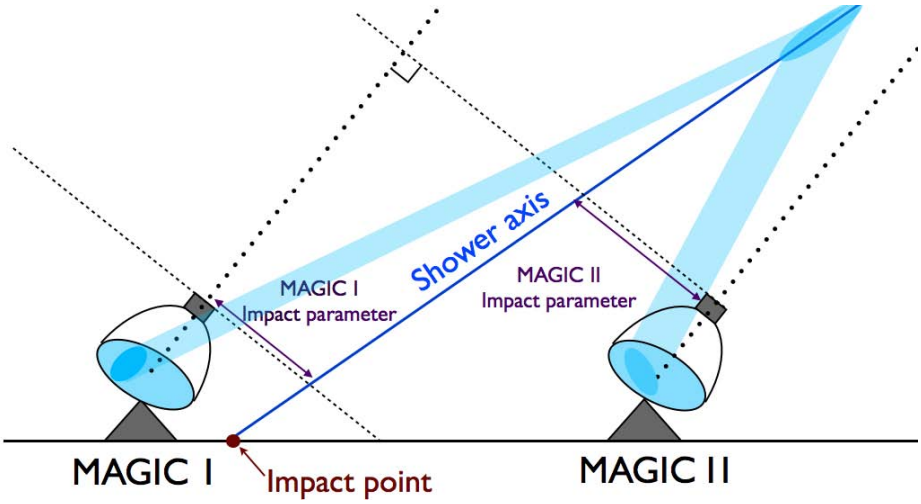

(a) Stereo event shower geometry.

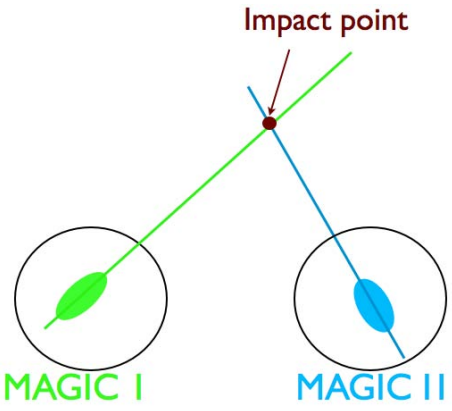

(b) Calculation scheme of the impact point on the ground.

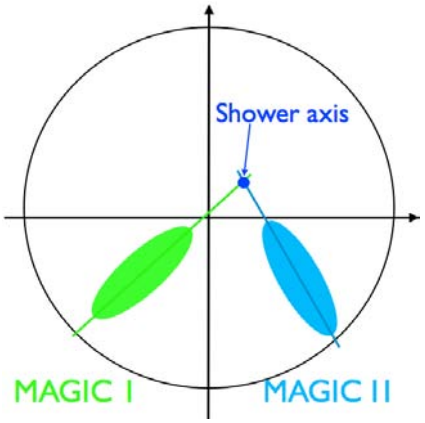

(c) Scheme of the shower direction determination.

Figure 2.26

single-telescope and stereo image parametrization is to separate γ-like showers from the rest.

For stereo observations we use RFs for γ/hadron separation and direction reconstruction, and LUTs for the energy estimation. To create the RFs and LUTs, we use a program called `coach`. For single-telescope, we use RFs for γ/hadron separation, direction reconstruction and energy estimation and all of them are produced by a program called `osteria`.

γ/hadron separation To evaluate how similar to a γ-ray shower an event is, we use a multivariate algorithm based on decision trees called *Random Forest (RF)* (Albert et al. 2008). It uses training samples representing γ-ray showers and hadronic showers. As it is shown in Figure 2.21, at this stage the MC sample is split in two subsamples: the *train* subsample, used to teach the RF how γ-like events look like, and the *test* subsample, that is used later in the analysis to calculate

the collection area and migration matrix and has to be different from the *train* sample not to have a biased result. A sample of real hadron data is also needed here to train the RF on what are the parameters of hadron-like events. The hadron sample must match the Zd conditions at which the RF needs to be trained. As the hadron to γ-ray rate is large, any sample of a non-detected source or a weak one is suitable to train the RF.

The algorithm works as follows: we select P parameters to discriminate between gamma rays and hadrons, then the training RF grows a number n (by default n=100) of decisional trees. The growing works as follows: One of the P parameters is randomly selected, and the data sample (containing gamma and hadron events) is separated in two subsamples (branches) based on this parameter. The cut of the parameter that better separates the sample is found by the RF by minimizing the Gini index (Gini 1921):

$$Q_{\mathrm{Gini}} = 4\frac{N_\gamma}{N}\frac{N_\mathrm{h}}{N} \tag{2.8}$$

where N_γ is the number of gammas, N_h the number of hadrons and N the total number of events. The procedure is repeated by randomly selecting another parameter and further separating the subsample until the final branch only contains events of one of the populations. This branch is assigned a 1 (or 0) depending if the events are hadrons (or gammas).

We apply the RF to the data sample using the program `melibea`. Every event has to pass through all the n decisional trees previously grown. The event is then assigned a *hadronness* value 0 or 1 depending if it ends up in a γ-branch or a hadron-branch. The final *hadronness* value of the event is given by the mean value of the hadronness of all the trees:

$$h = \sum_{i=1}^{n} \frac{h_i}{n} \tag{2.9}$$

where h_i is the *hadronness* resulting from passing the event through the i-th branch and h is the final *hadronness* assigned to the event.

Arrival direction reconstruction The determination of the arrival direction of the incoming γ-ray is easy for stereo observations (using the *crossing method* introduced in Section §2.2.3.5). For single-telescope observations we need to resort to the so-calledd "Disp" method (Fomin et al. 1994; Lessard et al. 2001). The Disp method has also proven to improve the arrival direction reconstruction for stereo observations, therefore it is used in stereo analysis as well.

The source position in a γ-ray shower produces an elliptical image at the camera. The distance from the image CoG to the source position is known as *disp* and can be determined using the following formula:

$$disp = A(size) + B(size)\frac{width}{length + \eta(size)leakage2} \tag{2.10}$$

where $A(size)$, $B(size)$ and $\eta(size)$ are second order polynomials of $\log(size)$ whose coefficients are determined using MC gamma rays. As illustrated in the left panel of Figure 2.27, the

source may be at two different positions for the same *disp*. The directional parameters introduced in Section §2.2.3.3 can be used to break this degeneracy.

This parametrization is not very efficient at high energies because many images are truncated. The method used for single-telescope direction reconstruction is a method based on the RF algorithm trained with MC gamma rays whose *disp* parameters are known. The RF is grown on a similar way as that explained for the γ/hadron separation, but the minimized parameter is the *disp* variance of each of the branches.

For stereo analysis, the *crossing method* gives a good estimate of the γ-ray arrival direction, but this method fails for parallel showers and very small reconstructed images. An improved method uses the *disp* information of both reconstructed showers. Figure 2.27 (right panel) illustrates this method. First, we calculate the four estimates of the source position (*disp*) for the shower images (two per image). Secondly, we calculate the distance between each pair of source position estimates from different images (the dotted lines in the right panel of Figure 2.27). Thirdly, we select the pair at the smallest distance which is the one taken for calculating the reconstructed direction of the shower. If this distance is larger than 0.22°, the reconstruction is not valid. Finally, the reconstructed direction is the average between the chosen pair of positions weighted with the number of pixels in each image. The θ distance shown in Figure 2.27 (right panel) is the angular distance between the reconstructed and the true position of the source. Its distribution can be used to extract the γ-ray signal as it will be shown in Section §2.2.3.7.

The *disp* method helps in the reconstruction of events with large impact parameter. Considering the 2-dimensional distribution of reconstructed arrival directions, we define the **angular resolution** as the angle that encloses 68% of the events. The left panel of Figure 2.28 shows the angular resolution of MAGIC as a function of the energy obtained using MC γ-ray events. It reaches a value of 0.11° at 250 GeV and it is as good as 0.06° above a few TeV.

Energy estimation For single-telescope observations, the energy estimation is performed by means of a RF. The RF is grown in a similar way as previously mentioned, but in this case we select different parameters and aim at minimizing not the Gini index, but the variance of E_{true} of the events in each of the subsamples.

In the stereo analysis instead we use LUTs. LUTs are filled with the true energy (E_{true}) and the RMS of MC simulated gamma rays. They are binned in *size* and *impact parameter*$/r_C$, where r_C is the Cherenkov radius defined in Section 2.2.3.5. The estimated energy (E_{est}) of each event is the weighted average of both telescopes where the weight is given by the RMS of the bin. Finally, we apply an empirical correction proportional to the cos(*Zd*).

The **energy bias** is defined as:

$$E_{\text{bias}} = \frac{E_{\text{est}} - E_{\text{true}}}{E_{\text{true}}} \tag{2.11}$$

to compute the energy bias for a given energy bin, we fit a gaussian to the energy biases of the individual events. The energy bias of the system is the mean of that gaussian. The **energy resolution** is defined as the σ of the gaussian. A plot comparing the current MAGIC energy resolution and bias at low and medium Zd and the resolution and bias previous to the upgrade

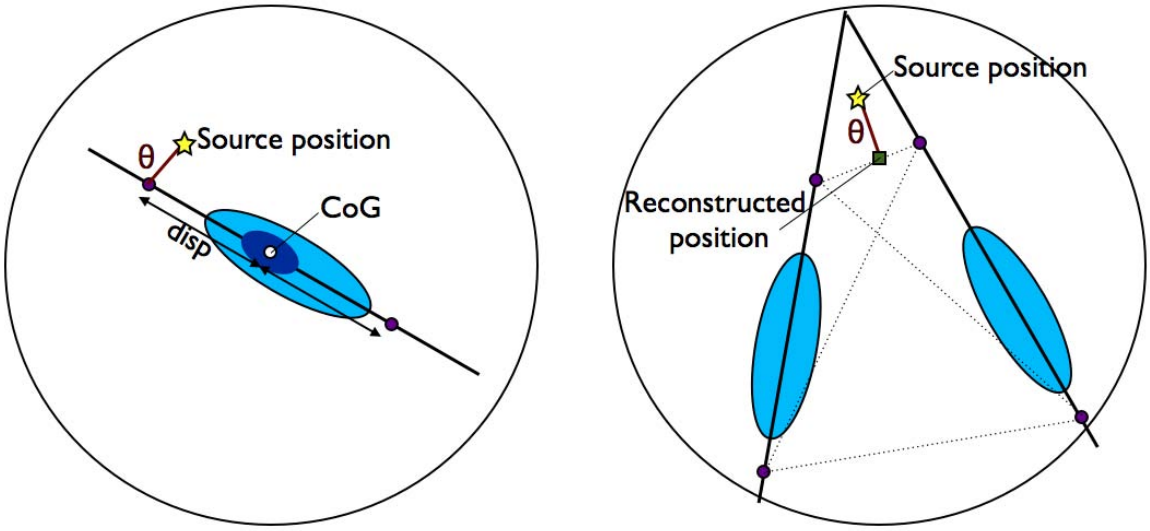

Figure 2.27: *Disp* reconstruction method for single-telescope (left panel) and stereo (right panel).

are shown in the right panel of Figure 2.28. We can see that the energy resolution is as good as 15 % at few hundred GeV. It worsens for higher energies because the impact parameter grows and truncated images become more frequent. For low energies it also gets worse due to misreconstructed images. The energy bias is close to 0 for energies > 100 GeV, however it rapidly increases below these energies due to threshold effects.

Finally, the **energy threshold** of the telescope is defined as the peak of the simulated energy distribution for a source with photon spectral index 2.6. It can be evaluated at several stages of the analysis, but most relevant is the threshold obtained after applying analysis cuts because it corresponds to the energy at which most of the events used for analysis are recorded. Events with energies below the threshold can be reconstructed as well, but the spectral points have significant errors. After applying a cut of 50 phe, *hadronness* and θ^2 cuts, the current energy threshold of the MAGIC telescope is ∼75 GeV for low Zd observations. A plot showing the energy distribution of gamma rays after analysis cuts of MAGIC for two Zd ranges is shown in Figure 2.29.

2.2.3.7 Signal extraction and sensitivity

Once we have evaluated *hadronness*, reconstructed energy and direction of the events, we can evaluate if the data sample contains a signal. For stereo analysis, a program called `odie` computes the angular distance θ between the reconstructed and the expected source position for every event and fills the so-called *signal histogram*, binned in θ^2. Assuming that the acceptance of the camera is the same for regions close to the center, the background would be flat over the whole histogram, while the γ-like events would accumulate at small values of θ^2. Only events that survive some other previously defined cuts in *hadronness, size...* are included in the signal histogram. These

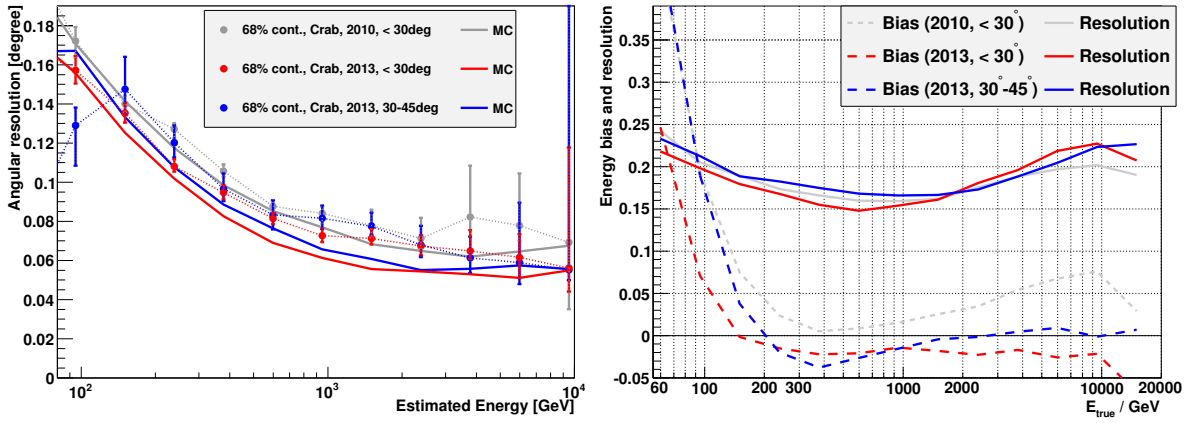

Figure 2.28: MAGIC angular resolution (left panel), energy resolution and energy bias (right panel). 2010 refers to the period before the readout upgrade to DRS4 and 2013 to the period after. Plots taken from Aleksić et al. (2014g).

cuts can be optimized on an independent data sample (usually Crab Nebula data). The current standard set of cuts used for the detection in several energy ranges can be found in Table 2.2.

Energy range	*Hadronness*	θ^2	$Size$[M1]	$Size$[M2]	$E_{\rm est}$
Low energies	<0.28	<0.02	>60	>60	-
Medium-to-high energies	<0.16	<0.009	>300	>300	-
High energies	<0.1	<0.007	>400	>400	>1000

Table 2.2: Standard cuts for the different energy ranges in the MAGIC analysis.

Once we have filled the signal histogram with the events surviving all the cuts and the signal region has been defined, we count the number of events in the signal region, $N_{\rm on}$. These events are not only gamma rays coming from the source, but also γ-like hadrons, $e^{\pm}$ and diffuse gammas. In order to estimate how many hadron events are inside the signal region, we fill a different θ^2 histogram, the *background histogram*, where θ is now the distance from the reconstructed position to the "off position", which is the position that is situated at the same distance as the source from the center of the camera, but on a different region (see Figure 2.20). The γ-ray events having small θ^2 with respect to the source position, are also included in the background histogram as it can be seen in Figure 2.30. As it was shown in Figure 2.20b, we can take more than one equivalent region to calculate the number of number of hadrons that there is in the signal region. Finally, the number of excess $N_{\rm ex}$ is given by:

$$N_{\rm ex} = N_{\rm on} - \alpha N_{\rm off} \tag{2.12}$$

where α is 1/(number of OFF regions). An example of a θ^2 histogram is shown in Figure 2.31.

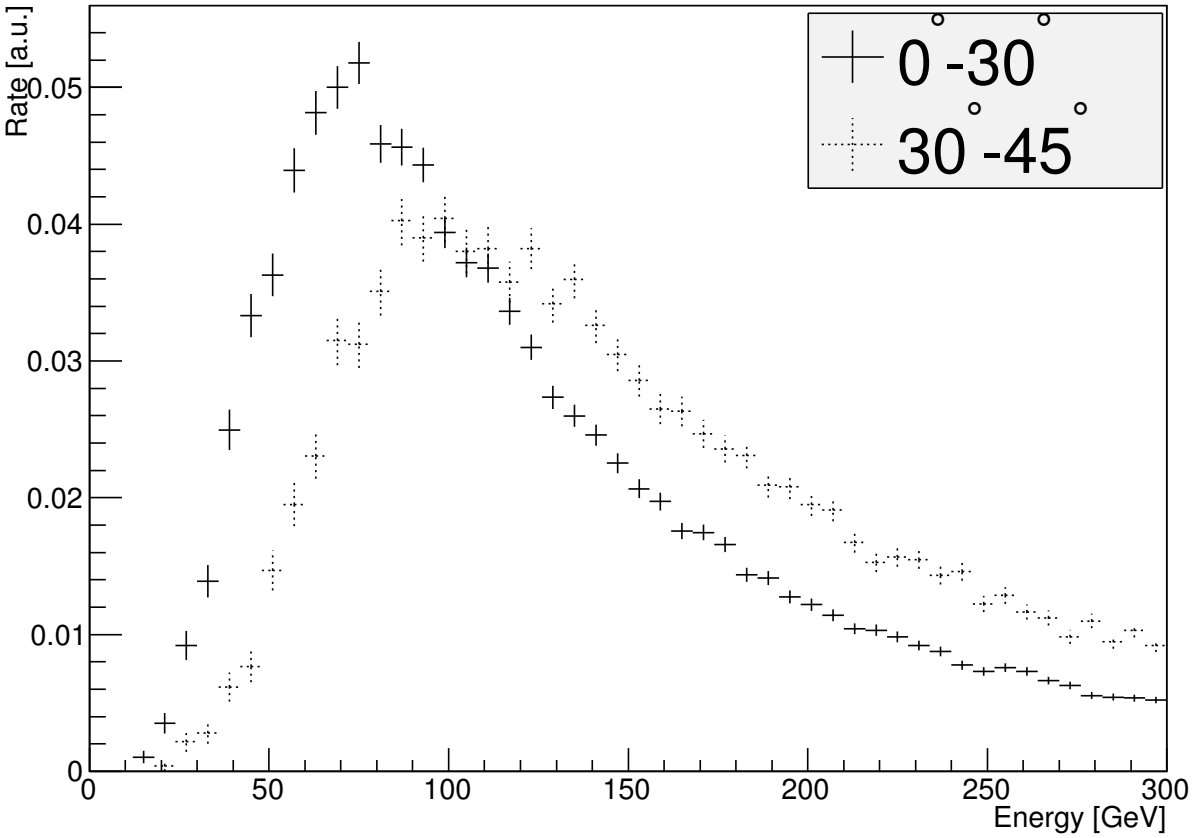

Figure 2.29: Rate of γ-ray events surviving analysis cuts for a Zd range between 0-30° (solid lines) and between 30-45° (dashed lines). Plot taken from Aleksić et al. (2014g)

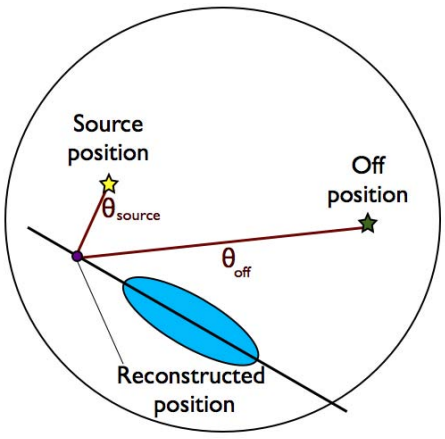

Figure 2.30: Sketch illustrating how θ is calculated respect to the source and off positions.

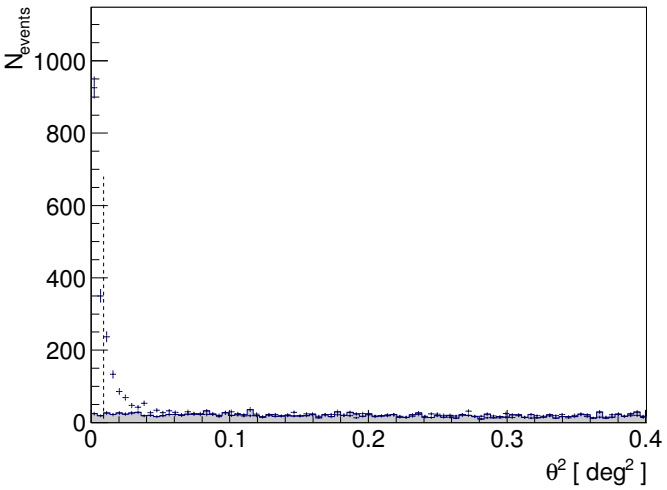

Figure 2.31: θ^2 distribution obtained for the Crab Nebula after medium-to-high hadronness and size cuts (Table 2.2). The grey histogram is filled with a θ^2 calculated with respect to the off position. The points correspond to an histogram filled with a θ^2 calculated with respect to the source position.

The significance of the signal is usually calculated using equation 17 from Li & Ma (1983):

$$\sigma_{\mathrm{LiMa}} = \sqrt{2\left(N_{\mathrm{on}} \ln\left[\frac{1+\alpha}{\alpha}\left(\frac{N_{\mathrm{on}}}{N_{\mathrm{on}}-N_{\mathrm{off}}}\right)\right] + N_{\mathrm{off}} \ln\left[(1+\alpha)\left(\frac{N_{\mathrm{off}}}{N_{\mathrm{on}}-N_{\mathrm{off}}}\right)\right]\right)} \tag{2.13}$$

but it can also be given as:

$$\sigma_{Nex/\sqrt{Noff}} = \frac{N_{\mathrm{ex}}}{\sqrt{N_{\mathrm{off}}}} \tag{2.14}$$

which is a Gaussian approximation of 2.13.

Sensitivity The sensitivity of the instrument is calculated as the minimum signal that can be detected in 50 hours with 5σ using the significance $\sigma_{Nex/\sqrt{Noff}}$. It is usually expressed in units of the Crab Nebula flux.

Given an observation of the Crab Nebula where a number of observed excesses N_{ex}, background events in the signal region N_{off} in a time t are observed, the significance in a time t_0=50 hours is given by:

$$\sigma_{Nex/\sqrt{Noff}}(t_0) = \sqrt{\frac{t_0}{t}}\frac{N_{\mathrm{ex}}}{\sqrt{N_{\mathrm{off}}}} \tag{2.15}$$

And the sensitivity, given as the minimum flux that can be detected in 50 hours with a significance 5σ in Crab units is:

$$Sensitivity = \frac{5\sigma}{\sigma_{Nex/\sqrt{Noff}}(t_0)} \tag{2.16}$$

The sensitivity is useful to compare the performance of different instruments and to estimate the flux that can be detected for a given amount of observation time.

There are two ways to give the sensitivity of an experiment: we can search for a set of cuts (*hadronness, size,* θ^2...) that give the best sensitivity above a given energy threshold. This is the so-called **integral sensitivity**. We can also search for the set of cuts that give the best sensitivity in a given energy range and compute the **differential sensitivity** in that range. The current MAGIC integral and differential sensitivities are shown in Figure 2.32.

2.2.3.8 Skymaps

Skymaps are two-dimensional histograms containing the arrival direction of all the γ-ray candidates. To select the events going to the histogram, the standard cuts applied to the data are the same as those shown in Table 2.2. They are produced using the source-independent information provided by the *disp* method. The program producing the skymaps in MAGIC is called `caspar`.

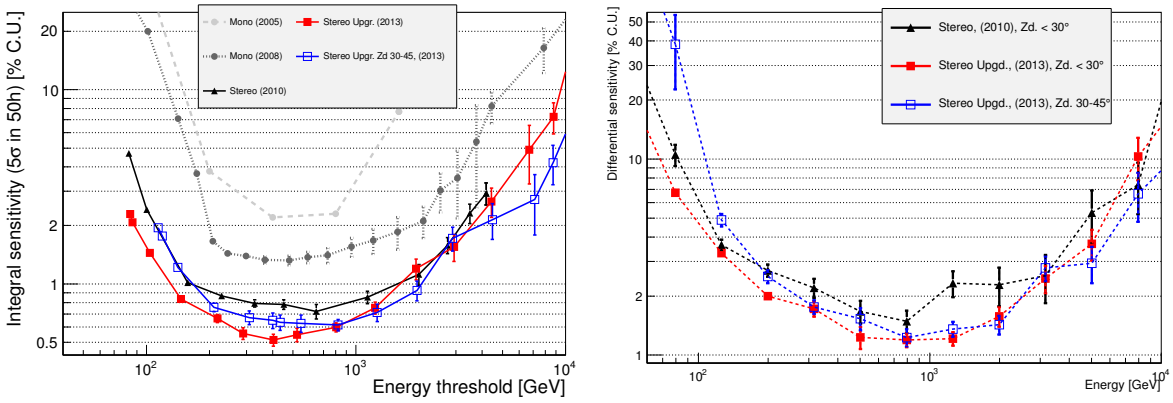

Figure 2.32: MAGIC integral (left panel) and differential (right panel) sensitivity as a function of energy. Plots taken from Aleksić et al. (2014g). Red curves correspond to the current MAGIC sensitivity for low Zd observations (between 0°-30°) and the blue one represents the current MAGIC sensitivity for the Zd range between 30°-45°. For comparison, the black curve represents MAGIC sensitivity before the installation of the DRS4 readout and the grey dotted and the grey dashed curves the sensitivity of MAGIC in single-teleescope mode, for MUX and Siegen readouts respectively.

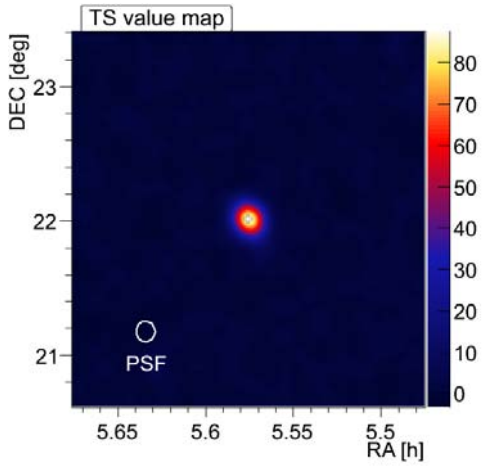

Figure 2.33: TS skymap of the Crab Nebula.

The most difficult task to produce a reliable skymap is the background estimation. Due to the inhomogeneities in the pixel response, stars in the FoV and observations at different Zd and Az, the background estimation is affected. An advantage of *wobble* observations is that background can be extracted from the same data sample as the signal. To avoid contamination from the signal region and correct the camera inhomogeneities, for each wobble position the camera is divided in two halves and the γ-ray candidates from the half that does not contain the source are accepted for the background skymap. For calculating the significance of a signal in a skymap, we use the Test Statistics (TS) significance, which is the LiMa significance applied on a smoothed and modeled background estimate.

An example of a TS skymap can be seen in Figure 2.33. When we have the signal and background skymaps, we subtract them to obtain the excesses histogram. This histogram is smoothed using the instrument's PSF added in quadrature with a Gaussian kernel to smear the number of excesses obtained. Finally, the σ_{smooth} used to smear the excesses histogram is given

by:

$$\sigma_{\text{smooth}} = \sqrt{\sigma^2_{\text{PSF}} + \sigma^2_{\text{Kernel}}} \tag{2.17}$$

The Gaussian kernel is usually taken equal to the PSF, so finally $\sigma_{\text{smooth}} = \sqrt{2}\sigma_{\text{PSF}}$

2.2.3.9 Spectrum and light curve

Spectrum The γ-ray differential spectrum of a given source is the number of photons per unit of energy, time and area. It can be written as:

$$\frac{d\phi}{dE} = \frac{dN_\gamma(E)}{dE\, dA_{\text{eff}}(E)\, dt} \tag{2.18}$$

To calculate it we need to compute the number of gammas in a given energy range, the collection area of the instrument and the effective observation time we spend on a given source. In MAGIC we use two dedicated programs to calculate the spectrum: the first one is called `flulxlc` (FLUX and Light Curve) and is used for single-telescope data, the second one is called `flute` (FLUx vs. Time and Energy) and is a simplified and advanced version of the first one that works for stereo data only. These programs use the `melibea` output of the data to calculate the *number of gammas* in each energy bin and the *effective time*. It also uses the `melibea` output of the MC gamma rays to calculate the *collection area* and the best cuts to extract the number of excesses in each energy bin (the scheme of this process is shown in Figure 2.21).

Number of gammas: $N_\gamma(E)$ is the number of excess events $N_{\text{ex}} = N_{\text{on}} - N_{\text{off}}$ in the energy range E. It is calculated in a similar way as it is done for the signal detection described in Section §2.2.3.7. A set of cuts (*hadronness,* θ^2) is selected in each energy bin, and the number of excess computed. The set of cuts is determined using MC in the following way: an efficiency is defined, and we change *hadronness* and θ^2 cuts until the number of surviving events exceeds this efficiency for each energy bin. These cuts are usually looser than the ones used to detect a signal, because that generally results in a better agreement of real and MC data and assures a better estimate of the *collection area*.

Effective time: It is the effective time of observation of a source. If we assume that the arrival time distribution of cosmic events follows a Poissonian distribution, the time difference between the arrival time of an event and the next one Δt, behaves exponentially. Given the Poissonian probability of observing n events in a time t for the event rate λ:

$$P(n,t) = \frac{(\lambda t)^n e^{-\lambda t}}{n!} \tag{2.19}$$

The probability that an event comes after a time t' is equal to the probability of observing 0 events in a time $t < t'$:

$$P(t' > t) = P(0,t) = e^{-\lambda t} \tag{2.20}$$

Since this probability can also be written as:

$$P(t' > t) = \int_t^\infty \frac{dP(t' = t)}{dt} dt \tag{2.21}$$

Therefore, the time evolution of the probability is given by:

$$\frac{dP(t' = t)}{dt} = \lambda e^{-\lambda t} \tag{2.22}$$

The event rate is given by the product of the time evolution probability times the number of recorded events N_0:

$$\frac{dN}{dt} = N_0 \lambda e^{-\lambda t} \tag{2.23}$$

being λ the rate of events recorded by the telescope that can be obtained from fitting to an exponential function the distribution of difference on arrival times between events Δt. An example of the distribution of Δt for a typical observation can be seen in Figure 2.34. Finally, the effective time can be written as the total number of events divided by the event rate:

$$t_{\text{eff}} = \frac{N_0}{\lambda} \tag{2.24}$$

The reason that the effective time is not coincident with the time elapsed between the beginning and the end of the observation is that there might be gaps in data taking (between runs) and that the data taking has a certain dead time after each event (as it was explained in Section §2.2.1.7).

Collection area: It is the geometrical area around the instrument where the gamma rays are detected. It is calculated using MC gamma rays and results from dividing the number of detected gamma rays surviving analysis cuts by the number of simulated gamma rays in a given energy range multiplied by the simulated area, or the area of an ideal telescope that would detect all the simulated gamma rays. Its mathematical expression is:

$$A_{\text{eff}}(E) = A_{\text{sim}} \frac{N_{\text{sel}}(E)}{N_{\text{sim}}(E)} \tag{2.25}$$

where A_{sim} is the simulated area, $N_{\text{sim}}(E)$ the number of simulated events in a given energy range and $N_{\text{sel}}(E)$ the number of events surviving cuts in the mentioned energy range. Equation 2.25 is only true if the MC gamma rays are simulated with the spectrum of the γ-ray source. Otherwise each event has to be weighted as it is explained in Appendix A.1.

The effective area depends on the Zd of the observations, being larger for larger Zd because the shower is produced further away in the atmosphere, as it was explained in Section §2.1.3. An example of the effective area covered by MAGIC at the trigger and analysis level is shown in Figure 2.35. The simulated area in MAGIC is currently a circle whose maximum radius, for each of the Zd ranges where the MC gamma rays are simulated can be found in Table 2.3.

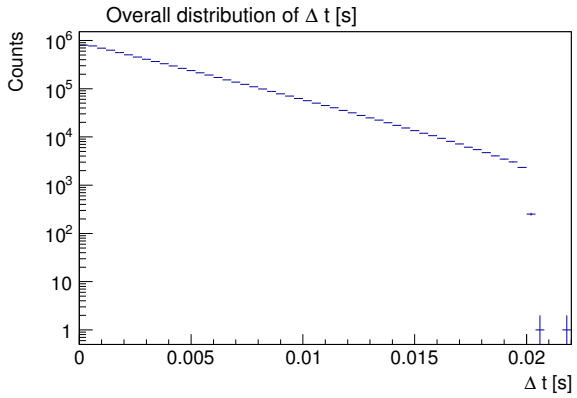

Figure 2.34: Distribution of time differences between events.

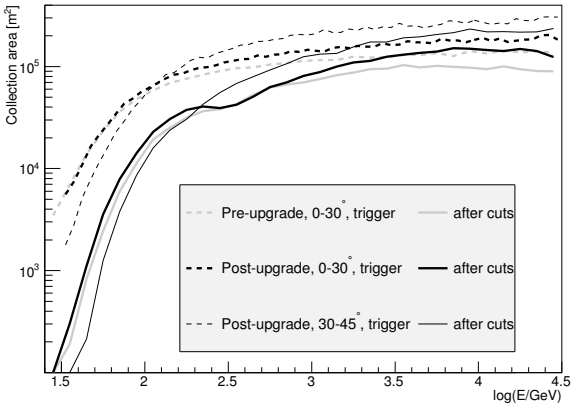

Figure 2.35: Collection area before (dashed lines) and after (solid lines) applying analysis cuts. The collection area for the telescope equipped with the DRS4 readout and Zd range between 0°-30° is represented with a thick black line and for the range between 30°-45° with a thin black line. For comparison, the collection area for the period before the MAGIC upgrade is also included in grey.

Zd range [°]	Maximum impact [m]
05 – 35	350
35 – 50	500
50 – 62	700
62 – 70	1000

Table 2.3: Maximum impact parameters simulated for each Zd range.

Light curve: Light curves show integral fluxes in a given energy range and in bins of time. The differential energy spectrum (equation 2.18) is calculated for each of the time intervals, and then integrated over the energy range:

$$\phi = \int_{E0}^{E1} \frac{d\phi}{dE} \quad [\mathrm{cm}^{-2}\mathrm{s}^{-1}] \tag{2.26}$$

Upper limits: Upper Limits (ULs) on the flux are computed when no significant γ-ray signal is found. Using the number of measured excess events N_{ex}, the number of off events N_{off} and selecting a Confidence Level (C.L.) and systematic error, we can calculate an UL to the number of expected signal events N_{ul} using the method described in Rolke et al. (2005). The C.L. usually

used to calculate MAGIC ULs is 95% and the systematic error assumed is 30 %. $N_{\rm ul}$ is the UL on the maximum number of expected events according to the measurements performed and the confidence level defined. As we do not have any information about the source, we also have to assume a spectral shape, usually a power-law with spectral index Γ=2.6.

$$\phi(E) = KS(E) = \left(\frac{E}{E_0}\right)^{-\Gamma} \tag{2.27}$$

The integral flux above an energy $E_{\rm min}$ can be written as:

$$\int_{E\rm min}^{\infty} \phi(E)\, dE = K \int_{Ec}^{\infty} S(E)\, dE = \frac{N_{\rm ul}}{\int_{E\rm min}^{\infty} \int_{0}^{t\rm obs} A(E)\, dE\, dt} \tag{2.28}$$

where $t_{\rm obs}$ is the observation time. Finally, the UL on the integral flux $K_{\rm ul}$ can be written as:

$$K_{\rm ul} < \frac{N_{\rm ul}}{T \int_{Emin}^{\infty} S(E)\, A(E)\, dE} \quad [\mathrm{TeV}^{-1}\mathrm{cm}^{-2}\mathrm{s}^{-1}] \tag{2.29}$$

2.2.3.10 Unfolding

Due to the non-idealities of the detectors, experimental results get usually distorted. To correct for the finite resolution of our telescope, we apply an unfolding procedure. In IACTs, events have an estimated energy, but their true energy is not known. Defining the detector response function to a measured quantity y ($E_{\rm est}$) from a true quantity x ($E_{\rm true}$) as $M(x, y)$, the measured distribution $g(y)$ can be written as a function of the true distribution $f(x)$:

$$g(y) = \int M(x, y)\ f(x)\, dx + b(y) \tag{2.30}$$

where $b(y)$ accounts for a possible background contribution in the measurement. Since the data is binned in bins of $E_{\rm true}$ and $E_{\rm est}$, the equation can also be written:

$$g_i = \int M_{ij}\ f_j + b_i \tag{2.31}$$

In the case of MAGIC , the tensor M_{ij} is given by the *migration matrix* of the detector and can be calculated from simulated γ-ray MC. It basically represents the probability that an event with $E_{\rm true}$ belonging to bin j ends up in bin i of the $E_{\rm est}$ distribution. The easier way to solve this problem would be to invert M_{ij}, but this is sometimes not possible. In this case, the best way to solve this problem is the least square minimization method, finding the value that minimizes the χ^2_0. This, however, gives unstable results, so a regularization term is added:

$$\chi^2 = \chi^2_0 + \frac{\omega}{2}\chi^2_0 + Reg(f) \tag{2.32}$$

where $Reg(f)$ is the regularization and ω is the inverse of the regularization strength, which is a way to adjust the weight given to the regularization within the χ^2 equation. Large values of

ω imply less regularization and usually produce spectra with fluctuations, but small values of ω produce too smooth unfolded distributions that can deviate from the data. The determination of an appropriate value for the regularization is very important when producing an unfolded spectrum. There are several methods to compute the regularization in MAGIC , they are described in Schmelling (1994); Bertero (1989); Tikhonov & Arsenin (1977)

There is another way of unfolding the data, the so-called *forward unfolding* method. It assumes a-priori the spectral shape that will be followed by the measurement, and minimizes the χ^2_0 with respect to these parameters. This is generally done analytically, forcing the solution to be continuous. The result is the best fit to the a-priori defined parameters, therefore no spectral points are available. Since no regularization is used, the result from the forward unfolding only depends on the assumed spectral shape.

The convergence on the result of all the unfolding methods has to be carefully checked. The spectra results shown by MAGIC are usually given using the *forward unfolding* method, although to produce the spectral points one of the other methods is used.

2.3 CTA

The Cherenkov Telescope Array (CTA) is an initiative to build a next generation ground-based VHE γ-ray instrument. It is proposed as an open observatory and it currently (May 2015) gathers about 1300 scientists from 29 countries worldwide. It is planned to have two sites, one in the southern hemisphere focused on galactic physics and another one in the northern hemisphere, mainly focused on extragalactic physics and transient events. The final site selection for both sites is expected to take place during the year 2015. An artist view of the CTA array is shown in Figure 2.36. The technical objectives of the future-generation CTA can be summarized as:

- Achieve the lowest possible energy threshold by an IACT to be sensitive to transient phenomena such as blazars, GRBs, novae and any other phenomena that emits photons in the $\mathcal{O}$(10-100) GeV band and lasts for days to weeks. This purpose will be achieved by the use of LSTs with their large reflectors able to collect the few photons produced by $\mathcal{O}$(10) GeV cascades. LSTs are designed to work in stereo, which translates in an increase in the collection area of the array and a more powerful gamma/hadron separation. The latter is especially important at the lowest energies where γ-like showers are similar to cascades generated by hadrons or accidental triggers.

- Improve the sensitivity at the medium energy band $\mathcal{O}$(0.1-1) TeV down to a few mCrab. This is achieved by collecting more photons and improving the angular and energy resolution for a better background rejection. The improved cameras and the increased number of MSTs with respect to the current arrays using similar telescopes (HESS, VERITAS) will make it possible.

- As the flux of γ-ray photons at $\mathcal{O}$(10) TeV is very small, to significantly detect them at these energies one has to increase the collection area. Background suppression at these energies is not a problem because of the steepness (power-law with a 2.7 photon spectral index) of the hadron spectrum. Several SSTs will be located in the outer parts of the array. They have high energy threshold ($\mathcal{O}$(1) TeV), but their only purpose is to extend the collection area of the array to collect the maximum number of VHE photons at energies > 10 TeV.

There are mainly three telescope types:

- **Large Size Telescope (LST):** They are designed to be light-weighted to achieve fast repositioning to catch GRBs. The structure is made of carbon-fiber tubes holding a tessellated parabolic reflector of 23 m diameter. The current design has a 27.8 m focal length, 4.5° FoV and 0.1° PMTs as pixels (Acharya et al. 2013). A maximum of four telescopes will be placed in the center of the array of each observatory. A drawing of the LST design can be seen in Figure 2.37a.

- **Medium Size Telescope (MST):** They are designed to have 12 m Davies-Cotton reflectors. The current design is to have 17 m focal length, 7–8° FoV and 0.18° PMT pixels. In the

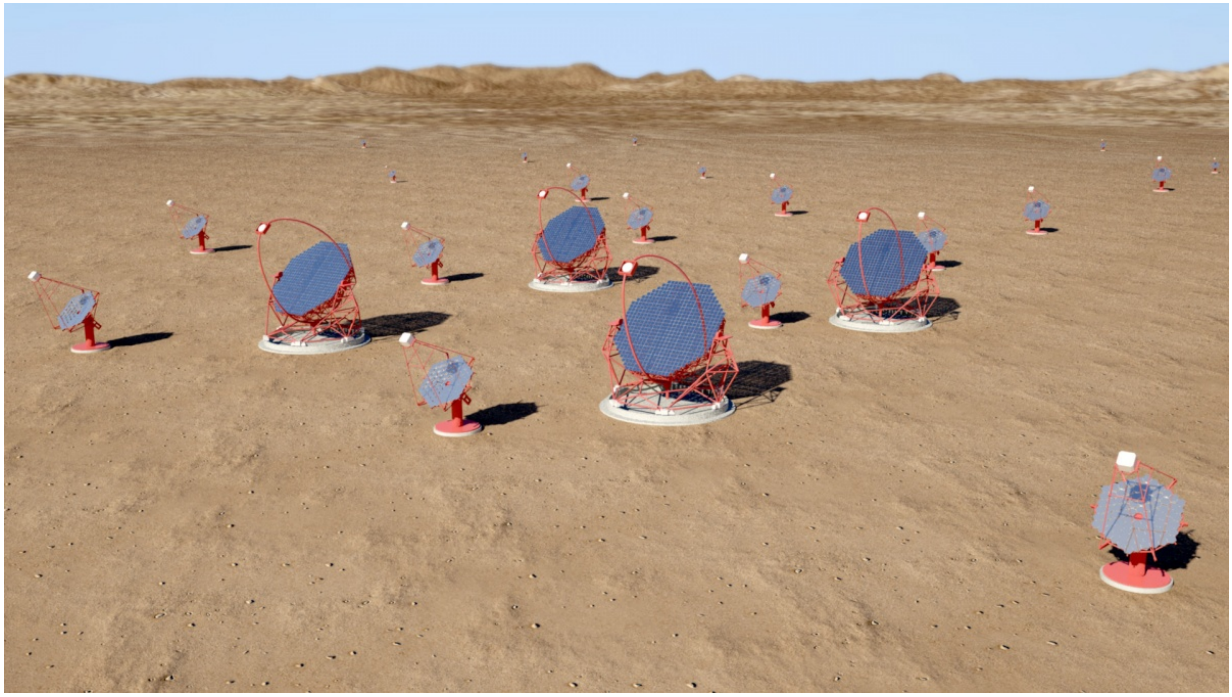

Figure 2.36: CTA design concept. One can see four LSTs in the center of the array and they are surrounded by MSTs. SSTs are placed farther away from the center of the array to extend the overall collection area.

order of thirty MSTs will surround the LSTs in each site. A picture of the MST prototype constructed in DESY Berlin is shown in Figure 2.37b

There is also a plan to construct a double mirror Schwarzschild-Couder Telescope (SCT) to extend the southern array with a maximum of 36 telescopes of this type (Vassiliev & Fegan 2008). They are currently planned to have a 10° FoV allowing a small plate scale that can be filled with smaller pixels such as SiPM. A drawing of the SCT telescope design is shown in Figure 2.37c.

⊙ **Small Size Telescope (SST):** A variable number between 35 – 70 SSTs will be placed in principle only in the southern observatory, focused on galactic physics and interested in the highest γ-ray energies. Several solutions have been designed to reduce the cost and be able to construct such a large number of telescopes. A prototype using the traditional Davies-Cotton optics with a 1 m reflector was built in Kraków and is shown in Figure 2.37e. The usage of the Schwarzschild-Couder optics has also been developed for this type of telescopes and a picture of the 2 m primary reflector ASTRI SST prototype constructed by INAF is shown in Figure 2.37d.

The physic cases are several (Acharya et al. 2013) and can be summarized as:

1. Study the origin and propagation of cosmic rays

2. Understand particle acceleration in several objects such as pulsars, PWNe, SNRs, novae, black holes and any other object where extreme acceleration takes place.

3. Search for new physics beyond the Standard Model and study the nature of dark matter.

The duration of this thesis took place during the Design and Prototyping phases of the CTA schedule, therefore all the contribution to the CTA project is technical. CTA is expected to start scientific operation in 2018, although the full array is not expected to be completed before 2020.

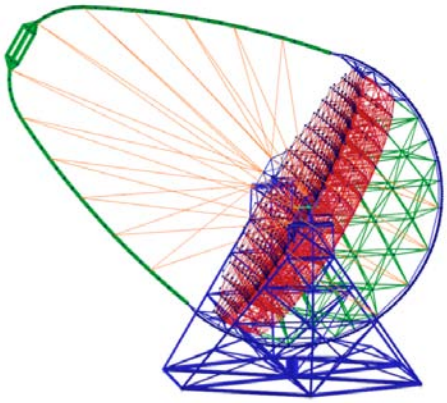

(a) LST drawing.

(b) Single-mirror MST prototype in DESY Berlin.

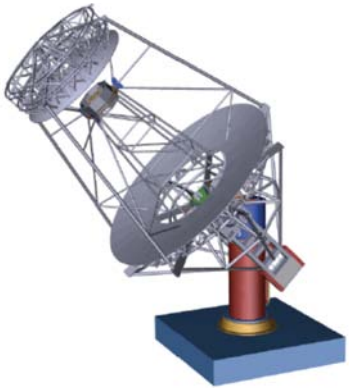

(c) Dual-mirror MST SCT prototype design.

(d) Single-mirror SST prototype in Kraków.

(e) Dual-mirror SST prototype on Mount Etna.

Figure 2.37: Prototypes and designs of the different telescope types for CTA.

Part II

Contributions to the lowering of the threshold of imaging atmospheric Cherenkov telescopes

Figure II: Artist view of four LSTs.

3 Single telescope trigger for CTA

The goal of the LSTs for CTA, as it was described in Section §2.3, is to achieve the lowest possible energy threshold. To push the threshold down in energy, one of the most important systems is the camera trigger, that selects the events that are recorded. Since most of the problems when lowering the energy threshold of the system is that the accidental triggers increase, the trigger system needs to powerfully distinguish between the events containing cosmic showers and the ones containing only noise. Arrays of Cherenkov telescopes typically use multi-level trigger schemes to keep the rate of accidental triggers produced by direct NSB and PMT APs low. At a first stage, individual telescopes produce a trigger signal from the pixel signals in the telescope camera. The final event trigger is then formed by combining trigger signals from several telescopes. We will present in this chapter the work performed to develop, test and characterize an analog trigger system for the analog cameras of LSTs and MSTs.

3.1 Description of the analog trigger concept

We designed a trigger system completely based on the analog treatment of the signals coming from the camera pixels (Barcelo et al. 2013; Tejedor et al. 2013). A schematic of the whole trigger system is shown in Figure 3.1. The photosensors are grouped in clusters of 7 pixels and their signals are first handled by a *L0 decision* trigger that has two trigger strategies implemented. The *majority* trigger option issues a rectangular pulse for the pixels that are above a certain DT and then makes an analog sum of all the rectangular pulses in the cluster. The *sum* trigger option issues the analog sum of the signals from a group of pixels. The signals coming from several clusters, with either of the two L0 options, go to an *L0 fan-out* board that copies and distributes them to the *L1 decision* trigger installed in each cluster. It adds up the signals coming from

neighboring clusters and issues a rectangular signal if the addition is above a certain threshold. The signals issued by the L1 are then distributed by the *L1 distribution* that collects the signals generated by the L1 decision boards and provide them to the Trigger Interface Board (TIB) and the readout.

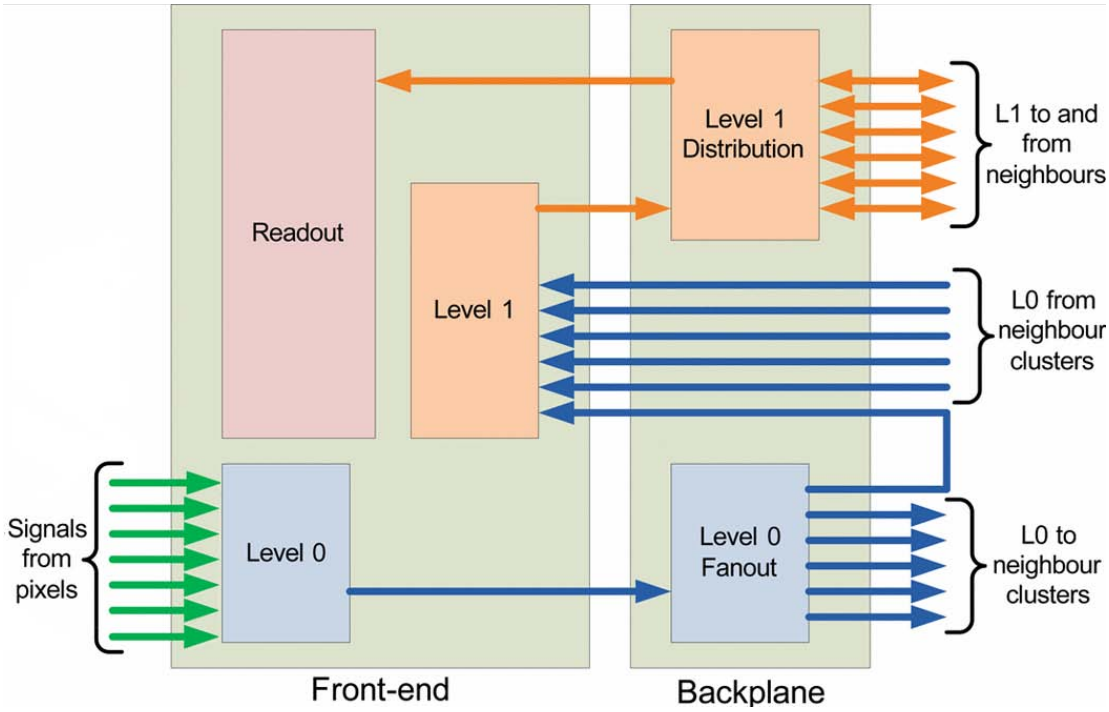

Figure 3.1: Trigger scheme for analog cameras for CTA. From Tejedor et al. (2013).

The work performed on the trigger system for CTA presented in this thesis was twofold: on one hand, we performed simulations to evaluate the difference in performance between using the different trigger options implemented in the analog trigger developed for the analog readouts of the MSTs (NECTAr, Vorobiov et al. 2011) and LSTs (*Dragon,* Kubo & Paoletti 2011). We also used simulations to investigate the effect of non-idealities such as wider PMT pulses in the LST performance. On the other hand, we characterized the test modules for the L0 trigger, first on its discrete component form, and later the L0 ASICs that will finally be used for the analog camera of the LST prototype.

3.2 Optimal design based on simulations

The simulation of the different trigger options is necessary to compare their performance. In this section we describe the results of comparing the performance of the sum trigger and the majority trigger. Furthermore, we have studied for the sum trigger option the gain between single-telescope and stereo observations and also the effect of non-idealities such as wider pulse amplitude of the PMTs.

3.2.1 Simulation characteristics

3.2.1.1 Software

The *Production-I* of MC simulations for CTA only implemented one trigger scheme. Most of the simulations summarized here were performed with the trigsim package (Wischnewski 2011). This package was meant to be later implemented in the standard CTA MC simulation package `Sim_telarray` (Bernlöhr 2008). It actually uses a special option of Sim_telarray that generates files with the arrival time of each phe produced in each pixel. Some results also come from the new implementation of other trigger schemes in `Sim_telarray`.

In *Production-II*, several trigger schemes are implemented and run. It also stores by default the information of arrival time for each phe produced in each pixel, if the shower generates more than a pretty low value of phe. Some results regarding different trigger options were also drawn that are in concordance with those presented in this section (Bernlöhr 2013).

3.2.1.2 Input parameters

It is important to clarify the input parameters of the simulation to understand the possible differences between the results of different simulations. When we do not state the contrary, these are the parameters used for the simulations:

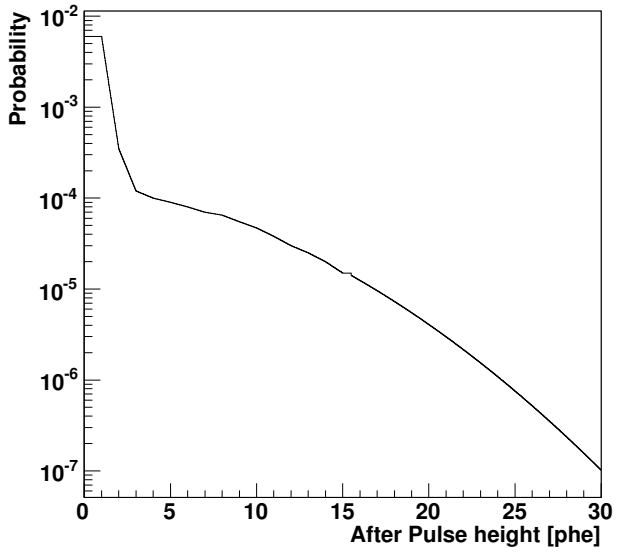

Figure 3.2: APs Distribution

- ⊙ Pulse shape: Gaussian with FWHM=2.6 ns;
- ⊙ APs distribution: Used the complete distribution of AP provided by Hamamatsu in April 2010. See Figure 3.2.
- ⊙ Cells=21 pixels patch with overlapping.
- ⊙ Clipping levels [for sum trigger]: Clip = 6 and 8 phe.
- ⊙ Simulation time 50 ns.
- ⊙ Different gate widths used (2, 4, 6 ns) + Time over Threshold (ToT).
- ⊙ Different cuts in the minimum number of phe (no cuts, 25 phe, 50 phe).

3.2.1.3 Showers

We used proton and gamma showers for the simulations. To calculate the cosmic ray rate we use files with a spectrum of energies simulated with a power-law with photon spectral index Γ=2 for energies in a range 0.005 TeV < E < 500 TeV. To calculate *collection areas*, we used gammas

with single-energies (0.01 , 0.03, 0.1, 1, 10, 100 TeV) and to calculate the *energy threshold*, we used files with a spectrum of energies simulated with a power-law with photon spectral index Γ=2 for energies in a range 0.01 TeV < E < 100 TeV. The spectrum was re-weighted to a power-law with photon spectral index Γ=2.6 to calculate the energy threshold, as it is explained in the Appendix A.1.

3.2.1.4 NSB Simulation

The first step was to check how the camera trigger rate induced by the NSB changes as a function of several parameters that could be tuned in the trigger. The expected rates of phe per pixel from the NSB depend on the site conditions, the QE of the photo-detector to be used as well as the pixels size and the dimension of the reflector surface. Different scenarios are simulated for the amount of NSB that is accepted in the triggers of each telescope (see Section §3.2.2.1). The NSB simulations were run for one single trigger cell and the results extrapolated to the whole telescope, taking into account the overlap between cells.

3.2.1.5 Telescopes

The characteristics of the different telescopes were selected according to the latest specifications accepted by the MC group for *Prod-I*. It is also important to know for each telescope the NSB levels we are working with. As the PMTs used are the same for each of them, the only difference comes from the different FoV of each pixel, dependent of the mirror area and focal length. For the considered two type of telescopes we have the following characteristics:

- **LST:** Mirror area=381.9 m^2; Focal length=28.0 m; Number of pixels = 1813; Extragalactic NSB = 208 MHz per pixel.
- **MST:** Mirror area=103.9 m^2; Focal length=15.6 m; Number of pixels = 1765; Extragalactic NSB = 173 MHz per pixel.

3.2.1.6 Camera Trigger

The camera trigger simulation performs the combinations of analog signals of pixels in a trigger region. Two possible combinations have been studied: in the first one, the so-called *analog sum trigger*, all the analog signals of the trigger regions are analogically added; in the second one, the so-called *analog majority trigger*, the analog signals of the pixels in one cluster are first compared with a threshold and the corresponding digital signals are then analogically added for all the clusters in the trigger region, and the resulting sum compared with another threshold.We will present results comparing these two options.

3.2.2 Comparison between different trigger options

It was agreed between the MC Working Package (WP) that two different scenarios will be considered for the simulations (Hinton 2012). Those options are presented and the determination of the operation point for each of them described.

3.2.2.1 Different scenarios proposed

1. *Safe:* DTs are fixed so that the single-telescope accidental rates due a NSB double as high as the extragalactic NSB are equal to the cosmic ray rate.

2. *Aggressive*: DTs are fixed so that the stereo accidental rates due a NSB at double as high as the extragalactic NSB are equal to 10% the cosmic ray stereo rate. This scenario would allow to lower the energy threshold and increase the collection area at the lowest energies.

3.2.2.2 Determination of the operation point

We computed the operation point where we would work in the different scenarios considered for the simulations.

1. *Safe:* For the safe scenario we performed the following steps: First of all, we run the single-telescope simulations for 1.5×proton rate (to account for the presence of nuclei heavier than protons) and NSB. We run the NSB simulations for a single cell and multiply the single-cell rate by a factor κ, given by:

$$\kappa = \frac{p \times n}{N_c}$$

where p=number of pixels in the telescope, n the number of times each pixel appears in the overlapping clusters (for our clusters n=3, except for the outer cells) and N_c the number of pixels in each cluster (for the analog clusters N_c=21).

We plot both rates and the point where both curves intersect gives the DT to be used for this scenario. An example of the method used can be found in Figure 3.3.

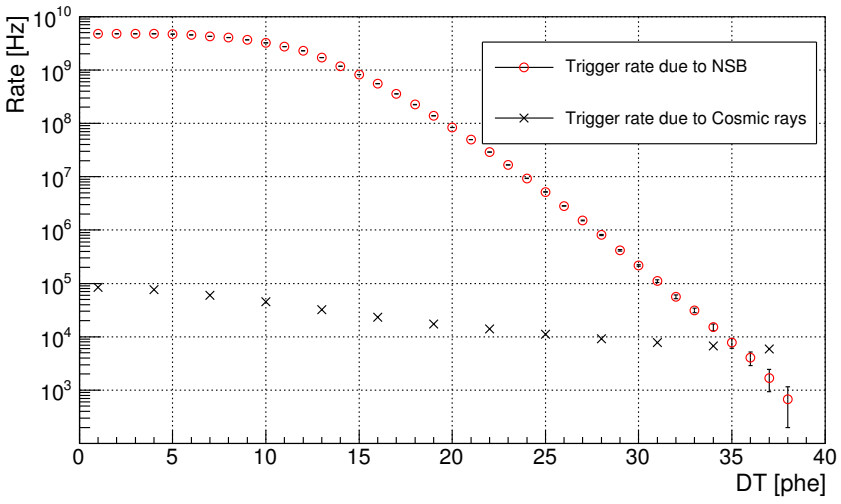

Figure 3.3: Trigger rate due to NSB (red circles) and due to cosmic rays (Black crosses) for an LST working in single-telescope mode. The crossing point gives the DT where we will operate.

2. *Aggressive:* To evaluate the operation point of this option, we simulated 1.5×proton rate and calculated the stereo NSB rate (see details in Appendix A.2). The crossing point between the 1.5×0.1×proton stereo rate and the NSB stereo one gives the DT at which both are equal.

			Sum trigger		Majority trigger	
			Safe	Aggressive	Safe	Aggressive
LST	DT [phe]		35	34	10	9
	Rate [kHz]	Single-telescope	6.5	6.7	3.4	4.0
		Stereo	2.4	2.5	0.35	0.39
MST	DT [phe]		34	31.5	10	9
	Rate [kHz]	Single-telescope	1.5	1.8	1.4	1.6
		Stereo	1.2	1.3	0.24	0.25

Table 3.1: DTs, single-telescope and stereo rates for the different simulated scenarios considered.

3.2.2.3 Results for the optimization of trigger options

The comparison between the performance of the sum and majority trigger is done using the *collection area* and *energy threshold* given by each trigger option for each telescope and for each DT scenario.

For any trigger strategy, one can reduce the trigger rate induced by the NSB as much as desired, but this will also mean a reduction of the collection area and increase in the energy threshold (defined in Sections §2.2.3.9 and §2.2.3.6 respectively). Hence, a sensible criteria to choose one trigger strategy would be checking the collection area and energy threshold one could get as a function of the trigger rate induced by the NSB.

Triggers still have to be reconstructed and classified as hadrons or photons. Therefore, one might expect that the best figure of merit would be the final sensitivity of the telescope (i.e., gamma efficiency over the square root of hadron efficiency). However, one has to keep in mind that a basic trigger scheme does not differentiate between real gamma and background events, but between NSB-induced events and γ-like events (either from gamma or hadron origin). So at the end, the trigger scheme which provides the largest collection area for γ-like events, while keeping the NSB-induced events under control, will very likely be the best trigger scheme, from the simulation point of view.

Finally, one still has to keep in mind that we have been so far only considering single-telescope trigger and CTA will work in stereo mode asking for two or more telescopes in coincidence. The assumption is that although the stereo requirement will change the effective collection area for CTA, the change will be quite independent on the single telescope trigger strategy. This should be true if the dependence of trigger probability on distance between the shower core and the telescope axis is similar for the different trigger strategies. This condition was checked for gamma-ray induced showers.

Collection Area The collection area has been computed for each of the simulated energies, for the different scenarios considered and for both the LST and MST telescopes.

LST We start with the comparison between different options for the LST. Apart from testing different trigger options, we also checked the effect of applying a cut in the minimum number of phe in each event. The cut is meant to check that the results do not change by eliminating the events producing the smallest images that will probably not be used for the analysis. The cut selected is 25 phe. The plots of the collection area and the ratio between the collection area of a given option divided by the collection area applying sum trigger with a clipping of 6 phe are shown in Figure 3.4.

It is shown that in general the *sum* trigger gives larger collection areas than *majority* for low energies. Between the two clipping options, the one using a higher value of clipping (8 phe) is a slightly better option to obtain larger collection areas at low energies (the ones relevant for the LSTs). This effect could be explained because of the lower energy showers triggering the system. They will produce one pixel with a very high charge and some pixels surrounding it with a lower one. Since the larger signal is cut due to the clipping, the option using a higher clipping value let lower energy showers trigger the system. We have also checked that the ratios hardly change when applying a cut in phe. Conclusions at very low energies (10 GeV) cannot be obtained, because of the very large uncertainties due to the low statistics with the used DTs. For energies larger than 1 TeV, the majority and sum trigger options are equivalent. This would be in principle expected, as the performance of the sum trigger is known to exceed the one of the majority trigger at low energies (< 100 GeV), but not necessarily at higher ones.

Let us now compare the aggressive and safe scenarios. As the aggressive scenario allows to lower the DT more than the safe one (not with the majority trigger), it triggers more showers, therefore the collection areas are slightly larger. In Figure 3.5 we show the ratio between the collection area of the safe aggressive and safe scenarios.

Due to the large errors in the extrapolation of collection areas for both scenarios, we find that, although a bit higher for the lowest energies with the aggressive option, both of them are, within errors, equivalent.

MST We also studied the performance of the analog trigger to be used with the analog cameras of the MSTs. The trigger options studied are the same as those investigated for the LSTs, also studying the effect of a minimum cut os 25 phe in the events accepted.

The sum trigger option gives slightly larger collection areas for energies > 1 TeV, but within the errors, all trigger options are equivalent. As it was already mentioned, the sum trigger is expected to show a better performance at the lowest energies, however for high energies both options are expected to perform similarly, as it is shown.

Figure 3.7 shows a comparison between the aggressive and safe scenarios for the MST. The DTs are again lower for the aggressive scenario, although the performance is equivalent within the errors as it was the case for the LSTs.

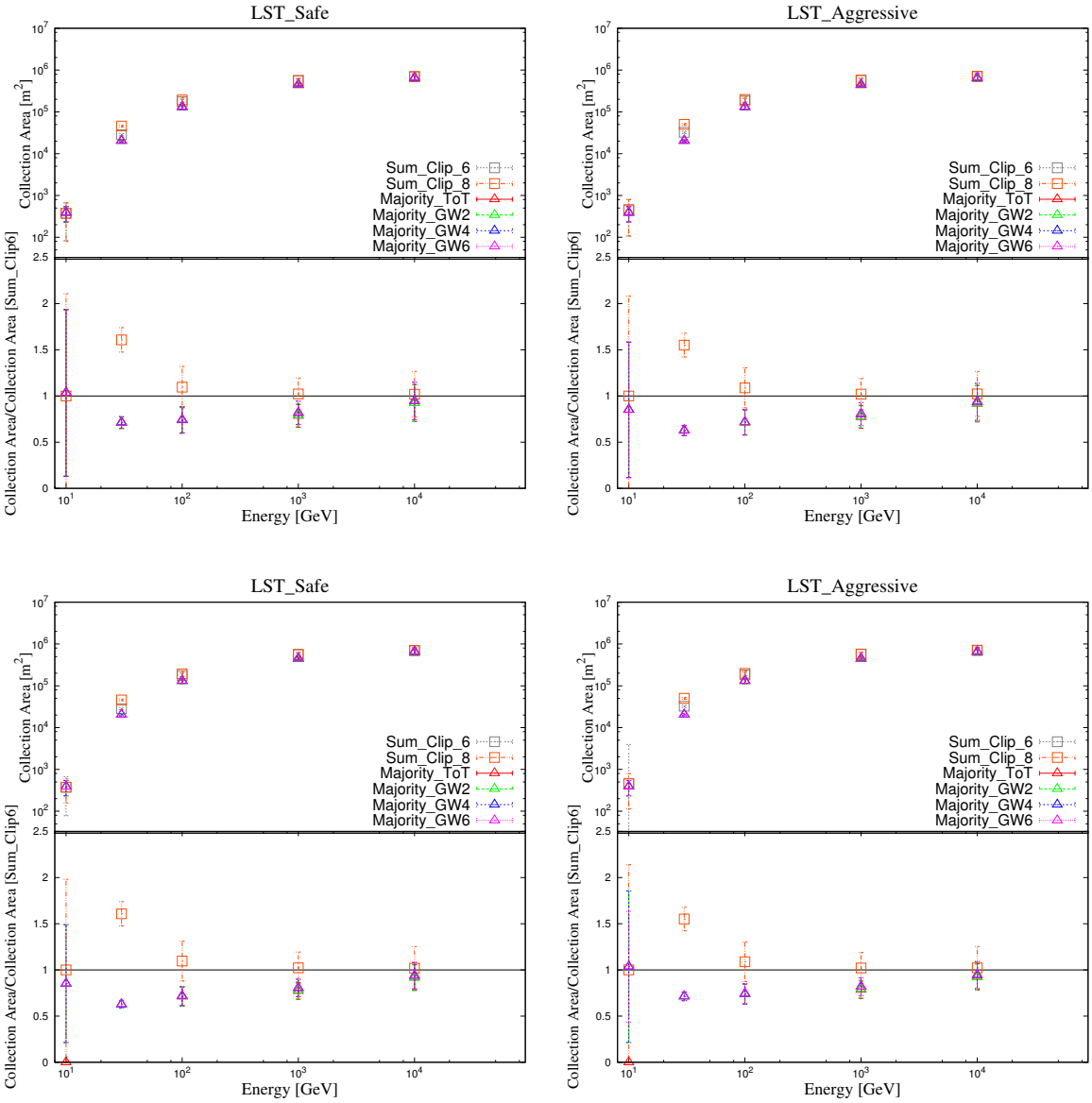

Figure 3.4: LST collection area for the safe (top left) and aggressive (top right) trigger scenarios with no cut in the minimum number of phe, and safe (bottom left) and aggressive (bottom right) scenarios with a cut of 25 phe. Sum_Clip_6 corresponds to the sum trigger with a clipping=6 phe, Sum_Clip_8 to the sum trigger with a clipping=8 phe, Majority_ToT to majority time over threshold, and Majority_GWN to the majority opening a trigger gate of width N ns.

Energy Threshold To compute the energy threshold we simulate a power-law spectrum with Γ=2.6 spectral index for energies between 0.01 and 100 TeV. The energy threshold is the mean of a gaussian fit around the maximum of the histogram containing the energy of the triggered energy distribution, as it is explained in Section §2.2.3.6. We can find in Table 3.2 the thresholds

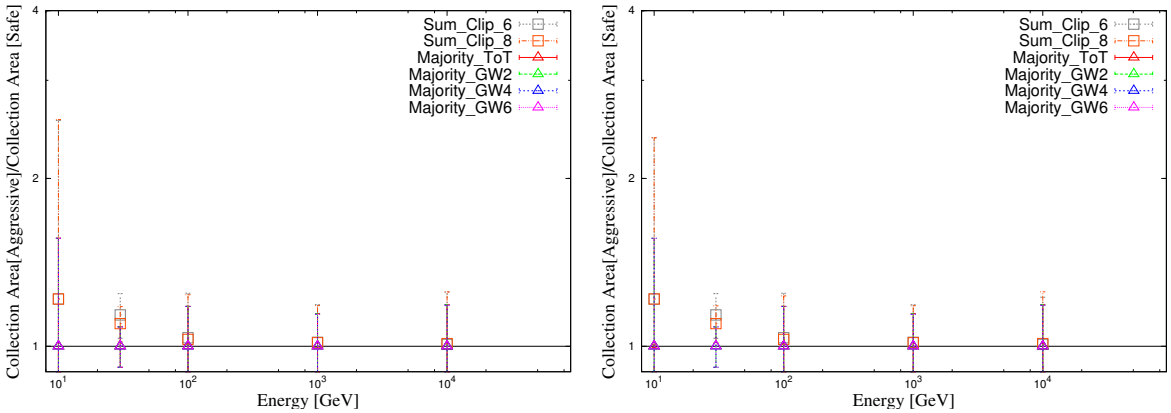

Figure 3.5: Comparison between safe and aggressive trigger scenarios for the LST with no cut in the minimum number of phe (left) and with a cut of 25 phe (right). The options plotted are the same as in Figure 3.4.

for the different options.

	Trigger Type	Energy Threshold [GeV]			
		Cut = 0 phe		Cut = 25 phe	
		LST	MST	LST	MST
Safe	Sum Clip [6 phe]	43.0±0.2	138±11	43.0±0.2	138±11
	Sum Clip [8 phe]	32.9±0.2	126.5 ±1.5	32.9±0.2	126.5 ±1.5
	Majority	52.0 ±0.3	146±7	52.0 ±0.3	146±7
Aggressive	Sum Clip [6 phe]	37.4±0.2	136±4	41.4±0.2	136±4
	Sum Clip [8 phe]	29.6±0.2	120.0±1.4	29.6±0.2	120.0±1.4
	Majority	38.3 ±0.4	137±5	38.3 ±0.4	137±5

Table 3.2: Energy thresholds for the different trigger options and scenarios.

We see that in every case, sum trigger provides lower energy threshold than majority trigger. This is a direct consequence of having a larger collection area at low energies. The cut in phe does not affect the energy threshold of any of the options. The aggressive strategy improves the trigger energy threshold of the telescope slightly.

3.2.3 Gain between single-telescope and stereo observation for the LSTs

According to the CTA requirements for the LST, the LST DAQ should be able to record events with a rate up to 7.5 kHz. The goal of the LST project is to be able to handle a recording rate of 15 kHz. To evaluate the gain obtained going from 7.5 kHz to 15 kHz recording rate, we computed the energy threshold for these trigger rates. We also evaluated the gain of moving from the requirement and goal single-telescope recording rate to the same rate in stereo. Since

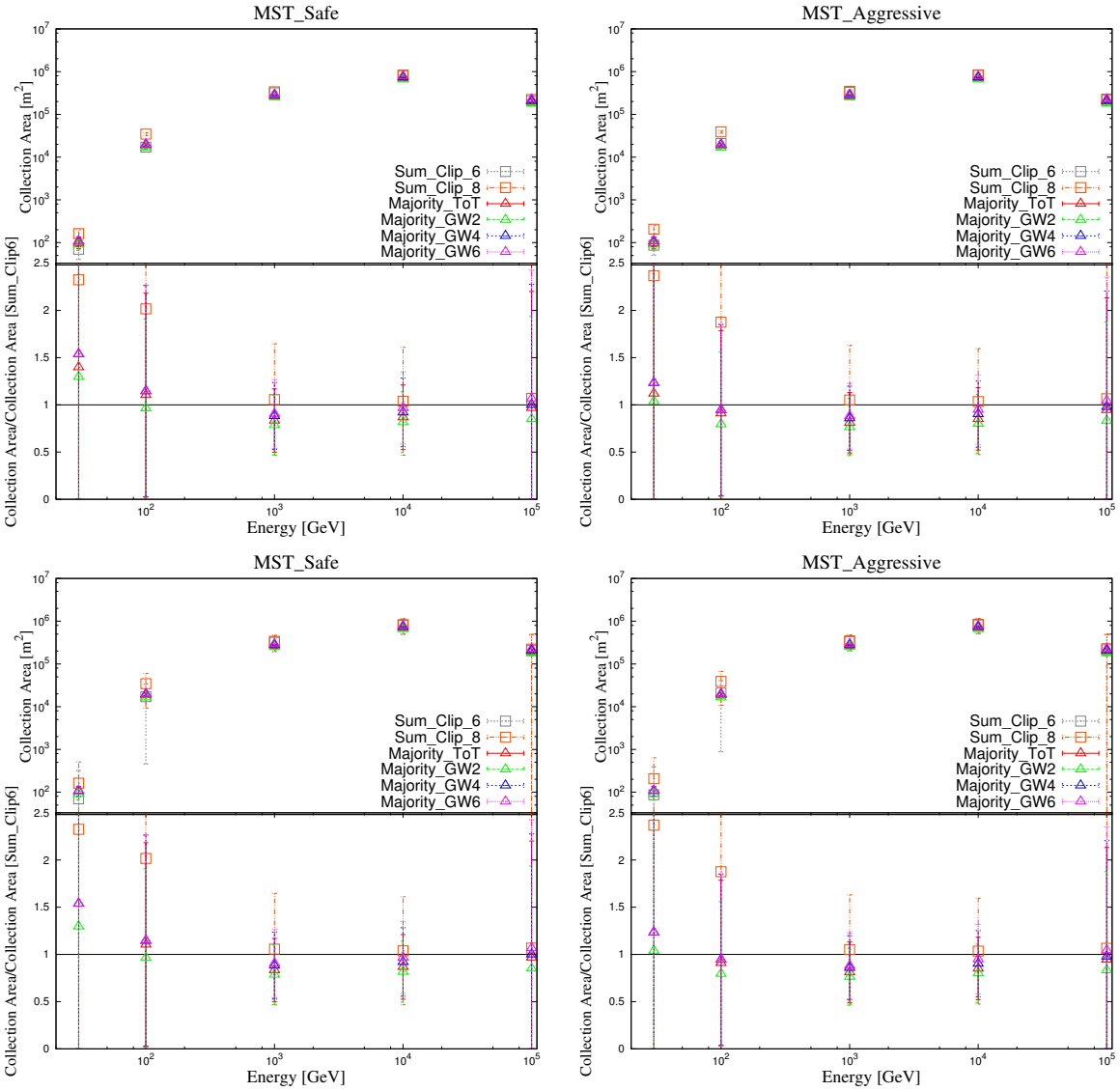

Figure 3.6: MST collection area for the safe (top left) and aggressive (top right) trigger scenarios with no cut in the minimum number of phe, and safe (bottom left) and aggressive (bottom right) scenarios with a cut of 25 phe. The options plotted are the same as in Figure 3.4.

the sum trigger with a clipping of 8 phe produced the best performance according to the results obtained in section §3.2.2.3 performed these simulations using these settings. To achieve the lowest possible energy threshold, we considered for the simulations an extragalactic NSB of 208 MHz per pixel, instead of the galactic NSB considered to compare the performance of the majority and sum triggers. We computed the single-telescope and stereo rates, and the energy threshold for 3 different scenarios in each of the observation modes:

- ⊙ Single-telescope (stereo) rate of 7.5 kHz

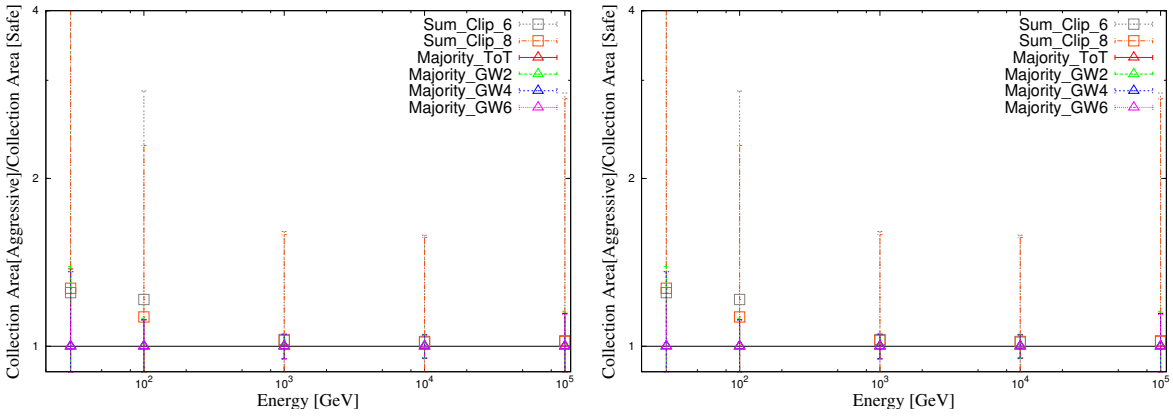

Figure 3.7: Comparison between safe and aggressive trigger scenarios for the MST with no cut in minimum number of phe (left) and with a cut of 25 phe (right). The options plotted are the same as in Figure 3.4.

- ⊙ Single-telescope (stereo) rate of 15 kHz
- ⊙ Crossing point between the NSB trigger curve and the cosmic-ray trigger curve.

The energy threshold for all the different configurations can be found in Table 3.3. Figure 3.8 shows how the single-telescope and stereo trigger rates depend on the DT.

Operation point selection criterium	DT [phe]	Single-telescope rate [kHz]	Stereo rate [kHz]	Energy threshold [GeV]
Single-telescope 7.5 kHz	26.9	7.5	2.7	20.6 ±0.2
Single-telescope 15 kHz	26.0	15.3	3.0	19.4 ±0.2
Single-telescope crossing point	27.0	6.6	2.7	20.7 ±0.2
Stereo 7.5 kHz	23.8	82.2	7.5	13.9 ±0.2
Stereo 15 kHz	23.0	151.0	15.5	13.7 ±0.2
Stereo crossing point	23.8	84.1	7.8	13.9 ±0.2

Table 3.3: Energy thresholds and rates for different DTs for single-telescope and stereo LSTs.

From these results we conclude that we gain less than 6% in threshold when going from the required rate of 7.5 kHz to the goal rate of 15 kHz. On the other hand, going from single-telescope to stereo observations decreases the energy threshold by ~30%.

3.2.4 Impact of the PMT pulse width on the trigger collection area

As it was described in Section §2.1.3, the faster the integration time of the signal, the less background light is integrated. The photosensors developed for the LST are last generation PMTs

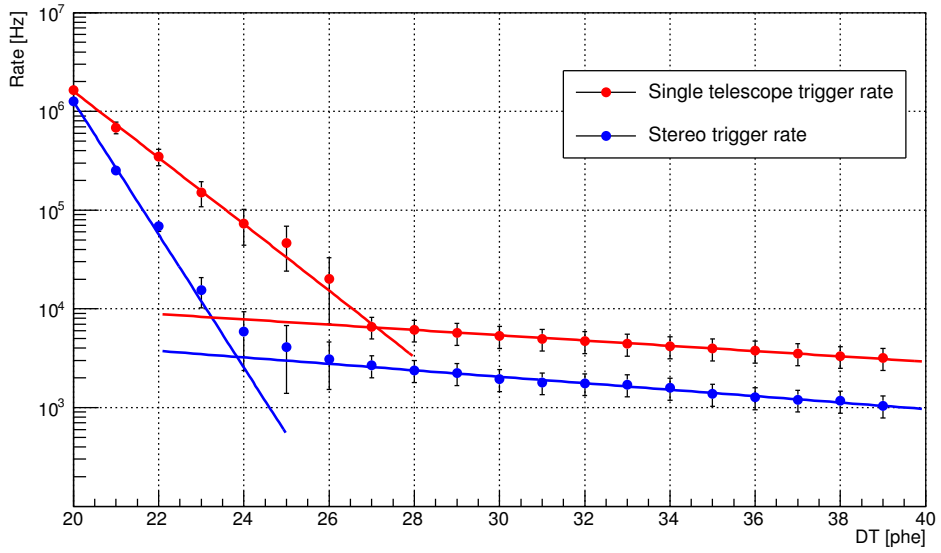

Figure 3.8: Single-telescope and stereo trigger rates for extragalactic NSB.

with peak QE exceeding 40% and designed to achieve the lowest possible AP rate. The AP rate is dependent on the materials used for the photocathode and also on the voltage applied between dynodes. If this voltage is reduced, the PMT signals get broader.

To evaluate the effect of pulse widening, we calculated the performance of the trigger for different pulse widths, ranging from 2.0 ns to 4.0 ns in steps of 0.2 ns. The goal for the LST PMTs is 2.6 ns, but we considered a broad range of pulse widths to ascertain the tendency in trigger threshold. We performed these simulations for the sum trigger with different clippings (6 and 8 phe) and three different trigger scenarios: safe and aggressive with galactic NSB and safe with extragalactic NSB. To compute the operation points, we used the method described in Section §3.2.2.2. The resulting DTs for each of the configurations and each of the FWHMs can be found in Table B.2 in Appendix B.2. The increase of DT to work at the same operation point as a function of the FWHM is shown in Figure 3.9.

The DT at the operation point increases almost linearly with the FWHM, implying also an increase in the energy threshold of the telescope. To compare the performance of the different options, we calculated the collection area achieved at different energies for the different options. Figure 3.10 collects the results for the ratio between the collection area reached by a given configuration divided by that corresponding to FWHM=2.6 ns for a given energy.

As expected, the widening of the PMT pulse only affects the lowest energies, as the variation due to the increase in the operation point affects the lowest energy showers triggered by the telescope. If we compare the performance between all the options simulated for the lowest energies, as it is shown in Figure 3.11, we can check the tendency of the performance when increasing the PMT width.

From the results shown in Figures 3.10 and 3.11, we derive that for energies lower than 30 GeV, the trigger collection area shrinks by 5 - 8 % every 0.2 ns for FWHM > 2.6 ns. For the safe

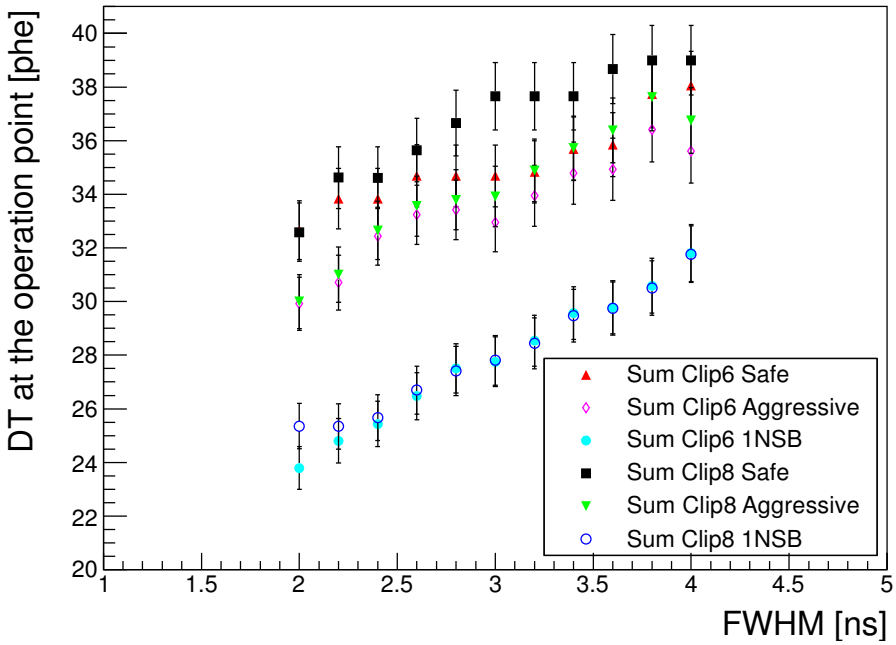

Figure 3.9: DT at the operation point as a function of the FWHM.

scenario, this effect is < 20 % for FWHM < 3.4 ns. This worsening is larger when the applied DTs are lower, as happens in the aggressive scenario or the one with extragalactic NSB (1*NSB). If we trigger deep in the NSB by lowering the DTs using these options, even a pulse width >3 ns reduces the collection area by > 20 %.

3.3 Characterization of trigger hardware

The hardware for the L0 decision trigger was developed at IFAE and the definition of its requirements, test and characterization were performed as part of this thesis. We will first briefly describe the results for the discrete component trigger, as it was the first option developed. We will give a more detailed description of the L0 ASIC trigger that is the option that will finally be installed in the analog cameras of CTA.

3.3.1 Discrete component trigger

The first option to implement the analog trigger into mezzanines connected to the analog readouts for CTA was to use discrete components (resistors, capacitors...). They met the cost, weight and power consumption specifications, although the performance was not optimal due to non-idealities in the circuits.

More concretely, the clipping was not constraining the signal height to a certain value as it was expected, but just producing an attenuation. To illustrate this effect, we show in Figure 3.12

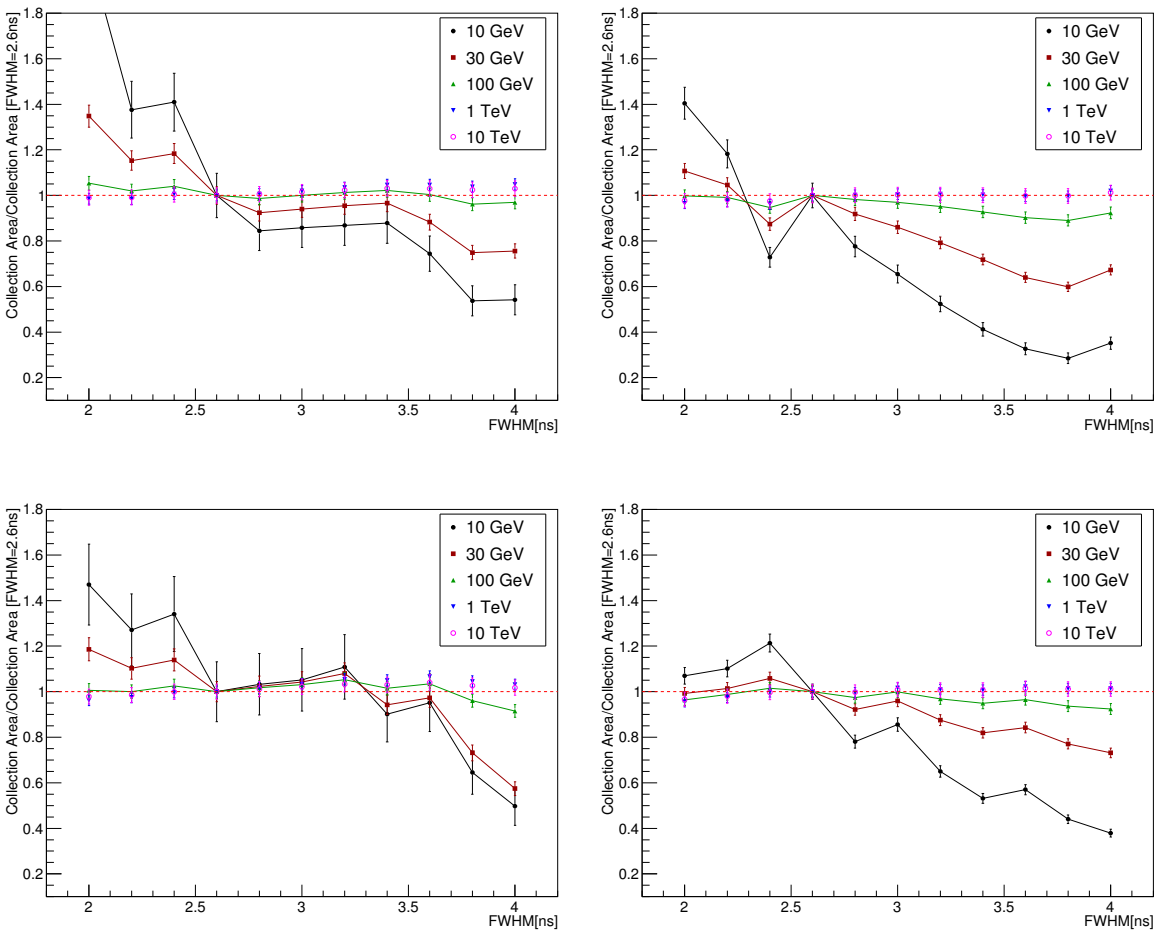

Figure 3.10: Ratios between the collection area for a given FWHM and that for FWHM=2.6 ns for different energies. On the top left we have the plot using sum trigger, a clipping of 8 phe and the safe scenario. On the top right, the same plot using a clipping of 6 phe. On the bottom left one can see the same plot as in the top left but considering the aggressive scenario and on the bottom right the same as in the top left but considering extragalactic background. The red dashed line indicates ratio = 1.

a plot of the transfer function that produces an ideal clipping. In Figure 3.13 we show the transfer function for the discrete component L0 board when applying a given clipping. The difference between an ideal clipping and the one provided by the discrete component boards is that for larger signals we do not get a linear response, but the output voltage still increases with the input. This has an unknown effect on the trigger performance that was not evaluated. As the performance of the discrete component trigger was not optimal, we decided to move to the ASIC trigger option that provided a better performance with a reduction in weight and power consumption and what is more important, also a reduction in cost.

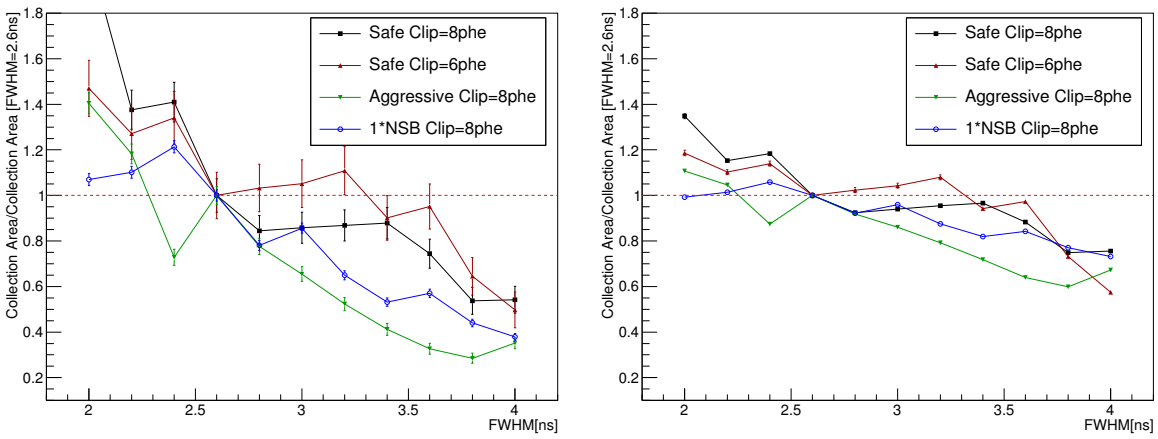

Figure 3.11: Ratios between the collection area for a given FWHM and that for FWHM=2.6 ns for 10 GeV and 30 GeV for all the scenarios considered. The red dashed line indicates ratio = 1.

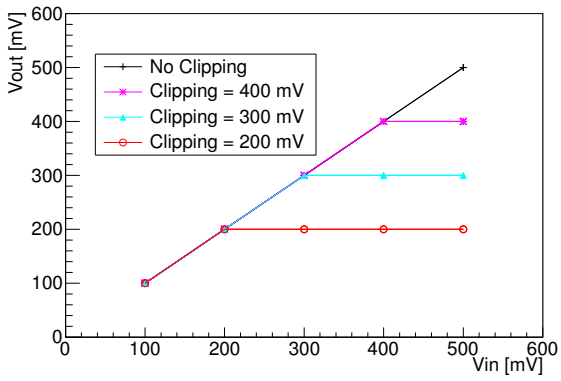

Figure 3.12: Transfer function of a system where an ideal clipping is applied. The black line represents the signal without any clipping, the magenta one the signal clipped at 400 mV, the cyan one the signal clipped at 300 mV and the red one the signal clipped at 200 mV.

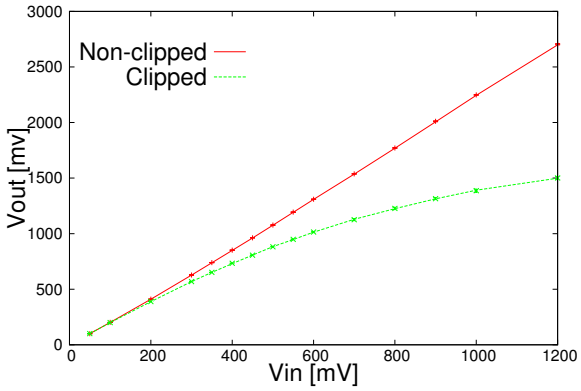

Figure 3.13: Transfer function of the analog discrete component trigger where the clipping is applied. In red we show the non-clipped signal and in green the clipped one.

3.3.2 L0 ASIC trigger

Application-Specific Integrated Circuits (ASICs) are integrated circuits, developed and designed to satisfy a specific application requirement. The work on the discrete components trigger, that produced a working and fully tested board, made possible the design of an ASIC with all the functionalities of the discrete components trigger. Moreover, the ASIC trigger reduces weight, space and cost, so all the groups designing the analog trigger for CTA decided to move from a discrete components trigger to a full trigger system made by ASICs (Barrio et al. 2014a,b).

The full analog trigger chain will finally be composed by an L0 decision ASIC, an L0 distri-

bution ASIC and an L1 decision ASIC, all of them mounted on their corresponding mezzanines. The L0 mezzanines include, before the L0 ASIC, adjustable delay lines to compensate the differences in transit time between PMTs to achieve a better synchronization of the individual signals at the trigger level. The L0 distribution ASIC is under test, the L1 decision was designed, tested and characterized at CIEMAT and the L0 decision ASIC was designed by UB and fully characterized and tested at IFAE.

The L0 decision ASIC uses an AMS 0.35 μm SiGe BiCMOS technology, having an area of $\sim$11 mm^2. The technology is common to that used for PACTA, ACTA and NECTAr chips, fact that reduces the cost of producing all of them in the same run. It processes analog signals of individual pixels in a cluster of 7 pixels. As it was mentioned, each ASIC contains two different L0 approaches, the *majority* trigger and the *sum* trigger. Both of them were designed by using full differential circuits to minimize the effect of long distances in the connection with other subsystems. As the trigger clusters are defined as groups of 7 pixels, the ASIC input signals are 7 differential analog inputs. Each differential pair goes through an attenuator circuit to the two L0 trigger options in order to equalize all pixel gains with a better precision. This attenuator lets adjust the gain of the signal from 1.35×Input Voltage (V_{in}) to 0.6×V_{in} in steps of 0.05 mV. The majority trigger concept compares the signal from each pixel to a voltage threshold by using a discriminator circuit. If the signal overcomes the threshold, a 100 mV signal is issued at the output of the channel. Each differential pair output of the discriminator is available as an LVDS output. The discriminator outputs are internally added and are also available as an analog differential output voltage (V_{out}). The sum trigger concept cuts the signals greater than a given value by using a clipping circuit, as it was explained in Section §2.2.1.6. There are 3 different clipping options that clip the signal at different ranges, and for each of those options there are 63 different *fine clipping* options. Afterwards, the signals from all the pixels in the cluster are added and the resulting signal sent to the L0 distribution subsystem by an analog differential output. The input for these trigger boards has an equivalence of 20 mV/phe. A block diagram of the L0 ASIC is shown in Figure 3.14.

Requirements: Following CTA internal requirements on durability, reliability and cost, we defined requirements for the L0 ASICs. These requirements and the results are collected in Table B.1 in Appendix B.1.

Characterization measurements: We measure the output voltage of the ASIC for different conditions and check the functionality of all the channels and functions. All the measurements are performed for 10 input voltages:

V_{in}=0.05, 0.06, 0.07, 0.08, 0.09, 0.1, 0.2, 0.3, 0.4, 0.5, 0.6, 0.7, 0.8, 1 V

We performed the characterization measurements for the 30 chips that were available after the first production.

Sum trigger: For the sum trigger part of the ASIC, we first checked the clipping functionality. Figure 3.12 illustrates how an ideal clipping works. All the possible settings for the sum part of every chip were tested. We measured for every input (14), channel (7), attenuation

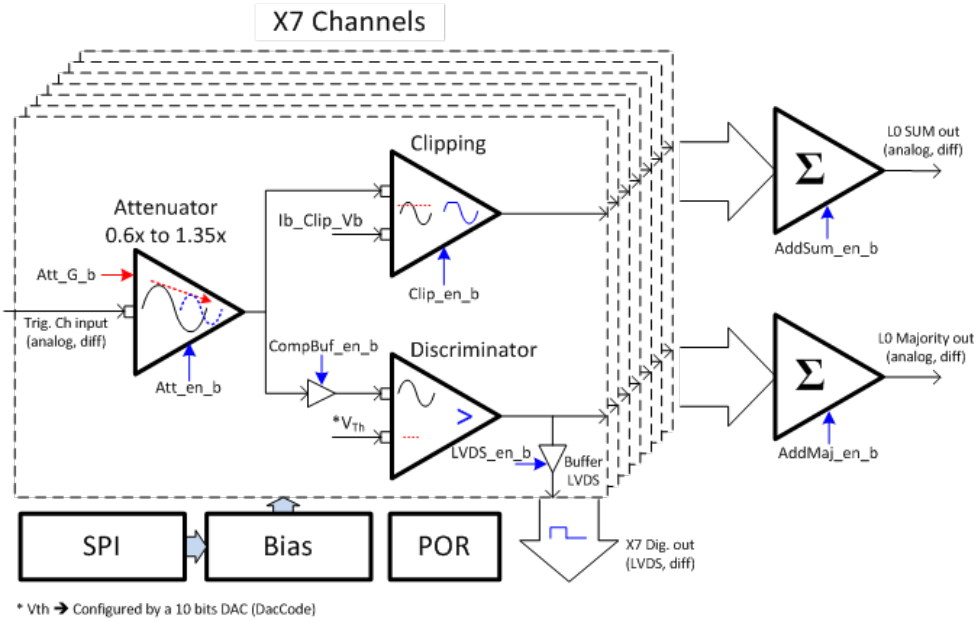

Figure 3.14: L0 ASIC block diagram. From Sanuy et al. (2013).

(16) and clipping options (only half of the fine clippings for each of the clipping options, i.e. 3×32), the corresponding output of the chip. The final measurement recorded is the mean of 10 measurements of this output. Figure 3.15 shows an example, for a given attenuation, of the sum output measured for all the input voltages aforementioned.

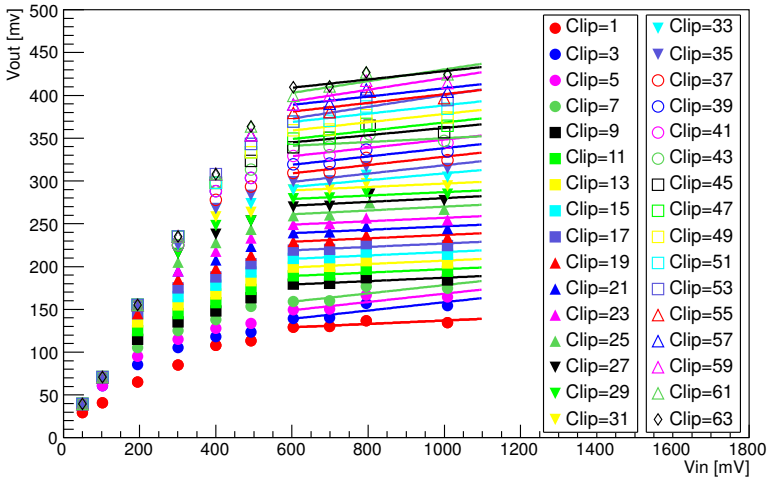

Figure 3.15: Sum trigger V_{out} vs ASIC V_{in} for a given attenuation and different values of fine clipping. The output signals are fit in the range between 600 mV and 1 V to calculate the saturation output voltage.

To characterize the clipping, we measured the evolution of the *Saturation output voltage*

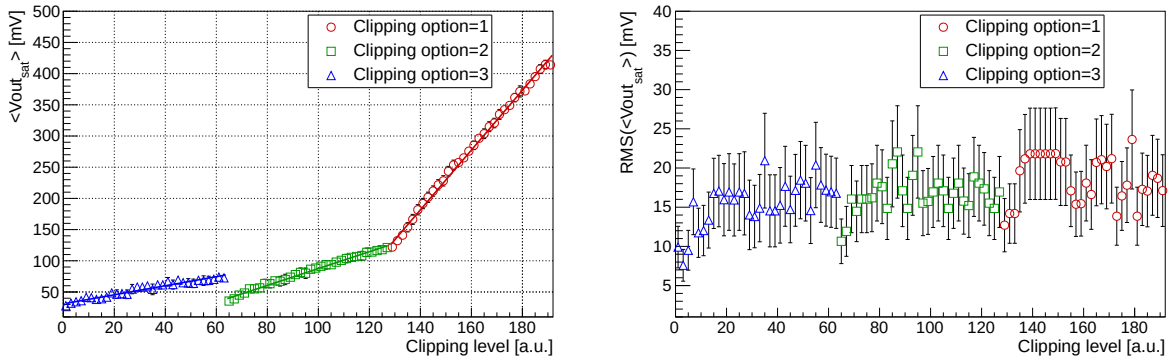

Figure 3.16: Mean saturation output voltage as a function of the clipping (left panel) and its RMS (right panel) for one chip. Three sets of points are shown in different colors, each one corresponding to each of the clipping options. Each of them is adjusted by a first order polynomial in the region between 600 mV and 1 V, also drawn.

($Vout_{sat}$), which is the output voltage limited by the clipping, as a function of the clipping value. For this measurement, we selected a value of high attenuation, plotted the V_{in} vs V_{out} for different inputs and fit the output voltage of the clipped part to a straight line, as it is shown in Figure 3.15. The value that is finally plotted as a function of the clipping will be the mean between the saturation output voltage for every channel of the chip <$Vout_{sat}$> and also its dispersion (RMS(<$Vout_{sat}$>)) for each of the fine clippings. We differentiate three curves corresponding to each of the clipping options.

To check that the clipping is not affected by the attenuation, for a given clipping value we measured the $Vout_{sat}$ for all attenuations. We repeated this measurement for 2 of the clipping options. For clipping option 1 we could not perform this measurement because the signals were too attenuated for large attenuation values and they were not reaching the level to be clipped. As the clipping should not depend on the attenuation selected, the $Vout_{sat}$ should be the same for the different attenuations. These measurements for one of the chips can be seen in Figure 3.17. The sets of points for each of the clipping options are fit with a first degree polynomial $f(x) = p_1 x + p_0$. All of them are compatible with p1=0, i.e. a $Vout_{sat}$ non dependent on the attenuation.

Finally, we measured that the adder of the sum output was working correctly. For a given attenuation and clipping we measured the output of the adder. We used an input signal of 50 mV and a high clipping value not to have clipped signals at the output. We measured the output of the adder for all the possible combinations of channels added. The measured output is divided by the number of channels added, therefore the final result should be the same for all the measurements. We plot the histograms of the output of the adder measured divided by the number of channels added for every number of channels added. The histograms are fit with a gaussian with parameters:

$$f(x) = A \exp\left(-\frac{x-\mu}{\sqrt{2}\sigma}\right)^2 \tag{3.1}$$

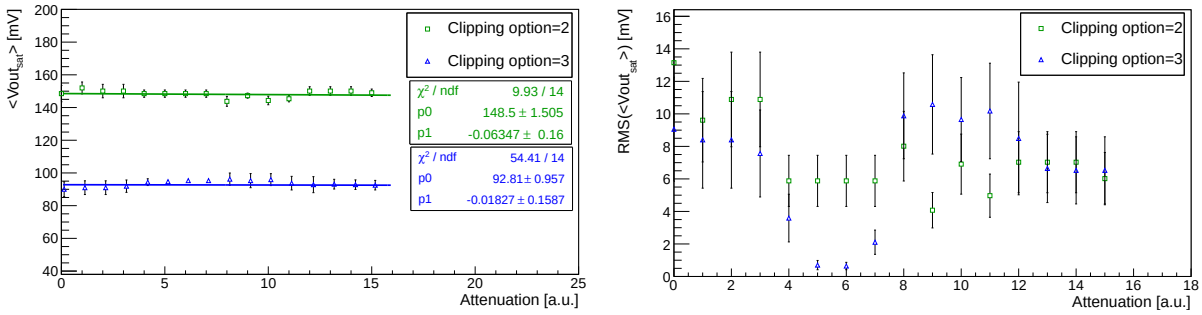

Figure 3.17: Mean saturation output voltage as a function of the attenuation (left panel) and its RMS (right panel) for one chip. Two sets of points are shown in different colors, each one corresponding to each of the clipping options. Results from the fit for the different clipping options are shown in the same color as the points for the corresponding option. The sets of points for each of the clipping options are fit with a first degree polynomial $f(x) = p_1 x + p_0$.

whose standard deviation σ is at the level of 1-2% of the mean. The results of this check are shown in Figure 3.18.

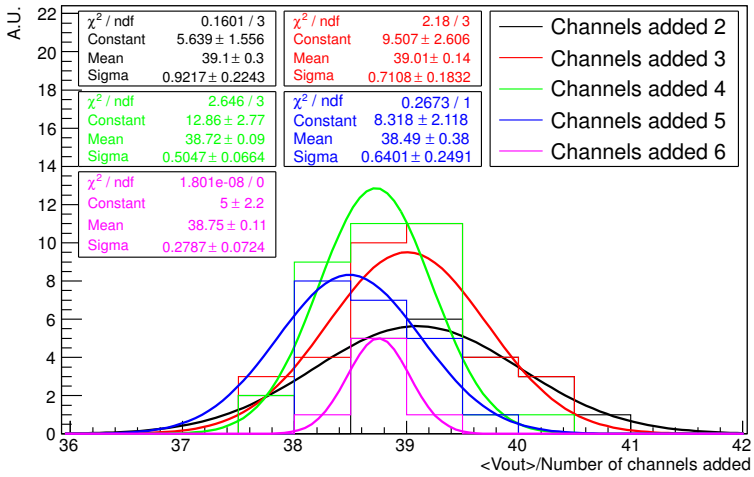

Figure 3.18: Output of the *sum adder* divided by the number of channels added for an input signal of 50 mV. Histograms for the different number of channels added are shown in different colors (2 channels in black; 3 channels in red; 4 channels in green; 5 channels in blue; 6 channels in magenta) and fit with a gaussian, represented by a line of the same color as the histogram. The results of the fit are shown in the plot with the same color as the fit. Constant corresponds to A, Mean to μ and Sigma to σ as they are expressed in equation 3.1.

Majority trigger: We define the DT for a given input signal with a given attenuation as the discriminator voltage at which the output signal goes to 0. For the majority option it is important

that the DT goes linearly with the input voltage. This linearity was determined by measuring the DT of all the channels for a given input and attenuation. We plotted the mean of all the channels. We fit the mean DT for several inputs and found that the mean DT as a function of the input is linear at a level ~5% for any input. An example of the mean DT of one chip as a function of the input voltage, for a given attenuation, is shown in Figure 3.19.

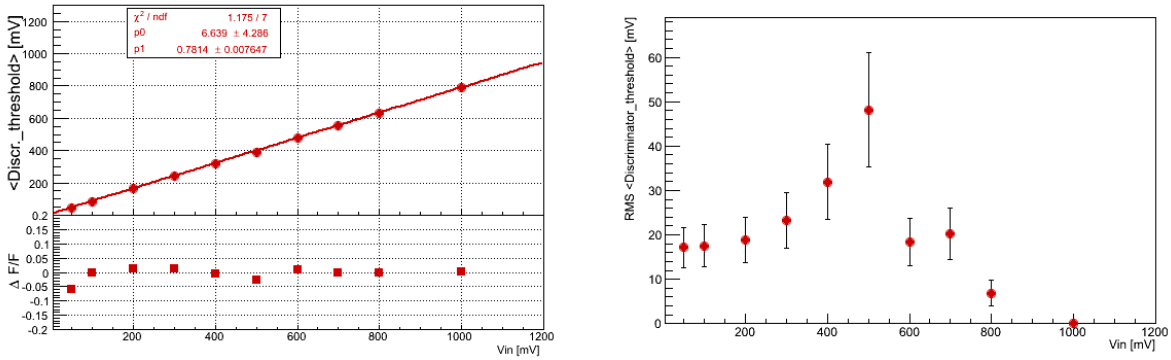

Figure 3.19: Mean DT as a function of the input voltage for one chip (left) and its RMS (right). The mean DT is fit with a first degree polynomial $f(x) = p_1 x + p_0$. The results of the fit are shown in the left figure. The errors are very small and fall within the points. The relative residuals of the fit are also shown in the bottom panel of the left figure.

Finally, the majority adder was also checked using the same procedure as for the sum adder, as it is shown in Figure 3.20. For a given attenuation we measured the addition of all the possible combinations of channels. The final output was divided by the number of channels added to fill different histograms, depending on the number of channels added. The histograms were fitted with the gaussian described in equation 3.1, whose standard deviations were at a level < 1%.

3.3.3 Conclusions

The test and characterization of the L0 trigger was presented in this section. For the L0 trigger using ASICs, we find that for the *sum* option the saturation output voltage grows linearly with the clipping level and it does not depend on the attenuation used. For the *majority* option, we find that the comparator is linear at a level < 5 %. The adders of analogue signals for both options work linearly.

We find that the option of using ASICs performs better than that using discrete components. Moreover, using this option, we reduce cost, weight and power consumption, so we conclude that this is the final option that should be used for the LST and MST analog cameras. As of March 2015, we have already completely characterized a test sample of 30 L0 ASICs. The failure rate for this sample is ~7%. For the final quality control, we have reduced the number of measurements to the minimum necessary to reliably perform all the characterization measurements and fully automatized the process to take 15 minutes/chip. We are currently testing and characterizing 250 additional L0 ASICs to be part of the LST prototype that will be installed in La Palma, Spain in 2016.

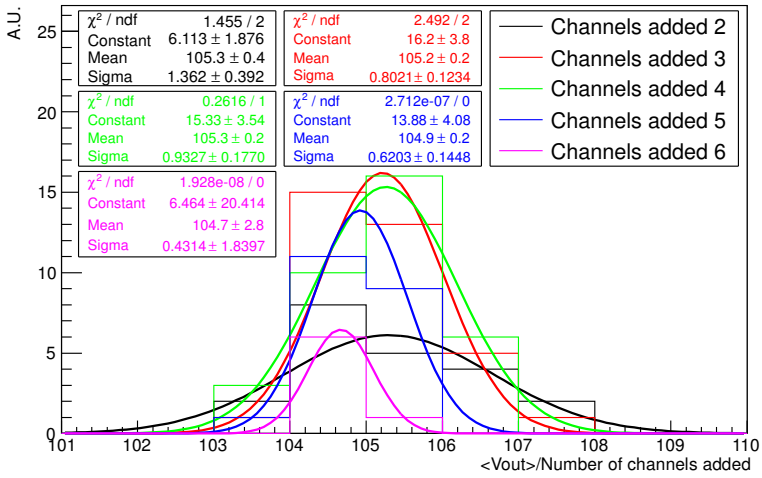

Figure 3.20: Output of the *majority adder* divided by the number of channels added. Histograms for the different number of channels added are shown in different colors (2 channels in black; 3 channels in red; 4 channels in green; 5 channels in blue; 6 channels in magenta) and fit with a gaussian, represented by a line of the same color as the histogram. The results of the fit are shown in the plot with the same color as the fit. Constant corresponds to A, Mean to μ and Sigma to σ as they are expressed in equation 3.1.

3.4 Concluding remarks

On the hardware side, we studied the response of L0 boards containing discrete components and an ASIC to produce the L0 trigger of the system. We found that, although the discrete component trigger meets the requirements of the L0 trigger, the response obtained with the ASIC trigger is much more satisfactory in terms of linearity of the attenuator, clipping and DT. Besides that, the ASIC trigger provides lower weight, consumption and cost. This is the option that is currently being fully characterized to be installed in the first LST prototype.

We found that for the LSTs, which are built to collect more light and have a lower energy threshold, the performance of the sum trigger is better at energies below 100 GeV. Among the sum trigger options under consideration, the best compromise between the cut given by the clipping and the suppression of the after pulses is given by a clipping level = 8 phe, although it is worth pointing out that there was no real optimization of the clipping value. We simply selected a few clipping values (6 phe, 8 phe) and the performance was checked among them. Moreover these clipping values were obtained before the change in geometry of the telescopes and QE of the PMTs. For the new configuration larger clipping values may even improve the performance. The MSTs are not designed to have good sensitivity at low energies (<100 GeV). Hence, the performance of majority and sum triggers have large uncertainties in this energy region because of the low number of triggers. The results for both triggers at higher energies are compatible within the errors. A comparison between the aggressive and safe scenarios shows an improvement of the collection area for the aggressive scenario at the lowest energies, although within the errors. The energy threshold is also slightly improved by the use of the aggressive

option. We also found that for both trigger options, a cut in the minimum number of phe of 25 phe in the events recorded does not affect the results obtained. It is therefore safe for further simulations to apply this cut and eliminate events with less than 25 phe without changing the results.

Nevertheless, as we are only considering galactic NSB, the DTs used to reproduce the safe and aggressive trigger scenarios considered are high, the collection area at low energies decreases and the energy threshold stays at a level > 20 GeV in every case. If we considered lower extra-galactic NSB, those DTs would be reduced, and therefore the energy threshold of the telescope would be lower as well.

Regarding CTA requirements and LST goals, the gain in energy threshold is small when moving from the 7.5 kHz requirement to the 15 kHz goal. The gain of moving from single-telescope to stereo observations is ∼30 % in energy threshold.

We also evaluated the impact of having PMTs with pulse widths wider than the goal of 2.6 ns. In general, we find that the worsening of the collection area is between 5 - 8 % every 0.2 ns with respect to that achieved with a pulse width of 2.6 ns. To be on the safe side and keep the worsening of the performance at a level $\lesssim$ 20 %, the pulse width of the PMTs should be smaller than 3.0 ns.

All these results should be confirmed and optimized when the telescope parameters are fixed and the final site for the telescopes decided. This will be done in the *Production-III* MC run, focused on the selection of the final telescope layout and the optimization of the system.

4

The Topo-trigger: A new stereo trigger for lowering the energy threshold of IACTs

The purpose of the hardware presented in this chapter is to decrease the energy threshold of the MAGIC telescopes without significantly increasing the data acquisition rate. To achieve this purpose, we developed an additional level of trigger that relies on the location in both MAGIC cameras where the trigger is issued to rule out accidental events. This allows to decrease the DT, which results in a reduction of the energy threshold of the instrument. We simulated the Topo-trigger concept using the standard MAGIC MC and tested it with real telescope data. In this chapter we show the concept and results of these tests.

4.1 Limitations of the trigger system in the MAGIC telescope

The trigger system in the MAGIC telescope is hardware limited at several stages. Every time an L1 trigger is issued, the L1 trigger system is busy for 100 ns, not accepting any other trigger in this time. This L1 trigger dead time is given by:

$$\text{Dead time} = \text{L1 rate} \times 100 \text{ ns}$$

In order not to lose $> 2\%$ of the cosmic ray events, we cannot accept L1 trigger rates larger than 200 kHz.

The rate of stereo accidental triggers is given by:

$$\text{Stereo accidental trigger rate} = \text{L1 rate [M1]} \times \text{ L1 rate [M2]} \times \text{L3 Coincidence window}$$

where L3 Coincidence window = 180 ns. The maximum stereo rate the current DAQ can record is ~3 kHz (Tescaro et al. 2013). The simulated stereo accidental trigger rate (open squares) and measured stereo accidental trigger rate (filled circles) of MAGIC are shown in Figure 4.1. We are currently working at the crossing point between the extrapolation of the stereo cosmic ray trigger rate and the stereo accidental trigger rate (shown as the crossing point between the two red lines). What we aim to do with the algorithm we are presenting in this work is to reduce the accidental stereo trigger rate to 10% of its value (open circles). We would then move to operate to the crossing point between the extrapolation of the stereo cosmic ray rate and the 10% of the accidental stereo trigger rate (the crossing point between the two blue lines).

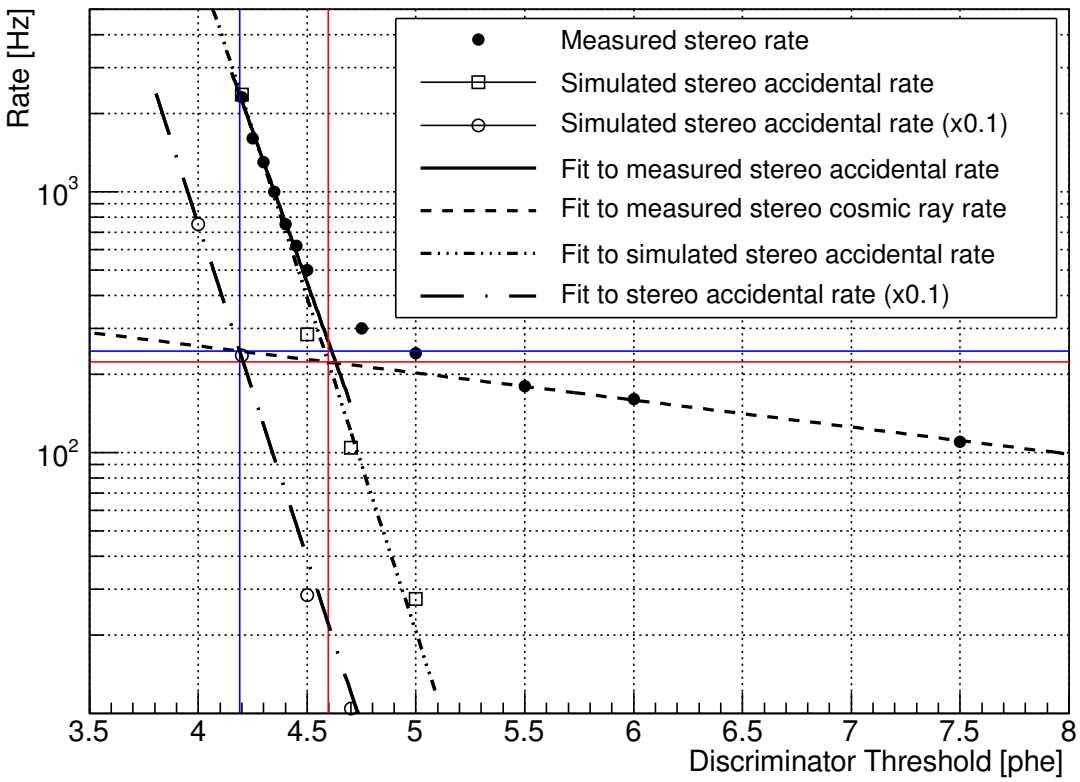

Figure 4.1: Measured and simulated stereo trigger rate for the MAGIC telescopes. The crossing point of the red lines determines the current operation point in the MAGIC telescope. The crossing point of the blue lines marks the operation point where we would go by decreasing the accidental rate to 10% of its value and maintaining the same rate recorded.

4.2 The Topo-trigger

The trigger logic implemented at this moment in the MAGIC telescope discriminate between showers and NSB using the spatial and time information of the pixels' signals for the single-telescope trigger level and the time information at the stereo level (for more information about MAGIC trigger, see Section §2.2.1.6). To get rid of additional accidental triggers, we could also use the spatial information at the stereo level.

4.2.1 Setup of MC simulations

For the simulation of gamma rays we used CORSIKA (Heck et al. 1998) software. The particles simulated are γ-ray photons with energies ranging between 10 GeV and 30 TeV, simulated with a power-law function with 1.6 photon spectral index. For all the calculations, the spectrum was re-weighted to a Crab-like spectrum with photon spectral index Γ=2.6, as it is explained in the Appendix A.1. The events are simulated at a 0.4° distance from the center of the camera, as it is the standard in MAGIC observations. We also simulated a sample of events at a distance ranging from 0.6° to 1.4° from the center of the camera to study the performance for off-axis events. The Zd ranges from 5 to 35 degrees, the Az angle ranges from 0 to 360 degrees and the maximum impact parameter simulated is 350 meters. We used 3×10^6 showers. The simulation performed is similar to that described in Section §2.2.3.1.

The current DT applied in the L0 individual pixel trigger currently used for the MAGIC simulations (*Nominal* DT) is 4.5 phe for MAGIC I (M I) and 4.7 phe for MAGIC II (M II). The different DTs used for the two telescopes are due to the differences in reflectivity of the mirrors and QE of the PMTs. The L1 trigger logic is 3NN and the L3 gate used is 180 ns. The DTs used to test the Topo-trigger are chosen such that if we manage to reduce the stereo trigger rate due to accidentals one order of magnitude, the stereo trigger rate is the same as for the Nominal DT. We reduced the DT to 4.2 phe in M I and 4.3 phe in M II (*Reduced* DT). The results for the stereo accidental trigger rates for *Reduced* and *Nominal* DTs can be found on Table 4.1. The differences between the accidental rates of M I and M II lies on the better reflectivity of M II mirrors and is also reproduced in the data. To partially compensate this difference, M II DTs are ~5% higher than M I ones.

	Accidental trigger rate [kHz]		
DT	M I	M II	Stereo
Nominal	25 ± 4	39 ± 5	0.18 ± 0.04
Reduced	78 ± 7	125 ±9	1.8± 0.2

Table 4.1: L1 trigger rates for different NSB, DTs and for the two MAGIC telescopes. The Nominal DT corresponds to 4.5 phe for M I and 4.7 phe for M II, while the Reduced one corresponds to 4.2 phe for M I and 4.3 phe for M II.

4.2.2 Spatial information available at trigger level

The basic idea is to implement online cuts on the spatial information available at the trigger level. In particular, we can use the 19 L1 trigger macrocell bits from the two telescopes to obtain information about the location of the image in the camera. A scheme of the MAGIC trigger system including the future Topo-trigger is shown in Figure 4.2. When a L1 trigger is issued in each telescope, a copy of the signal goes to the prescaler and another one to the L3 trigger. We intend to deliver another copy to the Topo-trigger. The Topo-trigger compares the macrocells triggered in each telescope every time a L1 trigger is issued and sends a veto signal to the prescaler when the combination of macrocells does not correspond to that triggered by a gamma ray.

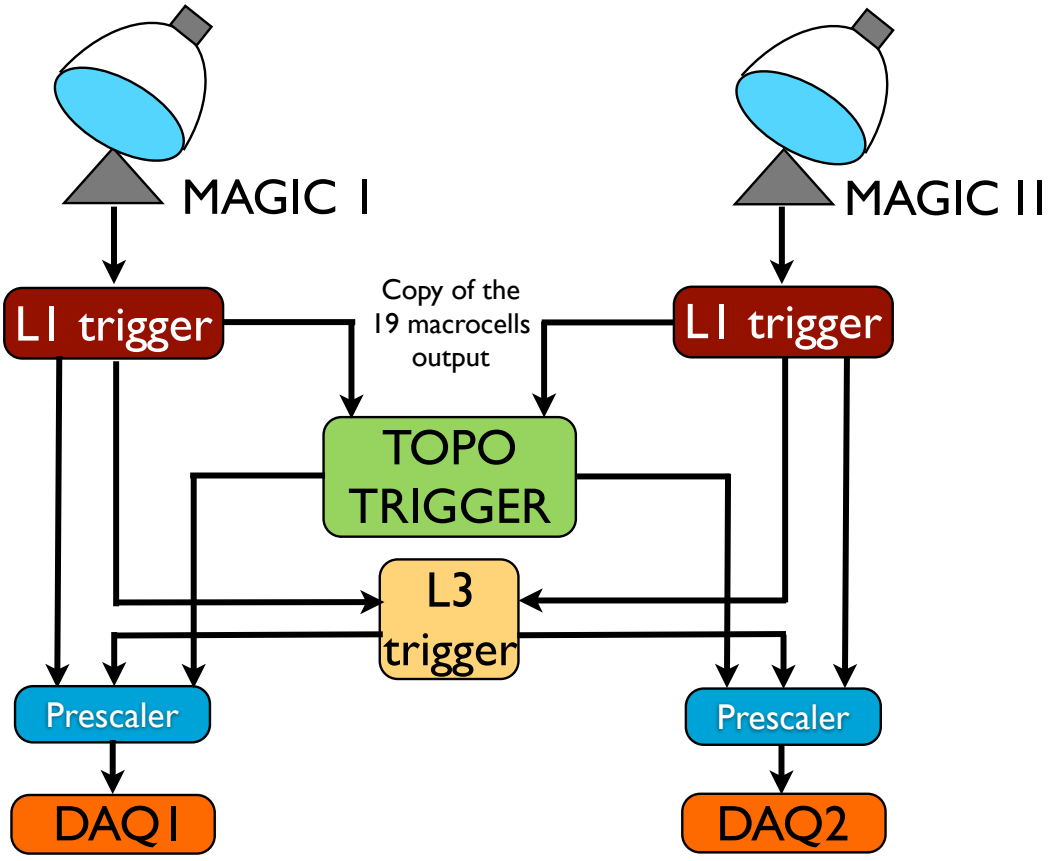

Figure 4.2: Scheme of the MAGIC trigger system including the implementation of the Topo-trigger.

4.2.3 Macrocell selection

Let us discuss the separation angle under which the shower is seen from the two MAGIC telescopes. We denote this angle alpha as is shown in Figure 4.3. The angle is maximum when

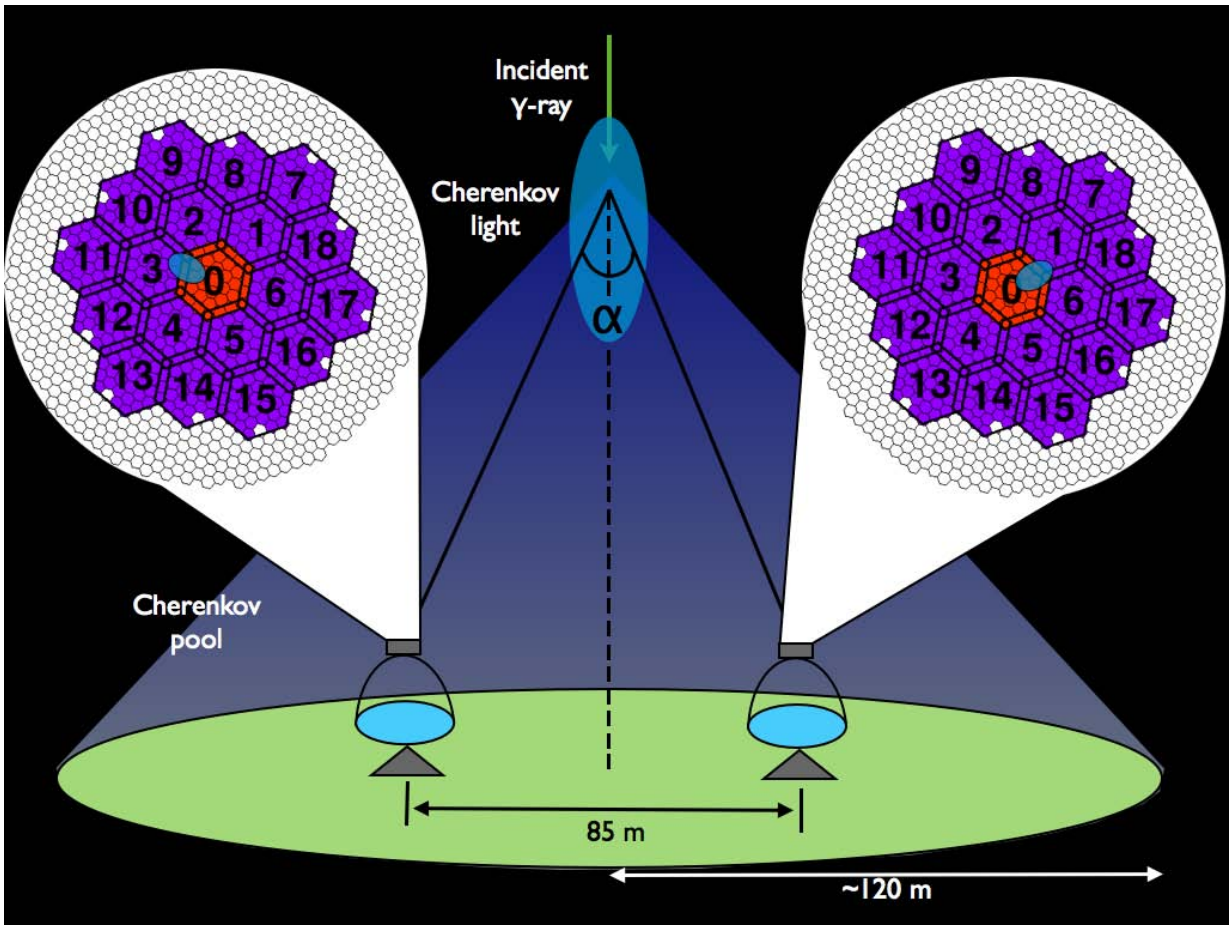

Figure 4.3: Scheme of the detection of Cherenkov light produced by a low energy γ-ray shower by the MAGIC telescopes. The angle α between the light arriving to both telescopes is smaller than 0.6° for all the showers produced at a height of $\sim$ 10 km.

the shower develops in between the two telescopes. The distance between M I and M II is 85 m and the assumed distance at which the shower is produced is 10 km a.s.l. (~7.8 km above the telescopes). The maximum angle separation between a point-like shower between the two telescopes is $\alpha \simeq 0.6°$. Taking into account the macrocell distribution shown in Figure 2.16 and that every pixel covers 0.1°, we conclude that the maximum separation of the showers seen in the two MAGIC cameras is 1 macrocell. We have to point out that the angle α calculated depends on the height at which the shower interacts with the atmosphere (high energy showers go deeper into the atmosphere, therefore produce larger α angles). This means that most of the showers trigger the same macrocell at both telescopes or neighboring macrocells. This is the essence of our new trigger level.

In the simulations, we record the macrocell digital output for 10 ns after the L1 trigger is issued. This digital output of each macrocell is 0 if the macrocell was not triggered during those 10 ns and 1 if it was triggered. As the events triggered by NSB are accidentals, we expect them to trigger only one macrocell. Using MC simulations, we calculated that the probability that an

accidental event is triggered by more than one macrocell is $P_{2M} = 0.4\% \cdot P_{1M}$, where P_{2M} is the probability of triggering 2 macrocells due to an accidental and P_{1M} the probability of triggering 1. As the fraction of events triggering more than one macrocell is much smaller than the one triggering only one, we selected the events that triggered only one macrocell in each telescope and studied them. In order to illustrate possible macrocell 1–1 combinations for gamma rays, we select showers that gave triggers in a given macrocell in M I and look at the macrocell distribution for these showers in M II. In Figure 4.4 we have two examples: in the top panel we have selected events for which only macrocell 0 (the central one, marked with an asterisk) is triggered in M I. On the bottom panel, we have selected events for which only macrocell 17 (one of the border ones) is triggered. The color of the left panel plots represents the fraction of events that triggered a given macrocell in M II. In the right panel plots we show how the events distribute in M II. Events in the first bin triggered the same macrocell in M I and M II (macrocell 0 (17) in the upper (lower) plot). Events in the second bin triggered in M II one of the macrocells of the first ring surrounding macrocell 0 (17), in this case, macrocells 1, 2, 3, 4, 5 and 6 (13, 14, 16 and 18). The third bin corresponds to the rest of the macrocells.

From the events triggering only one macrocell in each telescope, we will accept only events triggering the same macrocell in both telescopes or the neighboring ones. We will keep most of the events triggered by gamma rays, while getting rid of a large fraction of the accidental stereo triggers. Each telescope has N=19 macrocells, so there are N^2=361 possible different combinations of one-to-one macrocell. The Topo-trigger, in first approximation, accepts 103 of them. Showers are mainly distributed according to the distribution we have obtained with the simulations, but the triggers due to accidentals will be randomly distributed in the whole camera, and most of them will be triggering only one macrocell each time. It becomes clear that if we reject the triggers produced in the macrocell combinations that are not fulfilling the condition of being the same macrocell or the surrounding ones in both telescopes, we would reject:

$$\begin{matrix}\%\text{ Fraction of} \\ \text{rejected accidentals}\end{matrix} = \frac{361 - 103}{361} \times 100 = 72\%$$

We will apply further cuts based on the position of the macrocells respect to the source. Following the geometry shown in Figure 4.3, if the source is at a certain direction in the sky, we do not only know that the shower should fall in the same macrocell or the surrounding ones, but also which of the surrounding macrocells will be hit in the other telescope. If we divide the data in bins of Az, we can further select the macrocells that are accepted and increase our rejection power. We could make Az bins as fine as desired, but at some point there is no improvement. As the finer possible binning would be given by the size of the macrocells, since we have 12 outer macrocells we cannot improve further than establishing 12 bins in Az.

The tables with the macrocells selected in one telescope depending on the one triggering the other and the Az angle at which the telescopes are pointing can be found in Appendix B.3. By applying the macrocell selection to each Az bin, we obtain:

$$\begin{matrix}\%\text{ Fraction of} \\ \text{rejected accidentals}\end{matrix} = \frac{361 - 53}{361} \times 100 = 85\%$$

Let us now evaluate the impact of the cuts on the γ-ray events. We have applied the Topo-

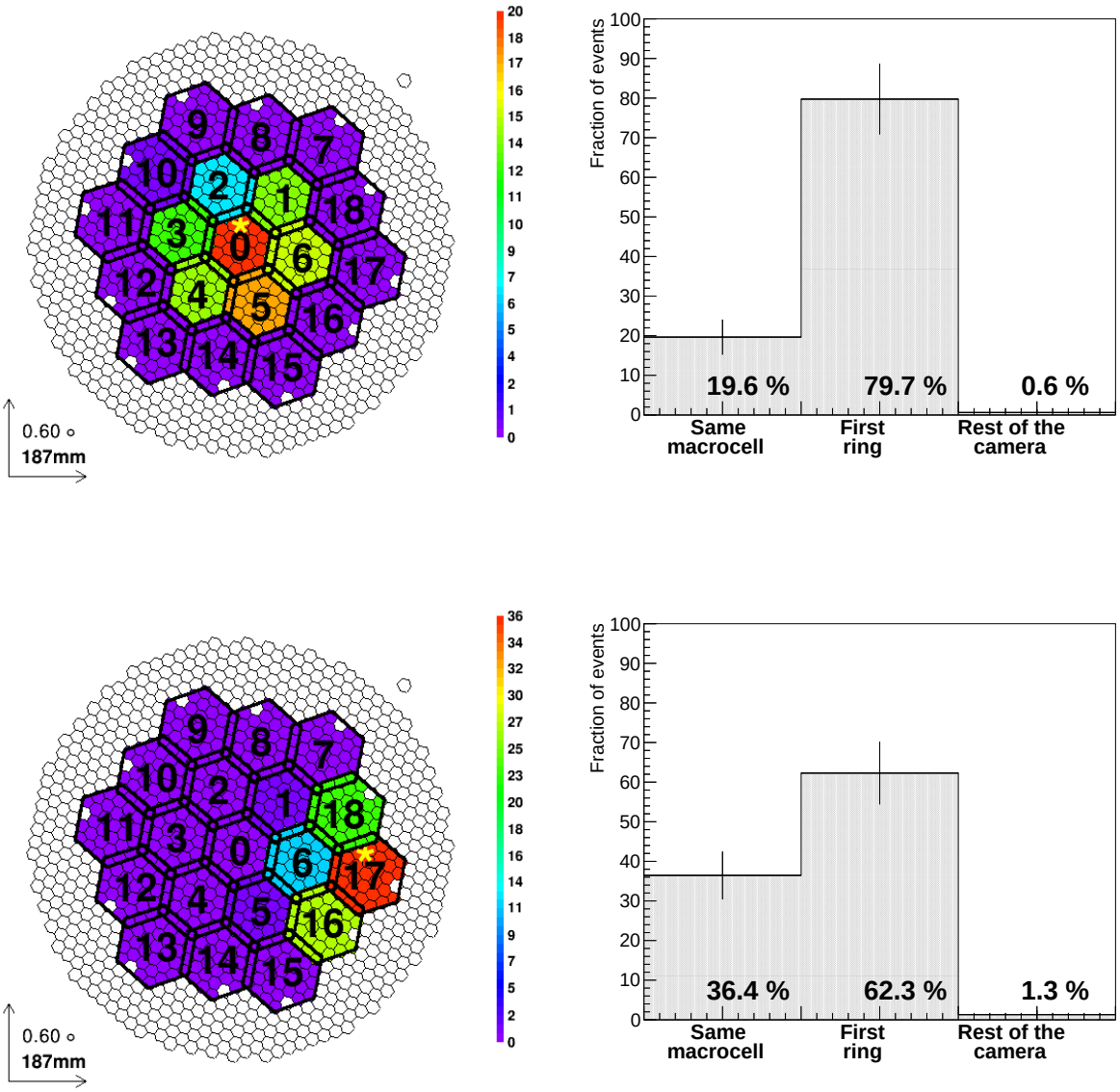

Figure 4.4: Macrocells triggered in M II when selecting one macrocell in M I for events triggering only one macrocell in each telescope for simulated gamma rays after analysis cuts (left panels) and the histograms of the distributions (right panels).

trigger macrocell selection to MC γ-ray events triggering with the Reduced DT configuration. The fraction of simulated gamma rays rejected by the algorithm is $\sim$ 2.4 %. As we will show in Section 4.2.4, the fraction of events rejected at the analysis level is significantly lower than this. In summary, according to MC, by applying the Topo-trigger macrocell selection cuts, we reject 85% of the accidental events but only 2.4 % of the γ-ray events at the trigger level.

Off-axis simulations

In the previous sections we have verified that the selection algorithm works applying it to the standard MC simulations with the source located at a 0.4° distance from the center of the camera. Now we want to check that the algorithm does not depend on the source position of the camera, but on the relative position of the telescopes with respect to each other. We simulated γ-ray events at distances from the center of the camera ranging from 0.6° to 1.4°. We did not include NSB in our simulations to study the effect in events triggered by a γ-ray shower. We examined the triggered macrocell distribution and applied the Topo-trigger macrocell selection mentioned in Section §4.2.3. The distribution of triggered macrocells is similar to the one obtained using the standard MC with the source at 0.4 ° from the camera center.

4.2.4 Expected performance

We will now calculate the collection area and energy threshold of the instrument after applying the Topo-trigger selection. We will proceed as it was explained in Sections §2.2.3.9 and §2.2.3.6. For the analysis of the MC gamma rays, we calibrate the data, clean the images applying the image cleaning method and apply a gamma/hadron separation with the so-called random forest algorithm as in the standard MAGIC analysis Zanin et al. (2013). We ran MC simulations for 2 cases, and for the second case we apply two different image cleanings:

a) Nominal DT with standard image cleaning.

b.1) Reduced DT with the standard image cleaning (6 phe for core pixels and 3.5 phe for the neighbour ones).

b.2) Reduced DT with an image cleaning with charge parameters reduced by 7 % (which is the mean DT reduction applied from Nominal to Reduced DT).

Figure 4.5 shows the true energy distribution of MC γ-ray events for the different trigger configurations. The black histogram represents the rate for the current trigger configuration of MAGIC (Nominal DT). The green histogram represents the rate for the Reduced DT configuration with DT=4.2 phe for M I and DT=4.3 phe for M II applying Topo-trigger macrocell selection with the standard image cleaning. The blue line represents the rate for the Reduced DT configuration with a 7% reduced image cleaning. We can see that the energy threshold goes down by up to 8 % at the analysis level.

The collection area in each energy bin is calculated as explained in Section §2.2.3.9. The collection area for both the Nominal DT and the Reduced one is shown in the top panel of Figure 4.6, and the ratio between the collection area obtained using the current MAGIC trigger configuration and the collection area obtained with the Reduced DT applying the Topo-trigger macrocell selection in the bottom panel of the same figure. The black points correspond to the collection area obtained with the current trigger configuration of MAGIC . The green points correspond to the collection area obtained reducing the DT to 4.2 phe in M I and 4.3 phe in M II and applying the Topo-trigger macrocell selection. The blue points represent the rate for the

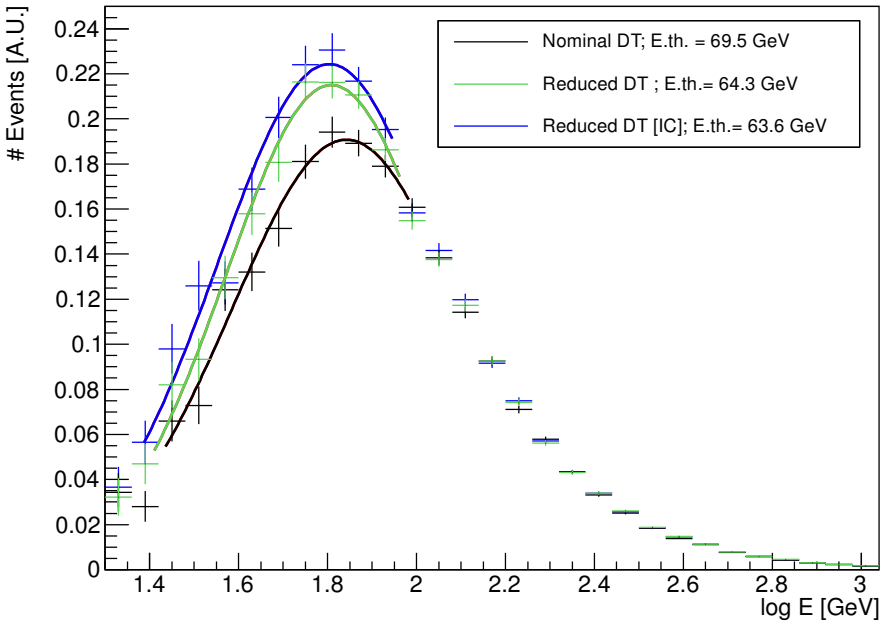

Figure 4.5: True energy distribution of MC gamma rays (in arbitrary units) for a source with a 2.6 spectral index for different trigger configurations.

Reduced DT configuration with a 7% reduced image cleaning. The red line in the bottom panel delimits the region where the Reduced DT option performs better than the Nominal DT (ratio > 1). We can see that the improvement in collection area using the Topo-trigger at the lowest energies is ∼60%, although the errors are very large due to the low statistics at those energies. At the energy threshold, where we have a peak in the number of events triggered, the improvement using the Topo-trigger is between 10–20 % with respect to the current MAGIC configuration. Moreover, this gain in events is still ∼5% for showers with energies between 70 GeV to 100 GeV. As expected, there is no effect for higher energies. At the highest energies (the last point in energy of Figure 4.6), there are only a few events that give trigger, therefore the fluctuations are large. We would like to stress that all these improvements are at the analysis level, i.e. for the events that are used to derive spectra, light curves and skymaps.

After applying the Topo-trigger cuts at the analysis level, we keep 98.8% of the total events that survived the analysis cuts. At the trigger level we were keeping only 97.6 % of those events, meaning that most of the events that were rejected when applying the macrocell algorithm, are not used for analysis either.

4.3 Piggy-back measurements

We installed a system to record the macrocell pattern for every event at the trigger system in La Palma. As the trigger DT was not lowered, we do not expect any improvement by applying the

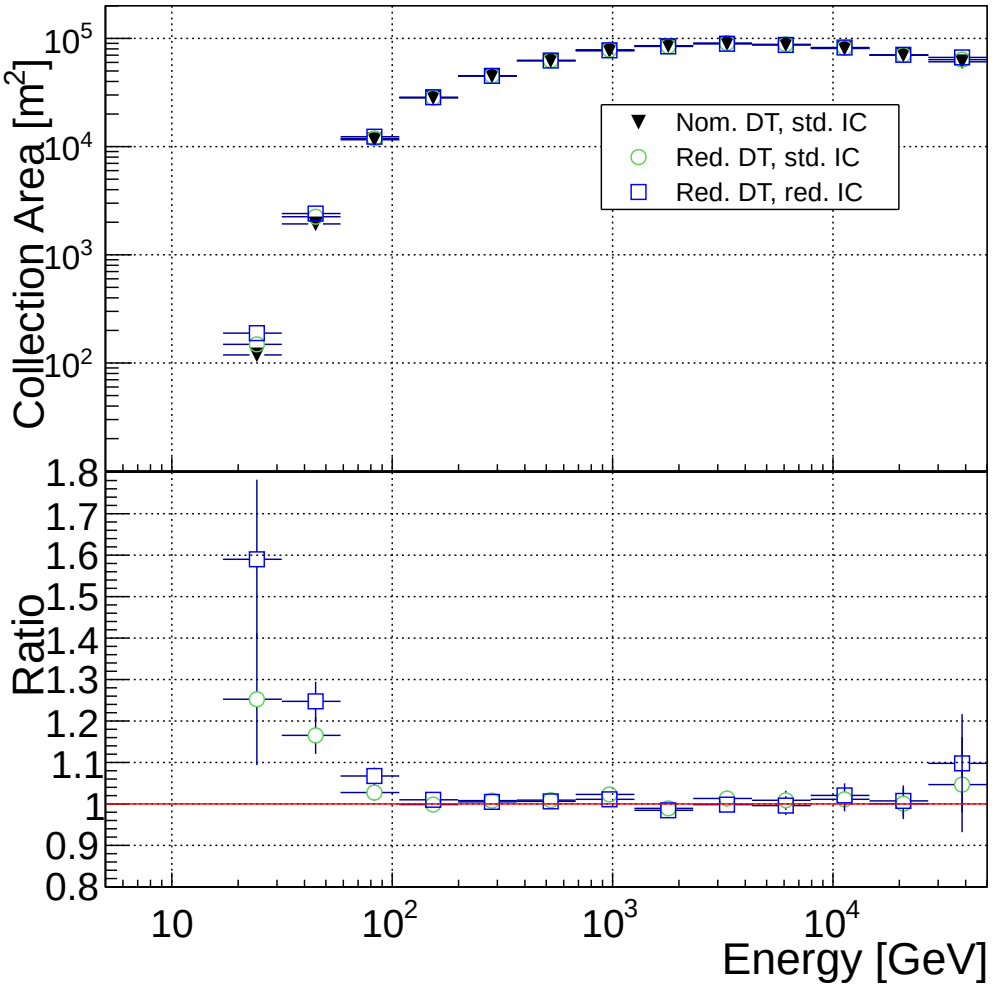

Figure 4.6: Collection area using the Nominal DT and the Reduced one applying cuts (top) and the ratio between the Reduced DT configurations and the Nominal DT one (bottom).

algorithm to the data. We only intend to verify that no gamma rays are lost at the analysis level due to the Topo-trigger macrocell selection applied in the software and hardware.

4.3.1 Description of the setup

We prepared a setup that records the digital output of the macrocells for every event recorded by the DAQ system Tescaro et al. (2013). A scheme of the setup used for recording the macrocell information is shown in Figure 4.7.

The signals of the camera go to the receiver boards where the first stage of the discriminator process (L0) is done. Once they have passed through the receivers, the NN logic is applied in each macrocell, as explained in Section §2.2.1.6. The output of each of the 19 L1 trigger macrocells

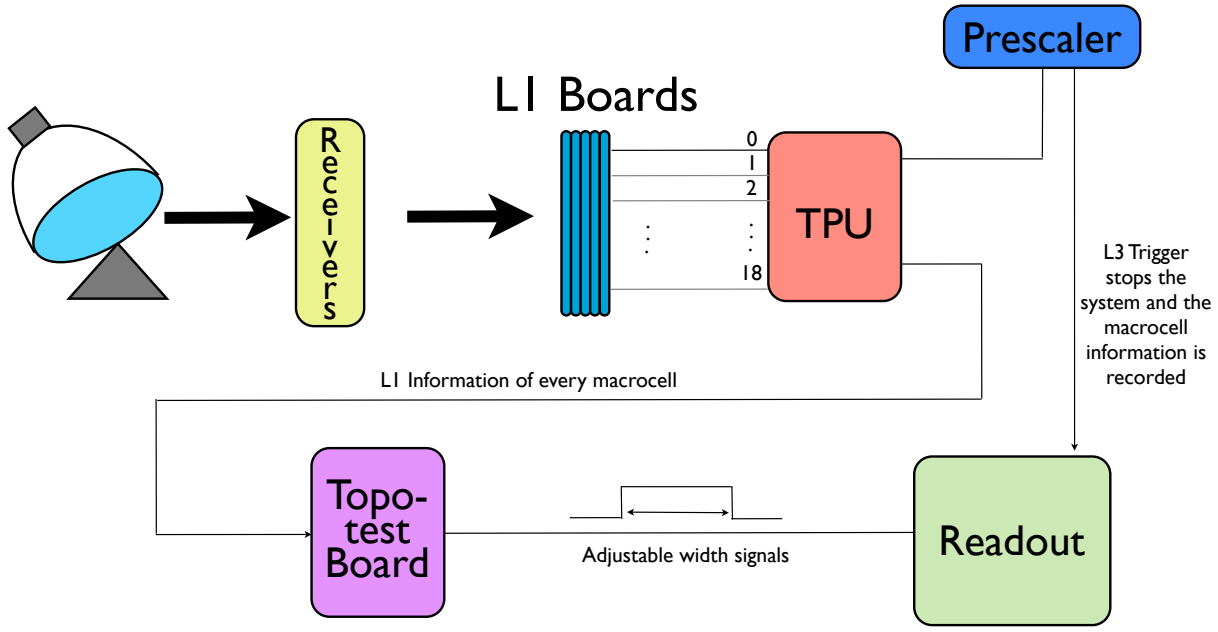

Figure 4.7: Scheme of the recording system installed at the MAGIC telescopes for the Topo-trigger piggy-back measurements.

goes to the TPU. It sends a square signal every time the L1 trigger condition is fulfilled in any of the 19 macrocells. The TPU has 5 outputs: one that goes to the L3 trigger with no delay, the second one to monitor L1 rate, the third is a sync signal that goes to the prescaler and is used to synchronize L3 output, the fourth is a delayed signal for the L1 and the fifth one, that is usually unused, latch the macrocell information. We send the output of the TPU to a patch board + Test Experimental Device (TED), which handles the digital signal coming from the 19 macrocells, stretches it and sends it to a pulsar board. The pulsar board stops and writes the information of the macrocells when it receives a trigger from the prescaler issued by the L3 trigger: we record the macrocell information of the events that triggered the stereo system.

4.3.2 Sensitivity and γ-ray rate comparison

We took Crab Nebula data at Az angles ranging from 100° to 175° and Zd between 6° and 22°. We analyzed these data using the standard analysis in MAGIC and applied the standard hadron/gamma separation and event reconstruction cuts for two energy ranges: medium-to-high

energies and low energies.

Medium-to-high energies We applied the standard γ/hadron separation, reconstructed energy and θ^2 cuts used for medium energies (described in Section §2.2.3.7), leading to an energy threshold of ~ 250 GeV. We calculated the sensitivity of the telescope and the γ-ray rate for the sample without applying any cut in macrocells and applying the Topo-trigger macrocell cuts. The result was that we have exactly the same number of background and gamma events after applying the Topo-trigger macrocell selection cuts, so the sensitivity and γ-ray rate are kept constant.

Low energies We also made an analysis applying the standard cuts for low energies. We computed the ratio between the sensitivity with and without macrocell cuts:

$$\frac{\text{Sensitivity}}{\text{ratio}} = \frac{\text{Sensitivity[macrocell cuts]}}{\text{Sensitivity[no cuts]}} = 1.005 \pm 0.007$$

And the ratio of γ-ray rate with and without macrocell cuts:

$$\frac{\gamma\text{-ray rate}}{\text{ratio}} = \frac{\gamma\text{-ray rate[macrocell cuts]}}{\gamma\text{-ray rate[no cuts]}} = 0.997 \pm 0.001$$

As we can see, there is a small loss in γ-ray rate (0.3 %). The sensitivity does not change within the errors. The loss in γ-ray rate is compatible with the expectations from the simulations shown in Section §4.2.4.

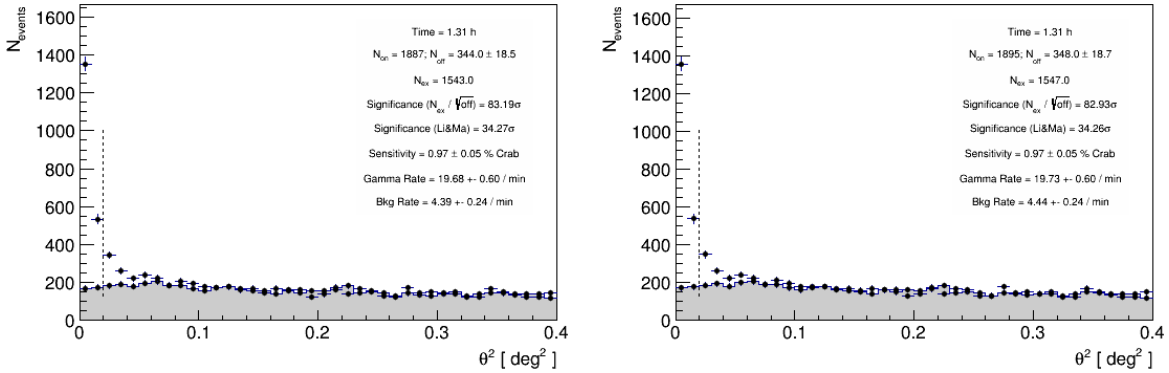

Figure 4.8: θ^2 plots applying (left panel) and without applying (right panel) the macrocell selection cuts to a Crab Nebula dataset.

The results for the sensitivity and γ-ray rate ratio between the data to which we applied the macrocell selection and the data without applying any macrocell selection are summarized in Table 4.2. These results confirm what we expected from the simulations: if we apply the macrocell selection to the events used for analysis, we keep basically the same detection efficiency.

	Sensitivity ratio	γ-ray rate ratio
Medium E	1	1
Low E	1.005 ± 0.007	0.997 ± 0.001

Table 4.2: Summary of the results for the sensitivity ratio and γ-ray rate ratio between the analysis applying the Topo-trigger macrocell cuts and without applying them for medium and low energies.

4.4 Discussion and conclusions

We have developed a novel stereo trigger system for IACTs which make use of the topological information of the showers in the camera. Combining the information of the Az angle at which the telescope is pointing and the L1 trigger macrocell hit in each telescope we can reject 85% of the accidental stereo trigger rate, which is the dominant at the lowest energies, without losing gamma rays. By studying the effect of applying the selection algorithm to off-axis data, we find that the discrimination power of the algorithm does not depend on the source position in the camera. We run simulations reducing the DT used for triggering the telescopes and applying this algorithm and we found that implementing this trigger translates into a decrease of up to 8% in the energy threshold and an increment of ∼60% in the collection area at the lowest energies and from 10–20% at the energy threshold, where most of the events are triggered. The algorithm developed allows to lower DTs without increasing the accidental rate. We installed a device to record the triggered macrocells of the events recorded by the MAGIC telescope. Without reducing the DT applied at the L0 trigger, we verified that the Topo-trigger macrocell selection tested in the MC does not lead to any loss in the sensitivity or in the γ-ray rate. The potential of this easy to implement algorithm is that it could also be used for any other system with a similar trigger based on macrocell or clusters that give you the information of the topological distribution of a trigger in the camera.

The board that will be used to veto signals from the L3 trigger is already installed in the MAGIC telescope and is currently under commissioning.

Part III

Pulsar Wind Nebulae

Figure III: Chandra image of 3C 58.

5 Introduction to Pulsar Wind Nebulae

5.1 Star fate

Main sequence stars are self-luminous celestial objects held together by their own gravity. They are constantly producing energy by nuclear fusion. The fate they suffer at the end of their lives depends on the mass of their helium cores and hydrogen envelopes at death (Heger et al. 2003). For a complete description of the final state of a star as a function of the initial mass and metallicity, see Figure 5.1. In the following, we present a breakdown of the objects that are formed at the end of the lives of stars, depending on their mass M.

- $M <$ 9-10 $M_\odot$: After the fusion of Hydrogen (H) and Helium (He), if the core of the star does not reach the temperature required to fuse Carbon (C) or Neon (Ne), the fusion reactions stop and the star can no longer be supported by fusion reactions against the gravitational collapse, then the star starts to contract. According to the Pauli exclusion principle, two electrons cannot occupy the same state, so the star stops collapsing when it reaches a degeneracy state and is sustained by electron degeneracy. This is possible if the mass of the star is smaller than the Chandrasekhar limit of 1.4 $M_\odot$ (Chandrasekhar 1931), beyond which the gravitational force cannot be supported by the electron degeneracy. This remnant is known as White Dwarf (WD).

- 9-10 $M_\odot < M <$ 40 $M_\odot$: After the fusion of all the heavy elements (C, Ne, Oxygen (O), Silicon (Si), Iron (Fe)), if the mass of the stellar remnant is larger than the Chandrasekhar limit, the electron degeneracy pressure cannot hold the core against the gravitational force. The star undergoes a collapse and releases some of its gravitational energy in a SN explo-

sion (see section §5.1.1). Depending on the initial mass of the object, it becomes a NS or a BH.

a) 9-10 $M_\odot < M < 25\ M_\odot$: Once the electron degeneracy is overcome and the core collapses, the temperature increases and free electrons and protons combine to form neutrons and neutrinos $p^+ + e^- \rightarrow n + \nu$. The object formed is called NS because it is mainly formed by neutrons (Grupen 2005). We will extend their description in Section §5.2.

b) $25\ M_\odot < M < 40\ M_\odot$: If the mass of the remnant of the stellar object is sufficiently high to overcome the neutron degeneracy pressure by its gravitational force, a BH is generated after the SN explosion.

⊙ $40\ M_\odot < M < 140\ M_\odot$ or $M > 260\ M_\odot$: If the star was initially much more massive, there is no visible SN explosion and a BH is directly formed.

⊙ $140\ M_\odot < M < 260\ M_\odot$: Nuclear reactions inside the star generate gamma rays which in turn produce $e^\pm$ pairs. This pair creation produces a thermal pressure drop that leads to a partial collapse. For massive stars with a mass in this range, the partial collapse is followed by a thermonuclear explosion that rips the star apart and leaves no remnant.

If the star's metallicity is larger than $M_\odot$, they typically end their lives as a NS, independent of their mass.

5.1.1 Supernovae

From the observational point of view, SNe are divided into two types, including several subclasses into each of them (Reynolds 2008).

⊙ **Type I:** They do not present H lines

- *Type Ia:* They show a strong ionized Si II (6150 Å) absorption line.
- *Type Ib:* They lack a spectral feature of Si II (6150 Å).
- *Type Ic:* Apart from H, they also lack He.

⊙ **Type II:** They present H lines

- *Type IIP:* They show a plateau in the light curve after reaching the maximum.
- *Type IIL:* They show a linear decline in the light curve after reaching the maximum.
- *Type IIn:* They show a spectrum with narrow emission lines.

All the SNe, except Type Ia, are produced by a explosion of the star driven by gravitational core-collapse. Type Ia has a thermonuclear origin and is thought to be generated by the nuclear burning of a carbon-oxygen WD. We will center the discussion of this part of the thesis in the study of the evolution of SNe that left after their explosion NSs that rotate very rapidly, also known as pulsars.

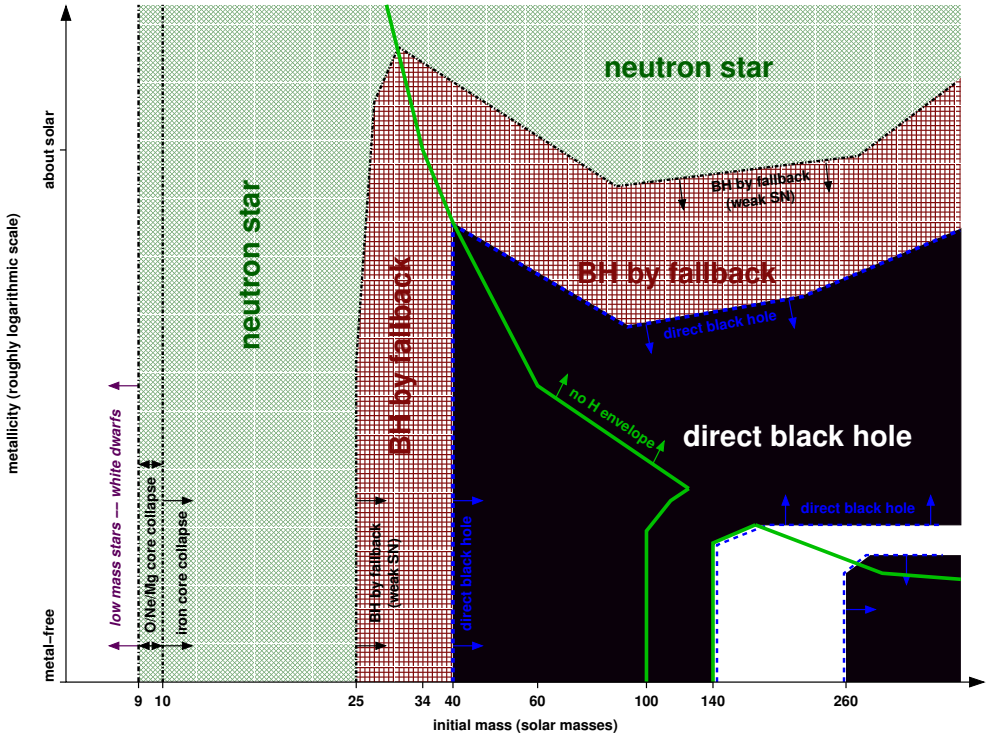

Figure 5.1: Diagram showing the fate of the stars depending on their initial mass and their metallicity. Plot from Heger et al. (2003).

5.1.2 Supernova Remnants

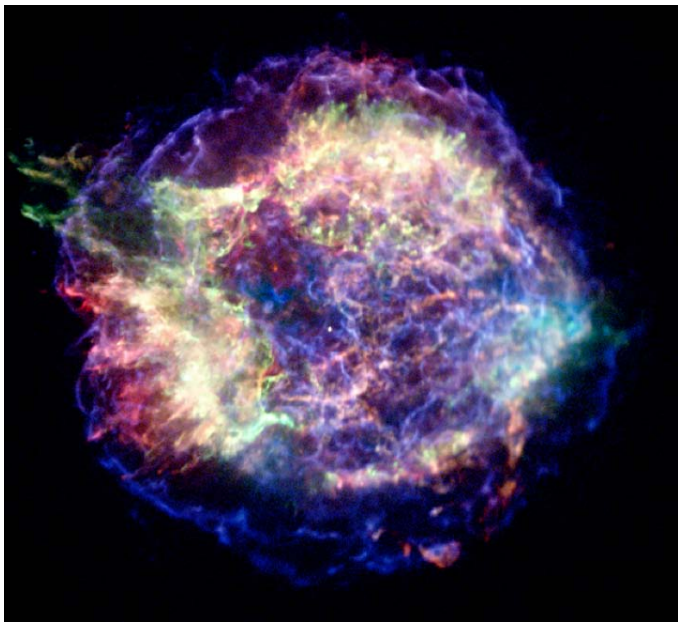

Figure 5.2: X-ray image of the SNR Cas A taken with *Chandra*. The color code is: red: 0.5-1.5 keV, green: 1.5-2.5 keV and blue 4.0-6.0 keV). The central white point corresponds to the central compact object. Credit:NASA/CXC/MIT/UMass Amherst/M.D.Stage et al.

Apart from the stellar remnants mentioned in Section §5.1, the material ejected by the SN explosion interacts with the ISM forming a SNR. There are three types of SNRs: if they have shell-like structure, then they are *shell-like SNRs*; if they are filled at the center at all wavelength and have a central object that constantly injects particles and energy to the remnant, they are known as *plerions* or *PWNe*; and if the PWN is surrounded by a shell-like SNR, the system is called *composite*. We will describe in Section §5.4 in more detail the SNR type where this part of the thesis focuses: the PWN. For a general review of SNRs at high energies, we refer the reader to (Reynolds 2008). Figure 5.2 is an image of the youngest SNR known in the galaxy, Cassiopeia A (Cas A).

5.2 Neutron stars

As it was briefly described in Section §5.1, NSs are formed in the gravitational collapse of a massive star. When the core of the star reaches a density of the order of the nuclear density, the collapse stops leaving as a remnant the most dense stellar object known so far, a sphere of radius ~ 10 km, density $\rho \sim 10^{17}$ kg m^{-3} and mass between 1.4 and 3 $M_{\odot}$. During the collapse, the star dramatically reduces its size, but as the angular momentum and magnetic flux are conserved, a high-magnetic field rapidly-spinning (with a period varying from 1 ms to 10 s) NS is created. They were first postulated by Baade & Zwicky (1934).

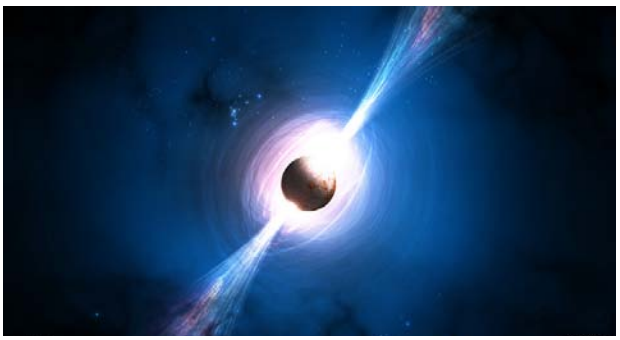

Figure 5.3: Artist view of a pulsar.

5.2.1 Inner structure of an NS

A sketch of the inner structure of a NS can be seen in Figure 5.4. A very thin atmosphere is believed to surround an extremely hard crust made of ions and electrons. Under this outer crust there is an inner one made of nuclei mixed with electrons and neutrons. Around 9 km from the center of the NS, an outer core made of superfluid neutrons with some superconducting protons lies under the inner crust. The composition of the inner core is completely unknown, but some exotic kind of matter such a quark-gluon plasma or strange matter might be present.

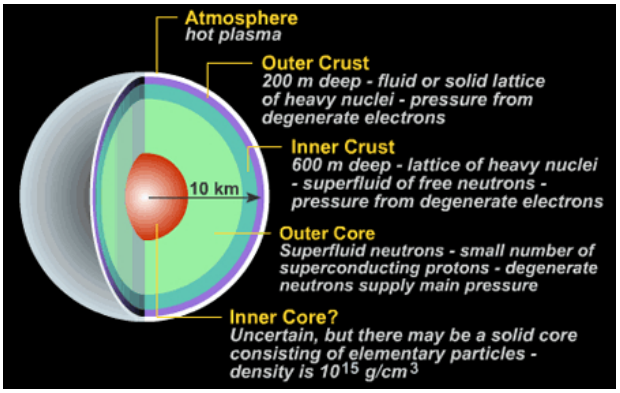

Figure 5.4: Internal structure of an NS. Image credit: Brooks/Cole Thomson Learning.

5.2.2 Classification

NSs typically have pulsations at different wavelengths, and can be classified according to the primary source of their emission and spin evolution: *Rotation-Powered Pulsars (RPPs)* derive their energy from the rotation of the pulsar, *Magnetars* from the magnetic field energy, *Isolated Neutron Stars (INSs)* from the latent heat of the NS matter, *Accretion-Powered Neutron Stars (APNSs)* from the energy released by matter accretion to the NS and finally *Compact Central Objects (CCOs)* that only manifest thermal X-ray emission (Harding 2013). A plot of the $\dot{P}$ as a function of their P for the NSs known can be seen in Figure 5.5.

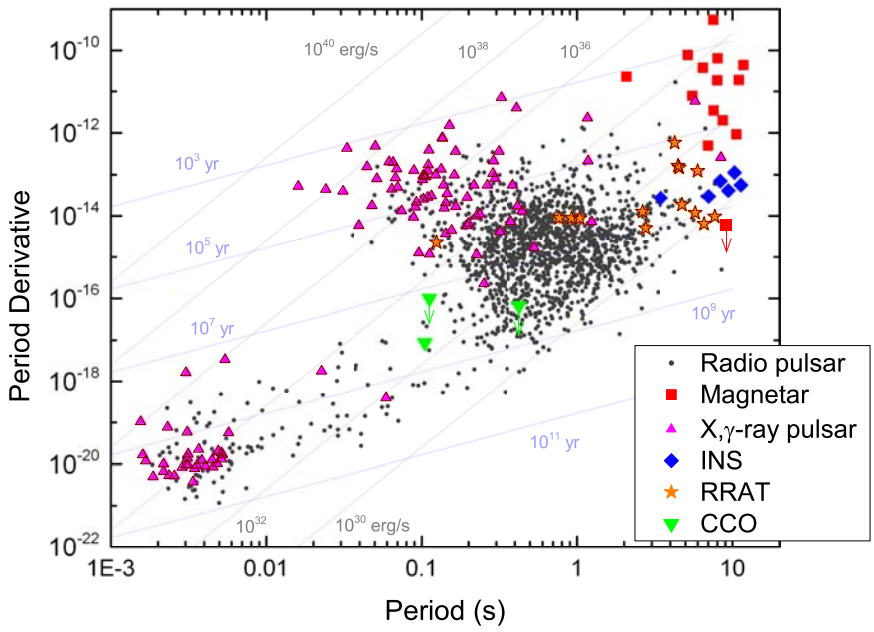

Figure 5.5: Plot of P vs. $\dot{P}$ for the currently known rotation-powered pulsars, INS, CCO, Rotating Radio Transients (RRATs) and magnetars. Lines of constant characteristic age, $P/2\dot{P}$, and dipole spin-down luminosity, $\dot{E}_{\rm sd}$, are also drawn. Plot from (Harding 2013).

5.2.3 NS magnetosphere

If we consider the NS as a perfect conductor, charge has to be built up in the surface due to the law of Gauss. This surface charge induces an electric field parallel to the magnetic field, therefore perpendicular to the NS surface. The electric field is so strong that it tears apart some of these charged particles that initiate $e^{\pm}$ cascades and populate with plasma the NS magnetosphere. The density of particles in the pulsar's magnetosphere is believed to be close to the Goldreich-Julian density (Goldreich & Julian 1969), defined as that required to screen the induced electric field

(Kirk et al. 2009):

$$\rho_{\rm GJ} = \frac{\boldsymbol{\Omega} \cdot \boldsymbol{B}}{2\pi c} \tag{5.1}$$

where $\boldsymbol{\Omega}$ is the angular speed, $\boldsymbol{B}$ the magnetic field and c the speed of light. A NS can be modeled as a rotating magnetic dipole (multipole fields drop more rapidly with the distance and become negligible at large distances). One can assume rigid rotation of the external dipole field and the plasma until the distance $R_{\rm L}$ the rotation velocity equals the speed of light:

$$R_{\rm L} = \frac{c}{\Omega} \tag{5.2}$$

The surface defined by the $R_{\rm L}$ is called *light cylinder*. The NS magnetosphere is the region between the NS and the *light cylinder* and the region between the light cylinder and the termination shock is known as the *wind zone*. Inside the light cylinder, the magnetic field can be approximated with that of a magnetic dipole. Inside this region magnetic field lines are closed, while magnetic field lines outside are open. $R_{\rm L}$ separates the zones of magnetic field that are causally connected to the rotation of the pulsar to those that are not. The particles attached to the open lines escape the *light cylinder* region. There is a *critical open line* whose electric potential is the same as in the ISM. e^- escape through higher-altitude lines while protons do it along lower-latitude ones (see Figure 5.6).

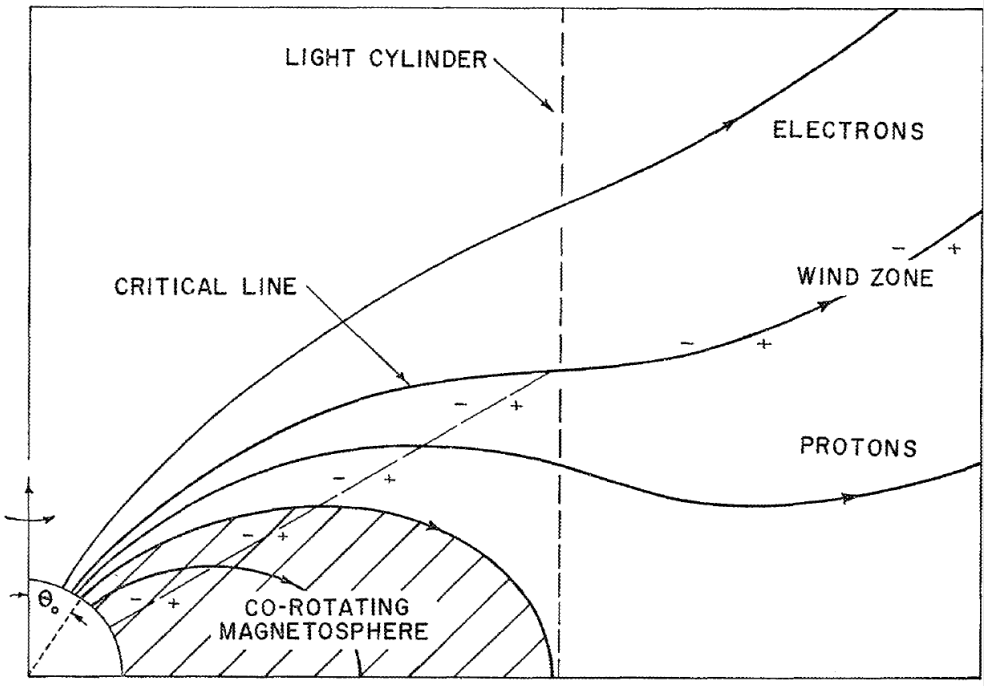

Figure 5.6: Sketch of a pulsar, its light cylinder and wind zone. Taken from (Goldreich & Julian 1969).

5.3 Pulsars

Pulsars are rotating NSs that produce periodic radiation by spinning their powerful magnetic field through space. NSs were proposed to be the central engine powering the Crab Nebula (Pacini 1967) almost at the same time of the discovery of the first radio pulsar by Jocelyn Bell (Hewish et al. 1968). Pulsars were associated with rotating NSs (Pacini 1968) in the context of magnetic dipole moment. This association predicted a loss in the rotational energy of the pulsar and therefore a period increase that was observed by Richards & Comella (1969). An artist view of a pulsar can be seen in Figure 5.3.

Spin-down power: Pulsars are constantly releasing their rotational energy in the form of EM emission and in the form of high-energy particles. We can compute the energy released by a pulsar as a function of P , $\dot{P}$ and I :

$$\dot{E} = -\frac{\mathrm{d}E}{\mathrm{d}t} = 4\pi^2 I \dot{P} P^{-3} = I\Omega\dot{\Omega} \tag{5.3}$$

where $I = 10^{38}$ kg m^2 is the moment of inertia of the pulsar and $\Omega = \frac{2\pi}{P}$ is the angular frequency of rotation of the NS. The spin-down power of all known pulsars ranges between 10^{28} and 10^{39} erg/s.

A general description of the pulsar's spin-down that takes into account energy loses is the following:

$$\dot{\Omega} = -k\Omega^n \tag{5.4}$$

where k is a constant and n the braking index that can be calculated using the second derivative of this equation:

$$n = \frac{\Omega\ddot{\Omega}}{\dot{\Omega}^2} \tag{5.5}$$

The values of n measured for the known pulsars range between 1.4 and 2.9.

Age: If we rewrite equation 5.4 using P and integrate it to calculate the age of the pulsar, we have (Manchester & Taylor 1977):

$$t_{age} = \int_{P_0}^{P} \frac{1}{KP'^{2-n}} dP' = \frac{P}{(n-1)\dot{P}} \left[1 - \left(\frac{P_0}{P} \right)^{n-1} \right] \tag{5.6}$$

where P_0 the initial period. If we assume n=3, the one corresponding to dipole radiation and also $P_0 << P$, the formula can be simplified to the form:

$$\tau_c = \frac{P}{2\dot{P}} \tag{5.7}$$

that corresponds to the characteristic age of the pulsar. This value usually overestimates the real age of the pulsar, indicating that the assumptions made are not exact.

Surface magnetic field: To calculate the surface magnetic field of the NS , we assume that it is originated by a dipole. The magnetic field due to a dipole is $\sim \mu R$ (Ostriker & Gunn 1969), where μ and R are the magnetic dipole moment and the radius of the NS respectively.

$$B_s \simeq 3.2 \times 10^{19} (P\dot{P})^{1/2} \text{Gauss} \tag{5.8}$$

Temporal evolution: Assuming that the braking index n is constant, one can take equation 5.6 and compute the time evolution of the period P (Pacini & Salvati 1973):

$$P(t) = P_0 \left[1 - \left(\frac{n-1}{2} \right) \frac{t}{\tau_c} \right] = P_0 \left(1 + \frac{t}{\tau_0} \right)^{\frac{1}{n-1}} \tag{5.9}$$

where $\tau_0 = 2\tau_c/(n-1) - t$ represents the time-scale of the spin-down process. Similarly, one can compute the magnetic field and spin-down power evolution:

$$B(t) = B_0 \left(1 + \frac{t}{\tau_0} \right)^{\frac{n-1}{2n-2}} \tag{5.10}$$

$$\dot{E}(t) = \dot{E}_0 \left(1 + \frac{t}{\tau_0} \right)^{-\frac{n+1}{n-1}} \tag{5.11}$$

where B_0 and $\dot{E}_0$ are the initial magnetic field and the initial spin-down power respectively. The NS magnetosphere is the region between the NS and the *light cylinder*.

5.3.1 Models for the pulsar γ-ray emission

Three scenarios have been proposed for the production of pulsed gamma rays, depending on the location of the emission region.

- ⊙ **Polar Cap (PC):** They predict emission near the surface of the NS , in the magnetosphere at a distance of ∼30 km from the pulsar (Sturrock 1971; Daugherty & Harding 1982; Arons & Scharlemann 1979). Gamma rays are emitted by curvature radiation from $e^{\pm}$ moving along the curved magnetic field lines above the polar cap of the pulsar. They predict a sharp super-exponential cut-off in the γ-ray spectrum.

- ⊙ **Slot Gap (SG)** and **Outer Gap (OG):** The emission region is placed farther out in the magnetosphere and extends up to the light cylinder. The SG was originally represented as an extension of the PC model. In the framework of the PC , Scharlemann et al. (1978) found that the potential gap above the pole increases when approaching to the last closed field line. Arons (1983) used this to propose that EM cascades could develop in this region, reaching higher energies due to their larger distance to the NS . Radiation from the SG produces a wider cone of emission than in the PC scenario (Harding & Muslimov 2005)

  The OG succeeds to explain most of the observational results from young, large-spin-down power pulsars. It was proposed by Cheng et al. (1986) and is based on the existence of a

charge-depleted volume that can form at low latitude. This gap is contained within the last closed field line, the null surface (defined as $\mathbf{\Omega} \cdot \mathbf{B} = 0$), the light cylinder, and an open magnetic field line which is limited by pair creation. The OG model was extended to explain the VHE γ-ray emission from the Crab pulsar (Hirotani 2011, 2013). The TeV emission is explained in terms of IC scattering of secondary and tertiary $e^{\pm}$ pairs created in the collision of primary gamma rays emitted by curvature radiation and Ultraviolet (UV)-Infrared (IR) photons. Figure 5.7 shows a picture of a pulsar illustrating the location of the PC , SG and OG regions drawn.

⊙ **Wind zone:** They place the emitting region of pulsed photons outside the magnetosphere, in the wind zone (Lyubarskii 1996; Kirk et al. 2002; Pétri 2011). There is also a model predicting VHE γ-ray emission by IC upscattering of photons from the wind (Aharonian et al. 2012). Emission at these energies is due to IC scattering of the X-ray photons produced in the magnetosphere or in the pulsar surface by the e^- or e^+ existing in the wind. According to Aharonian et al. (2012), acceleration takes place in a region between $20 - 50$ R_L, but this would imply a very sharp cut-off at 500 GeV. In order to match the maximum pulsed energy given by the recent observations (Zanin 2014), one has to extend the region where the X-rays interact with the wind to 70 R_L.

Due to the recent reports on pulsed emission up to TeV energies with very sharp pulse profiles (Zanin 2014), one finds that none of the proposed models is able to reproduce the broadband spectrum of the Crab pulsar giving at the same time a good description of the spin-phase folded light curve.

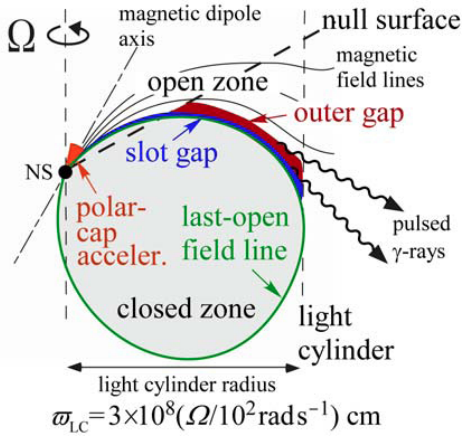

Figure 5.7: Sketch of the pulsar magnetosphere pointing the PC, SG and OG acceleration regions. Image from Hirotani (2008).

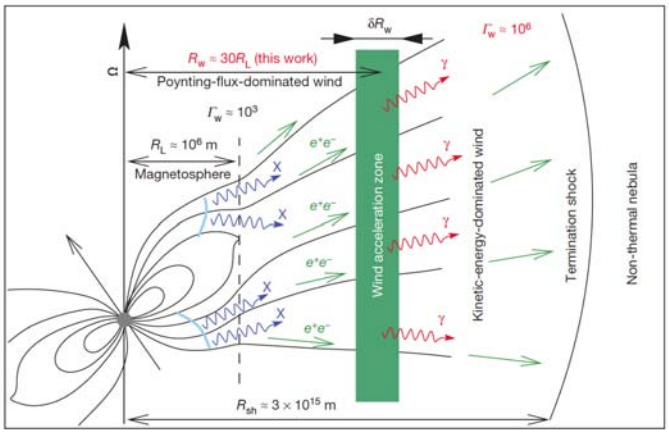

Figure 5.8: Sketch of the wind zone model. $e^{\pm}$ pairs are accelerated in the region tagged as wind acceleration zone, at a distance of several R_L from the pulsar. Image from Aharonian et al. (2012).

5.3.2 Observational signatures of pulsars at VHE gamma rays

There are only two pulsars detected at VHE to date: the Crab and Vela pulsars (Zanin 2014; Brun, P. 2014). Crab shows pulsed emission up to TeV, while for Vela no energy spectrum has been

reported so far. In the case of Crab's light curve, two peaks can be significantly distinguished above the background, although for Vela only one is detected (see Figure 5.9).

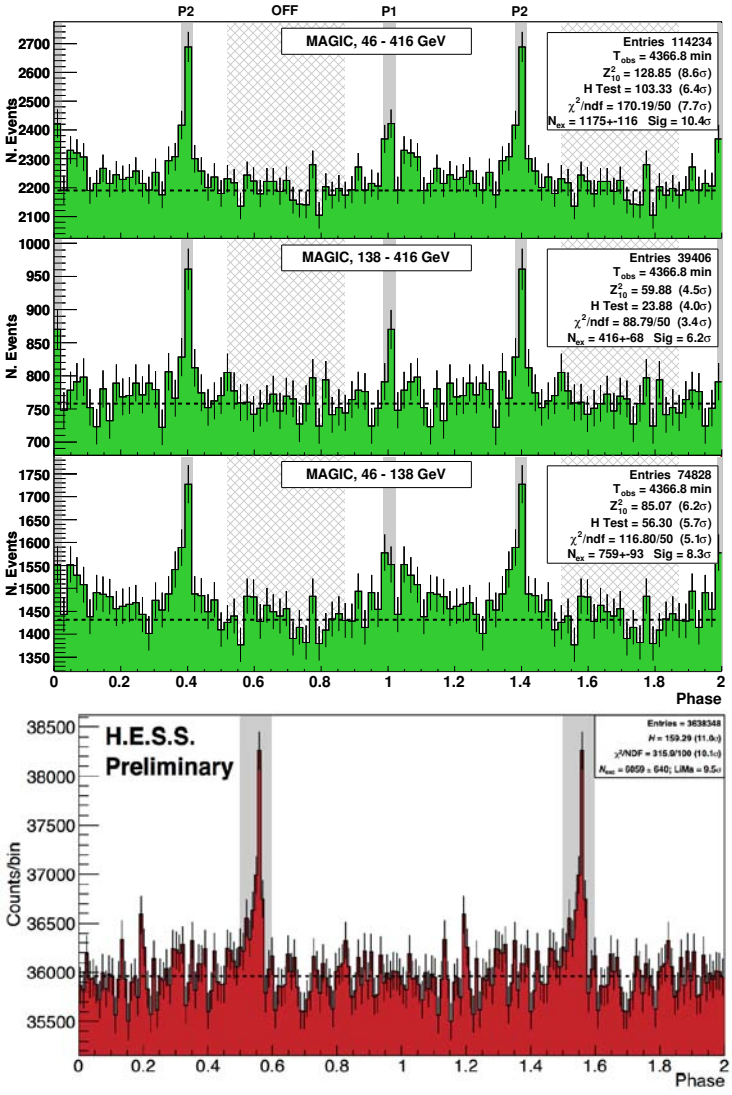

Figure 5.9: Crab (top panels, filled in green, from Aleksić et al. (2012b)) and Vela (bottom panel, filled in red, from Brun, P. (2014)) pulsars' light curves. Two phases are shown for clarity. The peak positions are marked by the solid shadowed areas, while the OFF position in the Crab light curve is marked by a dashed shadow area. Crab light curves are shown in several energy ranges.

The peaks at TeV energies are much narrower in both cases than those reported at GeV energies. The region between P_1 and P_2 is known as the bridge region. MAGIC recently reported the detection of VHE γ-ray emission up to 400 GeV from the bridge region (Aleksić et al. 2014b).

In Figure 5.10 we show the Crab pulsar spectrum up to 400 GeV reported by MAGIC , since the spectrum up to TeV energies is not public yet. The pulsed spectrum of both peaks is fit by a power-law with photon spectral index Γ=3.57±0.27 and differential flux at 100 GeV 13.0±1.6

TeV^{-1} cm^{-2} s^{-1} (Aleksić et al. 2012b). The bridge emission is fit with a power-law with photon spectral index Γ=3.35±0.79 and differential flux at 100 GeV 12.2±3.3 TeV^{-1} cm^{-2} s^{-1} (Aleksić et al. 2014b).

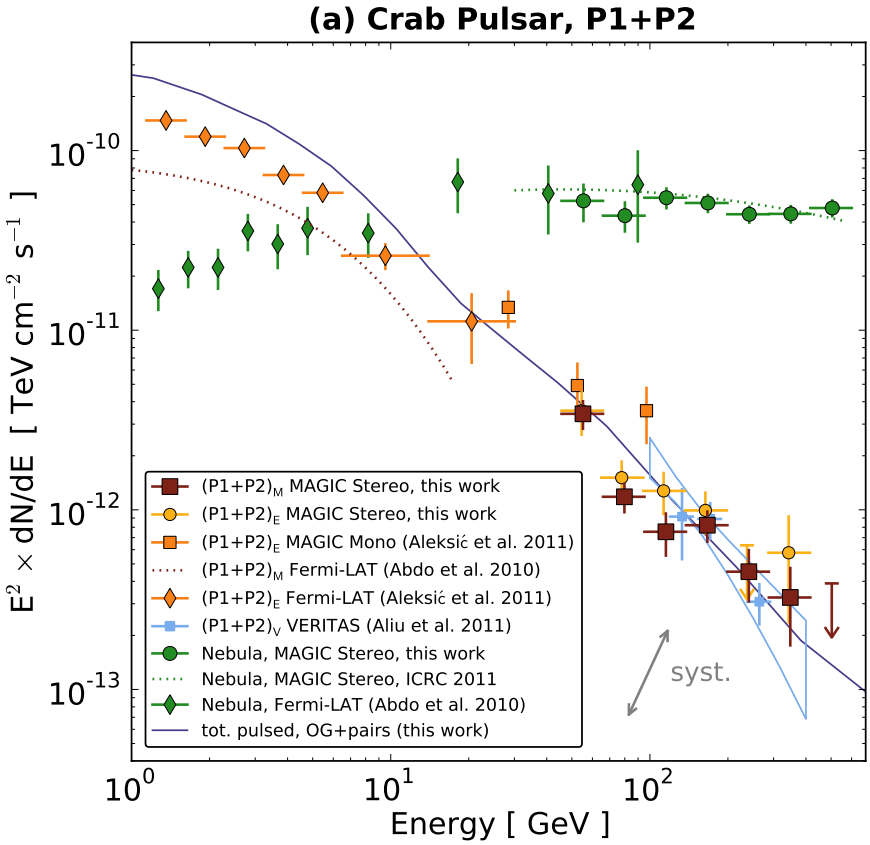

Figure 5.10: MAGIC Crab pulsar spectrum up to 400 GeV. Plot from Aleksić et al. (2012b).

5.4 Pulsar Wind Nebulae

If the SNR is centrally filled at all wavelengths, magnetic energy and relativistic particles are constantly being injected by a pulsar situated at its center and it is known as PWN (Weiler & Panagia 1978). PWNe are usually found embedded in the shell of SNRs larger than the PWN, but one can also find them entangled without the possibility of distinguishing one from the other.

The region between the light cylinder and the termination shock is known as the *wind zone*. The pulsar wind is generated in the acceleration of $e^{\pm}$ pairs that happens in the collapse of charge-separated gaps either near the pulsar polar caps or in outer regions that extend to the light cylinder. In practically all PWN models, the wind leaving the pulsar is Poynting flux dominated. In order to quantify this, we define a *magnetization parameter* σ as a ratio of the energy going out as EM radiation and the energy going out as kinetic energy of particles:

$$\sigma \equiv \frac{F_{E\times B}}{F_{\text{particle}}} = \frac{B^2}{4\pi\rho\gamma c^2} \tag{5.12}$$

where $F_{E\times B}$ is the Poynting flux, F_{particle} the particle flux and B, ρ, γ and c the magnetic field, mass density of particles, Lorentz factor and speed of light, respectively. The parameter σ typically has a large value as the wind leaves the pulsar ($\sigma > 10^4$) and all the models require a small value right behind the termination shock ($\sigma < 0.01$) in order to compensate flow and pressure. The ratio between the synchrotron luminosity and the total spin-down luminosity also requires a particle dominated wind at the termination shock, with a Lorentz factor of $\gamma \sim 10^6$, much larger than the one expected from a freely expanding wind. And here is where the famous *σ-problem* in PWNe pops-up: the change of nature of the wind is widely assumed in all the models explaining VHE emission from PWNe, but the mechanism behind this change is still unclear (Arons 2009). Nevertheless, some solutions have been proposed along the years and the magnetic reconnection seems to be the key of this acceleration (Porth et al. 2013).

As the wind slows down to compensate the pressure applied to the PWN by the ISM, a *termination shock* is formed. It is situated at a distance R_{s}, given by:

$$R_{\text{s}} = \sqrt{\frac{\dot{E}}{4\pi\omega c P_{\text{PWN}}}} \tag{5.13}$$

where ω is the equivalent filling factor for an isotropic wind and P_{PWN} is the pressure in the nebula. An usual assumption to estimate P_{PWN} is to consider equipartition between magnetic field and particles inside the PWN. This assumption, although widely extended, leads to higher magnetic fields than the ones derived from VHE γ-ray observations by different models (see for instance Table 3 of Torres et al. 2014).

We can observe several structures inside the PWNe, all of them originated by different phenomena. They are marked in the Crab Nebula *Chandra* image shown in Figure 5.11.

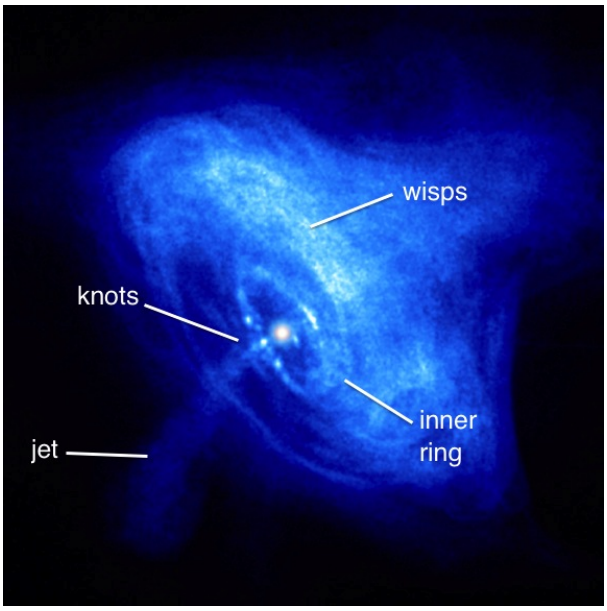

Figure 5.11: *Chandra* X-ray image of the Crab Nebula. One can see the internal structures of the pulsar as the *jet-torus* and the inner ring.

Jet-Torus PWNe usually show a toroidal structure brighter on one if its sides, accompanied by a bright jet and a weaker counter-jet (due to Doppler effects) that extend along the toroidal axis. This structure cannot be explained by an isotropic energy flux inside the PWN proposed by the models (Kennel & Coroniti 1984b), but it may be described by an equatorial flux. The torus may actually correspond to the pulsar's termination shock (Bucciantini et al. 2006).

Wisps They are ripples formed in the synchrotron nebula with variability in timescales down to days. Although the exact nature of these structures is not fully understood, they may be formed by synchrotron instabilities (Hester et al. 2002) or may be places where the $e^{\pm}$ plasma is compressed (Gallant & Arons 1994; Spitkovsky & Arons 2004).

Filamentary structures In PWNe as the Crab, a network of filaments surrounds the non-thermal optical emission. They are explained as Rayleigh-Taylor instabilities when the expanding relativistic bubble sweeps up and accelerates slower moving ejecta (Hester et al. 1996).

The PWN formation can be divided in several phases: first of all, the SNR shell moves forward freely. A shock, known as *forward shock* is formed by the interaction of the SNR material and the ISM (Gaensler & Slane 2006). At the beginning, the PWN is placed at the center of the SNR. Second, the shell enters the so-called "Taylor-Sedov" phase, where the unshocked ejecta starts to decelerate due to the mass of the ISM and a *reverse shock* is formed. It keeps advancing outwards the remnant at the beginning, but turns inwards eventually. The forward shock still compresses and heats material, but the reverse one decelerates and cools it, compressing the central PWN as well (see Figure 5.12). Once the reverse shock stops compressing the PWN, the latter expands again, but this time into the hot ejecta that surrounds it. At the beginning the pulsar escapes from its original position, leaving a relic PWN. Later, the PWN motion becomes supersonic and it forms a bow shock along the SNR. Finally, the pulsar escapes from its surrounding SNR being able to form a bow shock nebula if its movement is still supersonic, but most probably ends up in a low density region where it cannot be detected.

5.4.1 Broadband emission of PWNe

Although the pulsar wind is radiationless, one can study its properties by observing the *termination shock* formed when it is stopped by its interaction with the ISM (§5.2.3). When the particles move along the magnetic field lines compressed at the *termination shock*, they produce

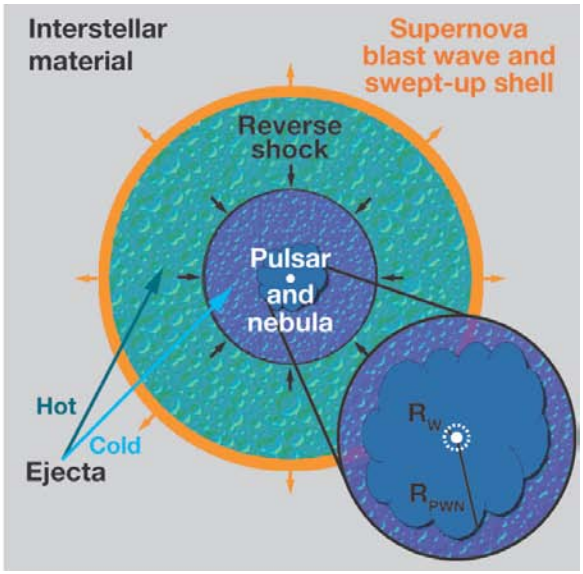

Figure 5.12: Schematic diagram of a composite SNR. In the expanded PWN view we can see the wind termination shock. Picture from Gaensler & Slane (2006).

synchrotron radiation ranging from radio to soft γ-ray energies and produce the so-called *synchrotron nebula*, situated right after the termination shock. The emission in the region ranging from soft gamma rays to VHE gamma rays is produced by IC up-scattering of low-energy photons inside the PWN. The IC scattering is produced all over the PWN. A sketch of the zones of synchrotron and IC emission can be seen in Figure 5.13.

5.4.1.1 Synchrotron emission

The synchrotron nebula extension depends on the magnetic field and lifetime of the particles. According to Ginzburg & Syrovatskii (1965), the cut-off frequency of the cooling spectrum is given by:

$$\nu_b = 10^{21} \left(\frac{B_{\rm PWN}}{10^{-6}{\rm G}} \right)^{-3} \left(\frac{t}{1{\rm kyr}} \right) {\rm Hz} \tag{5.14}$$

If we use a δ-approximation for the synchrotron cross-section, we can relate the energy of the synchrotron photons to the energy of the electrons (Ginzburg 1979):

$$E_{\rm syn} = \frac{h\nu_c}{3} \tag{5.15}$$

where h is the Planck constant and ν_c the critical frequency:

$$\nu_c = \frac{3eB(t)E_e^2}{4\pi m_e^3 c^5} \tag{5.16}$$

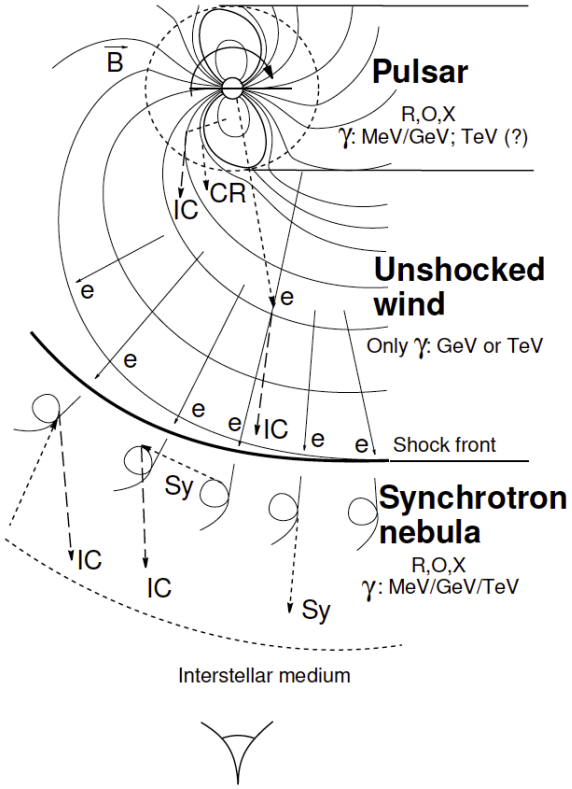

Figure 5.13: Sketch of the acceleration mechanisms inside a PWN and regions where they take place. Image from Aharonian (2004).

that is dependent of the magnetic field and the energy of the electrons. The size of the nebula is inversely proportional to the frequency, although this effect is significant only in PWNe with high magnetic fields like the Crab.

The synchrotron emission from a PWN comes from the region after the *termination shock*. Radio emission is characterized by a "flat" power-law distribution such that $S_\nu \propto \nu^\alpha$, being S_ν the flux density at a frequency ν and α the spectral index of the source, which takes values between $-0.3 < \alpha < 0$. There is an intrinsic spectral break at IR-to-optical frequencies, although an extra spectral component at these energies may be generated by dust emission, as can be seen in the Far Infrared (FIR) emission of the Crab Nebula shown in Figure 5.14. At X-ray frequencies, the emission is well-described by a power-law with a flux $F \propto E^{-\Gamma}$ with $\Gamma \sim 2$. An example of the broadband synchrotron emission of a PWN can be seen in Figure 5.14.

5.4.1.2 Inverse Compton emission

IC up-scattering of Cosmic Microwave Background (CMB), IR, optical-to-UV and X-ray photons can in principle happen all over the extension of the nebula (including *shocked and unshocked wind*). The IC emission of a PWN can be modeled using mainly three photon fields: the synchrotron radiation, that generates the Synchrotron Self Compton (SSC) process, dominant in

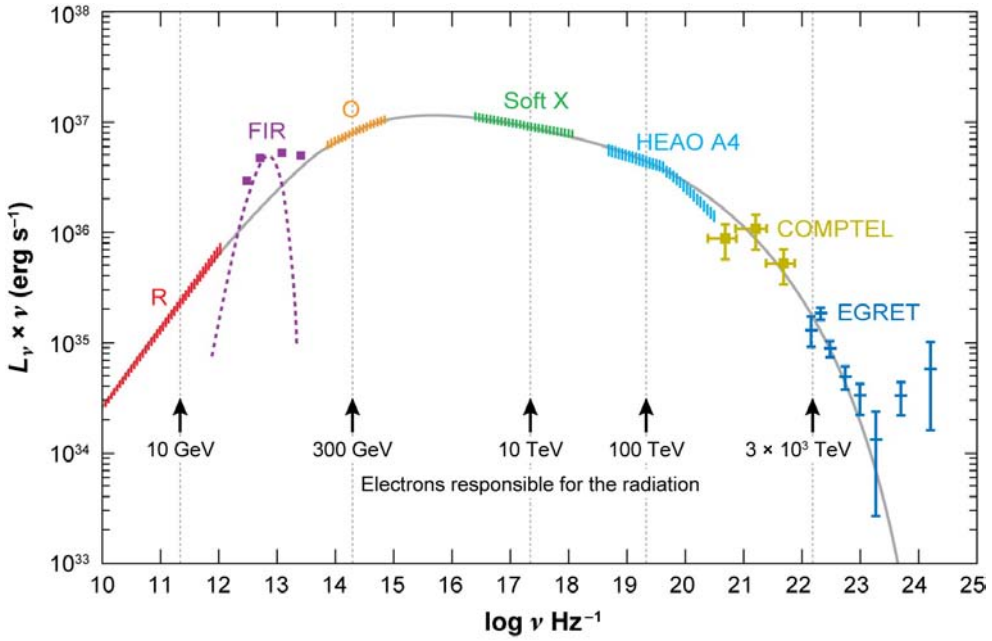

Figure 5.14: Synchrotron spectrum of the Crab Nebula. The grey solid line corresponds to the synchrotron emission of the nebula. The magenta dotted line represents the additional component produced by dust. Figure taken from (Gaensler & Slane 2006).

young PWNe ; the CMB, uniformly distributed in the whole nebula; and the FIR from galactic dust. A plot of the Crab Nebula IC emission of the Crab Nebula is shown in Figure 6.4.

IC emission becomes important for middle-age PWNe. Since high-energy synchrotron e^- lose their energies faster than those at lower energies, the population of the lower energies increases. TeV γ-ray photons require lower energy synchrotron e^-, therefore one expects to observe more radiation originated by IC for this type of sources.

VHE γ-ray emission from PWNe The VHE γ-ray emission of PWNe has its origin in the non-thermal IC scattering of the aforementioned photon fields present in the nebula. The first PWN discovered at VHE gamma rays was the Crab Nebula (Weekes et al. 1989) back in 1989. 26 years later there are more than 20 PWNe and PWN candidates detected at VHE (see Table B.9 in Appendix B.5).

These detections usually coincide with the falling part of the IC spectrum, so the emission is well-described by a single power-law with spectral indices between $1.3 < \Gamma < 2.8$. This is not the case for Crab, detected by MAGIC down to $\sim$ 50 GeV and whose spectrum has a more complex shape, such as a log-parabola (Aleksić et al. 2014g), or a different function as proposed in Aleksić et al. (2014e). At the highest energies the spectrum should curve due to the transition to the Klein-Nishina regime, but we need strong sources as the Crab to be able to measure this curvature.

5.4.2 Models

There have classically been two different approaches for modeling the emission of PWNe. On one hand, Magnetohydrodynamic (MHD) simulations succeed on explaining the morphological properties of PWNe. On the other hand, spherically symmetric one-dimensional PWNe spectral models do not take into account the energy-dependent morphology of the PWN, but successfully explain the spectrum. We will briefly describe both approaches.

5.4.2.1 MHD models

Kennel & Coroniti (1984b) were the first presenting a model that reproduced the morphological and spectral properties of PWNe through MHD simulations. The model consisted on solving the analytical equations for the pulsar wind in the simplified case of a symmetrically spherical MHD flow. The solution depends on the magnetization parameter σ, the spin-down power and the radius of the termination shock. The injection spectrum considered is a power-law with a cut-off that fits the observed spectrum. To calculate the synchrotron emission electron adiabatic and synchrotron losses are taken into account. The photon fields used as targets to calculate IC emission are synchrotron photons and dust IR emission. Several variations of the model using the same approach were later proposed (de Jager & Harding 1992; Atoyan & Aharonian 1996; de Jager et al. 1996; Hillas et al. 1998; Meyer et al. 2010) to account for different phenomena inside the nebula.

5.4.2.2 One-dimensional spectral models

There are also several models that make a one-dimensional approach without taking into account any energy dependence in the PWN morphology. Aharonian et al. (1997a) applied the diffusion-loss equation (solved for the first time by Syrovatskii (1959)) to study the IC emission from PWNe. To correctly account for the evolution of the lepton population inside the nebula, one has to introduce a time parameter in the equation. Some time-dependent models apply different approximates such as neglecting the escape term (Tanaka & Takahara 2010), or substituting the energy losses by the particle's escape time (Zhang et al. 2008), while others make no approximations (Martín et al. 2012). The photon contributions considered to calculate the broadband spectrum are also diverse, although Martín et al. (2012) considers all of them: synchrotron emission, synchrotron self-Compton, IC, and bremsstrahlung. A more detail explanation about several of the time-dependent models is given in Section §7.3.1.

6

The Crab Nebula: a gamma-ray factory in our backyard

6.1 Introduction

The Crab Nebula is the remnant of the SN explosion in 1054 AD reported by Japanese and Chinese astrologers (Ho & Ho Ping-Yü 1962). The "new star" was visible during daytime for several weeks, and in the night sky for 22 months (Clark & Stephenson 1977). The remnant was discovered by the English astronomer John Bevis in 1731 and became the first object in Charles Messier's catalog of nebulae and star clusters. The name of the nebula was given by William Parson, third Earl of Rosse in 1850, who found the similarity with the crustacean the first time he looked at the nebula as it can be seen in the drawing he made in Figure 6.1. Lundmark (1921) and Hubble (1928) proposed that the Crab Nebula was associated with the SN explosion in 1054, but it was not until 1941 when the Crab was unambiguously established as the remnant of the SN 1054 (Duyvendak 1942; Mayall & Oort 1942) (an optical image of the Crab can be seen in Figure 6.2). The Crab is placed at a distance of ~2 kpc (Trimble 1973) and its composition can be divided in several observables. Let us go in detail over its different components:

Figure 6.1: Lord Rosse's drawing of the Crab Nebula.

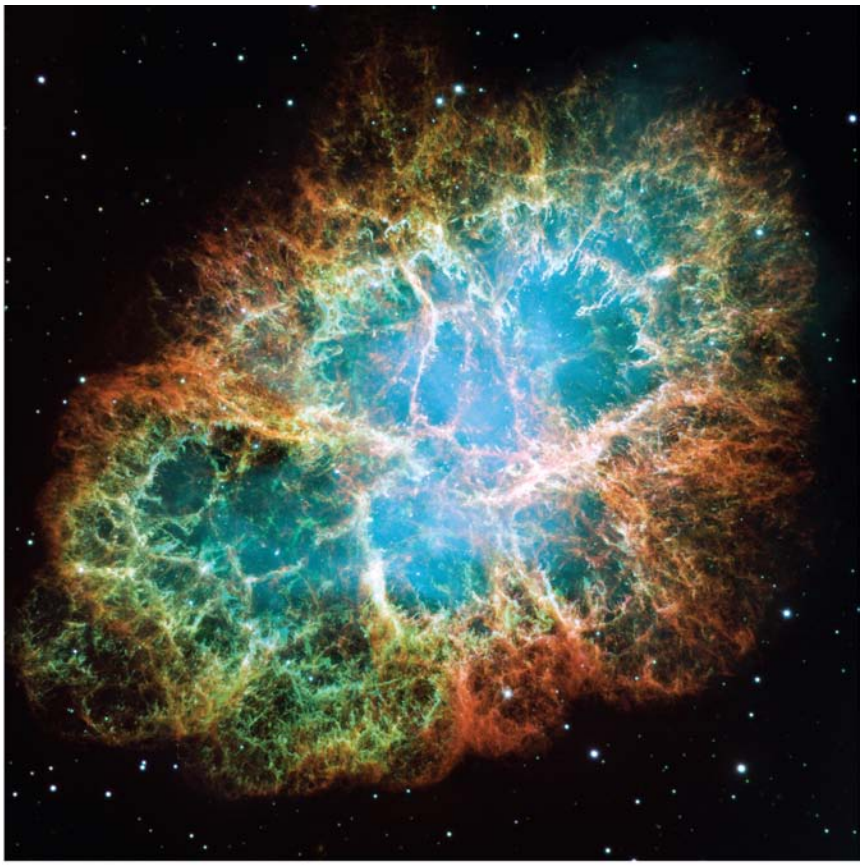

Figure 6.2: Optical image of the Crab Nebula by the Hubble telescope. Image from Hester (2008).

⊙ The Crab pulsar

The Crab pulsar (also known as PSR J0534+2200), located at the center of the SNR, is the engine that powers the nebula. It was discovered in radio by the Arecibo telescope (Staelin & Reifenstein 1968; Comella et al. 1969). It has a period P=33 ms and its first derivative is $\dot{P}$ =4.21 $\times 10^{-13}$ s s^{-1}. If we assume that the radius of the neutron star is ∼10 km and its mass 1.4 $M_{\odot}$, the pulsar's spin-down power is $L_{\text{spin-down}} = 4\pi^2 I \frac{\dot{P}}{P^3} = 5 \times 10^{38}$erg s^{-1}. Lyne et al. (1988) assumed a breaking index n=2.51 and calculated that the initial period of the pulsar was ∼19 ms, meaning that it has lost 3.6 $\times 10^{49}$ erg since its origin, which is less than 10% of the energy of the SN explosion that gave birth to the pulsar (assuming the fiducial value of 10^{51} erg). One has to mention that most of the rotational energy lost by the neutron star is not emitted in the form of pulsed emission, but it is carried away by a highly magnetized plasma. The Crab pulsar is detected at wavelengths ranging from radio to VHE gamma rays. It is characterized by a two-peaked light-curve with peaks varying across the electromagnetic spectrum in relative height but not in phase. After the aforementioned radio detection, pulsed emission was discovered from the Crab in optical (Cocke et al. 1969), X-ray (Fritz et al. 1969; Floyd et al. 1969) and γ-ray (Browning

et al. 1971; Kurfess 1971; Albats et al. 1972) wavelengths (see Figure 6.3 for a broadband spectrum). At VHE gamma rays the detection of pulsed emission from the Crab turned out to be more difficult, and it was not until 2008 when MAGIC discovered it (Aliu et al. 2008). The detection of pulsed emission at such energies ruled out pulsed emission models as the polar-cap where the production of the pulsed radiation is too close to the pulsar to achieve the energies measured. The VHE spectrum was first extended by VERITAS and MAGIC up to 400 GeV (Aliu et al. 2011; Aleksić et al. 2012b) and very recently, up to TeV energies by MAGIC (Zanin 2014). To achieve such high energies on the pulsed emission constrains the emission region to be at a larger distance than the predicted by most of the models. The MAGIC collaboration has also reported VHE γ-ray emission from the so-called *bridge* region, or region between the two peaks of the light-curve (Aleksić et al. 2014b).

⊙ **The Crab Nebula**

The PWN confined by the thermal ejecta from the SN is known as the Crab Nebula. It will be described in more detail in Section §6.2.

⊙ **The filaments and the shell**

A third component of the SNR are the filaments that are visible in the outer ring of the nebula of Figure 6.2. They form a cage where the PWN is confined. The last component consists of freely expanding ejecta beyond the visible edge of the nebula. It has been a crucial part of all theoretical models for several years, but it has only recently been observed (Sollerman et al. 2000).

6.2 The Crab PWN

The pulsar wind is radiationless ("cold wind") until it interacts with the ambient medium in a shock, situated at a distance of about $3{\times}10^{17}$ cm from the pulsar. As the wind does not emit radiation, the only way to study it is the synchrotron nebula surrounding it. As mentioned in §5.2.3, (Kennel & Coroniti 1984a) derived a MHD model of the Crab where they could explain its synchrotron emission only in the case that the magnetization of the wind was very low (σ=0.003) in the moment of the shock. They assumed an equipartition value between the magnetic field and the particle energy, deriving a magnetic field of $B = 300\ \mu$G. In newer models explaining the broadband emission of the nebula, the magnetic field is between 100 and 300 μG (de Jager & Harding 1992; Atoyan & Aharonian 1996; Hillas et al. 1998; Meyer et al. 2010; Martín et al. 2012), values lower than the equipartition, but in agreement with those inferred by interpreting the hardening of the integrated spectrum of the nebula between the radio and the optical band and electron cooling (Marsden et al. 1984). At the outer edge of the synchrotron nebula, there is a second shock driven by the pressure of the synchrotron nebula into the thermal gas surrounding it.

The size of the synchrotron nebula is smaller for larger frequencies. This is interpreted as due to a cooling of the high-energy electrons. Features where the emission of the nebula increases

are known as *wisps*. They vary in timescales of days and can be seen in radio, optical and X-rays, but their positions vary with frequency.

6.2.1 The broadband spectrum of the Crab Nebula

Two spectral components are observed in the Crab Nebula: the *synchrotron* part and the *inverse Compton* one as it was described in §5.4.1. A broadband spectrum of the Crab Nebula and its pulsar is shown in Figure 6.3.[1]. We will have a dedicated description of the IC part of the spectrum in §6.2.1.1

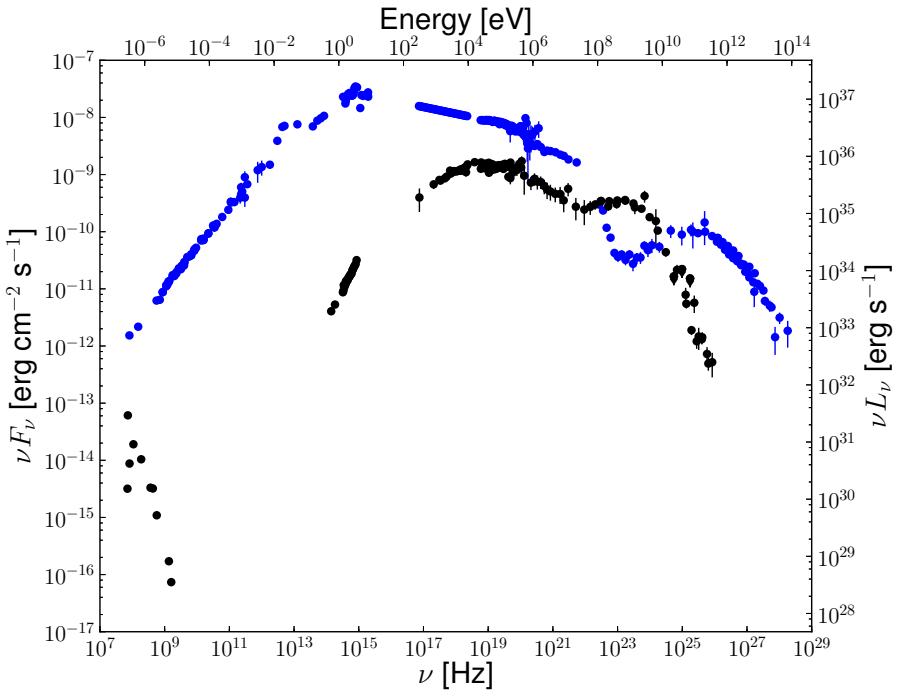

Figure 6.3: Broadband spectral energy distribution of the Crab Nebula (blue points) and the phase averaged emission of the Crab pulsar (black points). Plot taken from (Bühler & Blandford 2014)

6.2.1.1 The IC part of the spectrum

The Crab Nebula was discovered at VHE gamma rays (above 700 GeV) by the Whipple telescope, making it the first source detected by an IACT (Weekes et al. 1989). Since then, it is the standard candle in this energy band, having the highest flux amongst the steady VHE γ-ray sources. After Whipple discovery, the Crab has been used as a calibration source for the different telescopes using a similar technique. If we consider the latest MAGIC results on the Crab, its flux above 200 GeV is $2.3{\times}10^{-10}$cm^{-2}s^{-1}. This means that the γ-ray flux that current IACTs with

[1] A movie where you can see the dynamic of the synchrotron nebula in X-rays can be seen in http://chandra.harvard.edu/photo/2002/0052/animations.html

typical collection areas of the order of 10^9 cm^2 can detect is ∼4 gamma rays/minute (Aleksić et al. 2014g). With the current sensitivity of the MAGIC telescope and its low energy threshold, the Crab Nebula can be detected in less than a minute.

In the case of Crab, the emission measured by MAGIC overlaps with that measured by the *Fermi*-LAT satellite at MeV-GeV energies. One can clearly see the transition from the synchrotron-dominated emission (below 1 GeV) to the IC-dominated one (above 1 GeV) in Figure 6.4. Using MAGIC and *Fermi* data together, the energy of the IC peak can be determined. In Aleksić et al. (2014e), the IC peak was fit using several functions. For the fit using a log-parabola, the peak is at 53 GeV, although the range of the fit and the data used (MAGIC , *Fermi* or both), strongly influences its position. On the other hand, the fit does not have a high probability. This leads to the conclusion that the IC peak is not a well-defined feature of the Crab spectrum.

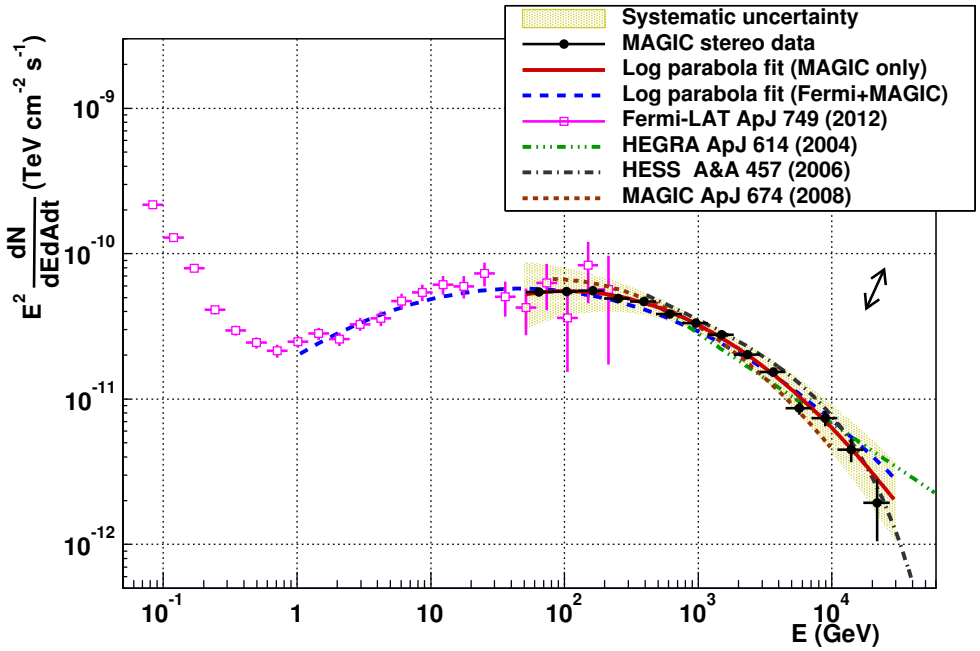

Figure 6.4: The IC part of the spectrum of the Crab Nebula (from (Aleksić et al. 2014e)). Magenta points are the results from *Fermi*-LAT analysis and black points the ones from MAGIC . The red solid line shows the fit of the MAGIC data by a log-parabola, while the blue dashed line, the fit of MAGIC and *Fermi*-LAT data together by a log parabola as well. The green dashed-tripple-dotted, black dashed-dotted and red-dotted lines show HEGRA, HESS and MAGIC previous fits respectively.

6.2.1.2 Spectra

In fact, the VHE spectrum measured by different IACTs show discrepancies at the highest energies:

1. The HEGRA collaboration used a **single power-law** to describe the spectrum between 500 GeV and 80 TeV (Aharonian et al. 2004b):

$$\frac{\mathrm{d}\phi}{\mathrm{dE}} = f_0 \left(\frac{E}{1\mathrm{TeV}} \right)^{-\alpha} \qquad [\mathrm{TeV}^{-1}\mathrm{cm}^{-2}\mathrm{s}^{-1}]$$

2. The HESS collaboration used a **power-law with an exponential cut-off**, as in Aharonian et al. (2006c) for energies between 440 GeV and 40 TeV:

$$\frac{\mathrm{d}\phi}{\mathrm{dE}} = f_0 \left(\frac{E}{1\mathrm{TeV}} \right)^{-\alpha} \exp\left(\frac{-E}{E_c} \right) \qquad [\mathrm{TeV}^{-1}\mathrm{cm}^{-2}\mathrm{s}^{-1}]$$

   where E_c is the cut-off energy.

3. The MAGIC collaboration used a **variable/curved power-law function** which is the best function that fits MAGIC data between 50 GeV and 30 TeV, due to the hardening at low energies (Aleksić et al. 2014e):

$$\frac{\mathrm{d}\phi}{\mathrm{dE}} = f_0 \left(\frac{E}{1\mathrm{TeV}} \right)^{-\alpha+\beta\mathrm{Log}_{10}(E/1\mathrm{TeV})} \qquad [\mathrm{TeV}^{-1}\mathrm{cm}^{-2}\mathrm{s}^{-1}]$$

   where β is the curvature of the function.

The parameters of each fit can be found in Table 6.1. A plot with the spectral points measured by the experiments, together with the spectral fit can be found in Figure 6.5.

Function	$\phi_0 \times 10^{-11}$ [TeV^{-1} cm^{-2} s^{-1}]	α	$\mathrm{E}_{\mathrm{cut}}$	β
Power-law	2.83±0.04	2.62±0.02	-	-
Power-law + exp. cut-off	2.26±0.08	2.39±0.03	14.3±0.01	-
Log-parabola	3.23±0.03	2.47±0.01	-	-0.24±0.01

Table 6.1: Different functions used to fit the VHE γ-ray spectrum of the Crab Nebula.

As it will be discussed in Section §6.2.1.3, a spectral softening at energies >10 TeV is expected due to the transition of the IC emission to the Klein-Nishina regime. Due to this transition, a power-law cannot be a suitable function to fit the VHE γ-ray spectrum of the Crab. In fact, if we take HEGRA data with their statistical errors only, fit them using the different functions and compare the goodness of the fits, we find that for a power-law (χ^2/Ndf=22.27/12), a power-law with a cut-off (χ^2/Ndf=13.47/11) and a log-parabola (χ^2/Ndf=12.23/11), the lowest fit probability is given by the power-law function.

6.2.1.3 Importance of the observation of the VHE tail of the nebula

The Thomson scattering is the elastic scattering of electromagnetic radiation by a free charged particle, as described by classical electromagnetism. It is just the low-energy limit of the Compton scattering: the particle kinetic energy and photon frequency are the same before and after the

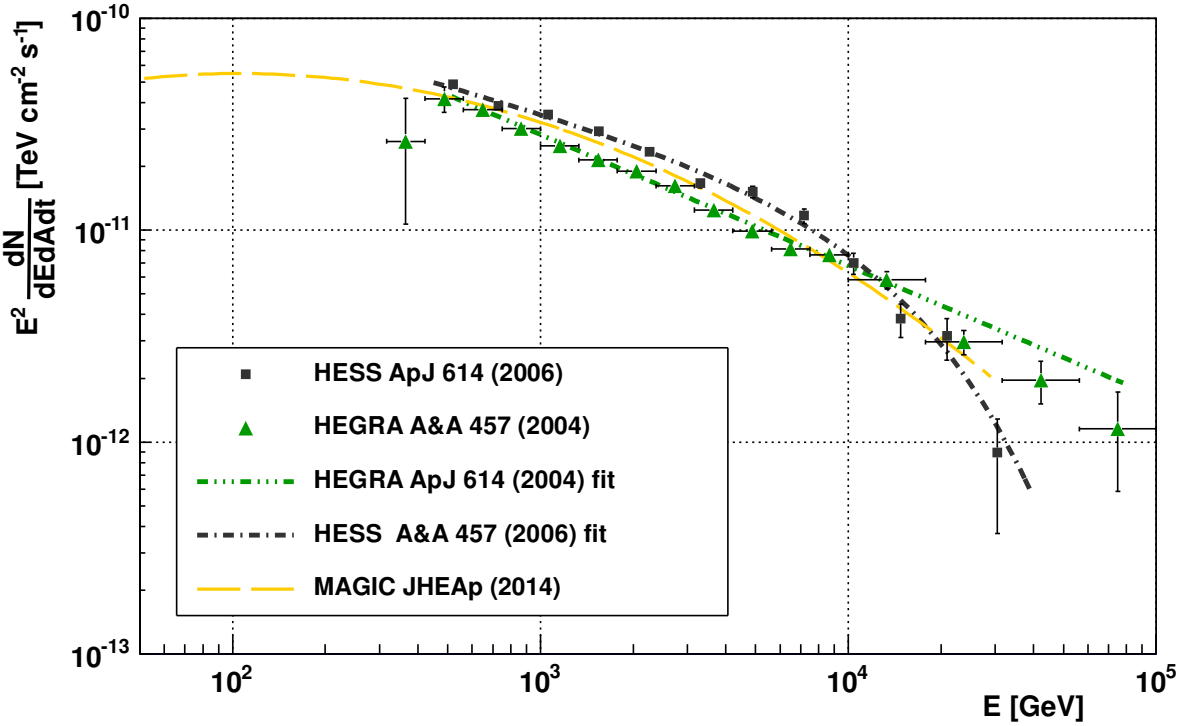

Figure 6.5: Spectral energy distribution of the Crab Nebula from the HESS, HEGRA and MAGIC telescopes.

scattering. This limit is valid as long as the photon energy is much less than the mass energy of the particle: $\nu << mc^2/h$ where ν is the frequency of the scattered photon, m the mass of the scattering particle, c the speed of light and h the Planck constant. IC here is equally treated as the Compton scattering. If we reach higher energies, quantum effects have to be taken into account using the Klein-Nishina formula, which gives the differential cross section of photons scattered from a free electron in lowest order of Quantum Electrodynamics (QED).

The motivation of the work presented here is to study the transition from the regime where the IC scattering of electrons with synchrotron photons is still classical (Thomson regime) to the regime where one has to take into account the QED effects (Klein-Nishina regime, Klein & Nishina 1929). Since the energy of the synchrotron electrons producing the IC scattering observed at VHE gamma rays can be of several hundred of TeV (see Figure 5.14), according to the aforementioned condition to be in the Thomson regime, we should start to measure effects on the spectrum due to the transition to the Klein-Nishina regime for energies above ~10 TeV. The measurement of this transition is very important to unveil the energy up to which the electrons are accelerated inside the nebula. As a final remark, the detection of persistent emission above a few tens of TeV might be caused by efficient acceleration of hadrons in the nebula, expected to be emitting gamma rays with energies > 10 TeV as it was proposed in Bednarek & Bartosik (2003); Horns et al. (2006); Amato et al. (2003)

6.2.1.4 Models

As we said in Section §5.4.2, there are two main approximations for modeling PWN broadband emission: On one hand we have models based on MHD simulations that reproduce the morphology and spectrum of the PWNe, and on the other hand we have symmetric one-dimensional models for the evolution of PWNe. The models explaining the emission from PWNe usually use the Crab to calibrate their parameters, so we refer the reader to Section §5.4.2 for further information about these approaches and some of the models derived from them. For the purpose of this work, we will extend the interpretation of MAGIC data in Aleksić et al. (2014e) in the framework of Meyer et al. (2010); Martín et al. (2012) models.

6.2.2 Variability

Optical variability from the Crab Nebula on monthly time scales has been known for long time (Lampland 1921). The integrated flux of the nebula varies by only $\sim$1 % per year in the radio, optical and X-ray ranges (Vinyaikin 2007; Smith 2003; Wilson-Hodge et al. 2011). The cooling time of $e^{\pm}$ emitting at higher than X-ray energies is of the order of years. The emission at these energies is therefore subject to a larger variability.

The discovery by *Fermi*-LAT and AGILE of enhanced emission from the Crab Nebula at relatively low energies > 100 MeV (Tavani et al. 2010; Buehler et al. 2010) and time scales of the order of hours was unexpected. This emission reaches up to 30 times the steady unpulsed flux of the Crab Nebula above 100 MeV on time scales down to 6 hours (Abdo et al. 2011; Tavani et al. 2011), meaning that the emission region should be smaller than 10^{-4} pc. Unfortunately, due to the angular resolution of the *Fermi*-LAT satellite at these energies, the Crab Nebula cannot be resolved, therefore the region of emission of the flares remains unknown. As of November 2014, nine flares have already been reported (Buehler et al. 2012; Ojha et al. 2012; Mayer et al. 2013; Striani et al. 2013; Buson et al. 2013; Gasparrini & Buehl 2014; Becerra et al. 2014). No enhancement of the emission has been detected at other wavelengths than HE gamma rays and no enhancement on the pulsed γ-ray emission of the Crab has been found either.

Observation of previous flares by IACTs did not produce any report of enhanced emission (Mariotti 2010; Ong 2010). Moreover, HESS and VERITAS also observed the Crab during the March 2013 flare that will be discussed in this chapter and did not find any flux enhancement (Abramowski et al. 2014b; Aliu et al. 2014). ARGO-YBJ collaboration reported several enhancements of emission at TeV energies coincident with flaring periods at HE (Aielli et al. 2010; Bartoli et al. 2012; Vernetto 2013), but they reanalyzed their data samples very recently and did not find any significant flux variability (Bartoli et al. 2015).

6.2.2.1 Models

The origin of the flares is still a mystery, although it seems that synchrotron emission is the only process that can account for the flaring emission. IC and bremsstrahlung electron cooling times are much longer than the duration of the flares, but the synchrotron cooling time of the electrons in the Crab can be of the order of the duration of the emission (Abdo et al. 2011).

Particles accelerated in MHD flows can only reach maximum energies of ∼160 MeV, so the only explanation is that either MHD conditions are not valid in the flaring region or that the emission is boosted toward us. MHD conditions are broken in magnetic reconnection events and beaming of particles occurs in the reconnection layer (Zweibel & Yamada 2009; Cerutti et al. 2012; Uzdensky et al. 2011; Sturrock & Aschwanden 2012). Diffusive shock acceleration does not produce the hard spectra observed and acceleration due to absorption of ion cyclotron waves is expected to act on long time scales. Magnetic reconnection was studied in the context of the flares and the spectra and evolution could be reproduced by Cerutti et al. (2013), being therefore the favored mechanism responsible for the particle acceleration during Crab Nebula flares. If the origin of the HE flares is due to variations in the electric and magnetic field of the PWN, this would have no effect in the IC component of the Crab, but if the flares are caused by an increase in the lepton population, one would also expect a variation at the corresponding IC energies. This increase can go from 1% (Lobanov et al. 2011) to values larger than 100% depending on the model (Bednarek & Idec 2011; Kohri et al. 2012).

Since γ-ray flares from the Crab Nebula were discovered in September 2010, several models have tried to explain the emission enhancement at GeV energies, some of them also predicting a significant increase of the emission at TeV energies, in principle measurable by the current generation of IACTs. Bednarek & Idec (2011) presented a model that explains the flare emission as a new population of electrons accelerated in the region behind the shock as a result of the reconnection of the magnetic field. They assume that the flaring region is moving relativistically towards the observer to account for the short time scales measured. The target photon fields for IC they consider are only the CMB and the synchrotron photons from the nebula. They assume different parameters for the spectrum of the injected electrons and a magnetic field of 2 mG. If only the break energy in the electron spectrum changes, the enhancement of the emission at TeV energies is very low and out of the reach of current IACTs due to the large systematic errors that affect the measurements. On the other hand, they predict a measurable increase in the TeV emission in the case that the break energy in the electron spectrum changes together with a flattening of the electron spectrum. This extra component has a ∼25% larger flux at 1 TeV than the quiescence one if the magnetic field in the flaring region is 40 mG. This difference increases with the energy and reaches ∼4 times the quiescence Crab flux at 10 TeV. Finally, they also propose that the difference between the Crab Nebula spectra measured by the different experiments (HESS and HEGRA) might come from different stages of electron acceleration in the nebula.

Kohri et al. (2012) consider that the flare is produced in a small blob of the synchrotron nebula that is Lorentz boosted towards us. The maximum energy of the synchrotron e^- is not violated due to the mentioned Lorentz boosting. They predict an increase in the IC component a factor Γ^2 ($\Gamma \equiv$ Lorentz factor) larger than the synchrotron one due to the boosting of the target photon field. They considered a "fiducial" model with a magnetic field $B = 223\ \mu$G and Γ=100 and predict an enhancement of the VHE γ-ray emission above 10 TeV of $\gtrsim$ twice its quiescence value.

6.3 Observations with MAGIC

The study of the Crab Nebula performed in this work seeks a twofold objective: on one hand, study the spectral shape at energies > 10 TeV and on the other hand, study the variability of the Crab Nebula during the flare that took place in March 2013.

6.3.1 Crab at high Zd

To achieve a better performance at higher energies it is essential to have the largest possible collection area. MAGIC with two telescopes cannot compete with four or five-telescope arrays such as VERITAS or HESS at energies above 1 TeV observing at low Zd. What one can do is to increase the collection area by observing at high Zd, by paying the price of increasing the energy threshold as we can see in Figure 6.6.

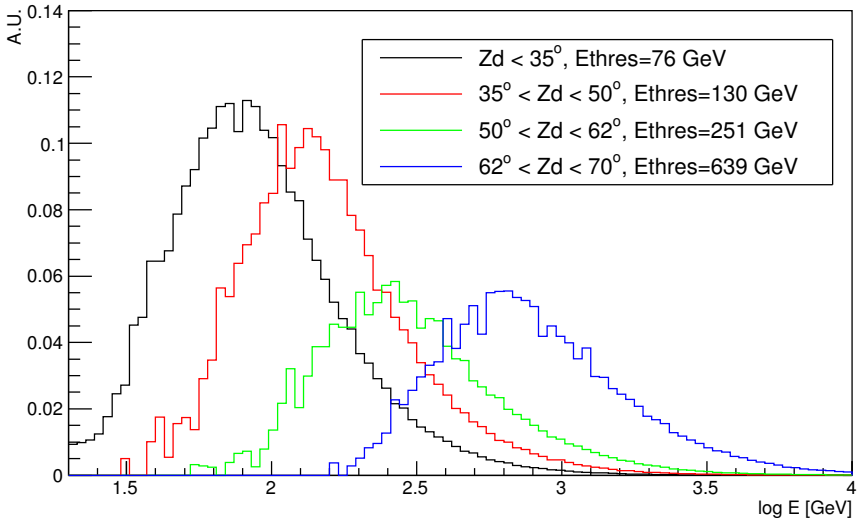

Figure 6.6: True energy distribution of MAGIC MC γ-ray events for different ranges of Zd. The energy threshold is conventionally defined as the energy of the peak of the distribution.

If we are interested in TeV energies, we can point the telescopes to high Zd to increase the collection area at the studied energies (see Figure 6.7). This increase translates on a better performance of the telescope at Zd > 50° for energies larger than 5 TeV with respect to the performance at lower Zd, as it can be seen in Figure 6.8.

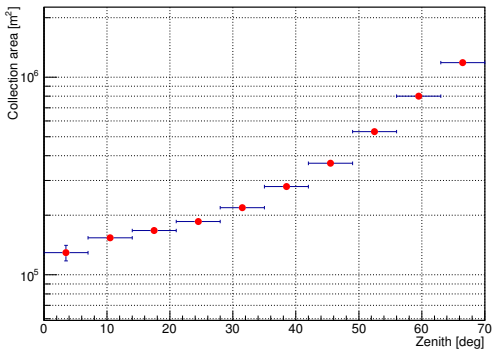

Figure 6.7: Collection area as a function of the Zd at 10 TeV.

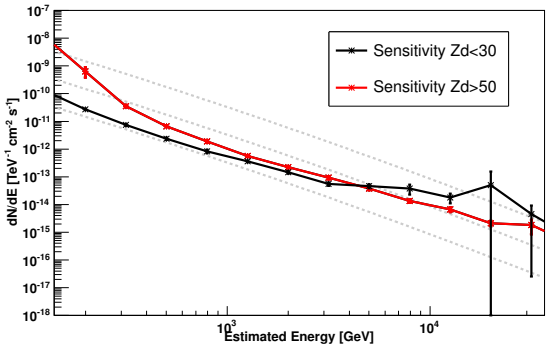

Figure 6.8: MAGIC differential sensitivity for Zd > 50° (red points) and Zd < 30° (black points).

6.3.2 Data sample and analysis procedure

MAGIC observed the Crab Nebula at high Zd (Zd > 50) in the period between November 2012 and April 2014. A summary of the observations can be found in Table B.4. For the observations at high Zd, we observed a total of 68.94 hours, but only 39.6 hours were left after data quality selection based on atmospheric conditions and technical problems.

We observed the Crab during the March 2013 flare for a total of 23.27 hours at Zd ranging from 5.9 to 70.3 degrees. Unfortunately, due to very bad weather conditions those days at the telescope site, only 3.79 hours from 11 and 12 of March were left after data quality selection. A breakdown of the of the observations during the March 2013 Crab flare at all Zd can be found in Table B.5. We compare this flaring data sample with that of data previously taken under the same Zd conditions. A plot with the flux detected by Fermi above 100 MeV, together with the MAGIC observation windows is shown in Figure 6.9.

The data were analyzed using the standard MAGIC analysis (see §2.2.3). The data sample used to calculate the Crab spectrum presented in this work expands over 3 observation periods with slightly different performance of the telescope. For each of the observation periods a different MC simulation matching the telescope performance is used.

6.3.3 Energy spectrum

The MC simulations reach an energy of 80 TeV. To take into account the effect of the bins with energies > 80 TeV due to the energy bias, we extrapolated the migration matrix and the collection area of the last bin where we have MC data. (see Figures 6.10 and 6.11). We checked the effect of applying this estimation by computing the different spectra without extrapolating the migration matrix and the collection area and the effect was negligible.

To take into account the energy resolution and energy bias of the telescope, the spectrum was unfolded using different algorithms (Bertero, Tikhonov and Schmelling, see Albert et al. (2007)). Since a single power-law, as expected, is not giving a good fit to the data (χ^2/NDF=31.86/9), in this work we show the fit of the unfolded spectrum using a log-parabola and a power-law with

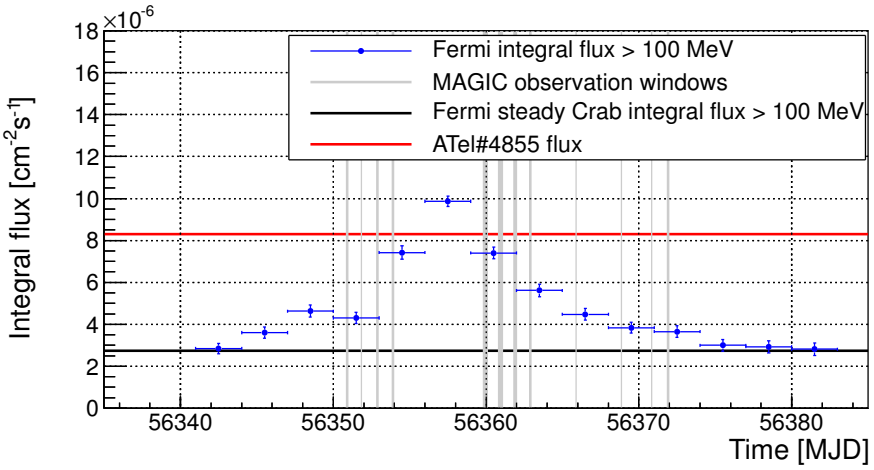

Figure 6.9: *Fermi*-LAT light curve above 100 MeV (blue points) of the Crab flare in March 2013 including MAGIC observation windows (grey lines). The black line points the *Fermi*-LAT steady flux above 100 MeV and the red one the flux reported in the ATel#4855 by the *Fermi* collaboration Ojha et al. (2013).

a cut-off. The unfolded spectra with the different fits are shown in Figure 6.12. The best-fit parameters, together with the goodness of the fit for the different unfolding methods and the two functions considered can be seen in Table 6.2. As we can see, all the unfolding methods agree within statistical errors.

Log-parabola fit					
Unfolding method	f_0 [TeV^{-1} cm^{-2} s^{-1}]	α	$E_{\rm cut}$ [TeV]	β	χ^2/NDF
Schmelling	$(3.03 \pm 0.04) \times 10^{-11}$	2.46 ± 0.04	-	-0.19 ± 0.04	3.52/8
Tikhonov	$(3.06 \pm 0.05) \times 10^{-11}$	2.47 ± 0.05	-	-0.17 ± 0.05	2.87/7
Bertero	$(3.06 \pm 0.04) \times 10^{-11}$	2.47 ± 0.04	-	-0.18 ± 0.04	2.38/7
Cut-off fit					
Schmelling	$(3.12 \pm 0.04) \times 10^{-11}$	2.49 ± 0.03	30 ± 8	-	5.27/8
Tikhonov	$(3.16 \pm 0.05) \times 10^{-11}$	2.50 ± 0.04	31 ± 11	-	5.69/7
Bertero	$(3.15 \pm 0.05) \times 10^{-11}$	2.49 ± 0.04	30 ± 10	-	5.54/7

Table 6.2: Crab Nebula spectral fit parameters for the different unfolding methods and two different functions used to fit the results of the observations at Zd>50°.

Although the log-parabola (with probability ~90%) gives a better fit than the power-law with a cut-off (with probability ~60-70 %), both functions give a good fit to the data. In addition, if we add the systematic uncertainty (Aleksić et al. 2014g), this probability increases. A plot comparing the results from the previous published experiments together with the results reported in this work for the Bertero unfolding (the one with the lowest χ^2) can be seen in Figure 6.13.

Due to the systematic uncertainty, one cannot rule out the possibility that MAGIC data is fit either with a power-law or with a power-law with a cut-off. What we can evaluate is, given HESS

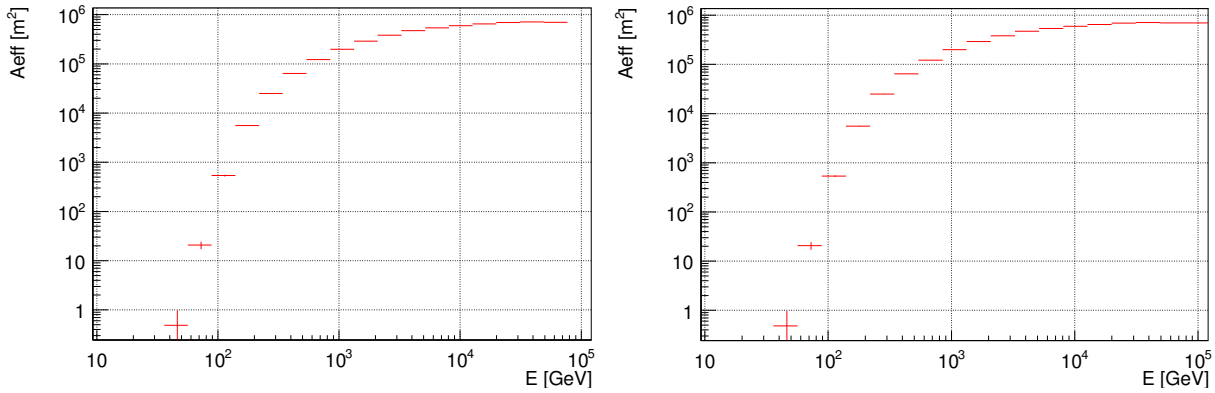

Figure 6.10: Non-extrapolated (left panel) and extrapolated (right panel) collection area for MC gamma rays.

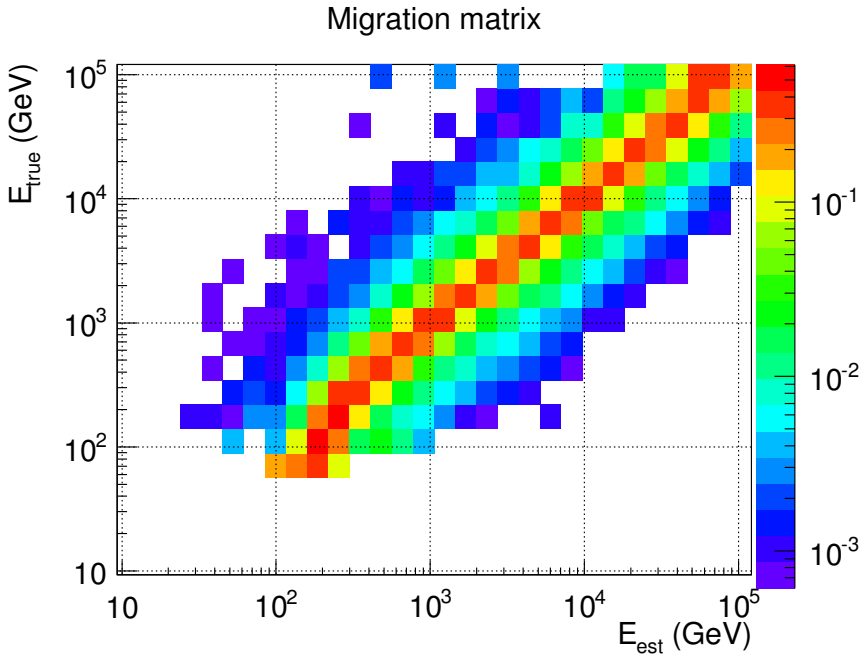

Figure 6.11: Migration matrix for the Crab Nebula observations at Zd > 50°.

and HEGRA fit functions, the probability that the number of events measured by MAGIC is compatible with one of those functions. To do it, we use a toy MC that takes the number of events in bins of estimated energy, the migration matrix between different energy bins, the collection area in bins of the true energy of the MC and the observation time. For every iteration of the toy MC, we use the collection area, time, migration matrix and assumed function to calculate the number of events that would be detected in every energy bin. We assume that the events follow a poissonian distribution and generate them using the poissonian probability. To account for the MAGIC systematic error, we assume an additional systematic uncertainty in the flux depending

on the energy range where the energy bin is (18 % for $E < 100$ GeV, 11 % for 100 GeV$< E < 1$ TeV and 16 % for $E > 1$ TeV). The distribution of generated events for every energy bin is what we compare with the events measured by MAGIC and calculate the probability that this number of events measured is compatible with the assumed function. An example of the distribution of generated events together with the measured value can be seen in Figure 6.14. In Table 6.3 we can find a summary of the results of the toy MC for energies above 34 TeV.

Function assumed	$N_{\text{meas.}}$	$< N_{\text{exp.}} >$	Probability [%]	σ
HEGRA	41.1	30.94	26.5	1.12
HESS	41.1	16.84	1.4	2.45

Table 6.3: Results from the toy MC for $E > 34$ TeV assuming a power-law (HEGRA) and a power-law with a cut-off (HESS). We give the number of events measured by MAGIC above this energy, the mean expected number of events according to the toy MC, the probability that this measurement is compatible with the assumed function and the corresponding significance.

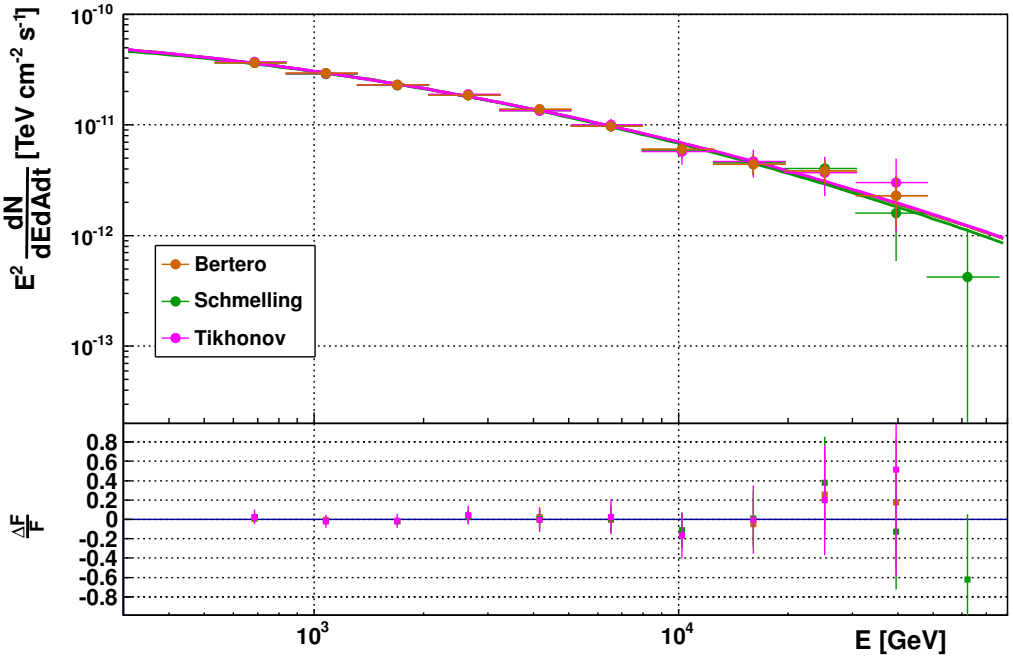

(a)

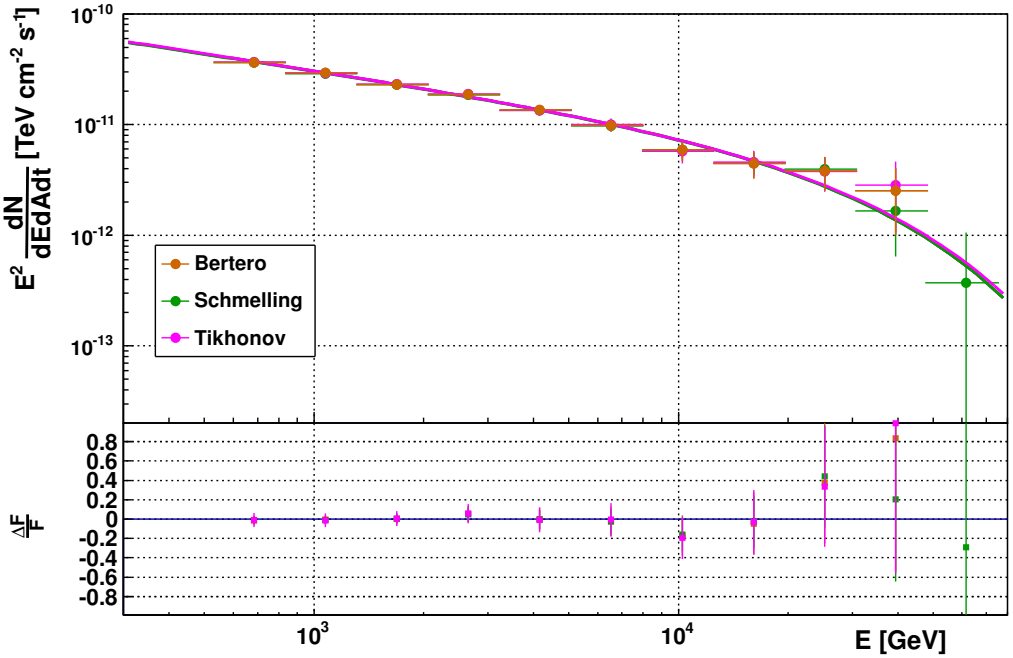

(b)

Figure 6.12: Crab Nebula SED measured by MAGIC during observations at Zd > 50° using three different unfolding methods. Figure (a) shows the result for a log-parabola fit (top panel) and its residuals (bottom panel). Figure (b) shows the result for a power-law with a cut-off (top panel) and its residuals (bottom panel).

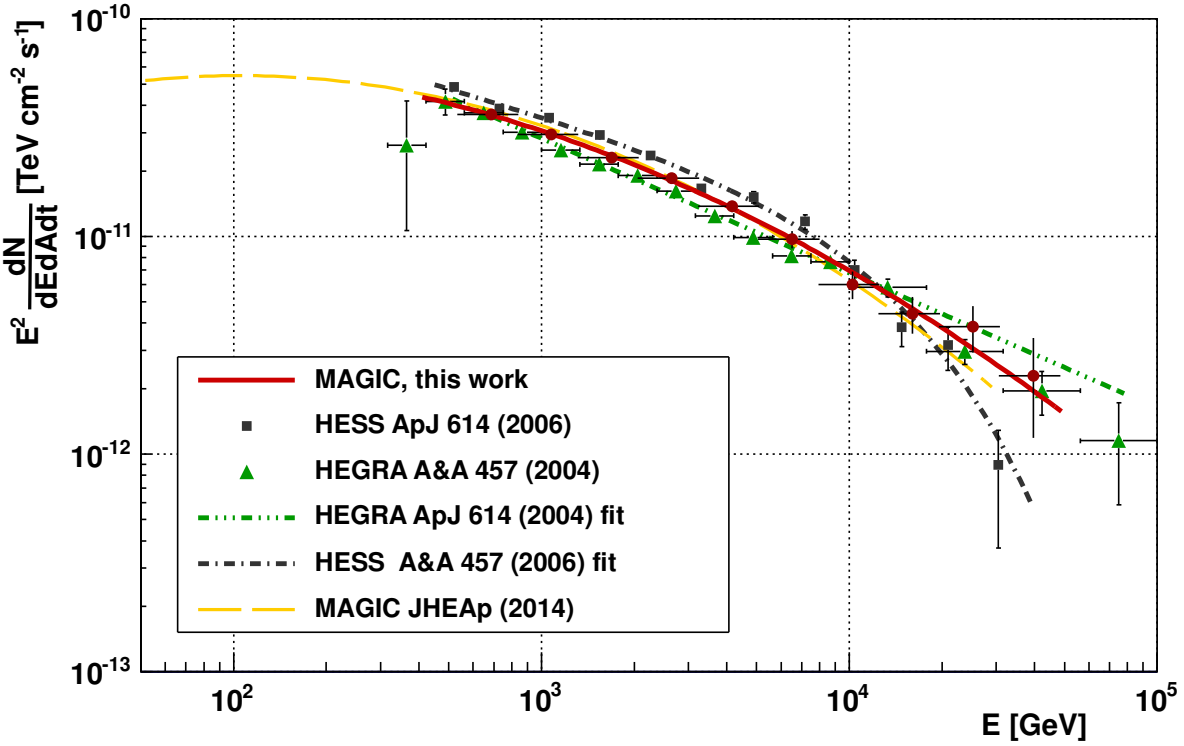

Figure 6.13: Comparison between the published Crab Nebula SEDs from different experiments and the results reported in this work.

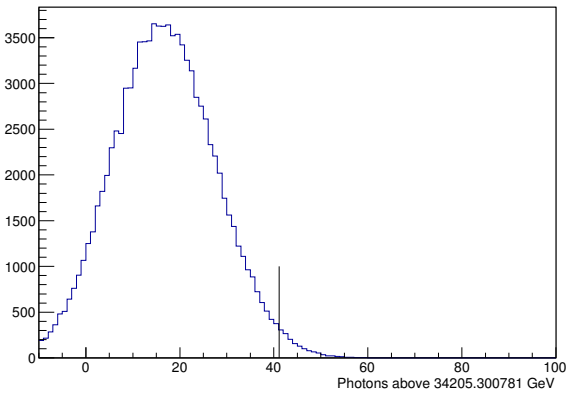

Figure 6.14: Example of the toy MC distribution of events with energies above 34 TeV assuming the power-law with a cut-off from Aharonian et al. (2006c). The black line marks the measured number of events on the MAGIC data. The probability of measuring this number of events, assuming that the power-law with a cut-off is the function that describes Crab Nebula data, is 1.4%.

6.3.4 Flux variability

As it was mentioned in Section §6.2.2, one could expect an increase of the TeV Crab Nebula flux during the flaring nights at GeV energies. Apart from the "flaring" sample mentioned in Section §6.3.2, we selected a "non-flaring" sample, taken several days before the flare under the same Zd of the flaring days. The results for the SED of the "flaring" and "non-flaring" sample are shown in Figure 6.15. Both curves are fit with a log-parabola function. A comparison of the fit parameters for the flaring and non-flaring days can be seen in Table 6.4. We can check that the results for all the parameters are compatible within statistical errors. The last spectral point is at ∼15 TeV and it is also constant for both data samples.

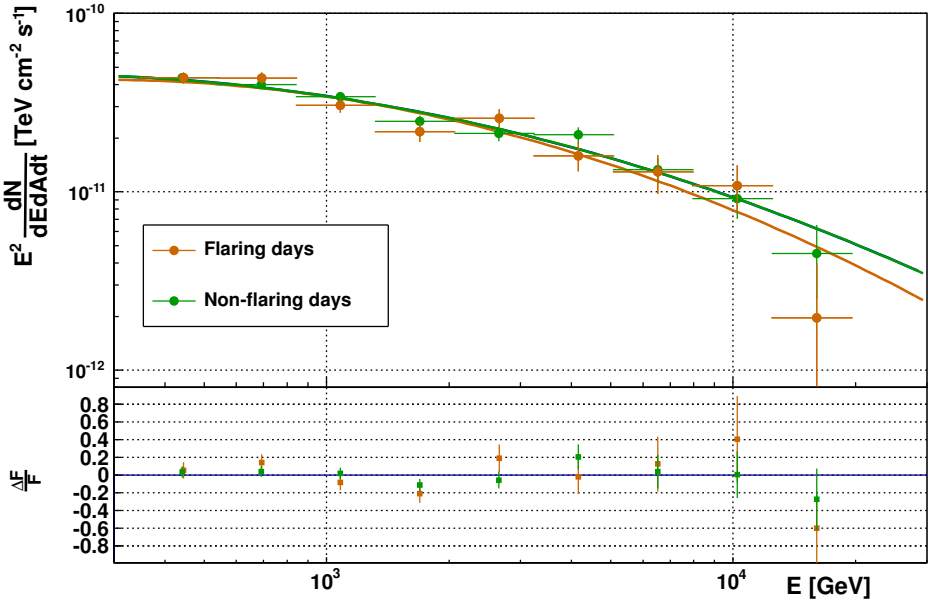

Figure 6.15: Crab Nebula SED during flaring and non-flaring days. In orange we have the points and fit to the flaring days and in green we have the points and fit to the non-flaring ones. In the lower panel we find a plot of the fits residuals.

	f_0 [TeV^{-1} cm^{-2} s^{-1}]	α	β	χ^2/NDF
Non-flaring days	$(3.44 \pm 0.08) \times 10^{-11}$	2.34 ± 0.02	-0.23 ± 0.05	8.08/7
Flaring days	$(3.42 \pm 0.10) \times 10^{-11}$	2.34 ± 0.03	-0.30 ± 0.07	13.40/7

Table 6.4: Crab Nebula fit parameters for flaring and non-flaring days.

We also studied the stability of the light curves above 1 and 10 TeV. We fit the daily integral flux of the flaring and non-flaring days. The fit above 1 TeV has a χ^2/Ndf = 7.3/6 and above 10 TeV has a χ^2/Ndf = 6.7/6, corresponding to a fit probability of 30 % and 35 % respectively. The light curves above 1 and 10 TeV are shown in Figure 6.16. The daily fluxes, the observation times and the results for the fits can be found in Table 6.5.

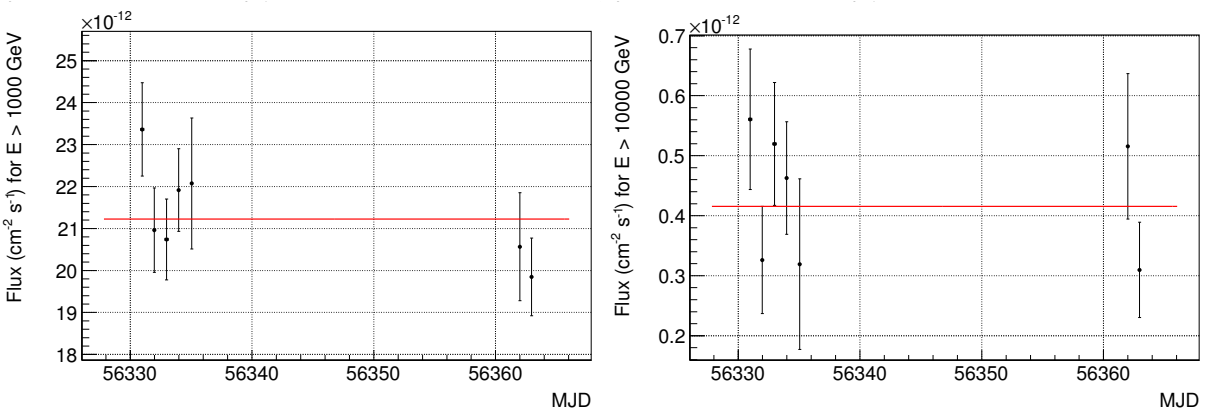

Figure 6.16: Crab Nebula light curve for energies above 1 TeV (left) and 10 TeV (right) of the period before (MJD< 56340) and during the flaring period of March 2013 (MJD> 56360).

Using the results of the fit for the flaring and non-flaring days, we compute the relative flux variation of the VHE data. Being F_{steady} the average flux for the non-flaring days and F_{flare} the average flux for the flaring days, the flux variation is given by:

$$\Delta F(E) = F_{\text{flare}}(E) - F_{\text{baseline}}(E) \tag{6.1}$$

Using the results from Table 6.5, the relative flux variation above 1 and 10 TeV is: $\Delta F/F_{\text{steady}}(E >$ 1 TeV)=-0.07±0.04 and $\Delta F/F_{\text{steady}}(E >$ 10 TeV)=-0.22±0.18. Using this relative flux variation, we can compute the UL on the flux of an additional component above 1 TeV and 10 TeV. If we assume that the relative flux change of the VHE component during flares has to be larger than 0, we can compute the 95% C.L. Bayesian UL using the formula:

$$\frac{\int_0^{x_{95}} \exp\left(-\frac{(\Delta F_E - x)^2}{2\sigma^2}\right) dx}{\int_0^{\infty} \exp\left(-\frac{(\Delta F_E - x')^2}{2\sigma^2}\right) dx'} = 0.95 \tag{6.2}$$

where σ is the error in the determination of ΔF_E. x_{95} is obtained by solving equation 6.2 and gives the UL to the additional component above a given energy. The solving of the integrals contained in equation 6.2 is explained in Appendix A.3. The flux ULs above an energy of 1 TeV and 10 TeV are shown in Table 6.6.

6.4 Discussion and conclusions

We tested different functions for the spectrum of the Crab Nebula in the energy range between 400 GeV and 80 TeV and we found that a single power-law does not provide a good description of the spectrum. Both log-parabola and power-law with a cut-off provide a good fit to the data, although the log-parabola provides a larger fit probability.

State	Date [MJD]	Duration of observation [s]	Flux ($E > 1$ TeV) [10^{-11} cm^{-2} s^{-1}]	Flux ($E > 10$ TeV) [10^{-13} cm^{-2} s^{-1}]
Steady	56330.99	10627.7	2.34±0.11	5.6±1.2
	56331.98	12179.6	2.10±0.10	3.3±0.9
	56332.98	12919.4	2.07±0.10	5.2±1.0
	56333.98	13037.0	2.19±0.10	4.6±0.9
	56335.05	3531.0	2.21±0.16	3.2±1.4
Flare	56362.00	4104.4	2.06±0.13	5.2±1.2
	56362.96	11154.1	1.98±0.09	3.1±0.8
	Fit non-flaring days		2.16±0.05	4.5±0.5
	Fit flaring days		2.01±0.08	3.5±0.7
	Fit all days		2.12±0.04	4.2±0.4

Table 6.5: Crab Nebula fluxes above 1 and 10 TeV for flaring and non-flaring days.

Energy [TeV]	ΔF_E UL	Flux UL [cm^{-2} s^{-1}]
> 1 TeV	0.8%	7.4×10^{-13}
> 10 TeV	13.3%	2.0×10^{-12}

Table 6.6: 95% C.L. flux ULs above 1 and 10 TeV for an extra component in the Crab Nebula spectrum during the March 2013 flare, expressed in absolute flux and relative to the steady Crab flux.

The measured spectrum is consistent with the measurement of HEGRA. The power-law with a cut-off gives a good description of MAGIC data in the energy range between 400 GeV and 80 TeV, but the cut-off energy is situated at an energy of 30 TeV, larger and not compatible within statistical errors with that measured by HESS. Using a toy MC and the MAGIC data, we can rule out HESS cut-off energy at a C.L. larger than 2 σ.

If we compare this result with the models used to fit the Crab Nebula spectrum between 50 GeV and 30 TeV in Aleksić et al. (2014e), we find that both models overestimate the Crab Nebula emission at $\sim$ TeV energies. We agree with the conclusion of the quoted paper that models have to be made more realistic to account for the broadband emission of the Crab Nebula.

Regarding the flux variability, we compare the daily light curve of the flaring days and the quasi-contemporaneous non-flaring days taken under the same conditions. We establish ULs at the 95% C.L. on the flux of an additional component at the level of 7.4×10^{-13} TeV cm^{-2} s^{-1} above 1 TeV and 2.0×10^{-12} TeV cm^{-2} s^{-1} above 10 TeV. A comparison of the spectra of the flaring and non-flaring days brings us to the same conclusion, having all the fit parameters the same results within the errors. If we assume that there is a linear correlation between the flare at MeV energies and a putative enhancement at TeV energies:

$$\Delta F_E\,[VHE] = C\;\Delta F_E\,[HE] \tag{6.3}$$

where C is a constant. The combined photon flux above 100 MeV from the Crab Nebula and

pulsar during the March 2013 flare is $F_{\rm flare}(12.5\pm0.8)\times10^{-6}$ cm^{-2} s^{-1} (Mayer et al. 2013), while the average nebula flux during the quiescence state is $F_{\rm nebula}(6.1\pm0.2)\times10^{-7}$ cm^{-2} s^{-1} and the average pulsar flux $F_{\rm pulsar}(20.4\pm0.1)\times10^{-7}$ cm^{-2} s^{-1} (Bühler & Blandford 2014). If we assume that the flare is produced by synchrotron emission in the nebula and we subtract the pulsar contribution to the nebula flare flux, we find that the relative increase of the Crab Nebula flux above 100 MeV is:

$$\Delta F_E\,[HE] = \frac{(F_{\rm flare} - F_{\rm pulsar}) - F_{\rm nebula}}{F_{\rm nebula}} = 17 \pm 3 \tag{6.4}$$

Therefore, the UL on the linear correlation between the Crab Nebula flux above 100 MeV and above 1 TeV during flares at a 95% C.L. is $C < 4.7 \times 10^{-4}$.

The flux ULs above 1 TeV and 10 TeV shown in Table 6.6 lead to ULs on the luminosity of an extra component during the March 2013 flare above the aforementioned energies of $L_{(E>1\rm TeV)} < 4 \times 10^{32}$ erg s^{-1} and $L_{(E>10\rm TeV)} < 10^{33}$ erg s^{-1}. Bednarek & Idec (2011) predict an increase larger than the UL reported in this work for several situations. According to their model, we can rule out magnetic fields larger than 40 mG in the flaring region because they would produce larger variations than measured. For lower magnetic fields and an injection of a new population of electrons with a change of their maximum energy together with a flattening of the spectrum, the prediction is also in conflict with the results we are reporting. We could argue that the magnetic field is significantly lower than 2 mG, although we have to note here that the magnetic field in the flaring region is given by the duration of the flare: the flaring time that an electron would emit synchrotron radiation is then:

$$t_{\rm flare} = 3 \times 10^5 {\rm s} \left(\frac{B}{\rm mG}\right)^{-1.5} \tag{6.5}$$

for electrons emitting gamma rays at 200 MeV. If we consider that the duration of the flare was $\sim$ 2 weeks, then the magnetic field of the flaring region should be $\sim$ 8 mG. We can conclude that, in the framework of Bednarek & Idec (2011) model, we have to consider an injection of electrons with a change only in their maximum energy, that could account for the flaring component at HE and would not produce any measurable enhancement at TeV energies.

In the context of Kohri et al. (2012) model, as we do not detect any variability above 10 TeV, we rule out a Γ boost of the flaring blob $\gtrsim$100, which is the one they take for their fiducial model.

7

The puzzling PWN 3C 58

7.1 General description

The SNR 3C 58 (SNR G130.7+3.1) has a flat radio spectrum and is brightest near the center, therefore it was classified as a PWN (Weiler & Panagia 1978). It is centered on PSR J0205+6449, a pulsar discovered in 2002 with the *Chandra* X-ray observatory (Murray et al. 2002). It was widely assumed that 3C 58 is located at a distance of 3.2 kpc (Roberts et al. 1993a), but recent H I measurements suggest a distance of 2 kpc (Kothes 2013). The age of the system was estimated to be $\sim$ 2.5 kyr (Chevalier 2005a) from the PWN evolution and energetics, however this is a matter of discussion that will be covered together with the distance estimation in Section §7.1.2. The pulsar has one of the highest spin-down powers known ($\dot{E} = 2.7{\times}10^{37}$erg s^{-1}). The PWN has a size of 9′×6′ in radio, infrared (IR), and X-rays (Bietenholz et al. 2001; Bocchino et al. 2001; Slane et al. 2004, 2008). Its X-ray luminosity is $L_{(0.5-10\,\mathrm{keV})} = 2.4 \times 10^{34}$ erg s^{-1}, which is more than 3 orders of magnitude lower than that of the Crab Nebula (Torii et al. 2000). 3C 58 has been compared with the Crab because the jet-torus structure is similar (Slane et al. 2004). Because of these morphological similarities with the Crab Nebula and its high spin-down power (5% of Crab), 3C 58 has historically been considered one of the PWNe most likely to emit gamma rays.

The pulsar J0205+6449 has a period P=65.68 ms, a spin-down rate $\dot{P} = 1.93 \times 10^{-13}$s s^{-1}, and a characteristic age of 5.38 kyr (Murray et al. 2002). Pulsed gamma rays where first detected by the *Fermi*-LAT. The measured energy flux is $F_{\gamma(E>0.1\mathrm{GeV})}$=(5.4±0.2)×10^{-11} erg cm^{-2}s^{-1} with a luminosity of $L_{\gamma(E>0.1\mathrm{GeV})}$=(2.4±0.1)×10^{34} erg s^{-1}, assuming a distance for the pulsar of 1.95 kpc (Xu et al. 2006). The spectrum is well described by a power-law with an exponential cutoff at E_{cutoff}=1.6 GeV (Abdo et al. 2013). No pulsed emission was detected at energies above 10 GeV (Ackermann et al. 2013). In the off-peak region, defined as the region between

the two γ-ray pulsed peaks (off-peak phase interval ϕ=0.64–0.99), the Fermi Collaboration reported the detection of emission from 3C 58 (Abdo et al. 2013). The reported energy flux is $(1.75\pm0.68)\times10^{-11}$erg cm^{-2}s^{-1} and the differential energy spectrum between 100 MeV and 316 GeV is well described by a power-law with photon spectral index $\Gamma = 1.61 \pm 0.21$. No hint of spatial extension was reported at those energies. The association of the high-energy unpulsed steady emission with the PWN is favored, although an hadronic origin related to the associated SNR can not be ruled out. 3C 58 was tagged as a potential TeV γ-ray source by the Fermi Collaboration (Ackermann et al. 2013).

The PWN 3C 58 was previously observed in the VHE γ-ray range by several IACTs. The Whipple telescope reported an integral flux upper limit of 1.31×10^{-11} cm^{-2}s^{-1} $\sim$ 19 % C.U. at an energy threshold of 500 GeV (Hall et al. 2001), and VERITAS established upper limits at the level of 2.3 % C.U. above an energy of 300 GeV (Aliu 2008). MAGIC-I observed the source in 2005 and established integral upper limits above 110 GeV at the level of 7.7×10^{-12} cm^{-2}s^{-1} (~4 %C.U.)(Aliu 2007; Anderhub et al. 2010). The improved sensitivity of the MAGIC telescopes with respect to previous observations and the *Fermi*-LAT results motivated us to perform deep VHE observations of the source.

7.1.1 SN 1181 AD

Figure 7.1: Historical record of the SN event in 1181 AD in the *Wenxian Tongkao*. Image taken from (Green & Stephenson 2003).

The new star of AD 1181, which was extensively observed in both China and Japan, was seen for fully six months. Such a lengthy duration of visibility in the various historical records is indicative of a SN. There are three Chinese records of the new star of AD 1181, from both the North (Jin) and South (Song) Chinese empires in existence at that time, and five Japanese accounts. None of these sources report any motion of the star. The most detailed surviving Chinese account of the guest star is found in the *Wenxian Tongkao* (Comprehensive study of civilization), an extensive work compiled around AD 1280. According to Chinese positional records, the guest star was "guarding the fifth star of the *Chuanshe* asterism". Regarding that the fifth star of the *Chuanshe* asterism is identified with SAO 12076 (Jinyu 1983, galactic coordinates $l \simeq 130^\circ$, $b \simeq 3^\circ$), this position is close to the position of 3C 58. Since the position of 3C 58 is situated in the same region and it hosts one of the largest spin-down power pulsars in the galaxy, it is believed to be the remnant of the SN of 1181 AD (SN 1181; Stephenson & Green 2002).

7.1.2 Distance and age

In spite of the positional coincidence, there are several arguments against the SN 1181 and 3C 58 association, giving to the SNR an age between 2.4 kyr to 7 kyr (Chevalier 2005b; Bietenholz 2006). Chevalier (2004, 2005b), calculated that the minimum energy necessary to produce the synchrotron emission is higher than the total energy released by the pulsar. The observed PWN size is larger than the expected for a PWN expanding into a normal SN for $\sim$ 800 yr. The mass ejected is also smaller than the expected from X-ray observations. All these problems were solved assuming an age of 2.4 kyr. Velocity measurements of the optical knots give an age estimation of 3-4 kyr (Fesen et al. 2008). Gotthelf et al. (2007) measured the proper motion of the pulsar and estimated an age of 3.75 kyr for a transversal velocity similar to that of Crab. According to NS cooling models, the UL to the thermal emission measured for 3C 58 is well below the expected temperature from standard cooling models and indicates an age for the system >>5 kyr. Slane et al. (2002) proposed that the explanation for such a low surface temperature is either some exotic cooling mechanisms acting in the NS or that the object is made of exotic matter, such as quarks (Weber 2005). The measurement of the radio expansion rate suggests an age of 7 kyr (Bietenholz 2006). The peak brightness of the SN explosion and the mass ejected in it are also too low to associate the object with the SN of 1181, unless the SN explosion were much lower than the canonical 10^{51} erg (Chevalier 2004). Apart from all these estimations based on different measurements, the pulsar characteristic age τ can be calculated with equation 5.6, leading to a characteristic age τ=5390 yr (Murray et al. 2002). This is nevertheless not a good measurement of its real age for young pulsars because they might have not significantly spun down. To sum up, there are several evidences based on different observations at several wavelength that point to an age for 3C 58 larger than ~830 yr.

All these age estimations are closely associated to the estimated distance to the PWN. 3C 58 distance is widely considered to be 3.2 kpc, determined from H I measurements (Roberts et al. 1993b). Nonetheless, there has recently been a deep study of newer H I data that claims a closer distance to the source. Based on H I data from the Canadian Galactic Plane Survey and recent distances measured to close objects, Kothes (2013) claims a distance of (2.0±0.3) kpc to 3C 58, which is compatible with the measured distance to PSR J0205+6449. This new distance, if correct, would change all the considerations about the age previously made in this section. In Table 1 of Kothes (2013), one can find a summary of the age evaluation using the different measurements and assuming a distance of 2 kpc. From his results, the assumption of 830 yr is the most supported by the different observational results. In summary, the estimates of age and distance are entangled and the real values are controversial.

7.2 MAGIC observations and results

MAGIC observed 3C 58 in the period between 4 August 2013 to 5 January 2014 for 99 hours. After quality cuts, 81 hours of the data were used for the analysis. A breakdown of the MAGIC observations can be found in Appendix B.4, Table B.6. The source was observed at Zd between 36° and 52°. The data were taken in *wobble-mode* (Fomin et al. 1994) pointing at four different

positions situated 0.4° away from the source to evaluate the background simultaneously with 3C 58 observations.

7.2.1 Search for steady emission

The analysis was performed using the analysis pipeline described in Section §2.2.3. As the source was weak and standard cuts are not optimized for detecting weak sources, we optimized the cut parameters for detecting a 1% C.U. point-like source on an independent Crab Nebula data sample at the same Zd range by maximizing the Li & Ma significance shown in equation 2.13. The cuts selected for the analysis were: θ^2 angle < 0.01 deg^2, hadronness < 0.18, and size in both telescopes > 300 phe. The SED was finally unfolded using all the methods described in Section §2.2.3.10. The unfolded spectrum using all the methods was compatible within statistical errors. We give the results of the unfolded spectrum using the Schmelling method, which is the one providing the lowest χ^2 .

The applied cuts and the Zd of the observations yield an energy threshold of 420 GeV. The significance of the signal, calculated with equation 2.13, is 5.7σ, which establishes 3C 58 as a γ-ray source. The θ^2 distribution is shown in Figure 7.2. As the five OFF positions were taken for each of the wobble positions, the OFF histograms were re-weighted depending on the time taken on each wobble position.

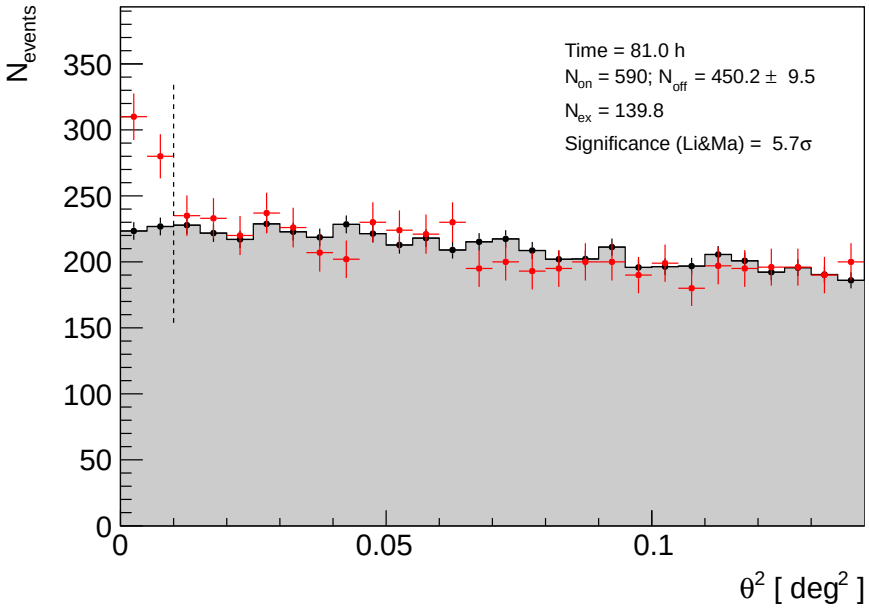

Figure 7.2: Distribution of squared angular distance, θ^2, between the reconstructed arrival directions of gamma-ray candidate events and the position of PSR J0205+6449 (*red points*). The distribution of θ^2 for the OFF positions is also shown (*gray filled histogram*). The vertical dashed line defines the signal region ($\theta^2_{\rm cut}$=0.01 deg^2), $N_{\rm on}$ is the number of events in the source region, $N_{\rm off}$ is the number of background events, estimated from the background regions and $N_{\rm ex}$=$N_{\rm on}$-$N_{\rm off}$ is the number of excess events.

We show in Figure 7.3 the relative flux (excess/background) skymap, produced using the same cuts as for the θ^2 calculation. The TS significance, which is the Li & Ma significance applied on a smoothed and modeled background estimate, is higher than 6 at the position of the pulsar PSR J0205+6449. The excess of the VHE skymap was fit with a Gaussian function. The best-fit position is RA(J2000) = 2 h 05 m $31(09)_{\rm stat}(11)_{\rm sys}$ s ; DEC (J2000) = 64° $51'(1)_{\rm stat}(1)_{\rm sys}$. This position is statistically deviant by 2σ from the position of the pulsar, but is compatible with it if systematic errors are taken into account. In the bottom left of the image we show the PSF of the smeared map at the corresponding energies, which is the result of the sum in quadrature of the instrumental angular resolution and the applied smearing, resulting in 4.7′ radius, at the analysis energy threshold. The extension of the signal is compatible with the instrument PSF. The VLA contours are coincident with the detected γ-ray excess.

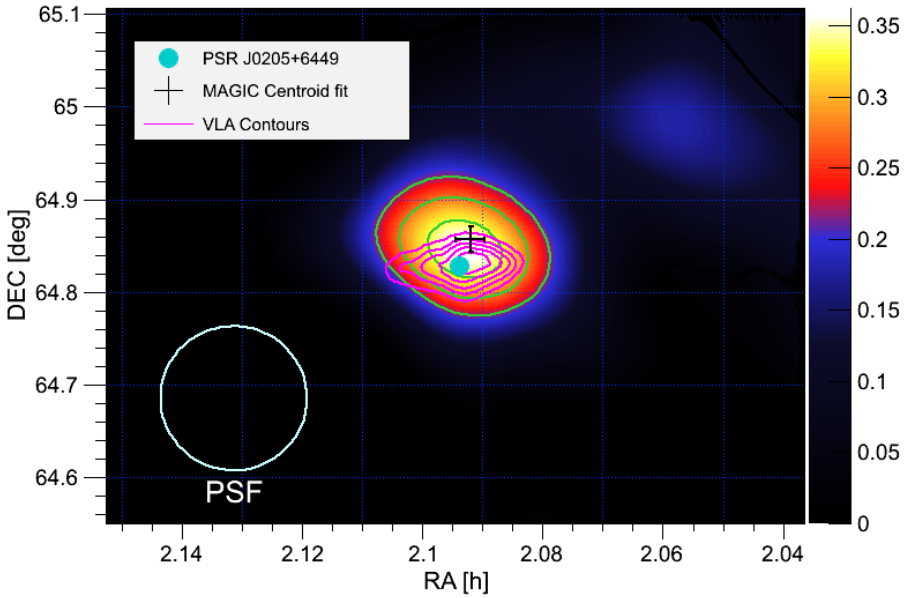

Figure 7.3: Relative flux (excess/background) map for MAGIC observations. The cyan circle indicates the position of PSR J0205+6449 and the black cross shows the fitted centroid of the MAGIC image with its statistical uncertainty. In green we plot the contour levels for the TS starting at 4 and increasing in steps of 1. The magenta contours represent the Very Large Array (VLA) flux at 1.4 GHz (Condon et al. 1998), starting at 0.25 Jy and increasing in steps of 0.25 Jy.

Figure 7.4 shows the energy spectrum for the MAGIC data, together with published predictions for the gamma-ray emission from several authors, and two spectra obtained with three years of *Fermi*-LAT data, which were retrieved from the *Fermi*-LAT second pulsar-catalog (2PC, Abdo et al. 2013) and the first *Fermi*-LAT high-energy catalog (1FHL, Ackermann et al. 2013). The 1FHL catalog used events from the *Pass 7 Clean class*, which provides a substantial reduction of residual cosmic-ray background above 10 GeV, at the expense of a slightly smaller collection area, compared with the *Pass 7 Source class* that was adopted for 2PC (Ackermann et al. 2012). The two γ-ray spectra from 3C 58 reported in the 2PC and 1FHL catalogs agree within

statistical uncertainties. The differential energy spectrum of the source is well fit by a single power-law function $d\phi/dE = f_0(E/1\ \mathrm{TeV})^{-\Gamma}$ with $f_0 = (2.0 \pm 0.4_{\mathrm{stat}} \pm 0.6_{\mathrm{sys}})10^{-13}\mathrm{cm}^{-2}\mathrm{s}^{-1}\mathrm{TeV}^{-1}$, $\Gamma = 2.4 \pm 0.2_{\mathrm{stat}} \pm 0.2_{\mathrm{sys}}$ and χ^2=0.04/2. The systematic errors were estimated from the MAGIC performance paper (Aleksić et al. 2014g). The integral flux above 1 TeV is $F_{\gamma(E>1\ \mathrm{TeV})} = 1.4 \times 10^{-13}\mathrm{cm}^{-2}\mathrm{s}^{-1}$. Taking into account a distance of 2 kpc, the luminosity of the source above 1 TeV is $L_{\gamma(E>1\ \mathrm{TeV})} = (3.0 \pm 1.1)\times 10^{32} d_2^2$ erg s^{-1}, where d_2 is the distance normalized to 2 kpc.

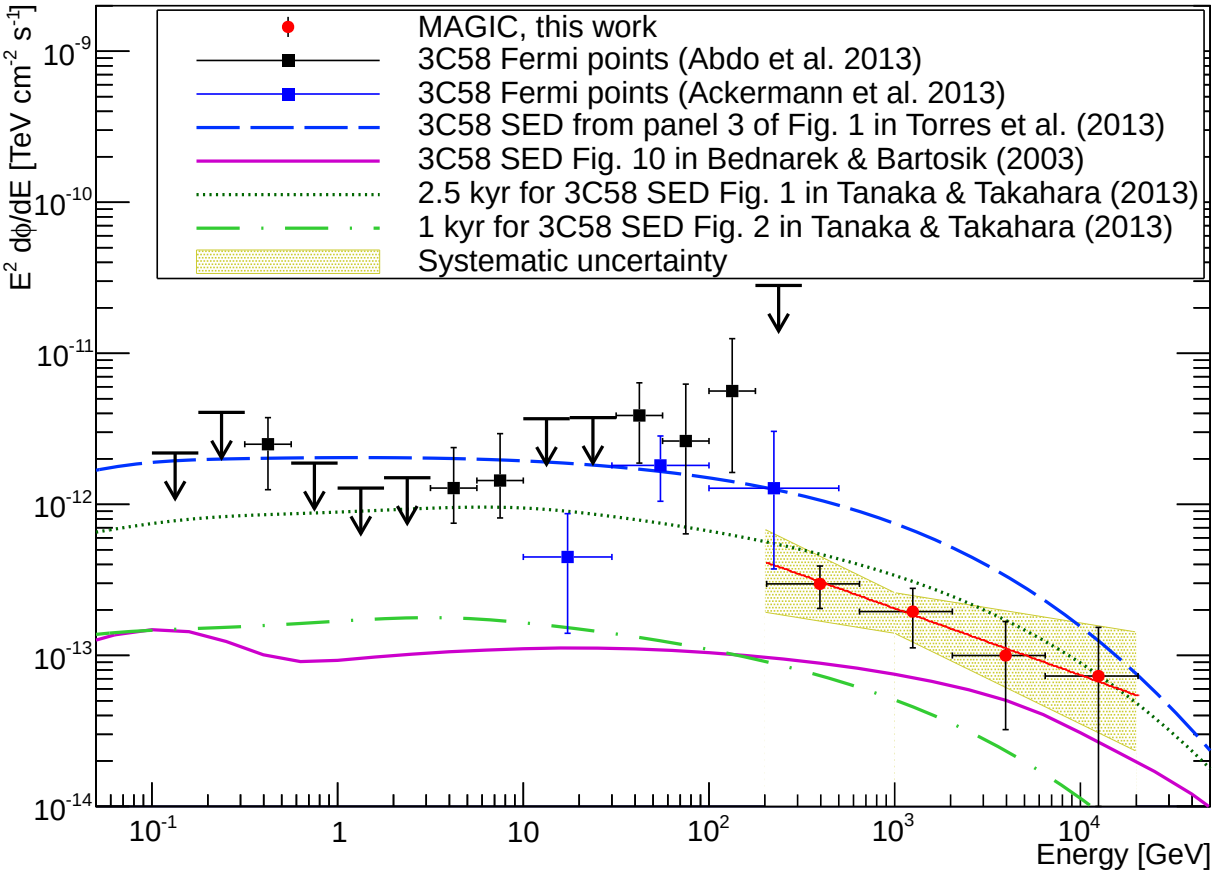

Figure 7.4: 3C 58 spectral energy distribution in the range between 0.1 GeV and 20 TeV. Red circles are the VHE points reported in this work. The best-fit function is drawn in red and the systematic uncertainty is represented by the yellow shaded area. Black squares and black arrows are taken from the 2PC (Abdo et al. 2013). Blue squares are taken from the 1FHL (Ackermann et al. 2013). The magenta line is the SED prediction for 3C 58 taken from Figure 10 of Bednarek & Bartosik (2003). The clear green dashed-dotted line is the SED predicted by Tanaka & Takahara (2013), assuming an age of 1 kyr, and the dark green dotted line is the prediction from the same paper, assuming an age of 2.5 kyr. The blue dashed line represents the SED predicted by Torres et al. (2013) assuming that the Galactic FIR background is high enough to reach a flux detectable by the MAGIC sensitivity in 50h.

7.2.2 Search for pulsed emission

The search for VHE pulsed emission from PSR J0205+6449 was performed using *psearch*, a program for pulsar timing analysis that corrects the arrival times to the solar system barycenter in the framework of MARS (López 2006). The ephemeris used was provided by the *Fermi*-LAT collaboration for contemporaneous data and tested on the satellite's data to check it. The cuts applied to the data were the same as the ones mentioned in Section §7.2. In principle, pulsed VHE emission is not expected at energies > 420 GeV according to the non-detection of pulsed γ-ray photons above 4 GeV reported by *Fermi*-LAT . Nevertheless, as it was mentioned in Section §5.3.1, there are models predicting a scenario with a second component due to IC in the spectrum of the pulsed signal from the Crab Nebula.

The phaseogram for the position of PSR J0205+6449 can be seen in Figure 7.5. No significant pulsed emission was found from the whole dataset. We calculate the UL with a 95% C.L. using the method presented in de Jager (1994). The UL for the pulsed emission above 420 GeV is $F_{\rm pulsed}$ <1.3×10^{-13} cm^{-2}s^{-1}.

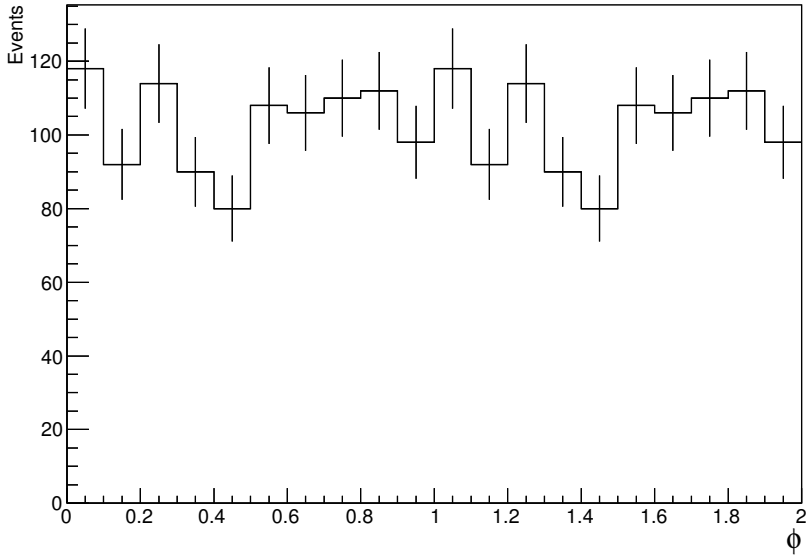

Figure 7.5: PSR J0205+6449 phaseogram above 420 GeV. Two periods are shown for clarity.

7.3 Discussion

7.3.1 Comparison with models

There are several models that predict detectable VHE γ-ray emission from PWN 3C 58. Bucciantini et al. (2011) presented a one zone model of the spectral evolution of PWNe and applied it to 3C 58 using a distance of 3.2 kpc. The VHE emission in this model is produced by IC

scattering of CMB photons and optical-to-IR photons, and by pion decay. They derive a nebula in equipartition where total energy is not conserved. The flux of gamma rays above 400 GeV predicted by this model is about an order of magnitude lower than the observation.

Bednarek & Bartosik (2003) proposed a time-dependent model in which positrons gain energy in the process of resonant scattering by heavy nuclei. The VHE emission is produced by IC scattering of leptons off CMB, IR, and synchrotron photons and by the decay of pions due to the interaction of nuclei with the matter of the nebula. The age of 3C 58 is assumed to be 5 kyr, using a distance of 3.2 kpc and an expansion velocity of 1000 km s^{-1}. According to this model, the predicted integral flux above 400 GeV is $\sim 10^{-13}$ $cm^{-2}s^{-1}$, while the integral flux above 420 GeV measured here is $5\times10^{-13}cm^{-2}s^{-1}$. Calculations by Bednarek & Bartosik (2005), using the same model with an initial expansion velocity of 2000 km s^{-1} and considering IC scattering only from the CMB, are consistent with the observed spectrum. However, the magnetic field derived in this case is $B \sim 14$ μG and it underestimates the radio emission of the nebula, although a more complex spectral shape might account for the radio nebula emission.

Tanaka & Takahara (2010) developed a time-dependent model of the spectral evolution of PWNe. They consider the PWN as a freely expanding sphere at a constant velocity, a reasonable assumption for a young PWN. The spectrum of the injected electrons is a broken power-law normalized using the magnetic fraction and spin-down power of the pulsar. The magnetic field is calculated using the conservation of the magnetic field energy. For the particle evolution, they solved the time-dependent diffusion-loss equation including the cooling effect of synchrotron, IC and adiabatic expansion, but ignoring particle escape. For the spectral evolution of the PWN, they considered synchrotron radiation, IC and SSC. To calculate the observability of 3C 58 at TeV energies they assumed a distance of 2 kpc and two different ages: 2.5 kyr and 1 kyr (Tanaka & Takahara 2013). For the IC scattering they consider CMB and optical-to-IR photons as a target photon fields. The photon density for the optical and IR photons is assumed to be 0.3 eV/cm^3. For an age of 2.5 kyr, they obtained a magnetic field $B \geq 17\mu$G, while for an age of 1 kyr, they obtained B=40 μG. The emission predicted by this model for an age of 2.5 kyr is close to the MAGIC result shown in this thesis, and the measurement of *Fermi*-LAT.

Martín et al. (2012) presented a different time-dependent leptonic model without making any approximations in the diffusion-loss equation. They include in the calculation of the emitted spectrum synchrotron, SSC, IC, and bremsstrahlung. The evolution of the magnetic field and the spectrum of the injected electrons is similar to that assumed by Tanaka & Takahara (2010). They assumed a distance of 3.2 kpc and an age of 2.5 kyr (Torres et al. 2013). The predicted emission, without considering any additional photon source other than the CMB, is more than an order of magnitude lower than the flux reported here. It can account for the VHE flux measured by MAGIC for an FIR-dominated photon background with an energy density of 5 eV/cm^3. This would be more than one order of magnitude higher than the local IR density in the Galactic background radiation model used in GALPROP ($\sim$0.2 eV cm^{-3}; Porter et al. 2006). The magnetic field derived from this model is 35 μG. To reproduce the observations, a large FIR background or a revised distance to the PWN are required. In the first case, a nearby star or the SNR itself might provide the necessary FIR targets, although there is no evidence for an enhancement in the direction of the PWN. As we mentioned in Section §7.1, a distance of 2 kpc has recently been proposed by Kothes (2013) based on the recent H I measurements of the Canadian Galactic

Plane Survey. At this distance, a lower photon density is required to fit the VHE data (Torres. 2014, priv. comm.).

We have shown different time-dependent models in this section that predict the VHE emission of 3C 58. The SEDs predicted by them are shown in Figure 7.4. They use different assumptions for the evolution of the PWN and its emission. Bucciantini et al. (2011) divided the evolution of the SNR into phases and modeled the PWN evolution inside every of them. The model fits the synchrotron part of the spectrum, but it has to assume a non-conservation of the total energy of the nebula. In Bednarek & Bartosik (2003) model, nuclei play an important role in accelerating particles inside the PWN and they also contribute to the VHE radiation through pion decay. It manages to fit the spectrum for energies higher than X-rays under certain assumptions, but they are not able to fit the synchrotron radio emission.

Tanaka & Takahara (2010) and Torres et al. (2013) modeled the evolution of the particle distribution by solving the diffusion-loss equation, but Tanaka & Takahara (2010) neglected an escape term in the equation as an approximation and Torres et al. (2013) fully solved it. Another difference between these two models is that Torres et al. (2013) included bremsstrahlung into their model, while Tanaka & Takahara (2010) did not. The differences in their predictions come mainly from the distance, target photon fields assumed and the magnetic fractions.

The models that fit the γ-ray data derive a low magnetic field, far from equipartition, very low for a young PWN, but comparable with the value derived by Slane et al. (2008) using other data. In Torres et al. (2014), they applied their model to several TeV detected PWNe. They found that all the PWNe detected at TeV energies have magnetic fields below equipartition (magnetic fraction η <0.5). This means that either only PWNe with low magnetic fraction emit in TeV at the reach of the current IACTs and we have an observational bias, or that this is a common characteristic among all PWNe and the assumption of equipartition inside the nebula is wrong.

7.3.2 VHE luminosity in the context of all VHE PWNe

Mattana et al. (2009) performed a study of how the X-ray (L_X) and VHE γ-ray (L_γ) luminosities of PWNe and PWN candidates compare with parameters of the central pulsar as the spin-down luminosity ($\dot{E}$) or the characteristic age (τ). In the paper they assumed that the electrons emitting in X-rays and in gamma rays are in the cool and uncool regimes, respectively. The population of cooled and uncooled particles in this regime is given by:

$$n_{\rm c}(E,t) \propto \int_{t-t_c}^{t} \dot{E}(t')dt' = \frac{\dot{E}_0 t_{\rm dec}^2 t_{\rm c}}{(t - t_{\rm c} + t_{\rm dec})(t + t_{\rm dec})} \tag{7.1}$$

$$n_{\rm u}(E,t) \propto \int_{0}^{t} \dot{E}(t')dt' = \dot{E}_0 t_{\rm dec}\left(\frac{t}{t + t_{\rm dec}}\right) \tag{7.2}$$

where $n_{\rm c}$ is the number of cooled particles, $n_{\rm u}$ is the number of uncooled particles, $\dot{E}_0$ is the initial spin-down luminosity of the pulsar, $t_{\rm dec} \sim 100 - 1000$ yr is a characteristic decay time and $t_{\rm c}$ the cooling time. For $t >> t_{\rm dec}$, the population of uncooled electrons becomes constant: $n_{\rm u} \propto \dot{E}_0 t_{\rm dec}$. If we are in this regime, the VHE γ-ray luminosity of the PWNe is constant and

only depends on the initial spin-down power of the pulsar and $t_{\rm dec}$. For $t >> max(t_{\rm dec}, t_{\rm c})$, the population of cooled electrons is: $n_{\rm c} \propto \dot{E}_0 t_{\rm dec}^2 t_{\rm c} t^{-2} \propto \dot{E} t_{\rm c}$. This means that the X-ray luminosity of PWNe in this regime should be proportional to $\dot{E}$ and inversely proportional to t^{-2}. In their phenomenological studies, Mattana et al. (2009) found a correlation between the L_X and the $\dot{E}$ and an anti-correlation of the ratio between gamma and X-ray luminosities (L_γ/L_X) and the $\dot{E}$. Comparing with the τ of the central pulsar, they found that the X-ray luminosity is anti-correlated with τ and the ratio L_γ/L_X correlated with it. They explicitly mention 3C 58 as a probable outlier from the aforementioned correlations due to its low magnetic field, that would prevent X-ray emitting electrons to reach the cooled regime.

We performed a study similar to that of Mattana et al. (2009), including the PWNe and PWN candidates detected afterwards. We have computed the L_γ in the range between 1 and 10 TeV, and L_X in the range between 2 and 10 keV. All the PWN parameters used for the study can be found in Table B.9 in Appendix B.5. In the plots, we highlight the results for the two PWNe studied in this thesis: the Crab Nebula and 3C 58.

In the top panel of Figure 7.6, a plot of L_γ as a function of $\dot{E}$ is shown. We also show lines corresponding to a fixed $L_\gamma/\dot{E}$, which is a measure of the efficiency of the PWN to convert the rotational energy of the central pulsar into VHE γ-ray emission. We find that 3C 58 is the least luminous and the most inefficient PWN converting rotational energy into gamma rays of the detected PWNe and PWN candidates at VHE gamma rays. The next most inefficient PWN transforming rotational energy into VHE γ-ray emission is the Crab Nebula. Figure 7.7 shows the histogram of the logarithm of the VHE γ-ray luminosities in the range between 1 and 10 TeV for all these PWNe. The VHE γ-ray luminosity should be constant and only dependent on $\dot{E}_0$ and $t_{\rm dec}$ of the central pulsar. The distribution is fit by a gaussian with μ=33.95±0.17 and σ=0.6±0.3. The luminosity of 3C 58 is deviated 2.6 σ from the mean of the distribution.

The middle and bottom plots of Figure 7.6 represent L_X and L_γ/L_X as a function of the $\dot{E}$ respectively. We find L_X and L_γ/L_X to be correlated and anti-correlated with $\dot{E}$ respectively, similarly as in Mattana et al. (2009). The best-fit relation between L_X and $\dot{E}$ is given by:

$$\log_{10} L_X = (-15 \pm 7) + (1.33 \pm 0.19) \log_{10} \dot{E} \tag{7.3}$$

and χ^2/Ndf=9.0/19. We can compare this quantities with the ones obtained by Possenti et al. (2002) in the 0.1 - 2.4 keV band: $\log_{10} L_X = (-14.36 \pm 0.01) + (1.34 \pm 0.03) \log_{10} \dot{E}$, with a very similar result as the one obtained in this work. Kargaltsev & Pavlov (2008) obtained in the energy range between 0.5 and 8 keV the relation $\log_{10} L_X = (-20.00 \pm 0.05) + (1.46 \pm 0.04) \log_{10} \dot{E}$, whose slope is also compatible with the result obtained in this work. Mattana et al. (2009) obtained in the energy range between 2 and 10 keV the relation $\log_{10} L_X = (-35.39 \pm 0.04) + (1.87 \pm 0.04) \log_{10} \dot{E}$, showing a softer correlation than the one obtained in this work in the same energy range. The relation between L_γ/L_X and $\dot{E}$ is:

$$\log_{10} L_\gamma/L_X = (34 \pm 9) - (0.9 \pm 0.3) \log_{10} \dot{E} \tag{7.4}$$

with χ^2/Ndf=16.3/20. Mattana et al. (2009) derived the relation $\log_{10} L_\gamma/L_X = (69.66 \pm 0.04) - (1.87 \pm 0.07) \log_{10} \dot{E}$, using the same energy range for the X-ray analysis as mentioned before and the range between 1 an 30 TeV for the γ-ray luminosity. The relation obtained in this

work is not compatible with that obtained in Equation 7.4. The different offset might come from the different energy ranges used when deriving both relations, but the difference in slope only comes from the additional data added to the sample.

As we can check in Figure 7.6, in spite of its low luminosity, 3C 58 does not constitute an outlier of the relation between luminosities and the $\dot{E}$, meaning the the assumption that the X-ray electrons are already cooled also applies for this nebula. In spite of not being an outlier, in the middle plot of Figure 7.6, we can see that L_X of 3C 58 is lower than the fit, making it into an inefficient source transforming rotational energy into X-rays.

In the top panel of Figure 7.8, we show L_γ as a function of τ, two quantities that are not correlated. In the middle and bottom panels of Figure 7.8 we show L_X and L_γ/L_X as a function of the $\dot{E}$. We find L_X and L_γ/L_X to be anti-correlated and correlated with τ respectively, similarly as in Mattana et al. (2009). The relation between L_X and τ is given by:

$$\log_{10} L_X = (40.9 \pm 1.4) - (1.7 \pm 0.3) \log_{10} \tau \tag{7.5}$$

with χ^2/Ndf=14.3/20. Kargaltsev & Pavlov (2008) found in the energy range between 0.5 and 8 keV the relation $\log_{10} L_\gamma/L_X = (42.41 \pm 0.01) - (2.03 \pm 0.01) \log_{10} \tau$, compatible with the results derived in this work. Mattana et al. (2009) derived the relation $\log_{10} L_\gamma/L_X = (43.66 \pm 0.04) - (2.49 \pm 0.06) \log_{10} \tau$, again softer than the relation obtained in this work. The relation between L_γ/L_X and τ is:

$$\log_{10} L_\gamma/L_X = (-5.9 \pm 1.4) + (1.5 \pm 0.3) \log_{10} \tau \tag{7.6}$$

with χ^2/Ndf=14.4/20. The relation in Mattana et al. (2009) is $\log_{10} L_\gamma/L_X = (-8.14 \pm 0.06) + (2.21 \pm 0.09) \log_{10} \tau$, not compatible again with that derived in this work.

3C 58 is not an outlier of the aforementioned correlations. We would like to note, however, that 3C 58 has lower L_X and lower L_γ/L_X than the one derived from the fits, meaning that its efficiency transforming rotational energy into EM emission is lower than the average.

Let us compare the results of the fit for the ratios between L_γ/L_X as a function of $\dot{E}$ and τ, as it is done in Mattana et al. (2009). From the fits shown in equations 7.4 and 7.6 we derive that $L_\gamma/L_X \propto \dot{E}^{-0.9\pm0.3}$ and $L_\gamma/L_X \propto \tau^{1.5\pm0.3}$. According to equations 7.1 and 7.2 where the cooled and uncooled particle populations are calculated, the theoretical ratio between luminosities, assuming that the X-ray particles are in the cooled regime and the γ-ray ones in the uncooled one, is $L_\gamma/L_X \propto t^2 \propto \dot{E}^{-1}$, very close to the relations obtained. The results obtained by Mattana et al. (2009) differ from the results drawn from the fits performed in this thesis. We note, however, that we used the same data set used by Mattana et al. (2009) adding the newly discovered PWNe and PWN candidates at VHE. On the other hand, the results drawn from the fits are in agreement with those from Kargaltsev & Pavlov (2008), obtained with a larger data sample.

7.4 Conclusions

We have detected VHE gamma rays up to TeV energies from the PWN 3C 58 for the first time. The measured luminosity and flux make 3C 58 into an exceptional object. 3C 58 is the weakest

VHE PWN detected to date, a fact that attests to the sensitivity of MAGIC. According to the currently existing models predicting VHE γ-ray emission from 3C 58, only a closer distance of 2 kpc or a high local FIR photon density can qualitatively reproduce its multiwavelength data. Since the high FIR density is unexpected, the closer distance with FIR photon density comparable with the averaged value in the Galaxy is favored. The age derived by the models in both cases is 2.5 kyr. The models that fit the γ-ray data derive magnetic fields which are very far from equipartition. We did not find any significant VHE γ-ray pulsed signal and established ULs above 420 GeV.

3C 58 is the least luminous VHE PWN, far less luminous than the original expectations. Its ratio $\sim L_\gamma/\dot{E} \simeq 10^{-5}$ is the lowest measured, similar to Crab, which makes it into a very inefficient γ-ray emitter. Assuming that the X-ray and γ-ray emitting particles are in different cooling regimes, we find that, for the PWNe detected at VHE gamma rays, L_X is correlated to $\dot{E}$ and anti-correlated to τ. The ratio between L_γ/L_X is anti-correlated to $\dot{E}$ and correlated to τ. We have found that $L_\gamma/L_X \propto \tau^{1.5\pm0.3}$ and $L_\gamma/L_X \propto \dot{E}^{-0.9\pm0.3}$, close to the expected values. Contrary to what it was thought, 3C 58 is not an outlier of these relations, although it shows an L_X and a ratio L_γ/L_X lower than the fit for the rest of PWNe, making it an inefficient accelerator also in the X-ray regime. The results presented in this chapter are published in Aleksić et al. (2014c).

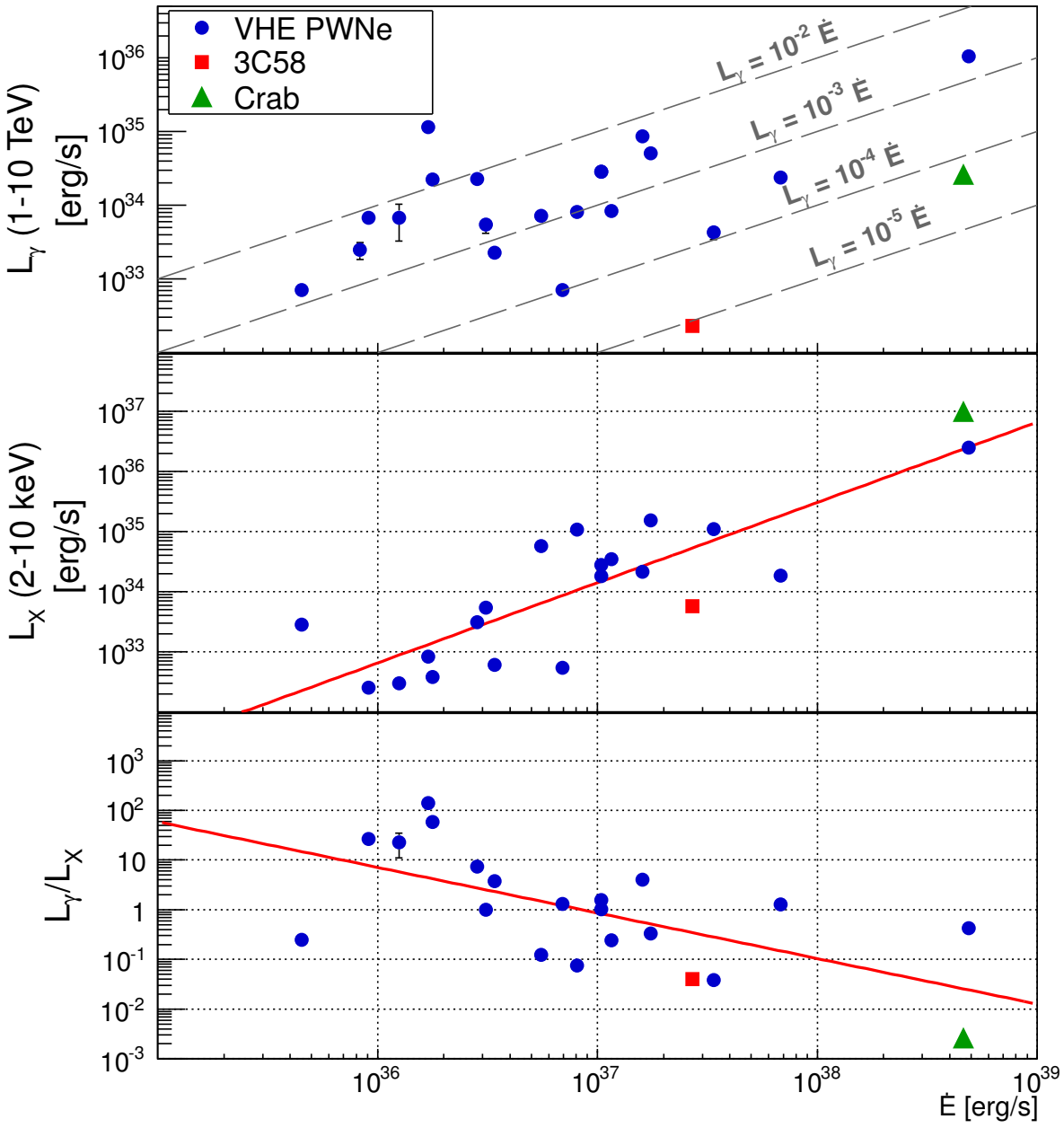

Figure 7.6: VHE γ-ray luminosity between 1 and 10 TeV (top panel), X-ray luminosity between 2 and 10 keV (middle panel) and ratio between luminosities (bottom panel) of PWNe and PWN candidates as a function of the spin-down power of the central pulsar.

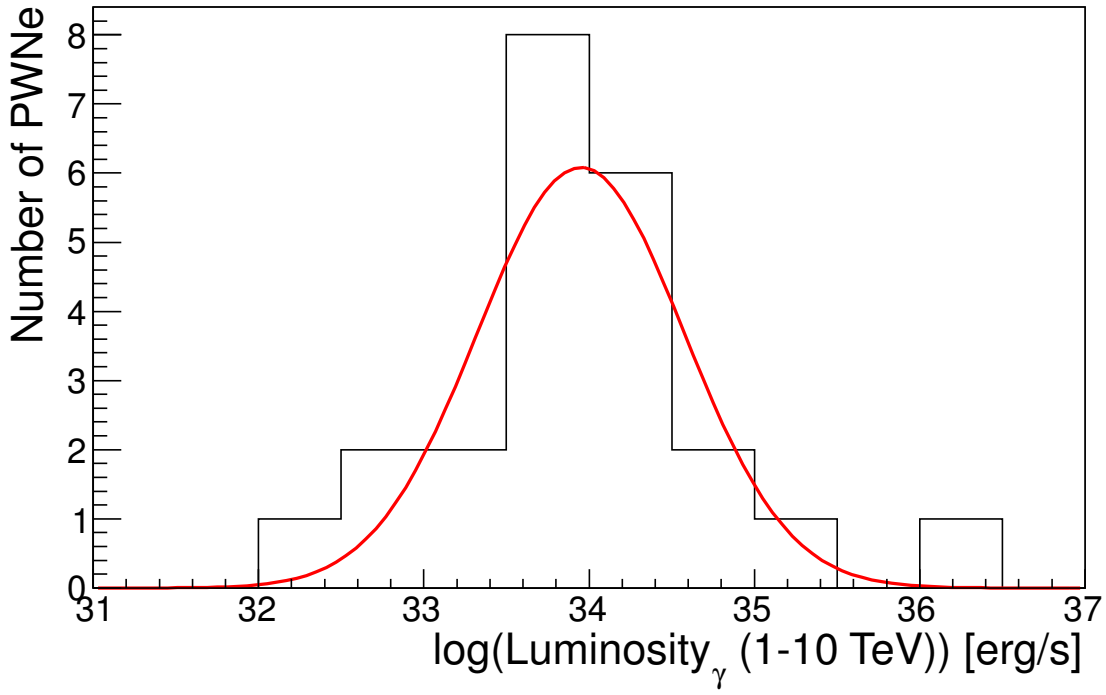

Figure 7.7: VHE γ-ray luminosity histogram of PWNe and PWN candidates detected at VHE gamma rays. The red line corresponds to a gaussian fit to the histogram.

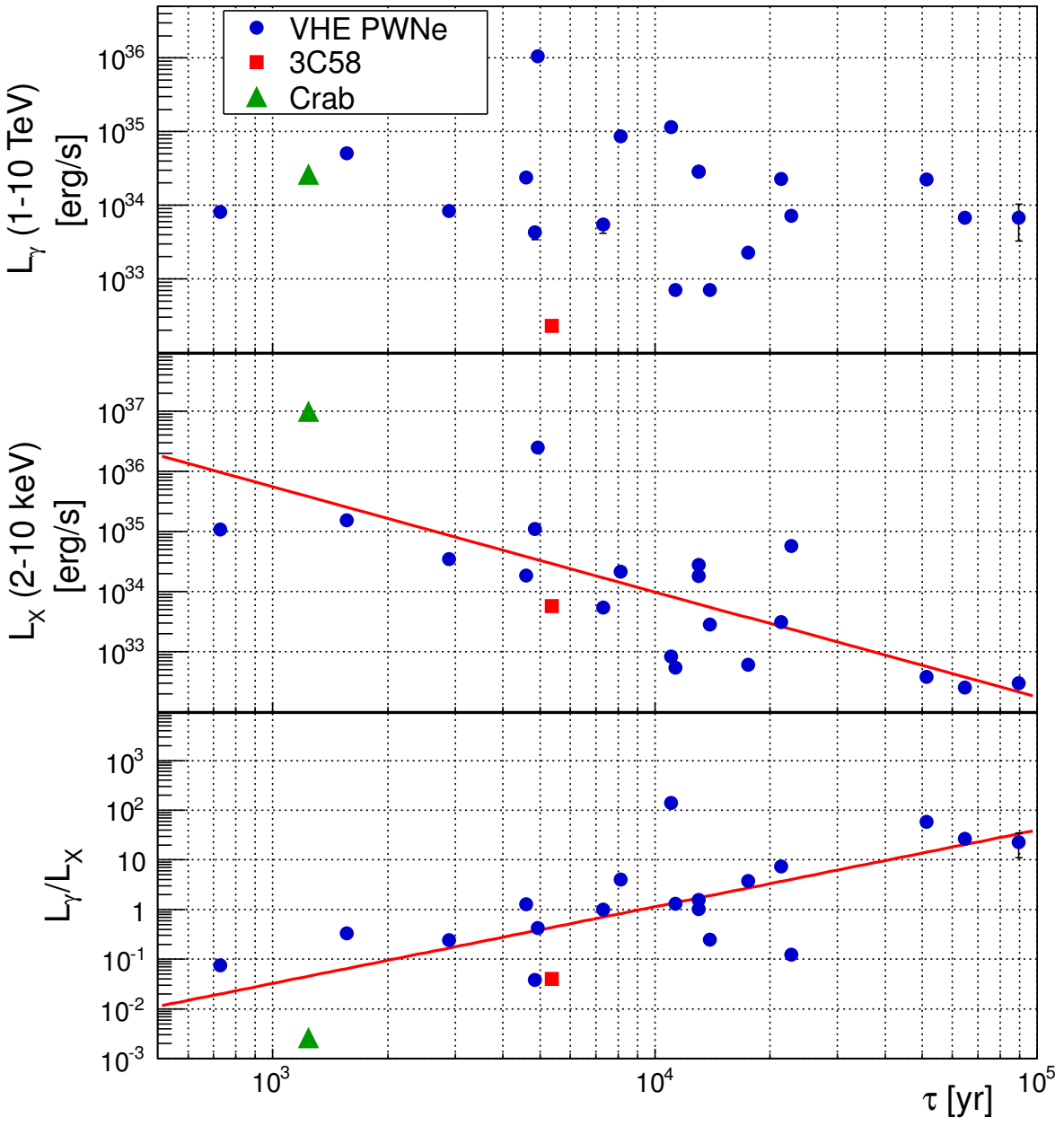

Figure 7.8: VHE γ-ray luminosity between 1 and 10 TeV (top panel), X-ray luminosity between 2 and 10 keV (middle panel) and ratio between them (bottom panel) of PWNe and PWN candidates as a function of the characteristic age of the central pulsar.

Part IV

Cataclysmic Variable Stars

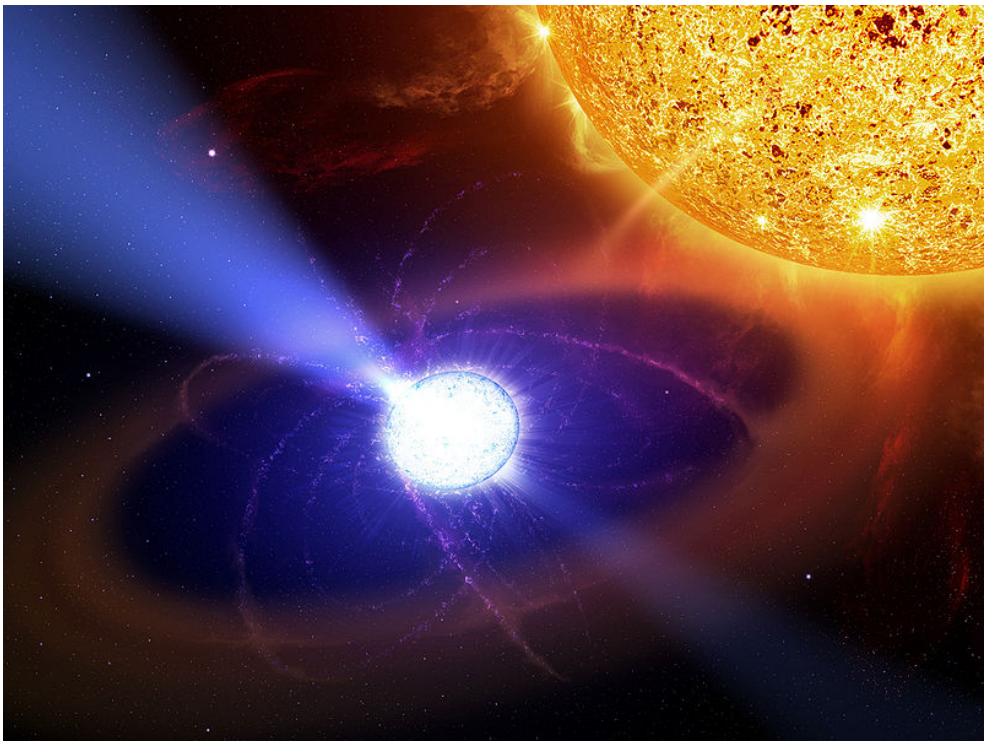

Figure IV: Artist view of AE Aqr.

8

Introduction to cataclysmic variable stars

8.1 Introduction

Cataclysmic Variables (CVs) are semi-detached binaries consisting of a WD (called primary) that accretes material from a companion star (usually a Red Dwarf (RD), known as secondary) that transfers matter to the WD. The distance between them is of the order of a few solar radii. The companion is usually gravitationally distorted into a tear-drop shape. If the WD is non-magnetic, an accretion disk surrounding the WD is formed. If it is magnetized, the accretion disk is disrupted or not even formed in the case of strongly magnetized WDs (Warner 2003).

CVs show episodes when the system increases in luminosity by several orders of magnitude for a period that goes from hours to days, known as an outburst. These luminosity variations were firstly explained by a process of mass transfer in binary systems (Walker 1954). The mass transfer allows the formation of accretion disks, essential to understand planet and galaxy formation, and CV stars are an unique laboratory to test them. Accretion is the most efficient form of transforming mass into energy known. It can also be found in objects such as BHs, although the complete physical mechanisms acting in the accretion disks formed around WDs are still under debate.

8.2 Composition

As we discussed in Section §5.1, a massive star with initial mass $M <$ 9-10 $M_{\odot}$ becomes a WD at the end of its life. On the other hand, there are smaller stars such as RDs that have masses between 0.1-0.3 $M_{\odot}$. They are thought to be fully convective, not building up a core and never

becoming a red giant. These stars have constant brightness and a slow consumption of their fuel, resulting in long life times. They are the most common type of star in our galaxy.

In CVs, the *primary* is the WD, and the *secondary* is the star which is transferring mass to the WD. In a binary system, the *Roche lobe* of one of the stars is the region where matter is gravitationally attached to that star. In CVs, since the companion star fills its Roche lobe, the system is called semi-detached (see Figure 8.1). The contact point of both Roche lobes, also known as Lagrangian point, is the saddle point of the potential between both Roche lobes. Matter is transferred through this point from the secondary to the primary (Connon Smith 2007). The stream of matter that crosses the Lagrangian point moves at a speed much lower than the orbital velocity, so it does not fall directly into the primary. If the magnetic field of the primary is not strong, the material starts to rotate around the WD forming an *accretion disk*. When the matter accreted from the secondary impacts the accretion disk, kinetic energy is released and the zone heated up, producing as a result a "hot spot". The whole process is illustrated in Figure 8.1.

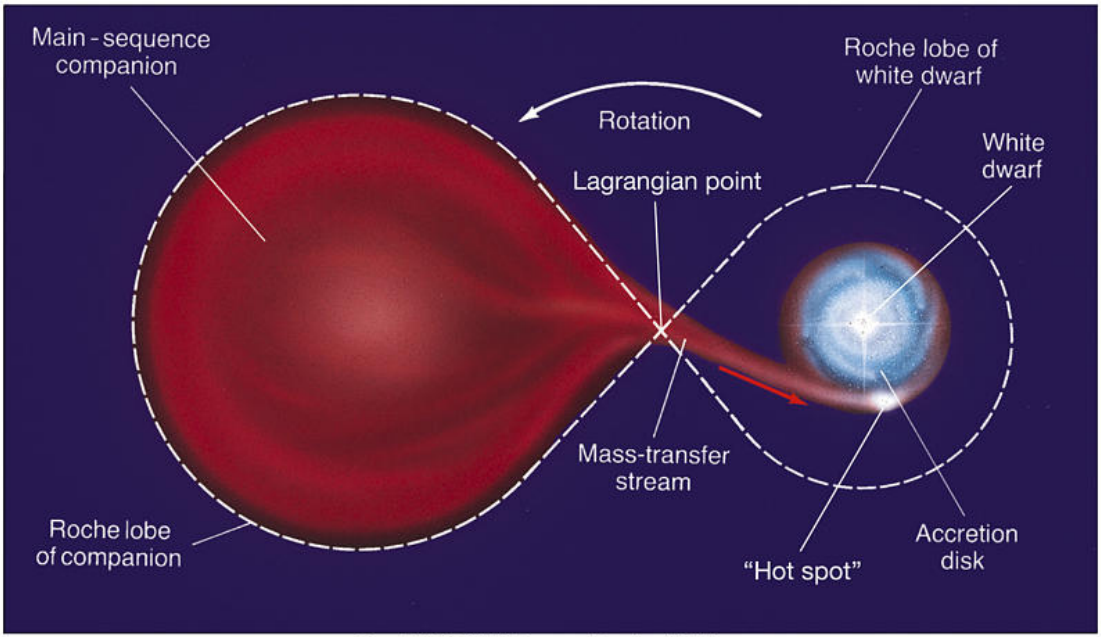

Figure 8.1: Scheme of a CV system viewed from the pole of the orbit.

8.3 CV fauna

Due to the diversity in several of their characteristics, it is difficult to place CVs in groups with common features. There are systems as AE Aqr (to which we dedicate Chapter §9) that do not fit into any of them and are proposed to constitute a class of CVs on their own (Ikhsanov & Beskrovnaya 2012). However, CVs are usually classified by the type of variation they manifest (for a review see Warner 2003) into Classical Novae (CNe), Recurrent Novae (RNe), Dwarf Novae (DNe), nova-like variables and magnetic CVs.

⊙ **Classical Novae** A CV is called classical nova or just *nova* when only an outburst has been reported and its brightness has increased from 6 up to 19 magnitudes (see appendix A.4) during this outburst. Novae explosions are caused by the accumulation of hydrogen-rich material on the surface of the WD. This results in a thermonuclear runaway that generates the nova (Bode & Evans 2012; Starrfield et al. 2012; Woudt & Ribeiro 2014). This system is illustrated in Figure 8.1.

There are records of *novae stellae* or "new stars" since 1500 BC by Chinese astrologers (Clark & Stephenson 1976), that might be attributed either to CN or SN events. No such reports have been found in Europe, maybe because Europeans maintained the aristotelian idea of an immutable sky until Tycho Brahe's discovery of a SN in 1572. The first true CN was discovered in Europe in 1670 and is shown in Figure 8.2.

Figure 8.2: Chart of the nova Vulpeculae (tagged as "nova 1670"), the first nova identified by European astronomers (Hevelius 1670). The star tagged as "Nova 1600" was believed to be a nova, but is currently known as P Cygni, an hypergiant luminous blue variable whose brightness variations are attributed to the ejection of its outer layers.

Symbiotic Novae: Symbiotic novae, like CNe, are also initiated by a thermonuclear explosion on the surface of the WD. However, in the case of symbiotic novae, the WD is immersed in the wind of a late-type companion star and the increase of brightness ranges from 9 to 11 magnitudes (Shore et al. 2011, 2012).

⊙ **Recurrent Novae**

They are previously identified CNe that repeat their emission.

⊙ **Dwarf Novae**

They show outbursts of 2 to 8 magnitudes caused by a release of gravitational energy due to the increase in the rate of mass transfer from the companion. They differentiate from CNe, apart from the mechanism generating the increase of emission, in the fact that there is no shell ejection, while in CNe part of the shell is lost during the outburst.

⊙ **Nova-like variables**

They are CVs that do not show outbursts. They can be systems that are in pre-nova or post-nova phases and have shown no outbursts during the last hundreds of years. Some of the nova-like systems show small flux increases in their light curve, but unlike other types of novae, they show them all the time.

⊙ **Magnetic CVs**

The sources included in this group have a WD with magnetic fields typically larger than 10^5 G.

Intermediate Polar:

Also known as DQ Her type, they show an accretion disk disrupted due to the magnetic field of the WD. At the innermost part of the disk, the falling matter follows the magnetic field lines forming accretion streams before reaching the WD surface. They are expected to show lower accretion rates than polars. A sketch of an intermediate polar is shown on the left panel of Figure 8.3.

Polar:

No accretion disk is formed because of the strong magnetic field. Matter transferred from the secondary forms an accretion stream that falls directly into the WD. A sketch of a polar is shown on the right panel of Figure 8.3.

Out of this classification, we have observed with the MAGIC telescope one classical nova (V339 Del), one symbiotic nova (YY Her), one dwarf nova (ASASSN-13ax) and one nova-like variable (AE Aqr).

8.4 Spectral characteristics

CVs emit from radio to HE gamma rays. Nevertheless, most of the observations are concentrated in the optical, where even amateur astronomers are able to measure their variability. Spectroscopy is used to measure the composition of the accretion disk and the orbital parameters of the system. Radio emission from CVs is usually weak, although it can be detected from novae in outburst or magnetic CVs. It is produced in large scale structures in the binary system (Drechsel et al. 1987). Observations in the IR allow the discovery of faint red secondary companions.

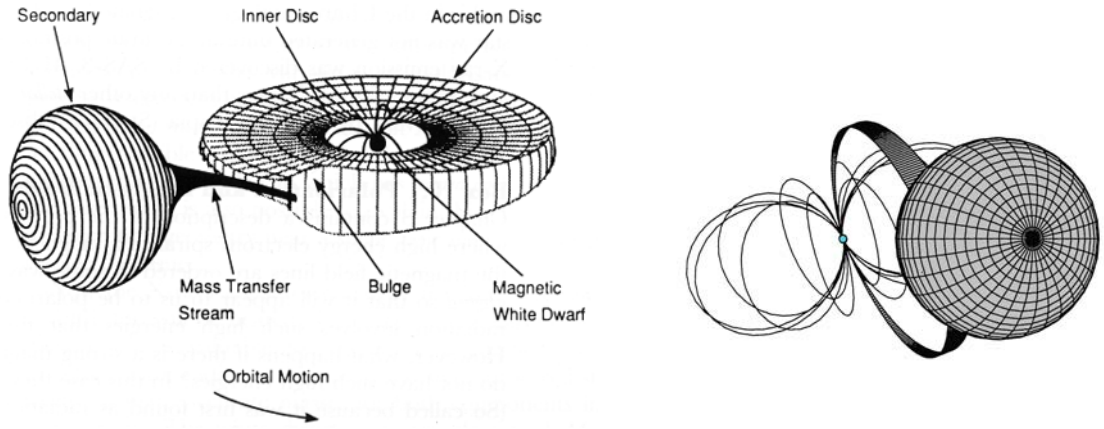

Figure 8.3: Sketch of a polar (left panel) and an intermediate polar (right panel) CVs.

UV observations are used to study the primary, although it might be obscured by the accretion disc depending on the observation angle. A thermal X-ray continuum is often detected by X-ray satellites in CN and magnetic CVs .

CVs have been proposed as candidates for non-thermal γ-ray emission. In AE Aqr a propeller model has been used to predict detectable VHE γ-ray emission under determined circumstances (Meintjes & de Jager 2000). The problem of this model is that makes assumptions that are not based on observations, such as the presence of a disk. Nevertheless, there are claims of VHE γ-ray emission from this source that are explained in detail in Section §9.1.

Since the discovery of transient γ-ray emission from the symbiotic nova V407 Cygni by *Fermi*-LAT (Abdo et al. 2010) and the subsequent report of transient emission from six additional novae (Cheung et al. 2013, 2014; Ackermann et al. 2014a; Cheung et al. 2015), CVs have been included among HE γ-ray emitters (E >100 MeV). Several models explain the HE γ-ray emission of novae in terms of leptonic or hadronic acceleration. According to these models, there is the possibility that particles are accelerated to TeV energies and produce VHE γ-ray emission. We describe the models explaining the HE γ-ray emission and predicting a VHE component in Section §10.1.

9

Multiwavelength campaign on AE Aquarii

9.1 Introduction

AE Aquarii (AE Aqr) is a bright nova-like CV consisting of a magnetic WD and a K4-5 V secondary. The orbital period of the system is $T_{\rm o}$=9.88 hours, and the spin period of the WD is $T_{\rm s}$=33.08 s (Patterson 1979), which is the shortest known for a WD. The system is located at a distance of 102^{+42}_{-23} pc (Friedjung 1997), and the spin-down power of the WD is $6{\times}10^{33}$ erg s^{-1} (de Jager et al. 1994). It was originally classified as a DQ Her star (Patterson 1994), but it shows features that do not fit such a classification, e.g., violent variability at multiple wavelengths, Doppler tomograms that are not consistent with those of an accretion disk (Welsh et al. 1998), and the fast spin-down rate of the WD ($\dot{P}$=5.64×10^{-14} s s^{-1}, de Jager et al. 1994). Recent X-ray measurements show that the spin-down rate is slightly higher, which is compatible with an additional term $\ddot{P}$=3.46 × 10^{-19} d^{-1} (Mauche 2006). AE Aqr is considered to be in a magnetic propeller phase, ejecting most of the material transferred from the secondary by the magnetic field of the WD (Wynn et al. 1997). It exhibits flares 50% of the time, varying in the optical band from B = 12.5 mag (during the low state) to B = 10 mag (during flares). Bastian et al. (1988) observed radio flares with fluxes in the range 1–12 mJy at 15 GHz. They show that the radio flares may be produced by relativistic electrons, which provides evidence of accelerated particles that radiate synchrotron emission in magnetized clouds. The time of both the optical and radio flares is random. Soft (0.5–10 keV) and hard (10–30 keV) X-rays have also been detected with a 33 s modulation (Patterson et al. 1980; Mauche 2006; Terada et al. 2008). A non-thermal origin of the hard X-rays is favored by Terada et al. (2008), who report an X-ray luminosity of $L_{\rm Hard\ X\text{-}rays} \simeq 5 \times 10^{30}$ erg s^{-1} for the isotropic emission. They also report a sharp feature in the hard X-ray pulse profile that has not been confirmed by subsequent observations (Kitaguchi

et al. 2014). Because of the large magnetic field and the fast rotating period of the WD, AE Aqr has been compared to pulsars (Ikhsanov 1998) and has been proposed as a source of cosmic ray electrons (Terada 2013).

The groups operating the Nooitgedacht Mk I Cherenkov telescope (de Jager et al. 1986) and the University of Durham VHE γ-ray telescopes (Brazier et al. 1990) reported TeV γ-ray emission from AE Aqr using the imaging atmospheric Cherenkov technique. The Durham group claimed that they detected gamma rays of energies above 350 GeV pulsed at the second harmonic of the optical period (60.46 mHz), as well as two bursts of TeV gamma rays (Bowden et al. 1992; Chadwick et al. 1995) lasting for 60 s and 4200 s with 4.5 σ and 5.3 σ significance, respectively. The Nooitgedacht group, using the Mk I telescope, reported pulsed signals above energies of a few TeV at frequencies close to the spin frequency of the WD (30.23 mHz), with significances varying from 3 σ to 4 σ. Meintjes et al. (2012) claim that the duty cycle of the occurrence of TeV periodic signals above 95% significance level is $\sim$ 30%. They find coincidence in the orbital phase of their detections with the time of superior conjunction of the WD (orbital phase 0), but the burst reported by the Durham group is not coincident with this orbital phase. In the reports made by the two groups, the fluxes measured for the pulsed emission and burst episodes are at 10^{-9}–10^{-10} cm^{-2}s^{-1} for E >350 GeV for the Durham group and E >2.4 TeV for the Nooitgedacht group.

The luminosity corresponding to these fluxes is in the range 10^{32}–10^{34} erg s^{-1}, where the latter is at the level of the spin-down power of the WD. After the reports of TeV emission of such extraordinary luminosities, models were proposed to explain the fluxes measured (Meintjes & de Jager 2000), as well as others predicting lower levels of emission (Ikhsanov & Biermann 2006). According to classical models of particle emission, the magnetic moment of some WDs in binaries might provide enough energy to accelerate particles to VHE (Chanmugam & Brecher 1985). The flux levels reported by the Durham and Nooitgedacht groups is measurable in less than one hour of observations with the current generation of IACTs. AE Aqr has been observed by different generations of IACTs since the detection claims were reported, but none have confirmed them. The Whipple telescope observed the source for 68.7 hours and did not find any evidence of emission (Lang et al. 1998). They reported flux ULs at 4×10^{-12} cm^{-2}s^{-1} for the steady emission and 1.5×10^{-12} cm^{-2}s^{-1} for the pulsed emission above 900 GeV. Later attempts by MAGIC and HESS did not lead to conclusive results (Sidro et al. 2008; Mauche et al. 2012).

The purpose of this campaign was to perform VHE observations of AE Aqr with MAGIC in a multiwavelength context, and hence confirm or rule out previous claims of γ-ray emission. We present in this work the results of the campaign, with emphasis on the search for signals in the VHE γ-ray range.

9.2 Observations

During the period between May 15 (MJD 56062) and June 19, 2012 (MJD 56097), we carried out a multiwavelength campaign on AE Aqr. The purpose of this campaign was to look for γ-ray emission during the different states of the source at other wavelengths. The log of the observation times during the campaign for all the instruments is shown in Table B.7 in Appendix B.4.

9.2.1 Optical facilities

We used data from three optical telescopes for the campaign. The observations are described in the following:

KVA

The KVA optical telescope is located on La Palma, but is operated remotely from Finland. It has a mirror diameter of 35 cm. The effective aperture ratio of the system is f/11 with a SBIG ST-8 CCD camera (0.98 arcsec/pix) (Takalo et al. 2008).

The AE Aqr observations were performed in the *B* band using 20-second exposures extending to about two hours of data per night during 19 nights. The magnitude of the source was measured from CCD images using differential photometry with 5″ radius aperture, and the data were reduced using the standard analysis software to analyze KVA data (Nilsson 2014). The seeing during the observations was 1″ FWHM. The typical error in the magnitude measurement is ∼0.04 mag. The comparison star used to calibrate the AE Aqr flux was the star 122 of the AAVSO AE Aqr finder chart.

Skinakas

The data from the Skinakas Observatory[1] in Crete (Greece) were obtained with the 1.3-m Ritchey-Chrétien telescope located on the Skinakas mountain at an altitude of 1750 meters. The telescope has a focal ratio of f/7.6. The data were acquired with an Andor Tech DZ436 2048x2048 water cooled CCD. The physical pixel size is 13.5 microns resulting in 0.28 arcsec on the sky. The camera was used in the 2-μs-per-pixel readout mode. The observations were taken with a Bessel *B* filter using 10-second exposures, while the cycle time from the start of one exposure to the next was 14 seconds.

The data from Skinakas were taken during about one hour for four nights, and they were reduced using IRAF routines. Differential photometry was performed using the photometry package DAOPHOT using 25 pixel (7″) radius apertures. The seeing conditions during the observations were 2″ FWHM. The typical error in the magnitude measurement is ∼0.005 mag. The AE Aqr data were flux-calibrated using stars 122 and 124 in the AAVSO AE Aqr finder chart.

Vidojevica

The Astronomical Station Vidojevica is located on Mt. Vidojevica (Serbia)[2] , at an elevation of 1150 m. The data were obtained with the 60-cm Cassegrain telescope. The telescope was used in the f/10 configuration with the Apogee Alta U42 CCD camera (2048 x 2048 array, with 13.5-micron pixels providing a 0.46 arcsec/pix plate scale). The *B* filter from Optec Inc. (Stock No. 17446) was used for all observations. The field centered on the target AE Aqr was observed with ten seconds of exposure time. Only a fraction of the full CCD chip FoV, roughly 5 arcmin

[1] http://skinakas.physics.uoc.gr/en/
[2] http://belissima.aob.rs/

on a side, was read out in approximately four seconds, resulting in 14 seconds of total cycle time between exposures.

The data were taken for periods between one and two hours for five nights and they were reduced using standard procedures in IRAF. The photometry was performed with Source Extractor, using five-pixel (2.3″) radius circular apertures. Typical seeing conditions during the observations were 2″ FWHM. The typical error in the magnitude measurement is ∼0.015 mag. The AE Aqr flux was calibrated using the same comparison stars as for Skinakas.

AAVSO

A number of AAVSO observers provided us with additional observations. However, due to the low time resolution of these observations and the lack of time coincidence with γ-ray observations, we did not include the AAVSO data into our timing analysis.

9.2.2 Swift

Swift (Gehrels et al. 2004) target-of-opportunity observations of AE Aqr were scheduled during 25 orbits from MJD 56062 to 56079 and from MJD 56091 to 56094. Data were obtained with the X-ray Telescope (XRT, sensitive over the energy range 0.3–10 keV Burrows et al. 2005), the Ultraviolet/Optical Telescope (UVOT), and the Burst Alert Telescope (BAT), although only the XRT data have been analyzed to support the MAGIC observations. The screened and calibrated XRT CCD/PC event data for ObsIDs 00030295011–00030295035 were downloaded from the HEASARC data archive[1]. The data were processed using the XRTDAS software package (v.2.9.3) developed at the ASDC and distributed by HEASARC within the HEASoft package (v. 6.15.1). On-source events were selected within a circle of a 30-pixel (69 arcsec) radius. The background was evaluated in an adjacent 60-pixel radius off-source region. Event energies were restricted to the 0.5–10 keV bandpass, and all event times were corrected to the solar system barycenter. The 25 ObsIDs consisted of 29 good-time intervals, which were combined into 25 satellite orbits, although one orbit was rejected because the exposure was too short (20 s), and three orbits were rejected because the source image fell on one of the dead strips on the detector. The net exposure during the remaining orbits ranged from 559 s to 1178 s, with ∼ 950 s being typical, and the total exposure was 19.94 ks.. The analysis was crosschecked using a flexible IDL script developed by C. W. Mauche to deal with event data from instruments on numerous science satellites including *ROSAT*, *ASCA*, *EUVE*, *Chandra*, *XMM-Newton* and adapted to Swift for this study.

9.2.3 MAGIC

MAGIC observed AE Aqr during 14 non-consecutive nights during the period between MJD 56073 and 56097. The observations were performed with a single telescope owing to a hardware failure in the M I camera. This worsened the sensitivity to ∼1.5% of the Crab Nebula flux above 300 GeV in 50 hours (Aleksić et al. 2012a). The source was observed at Zd ranging between 28°

[1] http://HEASARC.gsfc.nasa.gov/docs/archive.html

and 50°, and after quality cuts, 9.5 hours of data were obtained. The data were taken in *wobble mode*, as explained in Section §2.2.2.1). They were analyzed following the usual procedure in MAGIC , as explained in Section §2.2.3.

To search for pulsed emission, the arrival times of the events were corrected to the solar system barycenter using the software package TEMPO2 (Hobbs et al. 2006). To calculate the phases of the events, we used the ephemeris presented in de Jager et al. (1994) using the second-order correction proposed by Mauche (2006). We corrected the times for the orbital motion of the system using TEMPO2 as well. The ephemeris, particularly the phase of spin-pulse maximum, was checked using the Swift data (see Sect. 9.3.2). The UL for the pulsed emission were calculated with a 95% C.L. following the method described in de Jager (1994) that makes use of the H-test for the significance of weak periodic signals (de Jager et al. 1989). The simultaneity of the optical and MAGIC observations allows us to investigate the TeV flux of the source for different optical emission levels.

9.3 Results

The measured optical magnitudes are presented in section §9.3.1. In section §9.3.2 the results obtained with Swift are discussed. In section §9.3.3, we present the results of the search for a steady and pulsed γ-ray signal. The light curves of the multiwavelength campaign are shown in Figure 9.1.

9.3.1 Optical results

We present the results of all the optical observations together to check for consistency between the magnitudes measured by the different telescopes (top panel of Figure 9.1). We find that the measurements performed by the different optical telescope lead to similar results. The highest optical state was measured on MJD 56080, reaching $B = 11.08$ mag. The short time exposures (~ 10 seconds) mean that it is not possible to produce the optical spin-phase-folded light curve.

9.3.2 Swift results

The *Swift*/XRT event data were used to compute the X-ray light curve (Figure 9.1, middle panel) and the spin-phase-folded light curve (Figure 9.2). The background-subtracted XRT count rate varied by a factor of three, from 0.18 counts s^{-1} to 0.53 counts s^{-1}, with a mean of 0.27 counts s^{-1}. A similar ratio of mean-to-base and peak-to-base count rate ratios and a similar light curve morphology were observed during the long *Chandra* observation of AE Aqr in 2005 (Mauche 2009). The spin-phase-folded light curve was calculated using the ephemeris provided by Mauche (2006), with parameters:

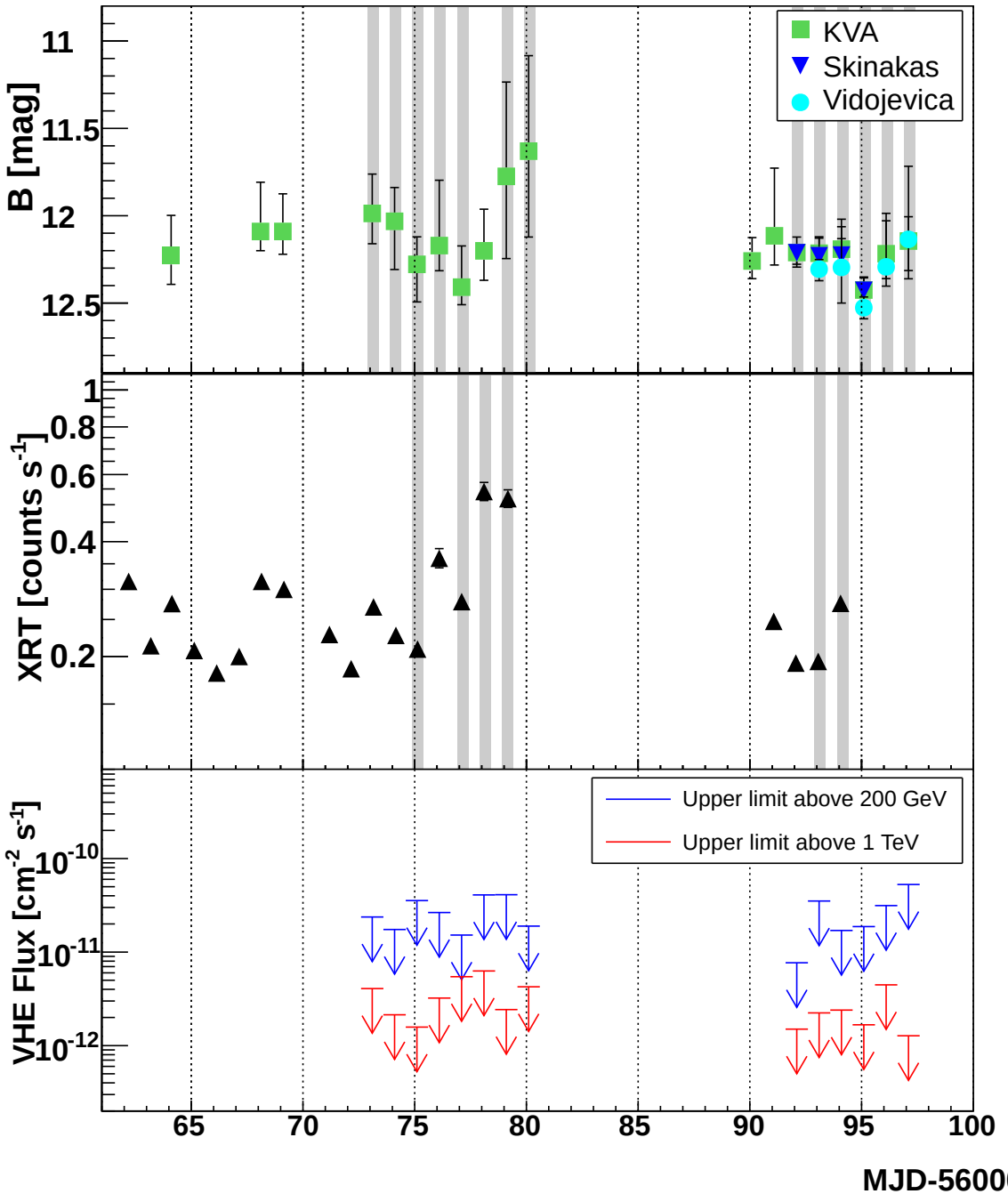

Figure 9.1: Light curves of the multiwavelength campaign. The plot includes *B* magnitudes measured by the optical telescopes (top panel), XRT count rate in the energy range 0.5–10 keV (middle panel) and MAGIC daily integral ULs assuming a power-law spectrum with a 2.6 photon spectral index above 200 GeV and 1 TeV (bottom panel). Vertical dotted lines every 5 days are plotted across all the panels for reference. For the optical data, since the source variability is very large, the point plotted is the average magnitude of the night and the error bars indicate the maximum and minimum magnitude reached during that observation night. The shaded areas indicate the X-ray and optical observations with simultaneous data with MAGIC.

Orbital period	$P_{\rm orb}$ = 0.411655610 d
Time of superior conjunction	T_0 = 2445172.2784 BJD
Spin period	$P_{\rm s}$ = 0.00038283263840 d
Spin period derivative	$\dot{P}_{\rm s} = 5.642 \times 10^{-14}$ d d^{-1}
Spin period second derivative	$\ddot{P}_{\rm s} = 3.46 \times 10^{-19}$ d^{-1}
Projected semi-amplitude	$a_{\rm WD} \sin i$ = 2.04 s.

The points were fit with a cosine function:

$$A(\phi_{\rm spin}) = A_0 + A_1 \cos[2\pi(\phi_{\rm spin} - \phi_{\rm off})] \tag{9.1}$$

with parameters

$$\begin{aligned} A_0 &= 0.260 \pm 0.004 \text{ counts s}^{-1} \\ A_1 &= 0.042 \pm 0.005 \text{ counts s}^{-1} \\ \phi_{\rm off} &= 0.15 \pm 0.02 \end{aligned}$$

and χ^2/dof=5.90/7=0.84. The fit function is shown in Figure 9.2.

As a result, the relative pulse amplitude is A_1/A_0=16%±2%, which is slightly higher than previously measured by *ASCA*, *XMM-Newton*, and *Chandra*, which are 13%, 10%, and 15%, respectively (see Table 2 of Mauche 2006). A shift of $\phi_{\rm off}$=0.15±0.02, which is not compatible with $\phi_{\rm off}$=0, is observed. That is an indication of the inaccuracy of the ephemeris used or a drastic variation in either $\dot{P}$ or $\ddot{P}$. Nevertheless, we use this result for the time of the maximum of the pulsed X-ray emission to look for pulsed gamma-ray signals.

9.3.3 MAGIC results

The energy threshold achieved for these observations, defined as in Section §2.2.3.6, for a power-law with a 2.6 photon spectral index is 250 GeV, although the number of events surviving the gamma/hadron separation cuts is still high below this energy, down to 200 GeV, where it falls rapidly. This result is obtained from MC simulations without applying any cut in reconstructed energy. We searched for steady and periodic emission in the MAGIC dataset. We computed ULs to the integral flux above two values of energy; namely, above 200 GeV, as the lowest energy with sufficient gamma-ray detection efficiency (for this observation); and above 1 TeV, to compare our results with the previous claims. Most of those observations were simultaneous with optical and X-ray ones. Therefore, we also study the correlation of optical/X-ray flux with the possible γ-ray emission.

9.3.3.1 Search for steady TeV emission

The total dataset did not show any significant steady signal. For the UL calculation, we assumed power-law functions with different photon spectral indices (2.0, 2.6, and 3.0). The results are listed in Table 9.1. We also computed integral ULs (95% C.L.) for the single-night observations,

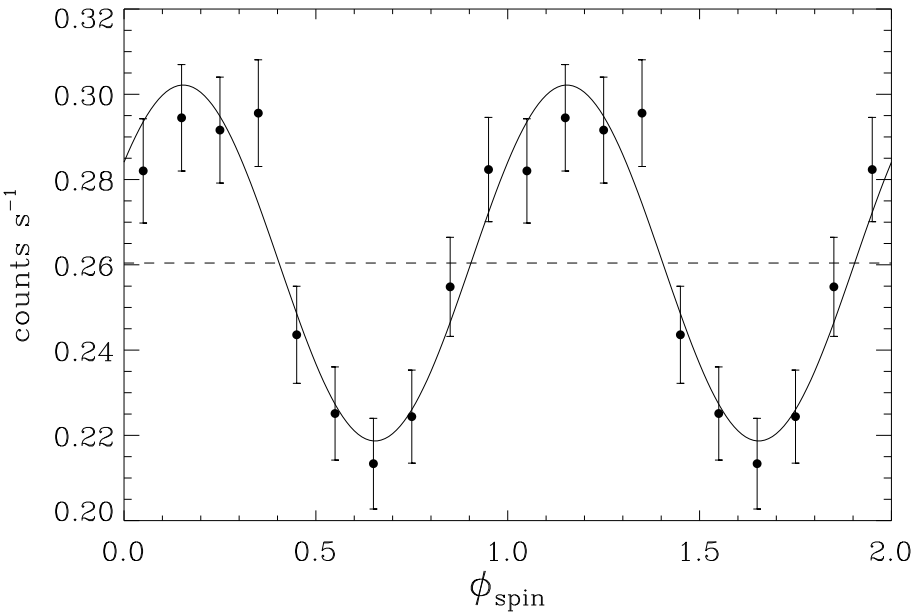

Figure 9.2: XRT spin-phase-folded light curve in the energy range 0.5–10 keV. Two cycles are shown for clarity. The errors quoted are the square root of number of counts in the source region plus the area-scaled number of counts in the background region, divided by the exposure. The continuous black line shows the best fit using equation 9.1. The dashed line represents the mean value A_0=0.260 counts s^{-1} obtained from the fit.

assuming a source steady emission with a power-law function with photon spectral index 2.6. These ULs can be found in Table 9.2 and are plotted in Figure 9.1 (bottom panel). The single-night ULs for TeV emission coincident with the highest states of the source in X-rays (MJD 56078 and 56079) and in the optical (MJD 56079 and 56080) are at the same level as the ULs for the remaining days.

Γ	UL (95 % C.L.) [cm^{-2}s^{-1}]	
	> 200 GeV	> 1 TeV
2.0	4.2×10^{-12}	7.6×10^{-13}
2.6	6.4×10^{-12}	7.4×10^{-13}
3.0	8.0×10^{-12}	7.4×10^{-13}

Table 9.1: MAGIC integral ULs to steady flux assuming a power-law spectrum with different photon spectral indices Γ above 200 GeV and 1 TeV.

We also studied the behavior of the source during different bright optical states. Based on the optical states observed during the multiwavelength campaign, we selected γ-ray events during times when $B < 12$ mag (1.22 hours) and $B < 11.5$ mag (0.34 hours). The integral ULs for those states are shown in Table 9.3.

Date [MJD]	UL (95 % C.L.) [$cm^{-2}s^{-1}$]	
	> 200 GeV	> 1 TeV
56073	2.4×10^{-11}	4.0×10^{-12}
56074	1.7×10^{-11}	2.1×10^{-12}
56075	3.6×10^{-11}	1.6×10^{-12}
56076	2.7×10^{-11}	3.2×10^{-12}
56077	1.5×10^{-11}	5.5×10^{-12}
56078	4.1×10^{-11}	6.3×10^{-12}
56079	4.1×10^{-11}	2.4×10^{-12}
56080	1.9×10^{-11}	4.3×10^{-12}
56092	0.8×10^{-11}	1.5×10^{-12}
56093	3.5×10^{-11}	2.2×10^{-12}
56094	1.7×10^{-11}	2.4×10^{-12}
56095	1.9×10^{-11}	1.7×10^{-12}
56096	3.1×10^{-11}	4.5×10^{-12}
56097	5.3×10^{-11}	1.3×10^{-12}

Table 9.2: MAGIC daily integral ULs to steady flux assuming a power-law spectrum with photon spectral index 2.6 above 200 GeV and 1 TeV.

9.3.3.2 Search for pulsed TeV emission

We searched for pulsed TeV emission at the rotation frequency of the WD (30.23 mHz) and its first harmonic (60.46 mHz). We did not find any hint of periodic signal for any of the two frequencies. For the UL calculation, we limited the signal region to 30% of the pulsar phaseogram, centered on the bin corresponding to the maximum of the XRT spin-phase-folded light curve (see Figure 9.2). The phaseograms for data above 200 GeV are shown in Figure 9.3. These ULs, calculated as explained in section 9.2.3, can be found in Table 9.4.

We also searched for periodic emission at different frequencies using the Rayleigh test (Mardia 1972). We scanned the complete dataset for periodic signals in the range between 20.0 mHz and 70.0 mHz in steps of 0.5 mHz (101 frequencies). This range is selected in order to cover the

B [mag]	UL (95 % C.L.) [$cm^{-2}s^{-1}$]	
	> 200 GeV	> 1 TeV
< 11.5	2.1×10^{-11}	1.6×10^{-12}
< 12	7.3×10^{-12}	1.2×10^{-12}

Table 9.3: MAGIC integral ULs to steady flux for different optical states above 200 GeV and 1 TeV and for a photon spectral index 2.6.

Frequency	UL (95 % C.L.) [$cm^{-2}s^{-1}$]	
	> 200 GeV	> 1 TeV
30.23 mHz	2.6×10^{-12}	2.6×10^{-12}
60.46 mHz	2.1×10^{-12}	3.7×10^{-12}

Table 9.4: MAGIC integral ULs for the pulsed emission at the spin frequency and its first harmonic above 200 GeV and 1 TeV for a photon spectral index of 2.6.

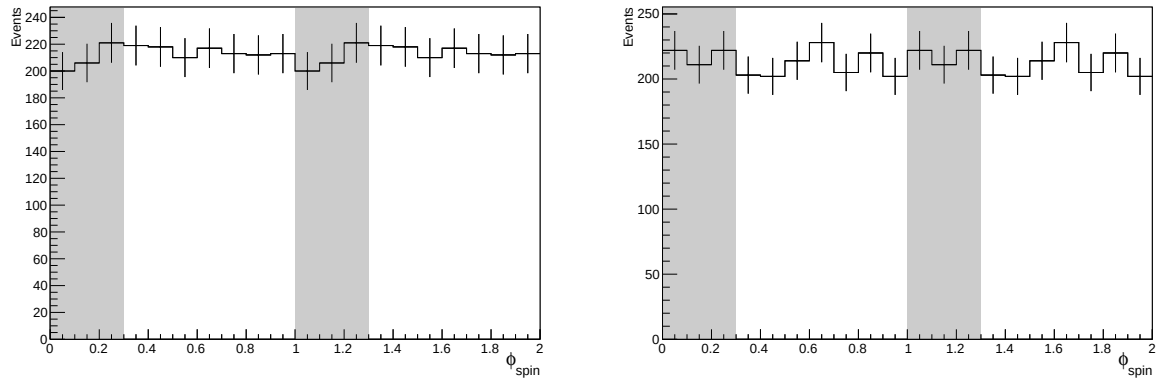

Figure 9.3: Phaseogram for the MAGIC data above 200 GeV for a frequency of 30.23 mHz (left panel) and 60.46 mHz (right panel). The shaded area corresponds to the region where the signal is expected assuming a duty cycle of 30%.

whole range of interest in the frequencies. For all the frequencies, we calculated the Rayleigh power z and the chance probability of getting that value or higher from pure white noise as P = exp(-z). The histogram of z values is fit with an exponential function $f(z) = A\exp(-bz)$. In case of purely white noise, we expect b=1 and $A = b \times N$, where N is the number of scanned frequencies. The result of the fit is A=115±22 and b=1.17±0.17. The complete dataset scan for significant periodic signals is shown in Figure 9.4. The result of the fit of the histogram in the inset of Figure 9.4 is compatible with white noise. The minimum pre-trial chance probability obtained is 3.5×10^{-3} for a frequency of 23.0 mHz, which corrected after trials (101 frequencies) gives a post-trial probability of 3.0×10^{-1}. Hence, no significant signal of periodic/variable behavior was found.

We applied the Rayleigh test to the daily datasets as well. The range of frequencies is the same as the one used for the complete dataset. The minimum pre-trial chance probability obtained for all the scans is 1.5×10^{-4} for a frequency of 54.0 mHz, achieved on MJD 56094. This probability, corrected after trials (101 frequencies × 14 observations), gives a 1.9×10^{-1} post-trial chance probability. The histogram with the distribution of Rayleigh power for all scanned frequencies and days is shown in Figure 9.5. The result of the fit of the histogram $f(z)$ is A=1450±60 and b=0.99±0.03, which is compatible with white noise.

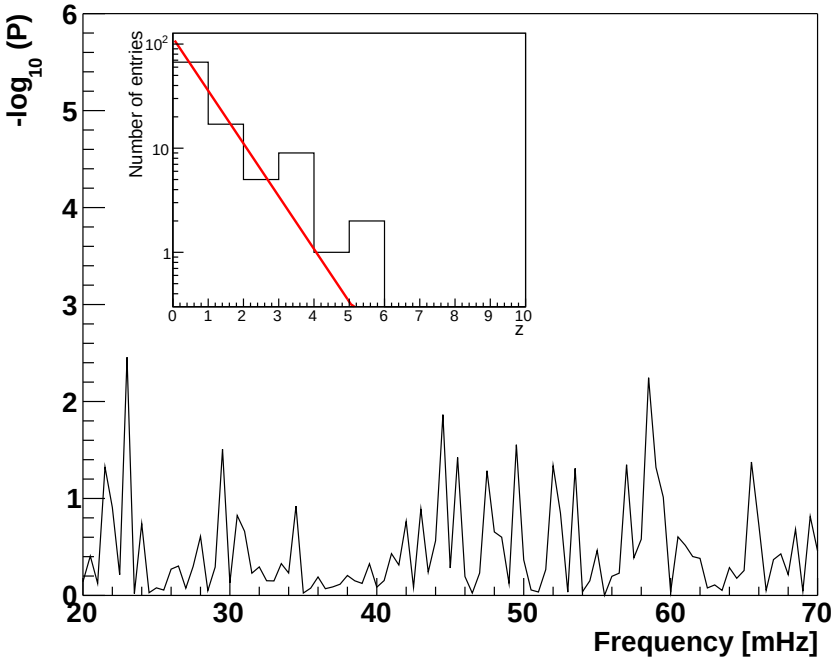

Figure 9.4: Periodogram of the frequencies in the range between 20.0 mHz and 70.0 mHz in steps of 0.5 mHz for the complete MAGIC dataset. The selected events have energies above 200 GeV. The plot in the inset represents the histogram of the Rayleigh power z for the complete MAGIC dataset.

9.4 Discussion

MAGIC observations did not confirm the previous reports of emission from AE Aqr. We report flux ULs from two to three orders of magnitude below the fluxes previously reported. Specifically, Meintjes et al. (2012), using the Nooitgedacht telescope, reported the detection of periodic signals with 95% C.L. significance in 30% of the observation time. Assuming that this is the typical behavior of the source and thanks to the higher sensitivity of MAGIC with respect to the Nooitgedacht telescopes, our observations should have produced signals with a large significance. We do not find any hint of a periodic signal. Regarding the reports of random VHE bursts from the Narrabri telescope (Bowden et al. 1992; Chadwick et al. 1995), because they do not follow any periodicity, they cannot be excluded by the results presented in this work. On the other hand, if one of such events had happened during our observations, we would have detected it.

There are several days when the source is at a state in the optical and X-rays higher than the baseline. In the B band, the source reached a state up to 1.5 magnitudes brighter than the quiescence state at magnitude 12.5. In X-rays, the highest state is about three times brighter than the baseline. This eruptive behavior is normal for this source. We searched for a correlation between the optical/X-ray emission and the γ-ray ULs. As shown in Section §9.3.3.1, flux ULs for the γ-ray emission are at the same level for all days, independently of the state of the source

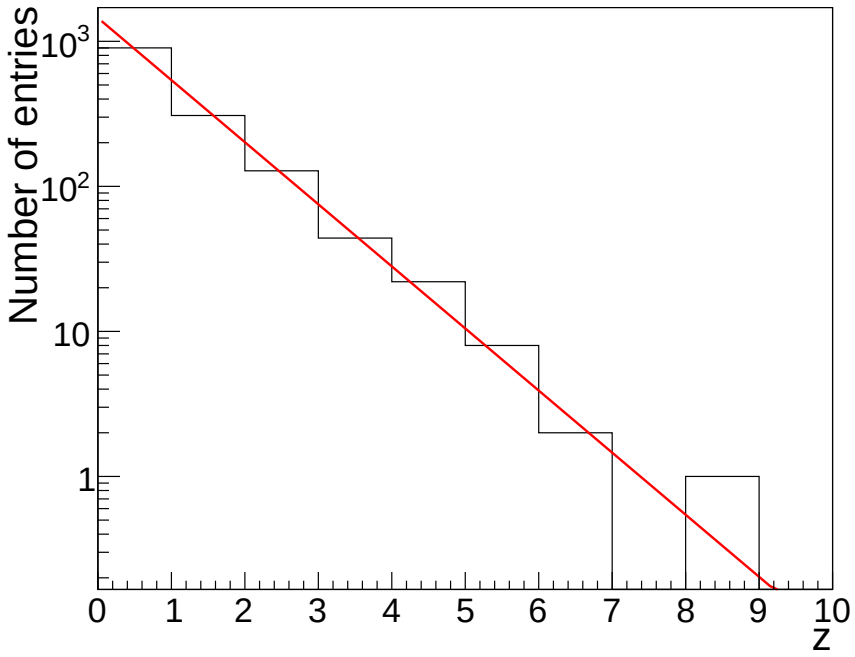

Figure 9.5: Histogram of the Rayleigh power z for events above 200 GeV for all frequencies and individual MAGIC observations.

in the optical or X-rays.

If we take the UL on the integral flux of Tables 9.1 and 9.4, we can calculate the UL of the γ-ray luminosity of AE Aqr. The UL on the luminosity for the steady emission of AE Aqr, considering a power-law function with photon spectral index 2.6, above 200 GeV is $L_{\gamma,E>200\mathrm{GeV}} < 6.8 \times 10^{30}\ d_{100}^2$ erg s^{-1}, where d_{100}^2 is the distance normalized to 100 pc and above 1 TeV is $L_{\gamma,E>1\mathrm{TeV}} < 3.9 \times 10^{30}\ d_{100}^2$ erg s^{-1}. The UL on the luminosity for the pulsed emission at 30.23 mHz and 60.46 mHz, considering a power-law with photon spectral index 2.6, above 200 GeV, are $L_{\gamma,E>200\mathrm{GeV}}[30.23\ \mathrm{mHz}] < 2.8 \times 10^{30}\ d_{100}^2$ erg s^{-1} and $L_{\gamma,E>200\mathrm{GeV}}\ [60.46\ \mathrm{mHz}] < 2.2 \times 10^{30}\ d_{100}^2$ erg s^{-1}.

To explain the large γ-ray fluxes measured in the past, Meintjes & de Jager (2000) proposed a model based on the propeller emission of particles that predicts large γ-ray fluxes, which are easily detected with the current generation of IACTs. The generation of VHE particles is based on the idea that a very high potential difference can be generated thanks to differences in the density of the gas present in a clumpy ring surrounding the WD. This model predicts luminosities of up to $L_\gamma \sim 10^{34}$erg s^{-1} during the largest bursts of the source, which would be able to explain the fluxes observed at $F > 10^{-10}$cm^{-2} s^{-1} by Meintjes et al. (1994) and Chadwick et al. (1995). To explain these luminosities, the model makes assumptions that do not match the observations, like the presence of an accretion disk. We present in this work ULs on the pulsed/steady γ-ray luminosities measured by MAGIC on the order of 10^{30} erg s^{-1}, which is several orders of magnitude below the prediction of the model.

Since there is evidence of non-thermal emission in the system, there has to be a mechanism that converts a fraction of the spin-down power into particle acceleration. To explain this non-thermal emission, there are mechanisms like the magnetic pumping in the magnetosphere (Kuijpers et al. 1997), which explains the radio outbursts as eruptions of bubbles of fast particles from the magnetosphere surrounding the WD, and the Ejector White Dwarf (EWD) model (Ikhsanov 1998), which describes a pulsar-like acceleration mechanism for AE Aqr and predicts the γ-ray emission of the system as well (Ikhsanov & Biermann 2006). Following the EWD model, the source emits TeV gamma rays during the optical highest state of the source ($B = 10$ mag) with a luminosity lower than $4{\times}10^{29}$erg s^{-1}. The UL for higher optical magnitudes derived in this work are one order of magnitude higher, therefore they do not conflict with our results. The future CTA (Acharya et al. 2013) will have a sensitivity that is roughly one order of magnitude better than the current sensitivity of MAGIC (Bernlöhr et al. 2013). The flux prediction for the high-level optical state is expected to be detectable by CTA.

9.5 Summary

We have observed AE Aqr simultaneously in VHE , optical and X-rays. This allows us to characterize the behavior of the source in different states. During our observations, the source displayed a level of brightness and type of variability that was consistent with previous observations in the optical and X-ray wavebands. We found a shift in the maximum of the spin-phase-folded X-ray light curve respect to the phase calculated with the most recent ephemeris of the source. We searched for steady γ-ray emission during the whole observation period, for enhanced emission coincident with different optical states and for pulsed γ-ray emission. We did not find any significant γ-ray signal from AE Aqr in any of the searches performed. We have established the most restrictive ULs so far for VHE emission (above 200 GeV and above 1 TeV) of this source, and of any other CV in general. The corresponding ULs are up to three orders of magnitude lower than some of the emission reports by the Nooitgedacht and Durham groups about two decades ago. The propeller model is a good candidate for explaining the emission from radio to X-ray energies. However, it is very unlikely to be responsible for the production of γ-ray photons in the way described in Meintjes & de Jager (2000), unless the probability of flaring events is less than reported. Finally, we note that the level of γ-ray emission predicted by the EWD model is consistent with our ULs, and it could be detected with CTA.

The results presented in this chapter are published in Aleksić et al. (2014d).